

AXIAL VECTOR AND PSEUDOSCALAR HADRONIC STRUCTURE

IN $\tau^- \rightarrow \pi^- \pi^- \pi^+ \nu_\tau$ DECAYS WITH IMPLICATIONS ON

LIGHT QUARK MASSES

A Thesis

Submitted to the Faculty

of

Purdue University

by

Jason W. Hinson

In Partial Fulfillment of the

Requirements for the Degree

of

Doctor of Philosophy

August 2001

To my parents, Dr. Billy and Mrs. Shirley Hinson, who raised me to be the person I am; my wife, Tabitha, who provided me with tremendous loving support; my baby daughter Hannah, a tiny miracle from whom I have gained great inspiration; and my Lord and Savior whose grace provided all I could ever need.

ACKNOWLEDGMENTS

I owe a great debt of gratitude to my thesis advisor, Edward Shibata. Ed has provided me with a tremendous amount of support and guidance over the years, without which I would have been lost. I could always count on him to offer straight answers and administer wise counsel, keeping me properly focused on the fundamentals of the work I pursued.

That pursuit would not have been possible without the hard work and dedication of the many people who keep CESR and CLEO running. When I first came to CLEO, I had the pleasure of working with Ahren Sadoff on dE/dx matters—one of many service tasks that must be performed. I gained great appreciation for such work, and am grateful to Ahren for the experience. To each and every one of the professors, students, technicians, and operators who have made data analysis possible at CLEO, I offer my sincere appreciation.

In particular, I would like to say a special word of thanks to Alan Weinstein whose expertise and vast knowledge provided an irreplaceable guide for my particular analysis. He repeatedly volunteered time out of a busy schedule to answer many of my questions and offered ample information on a wide range of concerns.

I would also like to thank Jean Duboscq for his willingness to listen to me chatter on with queries about my work and offer his own advice.

Using various analysis tools available at CLEO can sometimes prove confusing and aggravating, and I have many to thank for their guidance at one time or another, including Nobu Katayama, Craig Prescott, Rob Kutschke, and Brian Heltsley. I would like to say thank you to Dan Riley, Ray Ng, and Selden Ball for their excellent computer support, and to Joe Schmidt for his skillful assistance with hardware purchasing and installation.

I would be exceedingly remiss without mentioning Mary Bishai and Naresh Menon, fellow Purdue students, once officemates, and valued friends. Our many hours of spirited debates, lively discussions, and general raucousness made my stay at CLEO especially memorable and personally enriching. For that, I thank them.

In addition to my advisor, I offer my appreciation to the other members of my Ph.D. committee, Prof. David Koltick, Prof. Mark Haugan, and Prof. Tzee-Ke Kuo, for their willingness to serve. I would also like to thank Norman Fuchs who was on my committee before his retirement and whose work first sparked my interest in this particular analysis.

Finally, my deepest gratitude is offered to those to whom this thesis is dedicated: to my family—without their support I would never have made it here, and to my God who makes all things possible.

This work is supported in part by the U.S. Department of Energy, the National Science Foundation, and Purdue University.

TABLE OF CONTENTS

	Page
LIST OF TABLES	ix
LIST OF FIGURES	xii
ABSTRACT	xvii
1. A SURVEY OF CONCEPTS IN HIGH ENERGY PHYSICS	1
1.1 A Basic Description of High Energy Physics	1
1.2 Early Constituent Models	1
1.3 A Plethora of Particles	3
1.4 The Four Forces of Nature	6
1.4.1 Gravity	6
1.4.2 Electromagnetism	7
1.4.3 The Strong Force	8
1.4.4 The Weak Force	9
1.5 A Brief History of Quantum Mechanics	10
1.6 The Quantum Mechanical Description of Physics	17
1.7 Quantum Mechanical Properties of Particles	20
1.7.1 Bosons and Fermions	20
1.7.2 Parity	22
1.7.3 Charge-Conjugation	23
1.7.4 Time-Reversal	23
1.7.5 Isospin	24
1.7.6 G-Parity	25
1.7.7 Lorentz Behavior	25
1.8 Quantum Mechanical Treatment of Forces	27
1.8.1 A Simple Central Force	28
1.8.2 Scattering Cross-Sections	29
1.8.3 Describing Transitions	32
1.8.4 The Boson Propagator	36
1.8.5 Coupling Constants and Feynman Diagrams	38
1.8.6 Forces and Particle Decay	41
1.8.7 Revisiting the Four Forces	42
1.9 The Standard Model	45
1.10 Symmetries and Conservation Laws	50

	Page
1.10.1 Charge, Energy, and Momentum Conservation	54
1.10.2 Lepton Number and Baryon Number	55
1.10.3 Quark Generations and the CKM Matrix	56
1.10.4 Conservation Under \tilde{P} , \tilde{C} , and \tilde{T}	60
1.10.5 A Summary of Conserved Quantities	63
1.11 Renormalization	63
1.12 Gauge Invariance	69
1.13 Development of the Electroweak Theory	74
1.14 Modern Study of High Energy Physics	76
1.15 Particle Manipulation and Detection	77
1.15.1 Accelerating and Directing Charged Particles	78
1.15.2 Particle Detectors	82
2. THE CESR AND CLEO II EXPERIMENTS	89
2.1 The Cornell Electron Storage Ring	89
2.1.1 The Linear Accelerator	91
2.1.2 The Synchrotron	92
2.1.3 The Storage Ring	92
2.1.4 CESR Performance	94
2.1.5 Summary of CESR Operating Parameters	95
2.2 The CLEO II Detector	97
2.2.1 The Beam Pipe	100
2.2.2 The CLEO II Magnet	102
2.2.3 The Central Tracking System	103
2.2.4 The Time-of-Flight System	108
2.2.5 The Crystal Calorimeter	112
2.2.6 The Muon Detector	114
2.2.7 The Trigger System and Data Acquisition	117
2.2.8 General Event Reconstruction and Display	118
2.2.9 Summary of CLEO II Parameters and Resolution	119
3. INTRODUCTION TO THE ANALYSIS	125
3.1 Motivation for Studying the $\tau^\pm \rightarrow \pi^\pm \pi^\pm \pi^\mp (\bar{\nu}_\tau / \nu_\tau)$ Decay	126
3.2 Using a Model	127
4. DATA SAMPLE AND EVENT SELECTION	129
4.1 Backgrounds and Selection Results	136

	Page
5. THEORY AND MODEL	141
5.1 Description and Parameters of the Decay	141
5.2 The Differential Decay Rate and the Hadronic Current	143
5.3 Modeling the Extended Form Factors	145
5.3.1 Modeling the 1^+ Resonance	146
5.3.2 Modeling the 1^+ Substructure	149
5.3.3 Modeling the 0^- Resonance	151
5.3.4 Modeling the 0^- Substructure	152
5.4 Modeling the Reduced Form Factors	153
5.5 Model Variations	157
5.6 Final Form of the Differential Decay Rate	161
6. FITTING METHOD	162
6.1 Defining the True Kinematic Variables, \vec{x}	163
6.2 Correcting for Unmeasured Information	164
6.3 Correcting for Background	167
6.3.1 An Accepted Technique that Falls Short	167
6.3.2 Expanding that Technique to the Unbinned Case	170
6.3.3 Summary of Background Correction Method	171
6.4 Goodness of Fit	172
7. MONTE CARLO TESTS OF THE FIT	174
8. FIT RESULTS AND ANALYSIS	177
8.1 Presentation of Results	177
8.2 Systematic Errors	185
9. DISCUSSION	189
9.1 Model Comparisons	190
9.2 Significance of Isoscalar Resonances	192
9.3 Notes on Possible a_1' Hypothesis	192
9.4 Significance of Pseudoscalar Resonances	195
9.5 Comparisons to Other Results	197
9.6 Implications on the Light Quark Masses	204
10. CONCLUSIONS	206

	Page
BIBLIOGRAPHY	208
APPENDICES	
Appendix A: The Lagrangian and the Principle of Least Action	214
Appendix B: Notes on Four-Vectors and the Metric Tensor	218
Appendix C: Common Wave Equations	223
Appendix D: A Simple Example of a Symmetry Group	233
Appendix E: A Simple Example of Spontaneous Symmetry Breaking	236
Appendix F: The Lepton Tensor in $\tau^\pm \rightarrow \pi^\pm \pi^\pm \pi^\mp (\bar{\nu}_\tau / \nu_\tau)$ decays	238
Appendix G: Another Description of the Decay	240
Appendix H: The γ Distribution	246
Appendix I: Placing a Lower Bound on the Light Quark Masses	248
VITA	252

LIST OF TABLES

Table	Page
1.1 Summary of the four forces and their gauge boson field quanta. [25,29]	46
1.2 The fundamental fermions (all 1/2 spin) and their properties [29]: M = mass, Q = charge (in multiples of the electron charge, e), τ = mean life time (not applicable to quarks, but only to the hadrons they make up).	48
1.3 Hadron examples and their properties. [29]	49
1.4 Quantum numbers of the quarks.	59
1.5 Summary of conservation rules.	64
2.1 A summary of operating parameters for CESR during the running of CLEO II.	96
2.2 Parameters of the CLEO II superconducting coil.	122
2.3 Parameters of the CLEO II central tracking system.	122
2.4 Parameters of the CLEO II time-of-flight system.	123
2.5 Parameters of the CLEO II crystal calorimeter.	123
2.6 Parameters of the CLEO II muon detector.	124
2.7 Parameters of the CLEO II trigger system.	124
4.1 Summary of event selection criteria	133

Table	Page
4.2 Makeup of the τ background according to Monte Carlo studies. The “% of selected events” is the percentage of each mode in the final selection after accounting for difference between the PDG \mathcal{B} fractions and the percentage of input events found for each mode. The PDG basis modes sum to 99.995% due to round off, and the remaining 0.005% is arbitrarily assigned to all modes not found in the PDG basis.	140
5.1 Masses and widths of particles used in this analysis.	152
7.1 Results of a first test fit to Monte Carlo data.	175
7.2 Results of second test fit to Monte Carlo data	176
8.1 Results of the fit to the nominal model. Statistical and systematic errors are shown respectively. The branching fractions are calculated from the squared amplitudes and are normalized to the total $\tau^\pm \rightarrow \pi^\pm \pi^\pm \pi^\mp (\bar{\nu}_\tau/\nu_\tau)$ rate. They do not sum to 100% due to interferences between the amplitudes.	178
8.2 Results of fit to model variation 1. Statistical and systematic errors are shown respectively. The branching fractions are calculated from the squared amplitudes and are normalized to the total $\tau^\pm \rightarrow \pi^\pm \pi^\pm \pi^\mp (\bar{\nu}_\tau/\nu_\tau)$ rate. They do not sum to 100% due to interferences between the amplitudes.	179
8.3 Results of fit to model variation 2. Statistical and systematic errors are shown respectively. The branching fractions are calculated from the squared amplitudes and are normalized to the total $\tau^\pm \rightarrow \pi^\pm \pi^\pm \pi^\mp (\bar{\nu}_\tau/\nu_\tau)$ rate. They do not sum to 100% due to interferences between the amplitudes.	180
8.4 Systematic errors for the fit to the nominal model (continued on next table).	187
8.5 Continuation of systematic errors for the fit to the nominal model. .	188
9.1 Amplitudes used by ARGUS [73]. Their fit significance and relative branching fraction are also given. Coupling constants for these amplitudes were made Q^2 dependent to get an acceptable fit.	199

Table	Page
9.2 Amplitudes used by an earlier CLEO study of $\tau^\pm \rightarrow \pi^\pm \pi^0 \pi^0 (\bar{\nu}_\tau / \nu_\tau)$ decays [60]. Their reported significance and relative branching fractions are also listed.	202
Appendix	
Table	
D.1 Combinations of symmetry operators on an equilateral triangle. . .	235

LIST OF FIGURES

Figure	Page
1.1 Elements in the definition of the scattering cross section. All beam particles passing through the area $d\sigma$ are scattered into the solid angle $d\Omega$	30
1.2 Feynman diagrams for several electromagnetic processes	39
1.3 Feynman diagrams showing internal “corrective” processes for a scattering event.	65
1.4 Feynman diagrams showing internal “corrective” processes via self-interaction.	66
1.5 Feynman diagrams showing some radiative corrections to the electron’s magnetic moment.	68
1.6 A diagram depicting a simple proton linear accelerator. Alternating potentials on the tube segments propel the proton, and successively longer segments are needed so the proton traverses each segment in the same length of time while it is also being accelerated.	78
1.7 A generic RF cavity geometry showing electric and magnetic field lines. The peak of the oscillating electric field is strongest through the central axis of the cavity while the magnetic field is constrained towards the equatorial region of the cavity.	80
1.8 Cross-sectional diagrams of a dipole bending magnet (a) and a quadrupole focusing magnet (b). Thin arrows indicate the magnetic field lines while thick arrows show the force direction on a positive charge moving “into” the page.	81
2.1 Diagram of the Cornell Electron Storage Ring (CESR)	90
2.2 Peak (instantaneous) luminosities at CESR	94
2.3 Integrated luminosity per year at CESR	95

Figure		Page
2.4	A three dimensional illustration of the CLEO II detector displaying its cylindrical design.	97
2.5	A side view and end view of the CLEO II detector. The end view provides a different cut-away segment in each quadrant.	99
2.6	A close-up side view showing one quarter of the CLEO II detector.	101
2.7	A section of the PTL and CD systems showing cell layouts.	104
2.8	Cathode strip placement in the VD	106
2.9	Cell structure of the outer drift chamber (DR).	107
2.10	Cathode strip placement in the DR	108
2.11	Plot of specific ionization (dE/dx) versus momentum for different particle types	109
2.12	Side view of a single barrel TOF counter and connectors	110
2.13	Configuration of End-cap TOF counters	111
2.14	A graph of $1/\beta$ versus momentum (from measurements in the barrel TOF and drift chambers) for different particle types.	112
2.15	A section of the holder for crystals in the barrel CC	113
2.16	Layout of the end-cap crystals	114
2.17	Schematic of muon chamber tubes	115
2.18	Layout of muon chambers in a super-layer	116

Figure	Page	
2.19	A CLEO II event display example showing a $e^+e^- \rightarrow \mu^+\mu^-\gamma$ Monte Carlo (computer simulated) event. The central region shows an $r-\phi$ projection of tracks in the CD (PTL, VD, and DR). A thin strip surrounding the DR shows hits in the barrel TOF. Out from there, hits in the barrel CC are displayed as if looking down the inside of a tube, providing information on hits in ϕ and z (with inner circles nearer the east end and outer circles nearer the west end of the detector). Finally, an $r-\phi$ projection of hits in the barrel muon chambers is given. In the event shown, the μ^\pm CD tracks leave hits in the calorimeter and clear tracks in the muon chambers. This is also a radiative event, and the photon (γ) was measured in the calorimeter. Random hits also appear from various sources of noise.	120
2.20	A CLEO II event display example showing an $e^-e^+ \rightarrow B^-B^+$ Monte Carlo event with each B further decaying in the detector. The decay chain for each is shown. The B , D , K^0 , η , ν , and π^0 particles do not appear in the detector and in practice are inferred from the data. Particle labels have been added for illustration.	121
4.1	Display of p_{miss}^t vs. E_{miss} cuts and the effects on their 1-D projections. On comparison plots, the points mark data and the solid histogram marks the τ Monte Carlo	134
4.2	Event display of a Monte Carlo accepted event where the tag side is $\tau^- \rightarrow \rho^- \bar{\nu}_\tau \rightarrow \pi^- \pi^0 \bar{\nu}_\tau \rightarrow \pi^- \gamma \gamma \bar{\nu}_\tau$	137
4.3	Event display of a Monte Carlo accepted event where the tag side is $\tau^+ \rightarrow \mu^+ \bar{\nu}_\tau$. The hits in the muon chamber on the tag side can be seen clearly.	138
5.1	Feynman diagrams for a $\tau^- \rightarrow \pi^- \pi^- \pi^+ \nu_\tau$ process. The dominant resonance structure is shown through $a_1^- \rightarrow \pi^- \rho^0 \rightarrow \pi^- \pi^- \pi^+$. The two diagrams indicate an ambiguity from not knowing which π^- was produced from the ρ^0	142

Figure	Page
6.1 Demonstrations of the goodness of fit method by comparing log-likelihood distributions for data (represented by points) and Monte Carlo (represented by the solid histograms). Figure (a) displays such results for a fit with g.o.f. $\sim 0.6\sigma$, while (b) displays such results for a poor fit with g.o.f. $\sim 9.0\sigma$. The fits used for these plots were (a) the nominal fit to the data and (b) a fit without isoscalar resonances. Both fits are discussed below.	173
8.1 Display of nominal fit results in projections of Q^2 , s_1 , s_2 , β , γ , $\cos\theta$, and $\cos\psi$ (see Appendix G). The points represent the data, while the solid histograms show the fit results, and the shaded regions display the background distributions.	181
8.2 Display of nominal fit results in distributions of s_1 for various bins of Q^2 . The points represent the data, the solid histograms indicate the fit results, and the shaded regions display the background distributions.	182
8.3 Display of nominal fit results in distributions of s_2 for various bins of Q^2 . The points represent the data, the solid histograms indicate the fit results, and the shaded regions display the background distributions.	183
8.4 Display of nominal fit results on two dimensional distributions of s_1 and s_2 in different Q^2 bins. For each bin, data distributions are shown on the left while distributions generated from the fit are displayed on the right.	184
9.1 Display of s_1 distributions in various bins of Q^2 resulting from fitting without isoscalar resonances. The points represent the data, the solid histograms indicate the fit results, and the shaded regions display the background distributions.	193
9.2 Display of s_2 distributions in various bins of Q^2 resulting from fitting without isoscalar resonances. The points represent the data, the solid histograms indicate the fit results, and the shaded regions display the background distributions.	194

Figure	Page
9.3 An OPAL result showing a Dalits plot projection of their background- and efficiency-corrected data (points with error bars), a fit result to the KS model (solid line), and a fit result to the IMR model (dashed line). The dotted line shows the polynomial background contribution for the IMR model.	201
9.4 Plots comparing results from [60] adapted to the all charged mode (dashed histogram) to current results (solid histogram) and data (points). Shown are distributions in Q^2 , s_1 , s_2 , and a combination of s_1 and s_2 (two entries per event).	203
 Appendix	
Figure	
D.1 An equilateral triangle with vertices and symmetry axes marked. . .	233
G.1 A representation of the S system defined in the 3π rest frame such that z is perpendicular to the 3π plane and $x = \hat{q}_3$. Also shown are two of the Euler angles, β and γ (see Figure G.3).	242
G.2 A representation of the S' system defined in the 3π rest frame. The x' and z' axes are defined such that \vec{q}_τ lies in their plane (ψ being the angle between z' and the τ direction in this frame).	242
G.3 A display of the eular angles, α , β , and γ , which relate the S frame to the S' frame.	242

ABSTRACT

Hinson, Jason Ward. Ph.D., Purdue University, August, 2001. Axial Vector and Pseudoscalar Hadronic Structure in $\tau^- \rightarrow \pi^- \pi^- \pi^+ \nu_\tau$ Decays with Implications on Light Quark Masses. Major Professor: Edward I. Shibata.

After a survey of the basic concepts in high energy physics, a model-dependent analysis of the substructure in $\tau^\pm \rightarrow \pi^\pm \pi^\pm \pi^\mp (\bar{\nu}_\tau/\nu_\tau)$ decays is presented. The analysis is based on 145,000 decays skimmed from a sample of $4.3 \times 10^6 e^+ e^- \rightarrow \tau^+ \tau^-$ events collected by the CLEO II detector operating at the CESR collider. The hadronic transition current in the $\tau^\pm \rightarrow \pi^\pm \pi^\pm \pi^\mp (\bar{\nu}_\tau/\nu_\tau)$ decay is described by modeling the axial vector $a_1(1260)$ and pseudoscalar $\pi'(1300)$ primary resonances and their sub-resonances. An unbinned maximum likelihood fit is used to extract the complex amplitude for each sub-resonance, producing a distribution that accounts well for the data. Two model variations are also considered, including one in which corrections due to a more general chiral limit induce pseudoscalar-like terms from the axial vector components and introduce a non-resonant term. All models are found to reasonably describe the data. As expected, the decay is found to be dominated by s -wave $a_1 \rightarrow \rho\pi$, which contributed around 70 – 75% of the $\tau^\pm \rightarrow \pi^\pm \pi^\pm \pi^\mp (\bar{\nu}_\tau/\nu_\tau)$ rate, depending on the model used. Statistically significant

contributions are also found for d -wave $\rho\pi$ and $\rho'\pi$ amplitudes as well as amplitudes involving isoscalars, $f_2(1270)\pi$, $\sigma\pi$, and $f_0(1270)\pi$. The isoscalar contributions are particularly prominent, as are interferences involving those terms. As a whole, they contributed around 15 – 17% to the total $\tau^\pm \rightarrow \pi^\pm \pi^\pm \pi^\mp (\bar{\nu}_\tau/\nu_\tau)$ rate, depending on the model. Contributions from the pseudoscalar π' sub-resonances are generally statistically insignificant, though their minimal improvements are shown to lie where one would expect. Upper limits are placed on each of the considered π' contributions at 90% confidence. The results found for the pseudoscalar contributions are used to place a lower limit on the average of the up and down quark running masses [$\hat{m} \equiv (m_u + m_d)/2$] that appear in the QCD Lagrangian [57]. This produced a 90% confidence limit of $\hat{m}(1 \text{ GeV}^2) > 8.3 - 14.2 \text{ MeV}$, depending on the model. Though that result may be higher than expected, it is reasonable given the particulars of the analysis.

1. A SURVEY OF CONCEPTS IN HIGH ENERGY PHYSICS

This chapter is committed to providing a broad overview of the most fundamental concepts in high energy physics. It serves as both a source of general introductory material for the analysis discussion to follow and, for the interested reader, as a condensed guide into the field of physics to which this thesis is ultimately dedicated.

1.1 A Basic Description of High Energy Physics

High energy physics, also known as particle physics, is the field of science dedicated to studying the most fundamental building blocks of matter and their interactions. It is framed on the postulate that all matter in the physical universe consists of elementary particles, and that these particles can be categorized according to their physical properties. By deducing a relatively small number of particle types and understanding the basic ways they interact with one another, particle physics endeavors to produce an elementary framework that describes the intricacy and scope of the physical universe we experience.

1.2 Early Constituent Models

The modern stage of breaking matter down into elemental parts goes back to the early 19th century when the belief in constituent particles began to gain ground.

Any substance was believed to consist of many identical particles, each of which possessed the properties of that substance. By 1803, the chemist John Dalton had developed the main features of the basic atomic theory, which postulated that all matter is composed of small particles, called atoms. In 1869, chemists Dmitri Mendeleev and J. Lothar Meyer independently discovered that the atomic elements could be arranged by atomic weight to produce an orderly array that organized them into groups of similar properties. The *periodic table* helped bring order to the disarray of the atomic elements, though an ultimate interpretation of the ordering scheme was not understood until much later.*

In the late 19th century, various studies of the electromagnetic properties of atoms indicated that they likely possessed internal structure. In 1897, J. J. Thomson experimentally showed that beams in a cathode ray tube consisted of charged particles, each of which had the same charge-to-mass ratio, q/m [2]. This crucial experiment represented the discovery of the electron as a fundamental particle, and by 1900 it was generally acknowledged that electrons were somehow part of the atomic structure. Thomson modeled the atom as a positively charged volume with negatively charged electrons scattered throughout to produce a generally neutral atom. However, the famous Rutherford scattering experiment showed that a proper explanation of the atom had to place the positive charges into a concentrated region. In 1911, Ernest Rutherford proposed a model in which the positively

*Information concerning early atomic theory is found in basic chemistry texts, including [1].

charged particles (which he previously named protons) were contained in a central nucleus while the negative electrons orbited the nucleus, picturing the atom as similar to a planetary system [3].

Further experiments showed that the nucleus itself contained structure, and in 1932, James Chadwick discovered the neutron, a neutral particle that accompanies protons in the nucleus of the atom [4]. Thus, we picture the matter around us as being composed of electrons, protons, and neutrons. In the 1960's, first theory and then experiment concluded that protons and neutrons possessed internal structure as well, and were made of particles called quarks. These particles will be discussed in Section 1.9; however, the discovery of quarks and their significance came about only after a much more complicated picture of the fundamental particles arose.

1.3 A Plethora of Particles

While electrons, protons, and neutrons produce the matter we interact with daily, many particles of matter have been discovered in this century that do not generally exist within the atom. These exotic particles have short lifetimes and quickly decay into more stable particles; thus they are not part of ordinary matter. However, these particles can be produced in high energy collisions. Such collisions can occur naturally as high energy particles from outer space collide with particles in our upper atmosphere. Study of these cosmic rays and the particles they produce began in the 1930s.

By the early 1950s, physicists were moving from cosmic ray studies to more controlled laboratory experiments performed with particle accelerators. Particle accelerators use electric fields to accelerate charged particles to high energies and collide them with other particles. The energy released in these collisions can form exotic short-lived particles that can then be studied by instruments placed around the interaction point (see Section 1.15 for more information about particle manipulation and detection).

The study of cosmic rays and subsequent experiments with particle accelerators has generated a large number of particle discoveries. One of the earliest such discoveries was that of the muon (μ) in 1937 by Carl D. Anderson and Seth Neddermeyer [5]. It was a charged particle with properties similar to that of the electron, though it had a much greater mass and decayed into other particles in a short period of time. Knowing that muons were not part of the fundamental makeup of everyday matter, a theorist named Isidor Isaac Rabi is said to have met its discovery with the exclamation “who ordered that?”

The detection of the *pion* (π) [6] and the *kaon* (K) [7] in cosmic rays in 1947 is sometimes considered the birth of the most modern era of particle physics as it became obvious that uncommon particles existed and had to be taken into account to properly describe the physical universe. In the 1950s, the *Lambda* (Λ) particle and the heavier *Sigma* (Σ) and *Cascade* (Ξ) particles were discovered [8–10]. These particles were called *hyperons*; and, along with kaons, they possessed odd properties compared to protons, neutron, and pions. They were thus assigned

a unique attribute aptly called *strangeness*. In 1953, the electron neutrino (ν_e) was discovered [11]. Predicted in 1930 by Wolfgang Pauli, it is a neutral cousin of the electron that possesses little or no mass [12]. Neutrinos are stable particles, but they rarely interact with other matter. In 1963, the team of Schwartz, Lederman, and Rochester discovered a correspondent cousin to the muon, the muon neutrino (ν_μ) [13]. In 1977, Martin Perl discovered the tau (τ), a charged particle with properties similar to the electron and muon but much heavier than either [15]. Like the electron and the muon, the tau was assumed to have a nearly massless companion neutrino (ν_τ), and while analyses clearly indicated that tau decays produce neutrinos, the first direct evidence for the distinctive tau neutrino was recently produced in 2000 at Fermi National Laboratory (FNAL) [14].

To date, over 200 different particles have been discovered, producing a seemingly complicated picture of particle physics.* However, through the years a model has also been developed to describe all of these particles with a much smaller list of fundamental particle types and their interactions. The modern explanation of these fundamental particles is called the *standard model*, and it is discussed in Section 1.9. The standard model not only incorporates the fundamental particles of matter, but also describes the forces between the particles. The understanding of these forces has been developed over many years, in conjunction with the study of the particles of matter themselves.

*Part of the reason quarks were postulated was to help explain this particle zoo.

1.4 The Four Forces of Nature

In order for particles to form the universe that we experience, they must obviously interact with one another. Today physicists identify four fundamental forces necessary to describe all physical interactions. They are gravity, electromagnetism, the strong nuclear force, and the weak nuclear force.

1.4.1 Gravity

In 1687, Isaac Newton published work claiming that any two massive bodies attract one another by a force proportional to the product of the two masses and inversely proportional to the square of the distance between them [16]. This suggested that a force, gravity, somehow acted over great distances to allow one body to influence another. This was the first explanation of a modern day force, though many years later Albert Einstein would change our understanding of gravity.

In 1905, Albert Einstein published his special theory of relativity, which combined space and time into a single fabric, the space-time manifold [17]. The relationship between space and time explained how different observers moving with respect to one another would measure space and time differently, and how all such observers would measure the same, constant speed of light (c). This new relationship between moving observers required a change in the way we define energy and momentum so that these quantities would be conserved for all such observers, and this led to the realization that mass itself was simply a convenient form of energy ($E = mc^2$). In 1916, Einstein produced the general theory of relativity, which

successfully explained relativity in light of gravitation [18]. It was effectively a new theory of gravity in which curved space-time replaced Newton's gravitational fields. Objects are said to travel on what seem to be straight lines in space-time; however, mass—and in fact any form of energy—warps space-time into a curved manifold, and the straight lines through space and time become curved. Our three-dimensional view of objects moving through curved space-time is what we interpret as a gravitational force.

In Section 1.8, it will be noted that gravity still doesn't fit into the picture of the other three fundamental forces as neatly as physicists would like. However, it is certainly one of the four fundamental force of nature, and in relative terms, it is the weakest of the four (requiring very large masses before its effects are evident).

1.4.2 Electromagnetism

Electricity and magnetism were once considered entirely separate subjects*. However, in 1820, Hans Christian Oersted discovered that a compass needle could be deflected by an electric current in a wire, causing the needle to orient itself perpendicular to the wire. Within days of hearing of the discovery, Andre Ampère hypothesized that all magnetic phenomena were caused by charged particles in motion, and in 1831, Michael Faraday discovered that a changing magnetic field induced an electric current in a nearby wire loop. Maxwell and Lorentz finished

*A history of the development of electromagnetism can be found in a variety of basic texts including [19].

off the theory to combine electricity and magnetism, which were then understood to be two aspects of the same force: electromagnetism.

Relatively speaking, the electromagnetic force is many times greater than the gravitational force (the electromagnetic repulsion between two electrons, for example, is 10^{42} times greater than the gravitational force between them). Electromagnetism is the force that holds negatively charged electrons in their orbits around positively charged nuclei. When two objects meet, it is the electromagnetic force that keeps one from passing into the other. It is the force behind friction as well, and it produces the binding forces in chemistry. Waves of electromagnetic energy range from radio waves to visible light to microwaves to powerful gamma rays. Electromagnetism is obviously a pervasive force, and its effects are important in both the microscopic and macroscopic realms.

1.4.3 The Strong Force

The last two forces are termed “nuclear” forces because their effects are most prominent within the nuclei of atoms*. The strong force is believed to involve three “strong charges” and their inverse counterparts, termed *colors* and *anticolors* in a theory called *chromodynamics*. The aforementioned quarks possess these color charges and are attracted to one another in various ways via the strong force, thus forming various particles such as protons and neutrons. Protons and neutrons within a nucleus are held together by the strong attraction between their

*Basic texts containing information concerning both the strong and weak nuclear forces include [23, 25].

constituent quarks (otherwise, the nucleus would fly apart due to electromagnetic repulsion between the positive protons).

As its name might suggest, the strong force is the strongest of the four forces; however, it is found to be confined within extremely short-ranged interactions. For that reason, we do not experience the strong force in the macroscopic domain.

1.4.4 The Weak Force

The weak nuclear force is comparatively stronger than gravity but weaker than electromagnetism. Like the strong force (but for different reasons, see Section 1.8.7) the effects of the weak force are confined to a limited range. Because of its weakness and limited range, the weak force is generally dominated by the strong and electromagnetic forces, and it does not play a direct role in holding matter together (such as the strong force holding quarks together, the electromagnetic force holding electrons in their orbits in atoms, and the gravitational force holding planets in their systems). However, in cases where those other forces cannot cause an interaction, it is possible to directly observe the weak force. For example, a neutrino (with no charge and no “color”) can interact with an electron via the weak force, but not through the electromagnetic or strong forces. It is also possible to observe the weak force in interactions that cause one type of quark to change into another (because such a change is forbidden in strong and electromagnetic interactions, as will be noted later).

The weak force is perhaps best known for its role as a mediator of particle decay (another property of forces, as discussed later). The most well known weak decay is *nuclear beta decay* in which a neutron in the nucleus of an atom decays (through the weak force) into a proton, an electron, and an electron antineutrino ($n \rightarrow p e^- \bar{\nu}_e$). Further understanding of the relationship between forces and decays requires a discussion of quantum mechanics, as provided in the next few sections.

1.5 A Brief History of Quantum Mechanics

In the year 1900, Max Plank worked to describe a process known as *black body radiation* (radiation emitted by an object that absorbs all energy impinging on it, thus appearing black) [20]. To successfully describe the energy levels of such radiation, Plank took an extraordinary step by assuming that for a given frequency, only certain special energy levels could be emitted (specifically, the energy emitted at frequency ν had to be an integer multiple of $E = h\nu$, where h is now known as *Plank's constant*). This effectively quantized the energy levels for a given frequency, and Plank won the 1918 Nobel Prize for Physics for this work.

In 1905, Einstein published a paper concerning the *photoelectric effect*, which further espoused the quantization of energy [21]. It was known that light striking certain metals liberated electrons from the metal, but regardless of the light's intensity, it would only cause this photoelectric effect if its frequency was above some threshold (given the metal). Einstein suggested that energy from the light could not simply build up in the electron until it was liberated; rather, the light

had to interact in specific packets of energy (photons) dependent on the frequency of the light as Plank had suggested ($E = h\nu$). Thus, to liberate an electron, one quanta of light energy had to be strong enough to do the job—the frequency had to be above some minimal level while higher intensity (or number of quanta) alone would not suffice. Light had been known to travel like a wave, but Einstein's proposal suggested that it interacted with matter as particle-like quanta. Einstein won the 1921 Nobel Prize for Physics for this work

In 1913, Niels Bohr applied quantum theory to the structure of the atom [22]. Light emitted by excited hydrogen atoms had been observed to only possess certain energies. The specific levels of light energy emitted could be displayed as discrete bands in a light spectrum and was known as the Balmer series (measured by Johann Balmer in 1887 [23]). It was assumed that the light must come from electrons in the atoms losing energy as they shifted from higher energy states to lower ones. However, physicists were puzzled as to why such energy should only come at discrete levels or why the electrons wouldn't simply loose all their energy and fall into the nucleus. Bohr was able to account for the Balmer series with considerable accuracy. Under his model, electrons in the atom could only exist at specific distances away from the nucleus. Those distances had to be consistent with specific orbital angular momenta: $L \equiv mvr = nh$ where $n = 1, 2, 3, \dots$, thus quantizing angular momentum with a *quantum number*, n . The electrons could then only exist at certain energy levels and could only absorb and re-emit energy that allowed them to make quantized jumps between the energy levels without ever

existing in intermediate energy states. This explained why only certain, specific bands of light were seen in the Balmer series; however, the model was not complete, and the field of quantum mechanics exploded to better explain atomic theory and other experimental data.

In 1925, Werner Heisenberg developed what would turn out to be a complete and consistent description of quantum mechanics using matrix algebra. It was intrinsically a highly mathematical formulation. In 1927 he developed his famous *Uncertainty Principle*, which claimed that for certain sets of observables (called non-commuting), it was impossible for a quantum mechanical system to possess precise values for each observable in a given set. The most often noted set of non-commuting observables is that of momentum (p) and position (x), such that the uncertainty in these variables must be constrained by the inequality $\Delta p \Delta x \geq \hbar/2$ (where \hbar is a convenient notation for $\frac{h}{2\pi}$). A closely related set of non-commuting observables is that of energy and time* (i.e. the time at which a system is measured to have the given energy), thus $\Delta E \Delta t \geq \hbar/2$. [23]

While light was understood to exhibit both wave-like properties (in describing its motion) and particle-like properties (by interacting only as energy “packets”), in 1924 Louis de Broglie postulated that normal particles, like electrons, also possessed wave-like properties. The matter-wave of a particle at a given momentum (p) was claimed to have a *de Broglie wavelength* of ($\lambda = h/p$). [23]

*For an indication of why energy may be connected to time as momentum is connected to space, see Appendix B.

However, it was Erwin Schrödinger who, in 1926, formulated a more complete wave-like description of particles whose *wave functions* were determined from the Schrödinger wave equation—one of the most basic equations of quantum mechanics formed from classical Hamiltonian equations (see Appendix C). The square of a particle’s wave function was then interpreted by Max Born as the probability density of finding the particle . This provided a new picture of the physical universe: point-like particles moving in precise causal paths were replaced by cloud-like formations describing the probability of interacting with the particle over a given region. In atomic theory, no longer did the electrons follow precise orbits, but rather they existed in cloud-like “orbitals,” which described their probability distribution around the nucleus depending on quantized variables: their average distance from the nucleus and their orbital angular momentum. [23]

Meanwhile, better instrumentation and measurements revealed that the bands in the spectrum of light emitted by excited atoms were divided into smaller bands than previously noted (as mentioned above). Contemporary applications of quantum mechanics to atomic theory did not explain this *fine structure splitting*. In 1925, Wolfgang Pauli suggested a new quantum variable that gave each electron in an atom a “two-valuedness” and provided a more complete picture of quantum atomic theory. Samuel Goudsmit and George Uhlenbeck attributed this new property to an intrinsic angular momentum possessed by electrons. The energy levels of electrons in an atom weren’t simply a property of the orbital they were in (and thus their orbital angular momentum), but also depended on the alignment

of their intrinsic angular momentum. This provided more energy levels for the electron to “jump” between and thus predicted more energy bands in the spectra of light emitted by the atoms, properly accounting for the additional fine structure splitting seen in the light spectra. The resulting atomic theory was also able to explain the variety and characteristics of all known atoms, neatly accounting for their places in the periodic table. [23]

The intrinsic angular momentum of an electron was imagined to be created as if the electron were a small spinning ball of charge, and the quantum property was thus given the name “spin.” Electromagnetic effects caused by the “spin” of a particle (which gives it an intrinsic magnetic moment) can be measured along some given axis, often considered to be the z axis. Along that axis, a given particle will exhibit a specific, quantized angular momentum value (equal to some multiple of $\hbar/2$, depending on the particle type) that is either aligned or anti-aligned with that axis, thus providing a “two-valued” quantum number. Subsequent study of the electron “spin” indicated that its electromagnetic effects were not fully consistent with an actual spinning ball of charge, and thus the term “spin” is something of a misnomer for describing the quantum property of intrinsic angular momentum.

Another important step in quantum mechanics came when Paul Dirac, in 1928, provided an application of quantum theory consistent with special relativity (whose energy equations are intrinsically of second order). The resulting Dirac equation provided important insight into the quantum mechanical description of the electron. One result was the prediction of electrons in both positive and negative

energy states. Dirac interpreted the negative energy states in terms of particles with identical mass to the electron but with the opposite charge. He predicted these *antielectrons* (or *positrons*) in 1931, and they were established experimentally in 1932. Dirac further predicted that for all particle types there existed associated antiparticles, and this antimatter concept has since been experimentally verified, becoming an integral part of high energy physics. See Appendix C for more information. [23]

In 1941, Richard Feynman developed a description of quantum mechanics in which one considers every single possible way in which a system could progress from one state to another. For example, a photon could move from A to B along a straight path, along a curved path, along a path that bounced around in space a few times before reaching B, along a path that paused half way between the two before continuing, etc., etc. Each possibility was considered to have the same overall probability amplitude, but given the different paths taken, each had a different phase (in essence, the amplitudes were like clock dials pointing in different directions in a conceptual “amplitude space”). When one properly combined all the amplitudes from all the possibilities (essentially adding the vectors in the amplitude space) the result gave the overall probability amplitude of the given event. As it turns out, the amplitudes from many of the “odder” possibilities can tend to cancel one another out in the final result, and the path of “least action” generally provided the largest contribution to the probability amplitude (see Appendix A).

Though this technique was mathematically equivalent to the matrix and wave formulations mentioned above, it provided what many felt was a more natural way of thinking about quantum mechanical probabilities: The probability of an event was a combination of all possible histories that could conceivably create that event. All the possibilities were treated equally, with equal amplitudes, and only the action of each gave it a different phase. When combined in a natural way, this “sum over histories” provided the final probability amplitude of the event. Feynman also created diagramming tools (known as Feynman diagrams, which are discussed in Section 1.8.5) to help visualize and apply his technique to various particle interactions. Feynman’s technique was first applied to the quantum mechanical description of electromagnetic interactions (quantum electrodynamics, or QED), and its success in describing practically all electrodynamic phenomena has strongly associated Feynman’s name with QED [23, 24].

A wide variety of contributions by these and other important players in the realm of quantum mechanics has produced a current theory that is extremely accurate in its description of experimental outcomes and is arguably the most well established theory in modern physics. It has radically altered our description of fundamental physical phenomena (and also suggested strange metaphysical concepts such as non-locality, the breakdown of causality, the existence of many “parallel” realities, etc.—all of which are beyond the scope of this dissertation). Though debate continues over the philosophical implications of quantum mechanics, its mathematical description of physical phenomena provides an undeniably

powerful physics tool. A general overview of its description of physics will be presented in the following section.

1.6 The Quantum Mechanical Description of Physics

In quantum mechanics*, particles are treated mathematically as wave functions in space-time (typically denoted $\psi(\mathbf{x})$, where \mathbf{x} is a space-time four-vector as discussed in Appendix B). The position of the particles over time is described by a probability distribution derived by properly squaring the wave function ($|\psi|^2 = \psi^\dagger\psi$ in the most general case—see Appendix C). Measuring some physical property of a particle (e.g. its momentum, energy, position, etc.) is represented by an operator acting on the wave function. The expectation value of a measured property q (with an associated operator \tilde{Q}) is the average measured value of q expected from a system in a specific state. It is determined from the equation $\langle q \rangle = \int \psi^\dagger(\mathbf{x})\tilde{Q}\psi(\mathbf{x})d\mathbf{x}$, which is sometimes denoted $\langle q \rangle = \langle \psi|\tilde{Q}|\psi \rangle$. Examples of often used operators are the total energy (or Hamiltonian) operator, $\tilde{H} \equiv i\hbar\frac{\partial}{\partial t}$, and the momentum operator, $\tilde{p}_i \equiv -i\hbar\frac{\partial}{\partial x_i}$ (or $\tilde{\mathbf{p}} \equiv -i\hbar\vec{\nabla}$).

The actual form of a wave function for a given situation is derived from a proper wave equation (such as the aforementioned Schrödinger wave equation or Dirac equation discussed in Appendix C). In general, the wave equation is found by taking the classic equation of motion (from the Hamiltonian) for the given situation and replacing measured properties with their associated operators acting

*Information in this section can be found in a variety of texts including [23, 25].

on the wave function. The form of the wave function is then derived so as to satisfy the wave equation. Such a derivation is generally non-trivial, though solutions are known for certain special cases (such as a classic harmonic oscillator).

A wave function can be an eigenstate of a given operator such that the effect of the operator acting on the wave function is equivalent to multiplying the wave function by a scalar contained within some discrete set of constants (the associated eigenvalues). For example, for a static state (where $\psi^\dagger\psi$ is not a function of time), ψ is an eigenstate of the Hamiltonian operator such that $\tilde{H}\psi = i\hbar\frac{\partial\psi}{\partial t} = E\psi$ (where E is the energy of the system). Note that in this case, the wave function necessarily has the form

$$\psi(\vec{x}, t) = e^{-it\tilde{H}/\hbar}\psi_0(\vec{x}) = \tilde{T}(t)\psi_0(\vec{x}), \quad (1.1)$$

where ψ_0 is the form of the wave function at $t = 0$, $\tilde{T} \equiv e^{-it\tilde{H}/\hbar}$ is an operator describing the time evolution of the wave function, and \tilde{H} does not depend explicitly on t . Note that the inverse of \tilde{T} (\tilde{T}^{-1} such that $\tilde{T}^{-1}\tilde{T} = 1$) is also its complex conjugate ($\tilde{T}^{-1} = \tilde{T}^\dagger = e^{it\tilde{H}/\hbar}$) and it is thus said to be *unitary*. This also means that

$$\psi^\dagger(\vec{x}, t) = \tilde{T}^\dagger(t)\psi_0^\dagger(\vec{x}) = \psi_0^\dagger(\vec{x})\tilde{T}^{-1}(t). \quad (1.2)$$

The above representation of a static state is known as the *Schrödinger representation*, which attributes the time dependence of the system to the wave function itself. There is also the *Heisenberg representation* of the wave description, which attributes the time dependence to the operators involved. If one notes a generic

operator without time dependence as \tilde{Q}_0 and its time dependent representation as \tilde{Q} , then the expectation value must be the same in either representation:

$$\langle q \rangle = \int \psi_0^\dagger(\vec{x}) \tilde{Q} \psi_0(\vec{x}) d\mathbf{x} = \int \psi^\dagger(\vec{x}, t) \tilde{Q}_0 \psi(\vec{x}, t) d\mathbf{x}. \quad (1.3)$$

where in the first the time dependence is contained only in \tilde{Q} (the Heisenberg representation) and in the second it is contained in the wave function, ψ (the Schrödinger representation). Using Equations 1.1 and 1.2, one finds that $\psi^\dagger(\vec{x}, t) \tilde{Q}_0 \psi(\vec{x}, t) = \psi_0^\dagger(\vec{x}) \tilde{T}^{-1} \tilde{Q}_0 \tilde{T}(\vec{x}) \psi_0(\vec{x})$. Applying this to Equation 1.3 one finds

$$\tilde{Q} = \tilde{T}^{-1} \tilde{Q}_0 \tilde{T}, \quad (1.4)$$

which gives the time dependence of the operator \tilde{Q} in the Heisenberg representation.

If there is no further, explicit dependence of \tilde{Q} on t , then the time derivative of the operator (multiplied by $i\hbar$ for convenience) is

$$\begin{aligned} i\hbar \frac{d\tilde{Q}}{dt} &= i\hbar \frac{d\tilde{T}^{-1}}{dt} \tilde{Q}_0 \tilde{T} + i\hbar \tilde{T}^{-1} \tilde{Q}_0 \frac{d\tilde{T}}{dt} \\ &= i\hbar \left(\frac{i\tilde{H}}{\hbar} \tilde{T}^{-1} \right) \tilde{Q}_0 \tilde{T} + i\hbar \tilde{T}^{-1} \tilde{Q}_0 \left(\tilde{T} \frac{-i\tilde{H}}{\hbar} \right) \\ &= -\tilde{H} (\tilde{T}^{-1} \tilde{Q}_0 \tilde{T}) + (\tilde{T}^{-1} \tilde{Q}_0 \tilde{T}) \tilde{H} \\ &= -\tilde{H} \tilde{Q} + \tilde{Q} \tilde{H} \equiv [\tilde{Q}, \tilde{H}]. \end{aligned} \quad (1.5)$$

The notation $[\tilde{Q}, \tilde{H}]$ above is the *commutator* of \tilde{Q} and \tilde{H} . If one finds that $[\tilde{Q}, \tilde{H}] = 0$ (in which case \tilde{Q} is said to *commute* with the Hamiltonian) then $d\tilde{Q}/dt = 0$, such that the \tilde{Q} operator is constant over time. In such a case, its expectation value,

$\langle q \rangle$, must be a conserved physical quantity. Therefore, an operator that commutes with the Hamiltonian indicates a conserved physical observable.

1.7 Quantum Mechanical Properties of Particles

Properties of wave functions are extremely important for identifying particle types in high energy physics. The wave function description of particles belonging to a specific type will have specific properties. Understanding how a particle's wave function behaves under various operations or transformations defines a variety of particle characteristics. A number of these transformations will be discussed here.

1.7.1 Bosons and Fermions

One important transformation is exchange of identical particles. One can consider a system consisting of two identical particles, which is described by a single wave function. If one interchanges the two particles in the wave function, the statistical distribution of the particles (described by the square of the wave function) should not be affected since they are identical. Thus, the wave function itself could be completely unaffected by such an exchange, or it could become the negative of its former self (which wouldn't affect its square): $\psi_{1,2} \rightarrow \pm\psi_{2,1}$. Particles with *symmetric* wave functions follow the former rule. They have integral spin ($0, \hbar, 2\hbar, \dots$), obey Bose-Einstein statistics, and are thus called bosons (such are the particles that mediate forces as discussed below). Particles with *anti-symmetric* wave functions follow the latter rule. They have half-integral spins ($\frac{1}{2}\hbar, \frac{3}{2}\hbar, \dots$), obey Fermi-Dirac statistics, and are thus called fermions (which include all the

fundamental particles that make up matter: leptons, like the electron, and quarks, which make up protons and neutrons). In summary:

$$\begin{aligned} \text{bosons : } \psi_{1,2}^b &\rightarrow +\psi_{2,1}^b && \text{symmetric,} \\ \text{fermions : } \psi_{1,2}^f &\rightarrow -\psi_{2,1}^f && \text{anti-symmetric.} \end{aligned} \tag{1.6}$$

These characteristics are integral in understanding interactions between particles via the different statistical rules followed by each type (as named above). For example, the total wave function of a set of identical particles can be given as a product of two functions: one describing the spatial distribution of the particles, $\alpha(\text{space})$, and one describing their spin states, $\beta(\text{spin})$, such that $\psi = \alpha(\text{space})\beta(\text{spin})$. For a set of identical fermions, this function must be anti-symmetric—thus if two of the particles are exchanged, one must be able to distinguish the function before and after the exchange. If all the fermions are in the same spatial state, then α would obviously not change under a particle exchange (it would be symmetric). Thus the spin state, β , must be anti-symmetric. This cannot be the case if two or more of the fermions have the same spin. Thus, a system of identical fermions in the same spatial state can consist of, at most, two fermions with spins that are in different directions (or anti-parallel). For this reason, only two electrons in an atom can share the same orbital position state provided their spins are oppositely aligned (one with spin “up” and one with spin “down”). This is the “two-valuedness” of the electrons produced by their spins as noted earlier, and it causes the Pauli exclusion principle.

However, for identical bosons, the overall wave function is symmetric. Many bosons can exist in the same spatial state (making α symmetric under particle exchange) and with their spins aligned (or parallel, thus making β symmetric as well). This produces an acceptable, symmetric wave function in which many bosons share the same quantum state. An example of this is a laser in which many identical photons (which are bosons) can exist in the same physical space, thus producing a powerful, narrow beam of energy.

1.7.2 Parity

Another transformation useful for characterizing quantum systems is spatial inversion of coordinates ($x, y, z \rightarrow -x, -y, -z$), which is known as the (spatial) *parity* operation: $\tilde{P}\psi(\mathbf{r}) = \psi(-\mathbf{r})$. Since repeating the operator twice clearly results in no net change ($\tilde{P}^2\psi(\mathbf{r}) = \tilde{P}\psi(-\mathbf{r}) = \psi(\mathbf{r})$), the parity operator is *unitary*. If there is an eigenvalue (P) of the operator, it will be ± 1 . For some particle types, their wave functions are intrinsically symmetric under the parity operator (having even parity or $P = +1$), while some particles have odd parity ($P = -1$). It is also possible for a system to have no parity eigenvalue (e.g., if $\psi = \cos x + \sin x$ then $\tilde{P}\psi = \cos x - \sin x \neq \pm\psi$). Note that the parity operator can also be achieved by performing a “mirror reflection” in one dimension (e.g., $x \rightarrow -x$) and then rotating about that dimension by 180° . Since rotational symmetry is usually well established, it is often useful (and easier) to picture and examine parity as simply a mirror reflection.

The parity of a system of particles is determined by the intrinsic parity of each individual particle and by their orbital angular momentum (due to the quantum properties of angular momentum and its relationship to spatial inversion). If the i th particle has an intrinsic parity P_i , and the system has a total angular momentum quantum number, L , then the total parity eigenstate of the system is given by $P = \prod_i (P_i) (-1)^L$.

1.7.3 Charge-Conjugation

The *charge-conjugation* operation (\tilde{C}) provides another important particle characteristic. Under this operation, the charge of the particle is reversed, effectively changing the particle into its antiparticle (even in the case of neutral particles). As with (spatial) parity, charge-conjugation is obviously a unitary operator, and it is possible for a neutral particle to possess either even ($C = +1$) or odd ($C = -1$) charge-conjugation parity. For a particle (or system) with an overall charge, its wave function cannot be an eigenstate of the charge-conjugation operator.

1.7.4 Time-Reversal

As its name implies, the *time-reversal* operation (\tilde{T}) inverts the direction of time in the wave function description of a system ($t \rightarrow -t$). This is another example of a unitary operator. In classical, macroscopic cases, it is possible to imagine some situations that are invariant and others that are non-invariant under time-reversal. For example, since Newton's law of gravitation does not involve time, a movie of a satellite going around the earth looks just as realistic going forwards as backwards.

On the other hand, many thermodynamic phenomena do not display macroscopic reversibility (a movie of a ball bouncing to a stop—converting its energy into heat energy—will look improper when run backwards). However, for each microscopic interaction, the probability distribution of the interaction is invariant under time-reversal. The arrow of time visible in the macroscopic realm is a factor of the probability (or improbability) of various initial conditions.

The most important aspects of time-reversal come from its relationship with parity and charge-conjugation, which will be addressed in Section 1.10.4.

1.7.5 Isospin

The isospin property of a quantum mechanical system is a somewhat contrived yet useful notion. It was introduced at one point to treat protons and neutrons as different charged sub-states of a single particle, the *nucleon* [25]. Isospin is not associated with angular momentum or quantum mechanical spin; however, its properties are defined with the same mathematics. In an analogy with spin, nucleons are said to possess an isospin with a z component of $I_3 = \pm\frac{1}{2}$. The charge of a nucleon is then given as $I_3 + \frac{1}{2}$ *. The proton is thus assigned an isospin of $I_3 = +\frac{1}{2}$ and the neutron is assigned an isospin of $I_3 = -\frac{1}{2}$. The overall isospin of a nucleon is pictured as a vector in a three dimensional “isospin space,” and a particle or system can be classified by how its wave function is affected under rotations in isospin space. The most useful aspect of the isospin concept is

*Here and throughout this text, charges are noted as multiples of the electron charge, e .

that isospin is conserved in strong interactions, which defines certain allowed and disallowed decays.

1.7.6 G-Parity

Another somewhat contrived property assigned to quantum mechanical systems in high energy physics is called *G-parity*. It is a combination of a rotation (\tilde{R}) in isospin space (of 180° about the isospin-y-axis) followed by a charge-conjugation operation (\tilde{C}) such that $\tilde{G} = \tilde{C}\tilde{R}$. The usefulness of this property comes partially from the fact that while charged systems cannot be eigenstates of the charge-conjugation operator, it is possible for such a system to be an eigenstate of the G-parity operator. While this information is completely contained within isospin and charge-conjugation characteristics, G-parity provides a shortcut to the more useful information. As with all the previously noted characterizations, G-parity is most useful in establishing decay and interaction rules given G-parity conservation in various situations.

1.7.7 Lorentz Behavior

In four dimensional space-time there is a set of transformations (such as translations, rotations, and reflections) called the Lorentz group. In high energy physics, how a system behaves under such transformations helps define the system as one of five types. As an illustration, one can consider how a three-dimensional system behaves under the parity operation to describe these types.

Some systems do not have any dimensional components and thus do not change under the various transformations, making them *scalars*. However, there are scalar-like systems that do not have dimensional components but which change sign under the parity operation ($P = -1$), and they are termed *pseudoscalars*. A three dimensional vector (\vec{v}) with dimensional components (v^x, v^y, v^z) , will reverse sign under parity—when all the spatial dimensions are reversed one finds $\tilde{P}\vec{v} = (-v^x, -v^y, -v^z) = -\vec{v}$ such that $P = -1$. Systems that behave the same way under such transformations are thus called *vectors*. However, there is another set of vector-like systems that do not change sign under parity. For example, the cross product of two vectors ($\vec{a} \times \vec{b}$) is a three-component object like a vector, but under parity the two minus signs (one from \vec{a} and one from \vec{b}) essentially cancel so that the cross product is invariant under parity. Systems with one component per dimension that transform in this way are termed *axial vectors*. Finally, some systems in high energy physics require two indices to specify each element of the system and behave like second rank *tensors*.

These transformation identities are applied to specific particles by noting their intrinsic spin (J) and parity (P), which together are generally noted J^P as a convention. Particles with no spin have no inherent dimensionality and could be scalars ($J^P = 0^+$) or pseudoscalars ($J^P = 0^-$). Particles with spin and definite parity can either be vectors (e.g., $J^P = 1^-$) or axial vectors (e.g., $J^P = 1^+$). Similarly, applying these concepts to isospin space, particles with $I = 0$ are termed *isoscalars* while a particle with $I = 1$ would be an *isovector*.

1.8 Quantum Mechanical Treatment of Forces

In addition to describing particles via wave functions, quantum mechanics also provides a parallel description of forces. In classical physics, force interactions between two particles are said to be caused by the potential field of one particle acting on the other. In quantum mechanics, the potential field is essentially reinterpreted as a wave function for a quanta (specifically, a boson) associated with the given force. A force interaction is thus pictured as the exchange of bosons between two particles, with each force having its own associated boson(s). Because these quanta possess energy, conservation laws would not generally allow for this description; however, quantum mechanics grants latitude to energy conservation over a limited time via the Uncertainty Principle. If the overall uncertainty in a system's energy is ΔE over a given time, Δt , then the Uncertainty Principle requires that $\Delta E \Delta t \geq \hbar/2$. Therefore, a quanta can exist over that limited time without disturbing the Uncertainty Principle if its energy (δE) is such that $\delta E \Delta t \leq \hbar/2$. The quanta can exist for a limited time given its energy without being forbidden by conservation laws. Such ephemeral quanta are called *virtual* particles. Virtual particles are no more or less realistic or observable than the classical potential field, only their effects as a force are measured.

Because of the connection between the time a virtual particle can exist and its energy, the range of a force is limited by the mass of its associated field quantum [25]. If it has no mass, its energy could be infinitesimally small, it could exist for a long period of time given the Uncertainty Principle, and it could thus con-

ceptually reach an infinite range. However, a massive quanta must have an energy no smaller than its mass energy. The time such a quantum could exist is thus limited to $\Delta t \leq \hbar/2mc^2$, which restricts its range (given the limit of light speed) to $c\Delta t \leq \hbar/2mc$. This connection was first established in 1935 by Hideki Yukawa in an attempt to explain short-ranged forces between protons and neutrons in the atomic nucleus.

1.8.1 A Simple Central Force

As an example of the quantum mechanical description of a force, one can consider the description of a free, spinless virtual boson associated with a central force (a force emanating from a single point, like the static potential of a point charge). For generality, the boson is allowed to have a mass, m . Further, it is associated with a static potential whose time derivative is thus zero. Given this, one can describe the potential, $V(r)$, as the wave function of a free static particle ($\partial\Psi/\partial t = 0$) that satisfies the Klein-Gordon wave equation (see Appendix C). Here one evaluates the equation in spherical coordinates given that this is a central force emanating from the origin:

$$\nabla^2 V(\vec{x}) = \frac{1}{r^2} \frac{\partial}{\partial r} \left(r^2 \frac{\partial V(r)}{\partial r} \right) = \frac{m^2 c^2}{\hbar^2} V(r). \quad (1.7)$$

The general solution to that differential equation is given by

$$V(r) = \frac{g}{4\pi r} e^{-rmc/\hbar}, \quad (1.8)$$

where g is a constant from the integration and is identified with the general strength of the force. If the boson mass is set to zero, then this equation becomes the familiar central potential of, for example, an electrostatic point charge e ($V_e = e/4\pi\epsilon_0 r$) or a gravitational point mass m_0 ($V_g = Gm_0/r$).

This approach was proposed by Yukawa [25] in—as history would show—a somewhat too simplistic attempt to describe the strong force; however, though this description of a central force is simplistic, it has general uses as will be seen below.

In practice, each fundamental force has an associated *coupling constant* that is related to g above and thus describes the relative strength of each force. The coupling constant for each fundamental force will be discussed in Section 1.8.7. In general, coupling constants vary depending on the amount of momentum transferred in the interaction, but typical ranges are often used to discuss the relative strengths of the different forces.

1.8.2 Scattering Cross-Sections

The probability of a given force interaction is usually expressed in terms of a *cross-section*. One considers a particle, X, moving towards another particle, Y, such that X is “scattered” due to a force interaction as represented in Figure 1.1. After the interaction, there is some probability that X will be moving within some range $d\theta$ of a given angle, θ , with respect to its initial motion (see the figure). The region such a particle would enter is defined by a solid angle, $d\Omega$, given the

scattering angle, θ . The probability that X will be within a given solid angle is related to an area, $d\sigma$, through which the particle must pass before the interaction to end up within that solid angle of interest afterwards (again, see the figure). The larger the region through which the particle could pass to end up in the $d\Omega$ of interest, the more likely that particular interaction will occur. The $d\sigma$ area is the cross-section—the effective target area presented to the X particle for scattering into $d\Omega$ (as a function of the direction, θ , around which $d\Omega$ is defined). Therefore the cross-section of a given event is proportional to the probability of that event occurring.

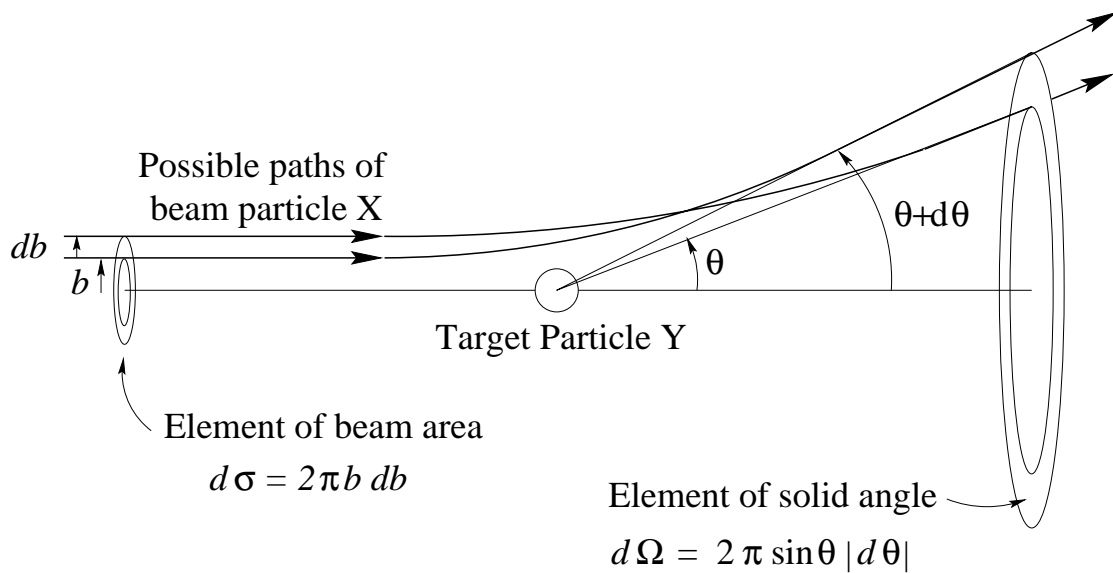


Figure 1.1

Elements in the definition of the scattering cross section. All beam particles passing through the area $d\sigma$ are scattered into the solid angle $d\Omega$.

In practice, X would generally represent a beam of particles aimed at a set of target particles, Y. The cross-section, $d\sigma$, would be defined per target particle and in terms of the rate at which particles are scattered into $d\Omega$ and the rate at which incident particles pass through a given area (i.e., the flux of the incident beam):

$$d\sigma = \frac{\text{rate of scattering into } d\Omega}{(\text{flux of incident beam})(\# \text{ of target particles})}. \quad (1.9)$$

The cross-section area is most often given in units of *barns* where 1 barn = 10^{-28} m².

A cross-section can also be expressed in terms of the momentum transfer needed to send the incident particles into the given $d\Omega$. In that case, the concept of “scattering into a range $d\Omega$ around a given angle, θ ” is generally replaced with “transferring a squared momentum within a range dp^2 of a given momentum, p^2 ”.

Given the cross-section of a particular process, σ , the rate, R, at which it will occur in a chosen experiment can be expressed in terms of an instantaneous *luminosity*, L(t):

$$R = L(t)\sigma. \quad (1.10)$$

The cross-section is generally a property of the particular interaction while the luminosity depends on the specifics of the experiment in which the interaction might be produced. For example, in an experiment in which N_1 incident particles are made to collide with N_2 target particles in an effective cross-sectional area A and at a frequency rate of f , the instantaneous luminosity is given by

$$L(t) = f \frac{N_1 N_2}{A}, \quad (1.11)$$

and is typically given in units of cm⁻²s⁻¹.

The total number of events generated over a given time is then found by integrating the rate:

$$N = \int R dt = \int \sigma L(t) dt = \sigma \int L(t) dt = \sigma \mathcal{L}, \quad (1.12)$$

where \mathcal{L} is thus the integrated luminosity over a given time and is often given in units of inverse picobarns (pb^{-1}), inverse femtobarns (fb^{-1}), etc.

1.8.3 Describing Transitions

To describe transitions arising from force interactions (or particle decay) one can consider the probability of a system initially in some well-defined state, Ψ_i , being later found in some final state, Ψ_f , as the result of some force potential, V , which comes into play at time $t = 0$. The potential changes the initial energy state described by the Hamiltonian, \tilde{H} , to produce the transitional Hamiltonian given by

$$\tilde{H}' = \tilde{H} + V. \quad (1.13)$$

This is said to be a perturbed form of the initial (unperturbed) Hamiltonian, and the potential provides the perturbation. The resulting calculations are thus handled by perturbation theory. To allow easy calculations below, one considers the potential to be a relatively small change resulting in a weak perturbation and a small transition rate (i.e., a first-order perturbation).

If one considers the initial state of the system to be stationary, then it will be an eigenstate of the initial Hamiltonian, \tilde{H} , and its energy will be one of the

associated eigenvalues:

$$\tilde{H}\Psi_n(\vec{x}, t) = E_n\Psi_n(\vec{x}, t). \quad (1.14)$$

Initially ($t < 0$) the system is in the eigenstate E_i . At time $t = 0$ the transition potential is “turned on,” and the resulting transition places the system into some other state—any of the possible eigenstates of the unperturbed Hamiltonian. Thus, the general form of the wave function can be written as a superposition of all the possible eigenstates:

$$\Psi(\vec{x}, t) = \sum_{n=0}^{\infty} c_n(t)\psi_n e^{-iE_n t/\hbar}, \quad (1.15)$$

where $c_n(t)$ is the time-dependent probability amplitude for being found in the n -th state. Thus before $t = 0$ one has $c_{n=i}(t \leq 0) = 1$ while $c_{n \neq i}(t \leq 0) = 0$, placing it in the well-defined initial state. After $t = 0$, c_n will be determined by the specific form of V .

Applying the perturbed Hamiltonian to the wave function yields the following:

$$\begin{aligned} \tilde{H}'\Psi &= i\hbar\partial\Psi/\partial t, \\ \sum_{n=0}^{\infty} \{\tilde{H} + V\} c_n(t)\psi_n e^{-iE_n t/\hbar} &= i\hbar \sum_{n=0}^{\infty} \frac{\partial}{\partial t} [c_n(t)\psi_n e^{-iE_n t/\hbar}], \\ \sum_{n=0}^{\infty} \{E_n + V\} c_n(t)\psi_n e^{-iE_n t/\hbar} &= \sum_{n=0}^{\infty} \left\{ i\hbar \frac{dc_n}{dt} + E_n c_n(t) \right\} \psi_n e^{-iE_n t/\hbar}, \\ \text{(reversing sides)} \quad i\hbar \sum_{n=0}^{\infty} \frac{dc_n}{dt} \Psi_n &= \sum_{n=0}^{\infty} V c_n(t)\psi_n e^{-iE_n t/\hbar}. \end{aligned} \quad (1.16)$$

It is of interest to determine the probability amplitude for a given final state, c_f , and to that end one can multiply both sides of the above equation by Ψ_f^\dagger on the left followed by integration with respect to volume in \vec{x} . The wave function Ψ_f^\dagger

will act on Ψ_n and V . Because Ψ_f and Ψ_n are eigenstates and thus orthogonal, the integral $\int \Psi_f^\dagger \Psi_n d^3x$ will be 0 except when $f = n$, in which case it is 1. The proposed operation thus produces the following:

$$\begin{aligned} i\hbar \sum_{n=0}^{\infty} \frac{dc_n}{dt} \int \Psi_f^\dagger \Psi_n d^3x &= \sum_{n=0}^{\infty} c_n(t) \left\{ \int \psi_f^\dagger V \psi_n d^3x \right\} e^{-i(E_n - E_f)t/\hbar}, \\ i\hbar \left(\frac{dc_f}{dt} \right) &= \sum_{n=0}^{\infty} c_n(t) M_{nf} e^{-i(E_n - E_f)t/\hbar}, \end{aligned} \quad (1.17)$$

where

$$M_{nf} = \int \psi_f^\dagger V \psi_n d^3x. \quad (1.18)$$

is called the matrix element controlling the transition from state n to state f .

As previously noted, one considers here a first-order perturbation, making the transition rate from the initial state small such that over a given time t one can consider $c_n(t)$ on the right side of Equation 1.17 to be relatively constant over time and insignificant for all but the initial state: $c_i(t) \simeq 1$, $c_{n \neq i}(t) \simeq 0$. Then, assuming the potential is static, an integration of Equation 1.17 over a given time, t yields

$$\begin{aligned} c_f(t) &= \frac{M_{if}}{i\hbar} \int_0^t e^{-i(E_i - E_f)t'/\hbar} dt' \\ &= M_{if} \left(\frac{1 - e^{-i(E_i - E_f)t/\hbar}}{E_i - E_f} \right) \\ &= 2iM_{if} e^{-i(E_i - E_f)t/2\hbar} \left(\frac{\sin [(E_i - E_f)t/2\hbar]}{E_i - E_f} \right), \end{aligned} \quad (1.19)$$

where the final step provides easier calculation below.

The square of the amplitude $|c_n(t)|^2 = c_n^\dagger(t)c_n(t)$ is the probability density that the system will have had a transition to state n after a time t . The rate at which

this transition will occur is thus given by

$$W_n = \frac{|c_n(t)|^2}{t}. \quad (1.20)$$

To find the total transition rate (the rate at which the system will undergo any transition), one sums over all the individual rates. Realistic collisions and decays involve many, largely continuous final energy states separated by an infinitesimal energy dE_f and having a number density given by dN/dE_f . The transition rate is then found by integrating:

$$\begin{aligned} W &= \int_{-\infty}^{+\infty} W_f dN \\ &= \int_{-\infty}^{+\infty} \frac{|c_f(t)|^2}{t} \frac{dN}{dE_f} dE_f \\ &= \frac{-4|M_{if}|^2}{t} \int_{-\infty}^{+\infty} \left(\frac{\sin^2 [(E_i - E_f)t/2\hbar]}{(E_i - E_f)^2} \right) \frac{dN}{dE_f} dE_f, \end{aligned} \quad (1.21)$$

where substituting $x = (E_i - E_f)t/2\hbar$ and $dx = -dE_f t/2\hbar$ yields

$$W = \frac{2|M_{if}|^2}{\hbar} \int_{-\infty}^{+\infty} \left(\frac{\sin^2 x}{x^2} \right) \frac{dN}{dE_f} dx. \quad (1.22)$$

The *phase space factor*, dN/dE_f is often denoted ρ_f . Performing the integration one finds the total transition rate:

$$W = \frac{2\pi}{\hbar} |M_{if}|^2 \rho_f, \quad (1.23)$$

where, to reiterate, the matrix element is given by

$$M_{if} = \int \psi_f^\dagger V \psi_i d^3 x. \quad (1.24)$$

When the first-order perturbation does not hold, Equation 1.23 can still apply, but the matrix element will not be determined by Equation 1.24, and Equation 1.23 provides the definition of the matrix element.

1.8.4 The Boson Propagator

A basic overview of interaction cross-sections can be given by applying the matrix element equation (Equation 1.24) to the simplified description of a central force from Equation 1.8, which acts on a particle through the exchange of a single boson of mass m . The single exchange is assumed to make the perturbation and the transition rate small. The particle in this simple example can be seen as a basic plane wave, thus the initial wave function is

$$\psi_i(\vec{x}, t) \propto e^{i\vec{k}_i \cdot \vec{x}}, \quad (1.25)$$

where the momentum is given by $\vec{p}_i = \hbar\vec{k}_i$. After the single boson exchange, the particle will have a final momentum $\vec{p}_f = \hbar\vec{k}_f$. Given the simple central force potential from Equation 1.8:

$$V(r = |\vec{x}|) = \frac{g}{4\pi r} e^{-mcr/\hbar},$$

and applying Equation 1.24 produces

$$\begin{aligned} M_{if} &\propto \int e^{-i\vec{k}_f \cdot \vec{x}} V(r) e^{i\vec{k}_i \cdot \vec{x}} d^3x \\ &= \frac{g}{4\pi} \int \frac{1}{r} e^{i(\vec{k}_i - \vec{k}_f) \cdot \vec{x}} e^{-rhc/\hbar} d^3x \\ &= \frac{g}{4\pi} \int \frac{1}{r} e^{i\vec{q} \cdot \vec{x}/\hbar} e^{-rhc/\hbar} d^3x, \end{aligned} \quad (1.26)$$

where $r = |\vec{x}|$, q is the momentum exchange produced by the virtual boson, and g is, again, a measure of the basic strength of the given force. The integral can be performed using spherical coordinates (r, θ, ϕ) by substituting

$$\vec{q} \cdot \vec{x} = qr \cos(\theta) \quad \text{and} \quad d^3x = r^2 \sin\theta d\phi d\theta dr.$$

Then

$$\begin{aligned}
M_{if} &\propto \frac{g}{4\pi} \int_0^\infty \int_0^\pi \int_0^{2\pi} \frac{1}{r} e^{iqr \cos \theta / \hbar} e^{-rmc/\hbar} r^2 \sin \theta \, d\phi \, d\theta \, dr \\
&= \frac{-g}{2} \int_0^\infty \int_{-1}^1 e^{iqr u / \hbar} e^{-rmc/\hbar} r \, du \, dr \\
&= \frac{-g}{2} \int_0^\infty \frac{e^{iqr/\hbar} - e^{-iqr/\hbar}}{iq/\hbar} e^{-rmc/\hbar} \, dr \\
&= \frac{-g\hbar}{2iq} \left[\frac{e^{r(iq-mc)/\hbar}}{(iq-mc)/\hbar} + \frac{e^{-r(iq+mc)/\hbar}}{(iq+mc)/\hbar} \right] \Big|_0^\infty \\
&= \frac{-g\hbar^2}{2iq} \left[\frac{2iq}{-[q^2 - (mc)^2]} \right], \\
M_{if} &\propto \frac{1}{q^2 - (mc)^2}, \tag{1.27}
\end{aligned}$$

where $g\hbar^2$ in the last step was absorbed into the proportionality.

Equation 1.27 is known as the *boson propagator term*, and given its relationship to this simple matrix element, its square will be part of the transition rate calculation (along with a phase space factor) and it is thus directly related to the cross-section for the single boson exchange. Note that for a massless boson, the propagator is simply $1/q^2$, and for a massive boson when q^2 is small, the boson propagator is roughly $1/(mc)^2$.

Another interpretation can be had by noting that Equation 1.26 is simply the Fourier transform of the potential (which is the spatial probability amplitude of the virtual boson). In general, it converts the probability amplitude in coordinate space for interacting with a virtual boson at some point in space-time, \mathbf{x} , to the probability amplitude in momentum space for interacting with a virtual boson

that provides some 4-momentum transfer, q^2 . The boson propagator term is thus proportional to the force amplitude in momentum space.

In reality, the potential, V , is provided by another particle, and the initial and final wave functions must thus describe the state of both particles. The above procedure would then be more complicated and would describe the cross-section for a scattering event between two particles. However, the boson propagator term would still come into play, and it provides a basic component for the calculation of various force interaction cross-sections.

1.8.5 Coupling Constants and Feynman Diagrams

As noted above, the coupling constant for each force is related to the constant g in the simple central force description. In general, the coupling constant helps determine the squared amplitude of the force coupling between the real particles and the virtual bosons that propagate a given force. Note that the simple matrix element in Equation 1.27 is proportional to g ; thus, along with the boson propagator, these coupling constants are useful in determining the cross-section of a given interaction, especially when properly implemented in Feynman diagrams.

Feynman diagrams portray particle interactions by displaying the paths of particles through space and time. Figure 1.2 shows a number of Feynman diagrams as examples. Space is represented vertically and time flows horizontally. Each fermion is represented by a line with arrows noting the motion of the particle, and each boson (photons in these diagrams) is represented by a “squiggly” line. A

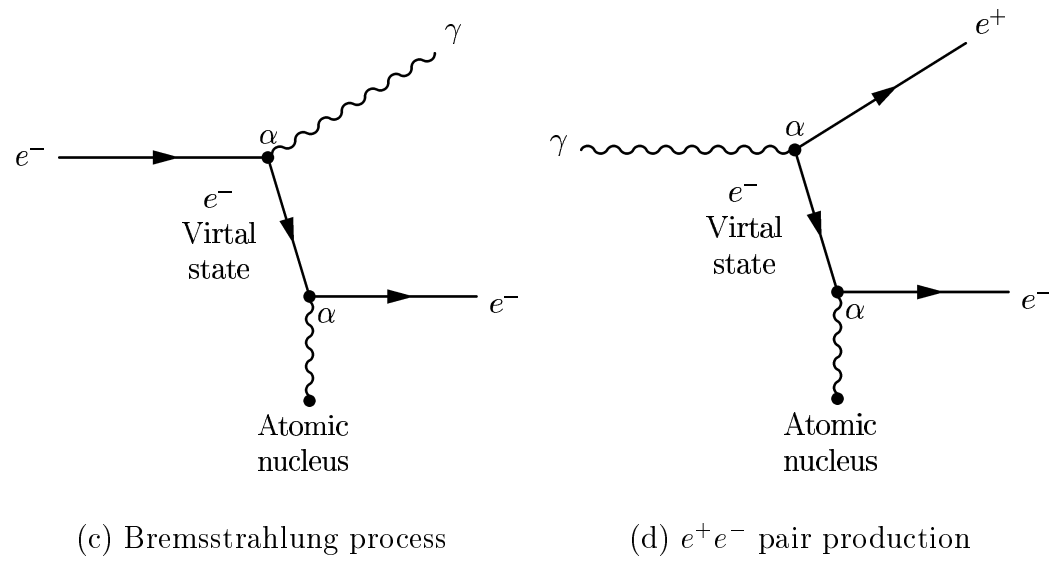
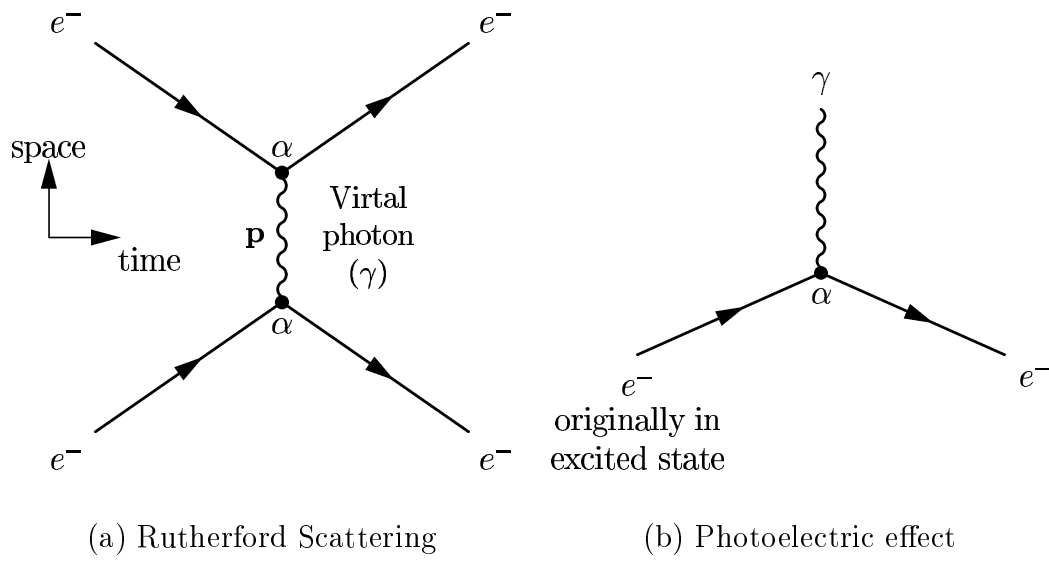


Figure 1.2

Feynman diagrams for several electromagnetic processes

line flowing into and then out of a vertex is often referred to as a *current*. Figure 1.2(a) shows an electromagnetic interaction between two electrons (scattering). A single, virtual photon is shown passing between them, transferring an amount of momentum and energy, $\mathbf{p} = (E, \vec{p})$ (a four-momentum transfer), between the two. At each interaction point (or vertex) is noted the coupling constant (α) for that interaction. The cross-section for the complete scattering event is a combination of all the coupling constants present as well as the momentum transfer (via the boson propagator term). In this case, the amplitude for each interaction is $\sqrt{\alpha}$, and with two interactions and a momentum transfer p^2 , the overall amplitude is proportional to $\sqrt{\alpha}\sqrt{\alpha}/p^2$. The $1/p^2$ term comes from the boson propagator for a massless photon. The cross-section is then expressed as $d\sigma/dp^2 \propto \alpha^2/p^4$. Because the α coupling constant occurs twice, this is called a second-order process.

Figure 1.2(b) shows an example of the photoelectric effect. The electron in the diagram must initially be bound in an atom for the process to conserve momentum. The emitted photon is labeled γ . Here there is only one interaction vertex, and this is a first-order process with a cross-section proportional to α .

Figure 1.2(c) displays a process known as bremsstrahlung (“braking radiation” in German). An incident electron is accelerated in the presence of a nucleus and radiates away a photon. Note that after the electron radiates and before it exchanges a virtual photon with the nucleus, momentum and energy cannot be conserved if the electron retains its true mass. Therefore, in the intermediate, the electron is said to be in a virtual state in which it is said to go “off mass shell.”

It is often possible to produce one Feynman diagram from another by replacing a particle going into (or out of) a vertex by its antiparticle going out off (into) the vertex (provided conservation laws apply). This is often referred to by noting that antiparticles are normal particles moving backwards in time. Figure 1.2(d) is produced from Figure 1.2(c) by replacing an incoming electron by an outgoing positron. It displays the process of e^+e^- pair production.

While Feynman diagrams can be used to implement formal rules for allocating coupling constants and momentum transfers to calculate cross-sections, they are often used, as in this text, to simply provide visual representations of force interactions by the exchange of virtual bosons.

1.8.6 Forces and Particle Decay

The transitions described in Section 1.8.3 via a matrix element,

$$M_{if} = \int \psi_f V(\vec{x}) \psi d^3x,$$

not only applies to force interaction but also to particle decay. The decay of a particle from some initial state to some final state can be described via a mediating force with potential, V . The transition rate for the decay is developed as given in Section 1.8.3.

Simply stated, one can note the following: In classical relativistic physics, energy came in three forms: mass energy, energy of motion (kinetic energy), and energy due to forces (potential energy). In quantum mechanics, the virtual boson mediators of forces can be considered the energy-carriers of the forces. When

a particle decays into other particles, its mass energy is transformed into other forms of energy, and in the intermediate state, it can exist as some form of “pure” energy (i.e., as a virtual boson associated with a particular force). One particle is transformed into a virtual boson that in turn transforms into other particles. Thus, any given decay is said to be mediated by a force whose associated boson forms the intermediate energy state in the decay. In the case of electromagnetic decay, part of a particle’s decay product can be real photons (the mediator of the electromagnetic force), which do not decay to other particles.

In a sense, a decay occurs when a virtual boson propagates a momentum transfer through time as the initial state particle couples to the final state particle. The decay is thus mediated by the associated force and its coupling constant. Such decays are often dominated by so-called *resonance structures* as the mediating boson preferentially decays to some unstable, intermediate state particle before further decay to the stable particles in the final state.

1.8.7 Revisiting the Four Forces

Given the quantum mechanical description of forces, it is now possible to characterize the fundamental forces in terms of the (gauge) bosons that propagate each of them. The electromagnetic force is mediated by the massless *photon* (γ), which accounts for its infinite range (and vice-versa). The theory describing this force is known as *quantum electrodynamics* (QED). The coupling constant for an electromagnetic interaction is known as the fine structure constant because

it was first used when explaining the fine structure splitting mentioned earlier. It is denoted α , and at small momentum transfer ($p^2 \rightarrow 0$) it has a value of $\alpha = e^2/4\pi\epsilon_0\hbar c = 1/137.0360$ (where ϵ_0 is the permittivity of free space from electrodynamics).

The weak nuclear force is mediated by the W^\pm and Z^0 massive bosons, and weak interactions can thus produce charge-exchanging events (where the W^\pm exchange is referred to as a “charged-current” reaction) or neutral interactions (via Z^0 exchange acting in a “neutral-current” reaction). Because the W^\pm and Z^0 are massive (observed and measured in 1983 to be $81 \text{ GeV}/c^2$ and $94 \text{ GeV}/c^2$ respectively [26]), the weak force is limited in its range. The weak coupling constant (at small momentum transfer) is given by the *Fermi constant*, G_F . Numerically, it is often given in terms of the proton mass as

$$G_F = 1.03 \times 10^{-5} \frac{(\hbar c)^3}{m_p^2 c^4} \quad \text{or} \quad \frac{G_F}{(\hbar c)^3} = 1.1664 \times 10^{-5} \text{ GeV}^{-2}. \quad (1.28)$$

However, in describing weak coupling at small momentum transfer, it can be expressed in terms of the boson propagator, as noted previously, with a weak charge (g) and the mass of the mediating boson ($M_{W,Z}$):

$$G_F = \frac{g^2}{\hbar c} \frac{(\hbar c)^3}{M_{W,Z}^2 c^4}. \quad (1.29)$$

In the late 1960s, Sheldon Glashow, Abdus Salam, and Steven Weinberg proposed a theory that effectively combined the weak and electromagnetic interactions into one theoretical framework (the *electroweak theory*) and suggested that the two forces would have the same coupling at high momentum transfers [27]. Given the

equations above, it suggested that $g^2 \sim e^2/\epsilon_0$. Plugging this into Equation 1.29, one can predict $M_{W,Z} \sim 89$ MeV, which is in accordance with the average of the measured masses of the W^\pm and Z^0 given above. See Section 1.13 for more information about the electroweak theory.

The strong nuclear force is mediated by massless, neutral bosons known as *gluons* and is described by a theory known as *quantum chromodynamics* (QCD) [28]. Unlike other mediating bosons, gluons possess the color charge that is associated with the force it mediates. Each gluon possesses a color-anticolor combination. With three color charges (labeled *red* (r), *blue* (b), and *green* (g)) and their anticolors (\bar{r} , \bar{b} , and \bar{g}), one might expect nine combinations; however, the wave functions describing the combinations $r\bar{r}$, $g\bar{g}$, and $b\bar{b}$ are not independent, and these are combined into two “orthogonal” states that are superpositions of the three combinations. Thus there are eight color-anticolor combinations and eight associated types of gluons ($r\bar{b}$, $r\bar{g}$, $b\bar{r}$, $b\bar{g}$, $g\bar{r}$, $g\bar{b}$, $(r\bar{r} - g\bar{g})/\sqrt{2}$, $(r\bar{r} + g\bar{g} - 2b\bar{b})/\sqrt{6}$).*

The color charge of the gluons causes them to have a strong self-interaction. One can imagine that the color field lines between two quarks (describing the strong potential between such color-charged particles) are pulled together by the self-interaction to form a *color tube* between the quarks. The strong potential then actually increases as one tries to pull the two quarks apart, and it will eventually contain more energy than would be required to create two new quarks. Two new quarks would then be created, each bound to one of the two original quarks,

*This is an SU(3) color octet—a notation described in Section 1.10.

thus creating two, new, shorter color tubes and reducing the overall energy in the system. This property of the strong force forbids one from being able to separate a single quark out of a hadron (a particle made up of two or three quarks). It also accounts for why the strong force is not experienced at macroscopic distances (because the gluons are confined to within the very short color tubes generated by their strong self-interaction). The strong coupling constant (α_s) at high momentum transfers (or short distances) is on the order of $\alpha_s < 1$ (though it is large compared to other coupling constants). However, at small momentum transfers (or large distances) the coupling constant becomes large ($\alpha_s \sim 1$), accounting for the quark confinement mentioned above.

The gravitational force is the one force not yet fully described by a quantum field theory. The description of gravity given in general relativity is not fully consistent with a quantum model. However, it is theorized that gravity may be mediated by a hypothetical, presumably massless particle called a *graviton*.

A summary of the forces and their mediators is given in Table 1.1.

1.9 The Standard Model

The concepts discussed above are combined into a mathematically consistent quantum field theory, *the standard model*, which attempts to describe all particles and interactions in the physical universe. In this standard model, all matter in the universe is composed of two types of ($\hbar/2$ spin) fermions: leptons and quarks. There are six leptons and six quarks (or quark flavors, not including different

Table 1.1
 Summary of the four forces and their gauge boson field quanta. [25, 29]

Force Name:	Electromagnetism	Weak Force	Strong Force	Gravity
Framework:	QED (and combined in Electroweak)	Electroweak theory	QCD	General Relativity/ Quantum Gravity?
Cause:	(electric) charge	“weak charge”	“color”	mass/energy density
Coupling Constant:	$\alpha = e^2/4\pi\epsilon_0\hbar c \approx 1/137$	$G_F(M_p c^2/\hbar c)^3 = 1.03 \times 10^{-5}$	$\alpha_s \sim 1$, large r < 1 , small r	$GM_p^2/\hbar c \sim 5 \times 10^{-39}$
range:	∞	$\sim 10^{-18}$ m	$\sim 10^{-15}$ m	∞
Field Quanta:	photon (γ)	W^\pm and Z^0	gluon	graviton??
mass:	0	~ 80 and ~ 91 MeV/ c^2	0	Assumed 0
electric charge:	0	± 1 and 0	0	Assumed 0
spin (J^P):	1^-	1	1^-	Assumed 2^+

“color” charges that the quarks can have), each with an anti-particle counterpart. These particles are grouped in pairs known as “generations” with three generations of leptons and three corresponding generations of quarks. In each generation of lepton is a massive, negatively charged particle (the *electron* (e), the *muon* (μ), or the *tau* (τ)) and its neutral, presumably massless neutrino counterpart (ν_e , ν_μ , or ν_τ). Each of the three generations of quarks consist of a quark with a $+2/3$ charge, the *up* (u), *charm* (c), or *top* (t , sometimes called *truth*); and a quark with a $-1/3$ charge, the *down* (d), *strange* (s), or *bottom* (b , sometimes called *beauty*). The anti-particle counterparts of these fermions are denoted by placing a bar over their name (\bar{e} , $\bar{\nu}_e$, $\bar{\mu}$, $\bar{\nu}_\mu$, $\bar{\tau}$, $\bar{\nu}_\tau$, \bar{u} , \bar{d} , \bar{c} , \bar{s} , \bar{t} , \bar{b}). A summary of the fermions and their properties is provided in Table 1.2

While the experimental discoveries of the leptons have been mentioned previously, the existence of quarks (three at the time, u , d , and s) was postulated by Murray Gell-Mann and George Zweig in 1964 to help explain the vast number of particle discoveries in terms of a small set of more fundamental constituents [30]. In the late 1960’s experiments at the Stanford Linear Accelerator (SLAC) scattering electrons off protons proved that protons possessed the internal structure caused by their u and d quark constituents [31].

The quarks are only found in combinations that form other particles, known collectively as *hadrons*. They are made up of either a quark-antiquark pair (called *mesons*, which have integral spin), or three-quark combinations (called *baryons*, which have half-integral spin). Examples of mesons and baryons are given in

Table 1.2

The fundamental fermions (all 1/2 spin) and their properties [29]: M = mass, Q = charge (in multiples of the electron charge, e), τ = mean life time (not applicable to quarks, but only to the hadrons they make up).

		Leptons		Quarks	
		<i>Name</i>	<i>Properties</i>	<i>Name</i>	<i>Properties</i>
Generation I	electron neutrino (ν_e)	M : < 10 eV/ c^2 Q : 0 τ : stable	up (u)	M : 1.5 – 5 MeV/ c^2 Q : +2/3 τ : –	
	electron (e^-)	M : 0.511 MeV/ c^2 Q : -1 τ : stable	down (d)	M : 3 – 9 MeV/ c^2 Q : -1/3 τ : –	
Generation II	muon neutrino (ν_μ)	M : < 0.17 MeV/ c^2 Q : 0 τ : stable	charm (c)	M : 1.1 – 1.4 GeV/ c^2 Q : +2/3 τ : –	
	muon (μ^-)	M : 105.7 MeV/ c^2 Q : -1 τ : 2.2×10^{-6} s	strange (s)	M : 60 – 170 MeV/ c^2 Q : -1/3 τ : –	
Generation III	tau neutrino (ν_τ)	M : < 18.2 MeV/ c^2 Q : 0 τ : stable	top (t)	M : \sim 170 GeV/ c^2 Q : +2/3 τ : –	
	tau (τ^-)	M : 1777 MeV/ c^2 Q : -1 τ : 2.9×10^{-13} s	bottom (b)	M : 4.1 – 4.4 GeV/ c^2 Q : -1/3 τ : –	

Table 1.3. The strange quark, for example, was so named because it helped explain the aforementioned “strangeness” of the K mesons, and the Λ , Σ , and Ξ baryons

Table 1.3
Hadron examples and their properties. [29]

Meson Examples			
<i>Particle</i>	<i>Quark Constituents</i>	<i>Mass (MeV/c²)</i>	<i>Lifetime</i>
π^+, π^-	$u\bar{d}, d\bar{u}$	139.6	2.6×10^{-8} s
π^0	$(u\bar{u} - d\bar{d})/\sqrt{2}$	135.0	8.4×10^{-17} s
K^+, K^-	$u\bar{s}, s\bar{u}$	493.7	1.3×10^{-8} s
K^0, \bar{K}^0	$d\bar{s}, s\bar{d}$	497.7	$K_S^0: 8.9 \times 10^{-11}$ s $K_L^0: 5.2 \times 10^{-8}$ s
D^+, D^-	$c\bar{d}, d\bar{c}$	1869.3	1.1×10^{-12} s
D^0, \bar{D}^0	$c\bar{u}, u\bar{c}$	1864.6	4.2×10^{-13} s
B^+, B^-	$u\bar{b}, b\bar{u}$	5278.9	1.7×10^{-12} s
B^0, \bar{B}^0	$d\bar{b}, b\bar{d}$	5279.2	1.6×10^{-12} s
Baryon Examples			
<i>Particle</i>	<i>Quark Constituents</i>	<i>Mass (MeV/c²)</i>	<i>Lifetime</i>
proton	uud	938.3	stable
neutron	udd	939.6	887 s
Λ^0	uds	1115.7	2.6×10^{-10} s
Σ^+	uus	1189.4	8.0×10^{-11} s
Ξ^0	uss	1314.9	2.9×10^{-10} s
Ω^-	sss	1672.5	8.2×10^{-11} s

(all of which contain strange quarks). In 1974, the first evidence was found for the charm quark—an “up-like” companion of the strange quark proposed by GIM as

noted in Section 1.10.3—by the discovery of the J/ψ (a bound state of $c\bar{c}$)*. When the bottom quark was introduced to explain the existence of the Υ (a $b\bar{b}$ meson discovered in 1977 at Fermi National Laboratory (FNAL) [33]), it was postulated to also have a heavier companion quark, the top, to round out the picture presented by the other quark generations. Direct evidence for the top quark was observed in 1994 at FNAL [34].

Thus, through the quark model, the vast number of mesons and baryons that have been discovered are all described via combinations of only six quark flavors and their antiquark counterparts.

The fermions interact with one another and decay through the four aforementioned forces and their mediating bosons, the γ , W^\pm , Z^0 , and eight gluons as noted previously. The allowed interactions and decays depend on a variety of conservation rules, generally arising from symmetries within the model.

1.10 Symmetries and Conservation Laws

Symmetries play an important role in physics in general and in high energy physics in particular (in fact it has been said that symmetry is the basis of all fundamental physics). A system is said to possess a *symmetry* under a given operation if after the operation it is left unchanged (i.e. it is invariant under the operation). Such operations are called *symmetry operations* for the system. A

*The J/ψ was discovered independently by at both Stanford Linear Accelerator (SLAC) and Brookhaven National Labs, thus explaining its two-symbol name [32].

physical example of symmetry is found in an equilateral triangle for which a variety of rotations and reflections leave the triangle looking just as it originally did (see Appendix D for a discussion of that example). All of the distinctive symmetry operations of a system can form an *group* (specifically, a *symmetry group*). A group is any set of operators that meet the following conditions:

1. For any two operators (\tilde{A} and \tilde{B}) in the group, the combinations $\tilde{A}\tilde{B}$ and $\tilde{B}\tilde{A}$ are also in the group (*closure*),
2. The operations are all *associative* such that for any three operators in the group (\tilde{A} , \tilde{B} , and \tilde{C}) one finds $\tilde{A}(\tilde{B}\tilde{C}) = (\tilde{A}\tilde{B})\tilde{C}$,
3. There is an *identity* operator \tilde{I} in the group such that $\tilde{I}\tilde{A} = \tilde{A}\tilde{I} = \tilde{A}$ for every operator \tilde{A} in the group, and
4. For each operator \tilde{A} in the group there exists an *inverse* operator $\tilde{B} = \tilde{A}^{-1}$ in the group such that $\tilde{A}^{-1}\tilde{A} = \tilde{A}\tilde{A}^{-1} = \tilde{I}$.

If all the operators in a given group commute with one another (i.e., $\tilde{A}\tilde{B} = \tilde{B}\tilde{A}$ for any two operators \tilde{A} and \tilde{B} in the group), then the group is called an *Abelian* group. If for every element one finds $\tilde{A}^\dagger = \tilde{A}^{-1}$, then the group is said to be *unitary*. The study of groups in general is known as *group theory*, and is a vital component of high energy physics.*

*The definition and discussion of symmetry groups can be found in texts such as Reference [35].

Naming conventions are given to various groups. An example of a continuous group (one with elements that can be varied over a continuous range) is one consisting of all rotations and reflections in three dimensions. This is the symmetry group for a 3-D sphere, and each element is represented as a 3×3 matrix. It is known as an orthogonal group because the determinant of each element is either $+1$ (for rotations) or -1 (for reflections), and it is named $O(3)$. Considering only the rotations (elements with determinants equal to $+1$) produces a special orthogonal group called $SO(3)$. The $SO(3)$ group governs the physics of angular momentum. Generalizing this to N dimensions, the $SO(N)$ group is a symmetry group of an N dimensional sphere. If one considers a vector in N dimensions positioned at the origin and with length equal to the radius of an N dimensional unit sphere, then an operator in the $SO(N)$ group can change the orientation of the vector, but must leave its length unchanged. Such a vector could also be composed of complex components, and the full symmetry group that leaves the length of such a vector unchanged is referred to as the N -dimensional special unitary group, $SU(N)$ (i.e., it is the symmetry group of a complex N dimensional unit sphere). In addition, the group of scalar rotations on the complex number plane is called the one-dimensional unitary group and is denoted $U(1)$. These groups [$SU(N)$ and $U(1)$] have vital implications in high energy physics where force interactions that

are symmetric under a given group imply a variety of characteristics and have helped predict the existence of particles[†] [25, 35].

One of the most important roles of symmetries is in their relationship to conservation laws. This is a principle known as *Noether's Theorem*, postulated in 1917 by Emmy Noether, which states that for every continuous symmetry of the laws of physics there must exist a conservation law and vice versa [36]. For example, one can consider symmetry under spatial transformation. Because the physics of a system isn't changed if one moves the coordinate system through space, the Hamiltonian operator is generally invariant under spatial translation. The translation operator for an infinitesimal translation, $\delta\vec{x}$, would be defined as \tilde{D} such that $\tilde{D}\psi(\vec{x}) = \psi(\vec{x} + \delta\vec{x})$. This operation can be expanded about \vec{x} (where one can ignore higher orders of the infinitesimal $\delta\vec{x}$):

$$\tilde{D}\psi(\vec{x}) = \psi(\vec{x} + \delta\vec{x}) = \psi(\vec{x}) + \delta x^i \frac{\partial\psi(\vec{x})}{\partial x^i} = \left(1 + \delta\vec{x} \cdot \vec{\nabla}\right) \psi(\vec{x}). \quad (1.30)$$

Thus

$$\tilde{D} = \left(1 + \delta\vec{x} \cdot \vec{\nabla}\right). \quad (1.31)$$

Given the form of the momentum operator noted in Section 1.6 ($\tilde{\mathbf{p}} \equiv -i\hbar\vec{\nabla} = (\hbar/i)\vec{\nabla}$), one can rewrite the \tilde{D} operator as

$$\tilde{D} = \left(1 + \frac{i}{\hbar}\delta\vec{x} \cdot \tilde{\mathbf{p}}\right). \quad (1.32)$$

[†]Specifically, the η^0 meson and the Ω^- baryon were predicted because, before their discovery, there were missing members in representations under an assumed SU(3) symmetry of the strong force that binds their quarks together.

Since the Hamiltonian is not affected by translation, \tilde{D} must commute with \tilde{H} , and from the form of the operator in Equation 1.32, it is obvious that if $[\tilde{D}, \tilde{H}] = 0$ then $[\tilde{\mathbf{p}}, \tilde{H}] = 0$, implying momentum conservation (from Section 1.6). That is, *the symmetry of physical systems under spatial translation demands conservation of linear momentum.*

Similarly, symmetry under rotation implies conservation of angular momentum and symmetry under time translation implies conservation of energy. In Section 1.12, a connection will be drawn between gauge symmetry and conservation of charge. One finds that, via Noether's Theorem, symmetry is responsible for the fundamental conservation laws in physics.

1.10.1 Charge, Energy, and Momentum Conservation

As noted, symmetries involving gauge invariance, invariance under temporal translations, invariance under spatial translations, and invariance under spatial rotations each demand that interactions in the standard model all conserve charge, energy, linear momentum, and angular momentum respectively.

There are important points to note concerning angular momentum conservation in quantum mechanics. The angular momentum of system of particles will consist of two contributions: The intrinsic angular momentum of each particle, s_i , combine to form one contribution (generally labeled $S = \sum_i \pm s_i$), while the particles can also orbit around one another to form an orbital angular momentum contribution (labeled L). These angular momentum contributions combine as vectors to form

the total angular momentum of the system $\vec{J} = \vec{S} + \vec{L}$. Thus the magnitude of \vec{J} ($|\vec{J}| = J$) will be between limits $|S - L| \leq J \leq S + L$; however, because angular momentum is quantized, J can only take values between those limits in steps of 1 ($J = |S - L|, |S - L| + 1, \dots, S + L$).

1.10.2 Lepton Number and Baryon Number

In general, fermions can only be created or destroyed in fermion-antifermion pairs, but for the lepton fermions, a further set of conservation rules apply involving the generational differences mentioned previously. Certain gauge symmetries imply that electroweak interactions between the leptons only happen directly between leptons in the same generation (e.g., a μ^- decaying to a neutrino through the weak force could only decay to a $\nu_\mu + W^-$, where the W^- will further decay to other particles). The conservation law suggested by the symmetry would demand that lepton interactions only occur in ways that preserve the total number of leptons minus the number of antileptons in each generation before and after the interactions. Each lepton is thus assigned a quantum number known as a *lepton number* (or identity number) specific to its generation. They are denoted L_e , L_μ , and L_τ for the three generations, and while the leptons are assigned a lepton number of +1, the antileptons are assigned a corresponding lepton number of -1. All interactions are then required to conserve the total lepton number for each

generation. For example, the decay:

$$\begin{aligned}\mu^- &\rightarrow e^- + \bar{\nu}_e + \nu_\mu, \\ L_e &= 0 = +1 + -1 + 0, \\ L_\mu &= +1 = 0 + 0 + +1,\end{aligned}$$

is allowed because of the lepton number conservation as indicated, while $\mu \rightarrow e + \bar{\nu}_e$ alone would violate lepton number conservation. In that sense, pure cross-generational changes amongst the leptons (without creation or annihilation of an associated antilepton) is not permitted by any known process. Searches have yet to find processes that allow non-conservation of lepton number.

Further, the baryon combinations of the quarks, being three-quark combinations, are also particles of half-integral spin, so they too obey fermion conservation laws. Each baryon is thus assigned a baryon number (B) of +1 while each antibaryon is assigned a baryon number of -1 , and the total baryon number is conserved in all interactions. Mesons, on the other hand, having integral spin (bosons), do not obey such conservation rules.

1.10.3 Quark Generations and the CKM Matrix

Individually, quarks obey fermion conservation rules, and to effect this, each quark is given a baryon number of $+1/3$ while each antiquark is given a baryon number of $-1/3$. This then gives baryons (made of three quarks) their baryon number of ± 1 and mesons (made from quark-antiquark combinations) no baryon number.

One might further expect that the inter-generational conservation rules of the leptons would also be held between generations of the quarks; however, such rules are only found to apply to electromagnetic and strong interactions while weak interactions allow inter-generational processes with quarks. For example, the weak decay of a sigma baryon into a neutron and a pion ($\Sigma^- \rightarrow n + \pi^-$) involves a heavy strange quark being transformed into a lighter up quark via a W^- boson emission (which transforms into the pion): $dd(s) \rightarrow dd(u) + W^-$ (a change in “strangeness” of $\Delta S = -1$). However, such generation-changing decays are found to be suppressed compared to intra-generational decays (such as the well known nuclear beta decay: $n \rightarrow p + e^- + \bar{\nu}_e = ud(d) \rightarrow ud(u) + W^-$). This indicates that the generational hierarchy does exist for quarks but is not as rigid as the lepton case. The Cabibbo theory (1963) [37] accounted for this by proposing that the proper quark states for the down and strange quarks (d' and s') were a mixing of their physical states via a “rotation” through a mixing angle called the Cabibbo angle (θ_C):

$$\begin{pmatrix} d' \\ s' \end{pmatrix} = \begin{pmatrix} \cos \theta_C & \sin \theta_C \\ -\sin \theta_C & \cos \theta_C \end{pmatrix} \begin{pmatrix} d \\ s \end{pmatrix}. \quad (1.33)$$

This properly produced a generational hierarchy between the four quarks in the first two generations: (u d') and (c s'). However, at the time the Cabibbo theory was proposed, the charm quark had not been discovered. In 1970 [38], S. L. Glashow, J. Iliopoulos and L. Maiani (GIM) proposed the existence of the charm quark to accompany the s' in the Cabibbo representation. In 1972,

Kobayashi and Maskawa [39] generalized this to the six quark case with the rotation matrix (the Cabibbo-Kobayashi-Maskawa (CKM) matrix, V) acting on the quark states with $-1/3$ charge:

$$\begin{pmatrix} d' \\ s' \\ b' \end{pmatrix} = \begin{pmatrix} V_{ud} & V_{cd} & V_{td} \\ V_{us} & V_{cs} & V_{ts} \\ V_{ub} & V_{cb} & V_{tb} \end{pmatrix} \begin{pmatrix} d \\ s \\ b \end{pmatrix}. \quad (1.34)$$

Experimental determination of these matrix elements through the study of various particle interactions is a major area of interest in high energy physics.

Given the generational conservation under the strong and electromagnetic forces, quantum numbers (similar to the lepton numbers) are assigned to the quarks, though, as noted, they are not conserved under the weak force. Historically, the up and down quarks were distinguished by assigning them isospin properties*. The up quark is given a total isospin and isospin z-component of $(I, I_3) = (\frac{1}{2}, +\frac{1}{2})$, while the down quark is assigned an isospin $(I, I_3) = (\frac{1}{2}, -\frac{1}{2})$. For the other quarks, their quantum numbers are associated with their names: “strangeness” (S), “charmness” (C^* , to distinguish it from a charge conjugation eigenstate, C), “bottomness” (B^* , to distinguish it from baryon number), and “topness” (T). Each quark is assigned a value of ± 1 for its associated quantum number and zero for the numbers associated with the other quarks as noted in

*Recall from Section 1.7.5 that neutrons and protons were claimed to be two aspects of one particle, distinguished by their differing isospins. This can be accomplished in the quark model by assigning different isospins to their up and down quark constituents.

Table 1.4. As with quantum numbers in general, an antiquark's quantum numbers are the negative of its corresponding quark. Hadrons have values for these quantum numbers found by adding the numbers for their given constituents. As a result of these assignments, the charge (in terms of the electron charge, as usual) of any given quark or hadron can be found from the following combination:

$$Q = I_3 + \frac{1}{2}(B + S + C^* + B^* + T), \quad (1.35)$$

where the part in parentheses is given the term *hypercharge* and is denoted Y .

Table 1.4
Quantum numbers of the quarks.

Quark	B	I	I_3	C^*	S	T	B^*	Q
u:	$\frac{1}{3}$	$\frac{1}{2}$	$+\frac{1}{2}$	0	0	0	0	$+\frac{2}{3}$
d:	$\frac{1}{3}$	$\frac{1}{2}$	$-\frac{1}{2}$	0	0	0	0	$-\frac{1}{3}$
c:	$\frac{1}{3}$	0	0	+1	0	0	0	$+\frac{2}{3}$
s:	$\frac{1}{3}$	0	0	0	-1	0	0	$-\frac{1}{3}$
t:	$\frac{1}{3}$	0	0	0	0	+1	0	$+\frac{2}{3}$
b:	$\frac{1}{3}$	0	0	0	0	0	-1	$-\frac{1}{3}$

Conservation of all these quantum numbers under the strong force helps to predict a variety of allowed and disallow decays. A summary of the conservation/non-conservation of these and other quantities is provided in Table 1.5.

1.10.4 Conservation Under \tilde{P} , \tilde{C} , and \tilde{T}

Conservation under the parity operation (\tilde{P}), the charge-conjugation operation (\tilde{C}), and/or the time-reversal operation (\tilde{T}) implies that a system whose wave function is even (odd) under a given operation before some interaction or decay is still even (odd) afterwards. Such interactions are said to be \tilde{P} , \tilde{C} , and/or \tilde{T} invariant. An interaction that is not invariant under a given conjugation operation implies that the conjugated form of the interaction is either non-physical or occurs with a different probability than the original form. In electromagnetic and strong interactions, processes are found to be invariant under each of these operations. However, weak interactions are essentially found to allow violation of all three.

Until the 1950s, it had generally been assumed that mirror-reflection should not alter any physical process. An experiment to illustrate parity violation in weak decays was first proposed in 1956 by T. D. Lee and C. N. Yang [40] and was carried out in an experiment directed by C. S. Wu [41]. In it, beta-decay (decays emitting electrons) of a radioactive cobalt-60 (^{60}Co) atom found it tended to emit the electrons preferentially in the direction opposite to the spin of the cobalt atom. The mirror reflection of the decay changed the spin, but not the direction of the emitted electrons, though the complete parity operation changes the direction of the electrons but not the spin direction. In either case, the result is a process that exhibits directional properties not found in nature.

An obvious source of parity- and charge-conjugation-violation in weak β -decay is found in neutrinos and antineutrinos (which are emitted as part of the de-

cay). Neutrinos, being without charge or color, only interact via the weak force. Neutrinos (antineutrinos) also possess a unique, intrinsic *handedness* in that their direction of spin is always found to be opposite (the same as) their direction of motion. A measure of this property is found in *helicity*: given a particle's spin direction as $\hat{\sigma}$ and its direction of motion (from its momentum) as \hat{p} , its helicity is given by $H = \hat{\sigma} \cdot \hat{p}$. Neutrinos are found to always have negative helicity (left-handed) and antineutrinos have $H = +1$ (right-handed) [25].* While parity causes the neutrino direction to reverse, the spin direction is an axial vector, and thus does not change under parity. Therefore helicity is odd under the parity operation, and the operation changes a left-handed neutrino (or right-handed antineutrino) into a right-handed neutrino (or left-handed anti-neutrino), which does not exist in nature. Thus, applying parity to an interaction involving neutrinos produces a non-physical system. Similarly, applying charge conjugation (which exchanges particle for antiparticle) to such an interaction changes a neutrino into an antineutrino (and vice-versa) without switching the helicity, thus again producing wrongly-handed neutrinos and anti-neutrinos. Weak interactions therefore allow violations of both \tilde{P} and \tilde{C} , and though this was demonstrated using neutrinos, it is a general property of the weak force.

Note that in the above examples, the combination of \tilde{P} then \tilde{C} (or vice-versa) reproduces an allowed interaction with neutrinos. The parity operation changes

*If neutrinos are truly always left-handed, then they must travel at the speed of light (or one could boost into a frame in which their direction changes but spin does not). This attests to their (nearly) zero mass.

the direction but not the helicity, but charge-conjugation changes the particle to its antiparticle counterpart, thus making the helicity correct again. It is found in general that weak interactions are highly symmetric under the combination of $\tilde{C}\tilde{P}$; however, in 1964, weak decays were discovered (involving the K^0 meson) that violated $\tilde{C}\tilde{P}$ [42]. Two states of the K^0 , named after their comparative life-times, are the K -short (K_S^0) and K -long (K_L^0). The K_S^0 is a superposition consisting primarily of a $\tilde{C}\tilde{P} = +1$ amplitude with only a small amount of $\tilde{C}\tilde{P} = -1$ (and vice-versa for K_L^0). Under $\tilde{C}\tilde{P}$, the two should exchange identities completely, and any decay of one should thus occur with the same probability as the same decay of the other; however, it is found that, for example, in the decay of $K_L^0 \rightarrow \pi^+ + \pi^-$, the amplitude for K_L^0 is slightly larger, thus violating $\tilde{C}\tilde{P}$ invariance. If $\tilde{C}\tilde{P}$ were not violated, one would also expect the same amplitudes for $K_L^0 \rightarrow \pi^- + e^+ + \nu_e$ and $K_L^0 \rightarrow \pi^+ + e^- + \bar{\nu}_e$; however this symmetry is also found to be violated to a small degree. Explanations of this $\tilde{C}\tilde{P}$ violation in weak decays have been a focus of various theoretical works since it was discovered.*

While violations of \tilde{P} , \tilde{C} , and $\tilde{C}\tilde{P}$ have been found in weak interactions, it is believed that all interactions should be symmetric under the combination $\tilde{C}\tilde{P}\tilde{T}$ [25]. This *CPT theorem* can be deduced from very basic properties of relativistic quantum field theory. *CPT* invariance is what demands that particles and antiparticles have the same masses and lifetimes, and it requires integral spin and half-integral

* $\tilde{C}\tilde{P}$ violation is a basic requirement of theories attempting to explain how a universe assumed to start with equal matter and anti-matter could become dominated by matter. Thus $\tilde{C}\tilde{P}$ violation has been an intensive field of study.

spin particles to obey Bose-Einstein and Fermi-Dirac statistics respectively. Thus, since weak decays allow violation of $\tilde{C}\tilde{P}$, then they should also allow violation of \tilde{T} in order for $\tilde{C}\tilde{P}\tilde{T}$ to hold.

1.10.5 A Summary of Conserved Quantities

Table 1.5 is provided below to summarize the conserved quantities under each of the three forces that are well described by quantum field theories. In some instances where quantities are not conserved (specifically, for certain weak interactions) the table indicates the changes believed to be allowed in the quantum number where applicable [25].

1.11 Renormalization

The predictive power of the standard model depends on its ability to calculate such things as cross-sections and transition rates given its descriptions of the fundamental forces and their coupling constants. However, a problem arose (first noted in the application of QED) as attempts were made to calculate such quantities for realistic interactions. The problem can be illustrated using Feynman's "sum over histories" concept. Consider two electrons interacting via a virtual photon exchange (a QED process). To correctly predict the cross-section of such an event, one must include various corrections due to possible transitions that the photon can undergo. For example, the photon could split into a virtual electron-antielectron pair, which could then recombine into the virtual photon; or the same thing could happen but with the pair exchanging another virtual photon before

Table 1.5
Summary of conservation rules.

Quantity Considered	Interaction (Yes = Quantity is Conserved)		
	Strong	Electro-magnetic	Weak
Energy/Momentum:	Yes	Yes	Yes
Charge:	Yes	Yes	Yes
Color:	Yes	Yes	Yes
Weak Isospin:	Yes	Yes	Yes
L_i (lepton number):	Yes	Yes	Yes
B (baryon number):	Yes	Yes	Yes
S (strangeness):	Yes	Yes	no ($\Delta S = 0, 1$)
C^* (charmness):	Yes	Yes	no ($\Delta S = 0, 1$)
B^* (bottomness):	Yes	Yes	no ($\Delta B^* = 0, 1$)
T (topness):	Yes	Yes	no ($\Delta T = 0, 1$)
I (isospin):	Yes	no	no ($\Delta I = 1$ or $\frac{1}{2}$)
I_3 :	Yes	Yes	no
\tilde{G} (G-parity):	Yes	no	no
\tilde{P} (parity):	Yes	Yes	no
\tilde{C} (charge conjugation):	Yes	Yes	no
$\tilde{C}\tilde{P}$ (or \tilde{T}):	Yes	Yes	no (rare violations)
$\tilde{C}\tilde{P}\tilde{T}$:	Yes	Yes	Yes

they recombine; etc. (see Figure 1.3 for Feynman diagrams of these examples).

Even the basic problem of a free electron moving between two points in space-time includes corrections due to the self-interaction of the electron—it can emit and

re-absorb virtual photons, which too can split into particle-antiparticle pairs that rejoin, etc. (see Figure 1.4 for Feynman diagrams of these examples). Any one of these corrective transitions can occur in a number of ways (with different emission and absorption points, for example), and as one considers possibilities with more and more transitions, the corrections include more and more vertices and thus involve higher and higher orders of the coupling constant.

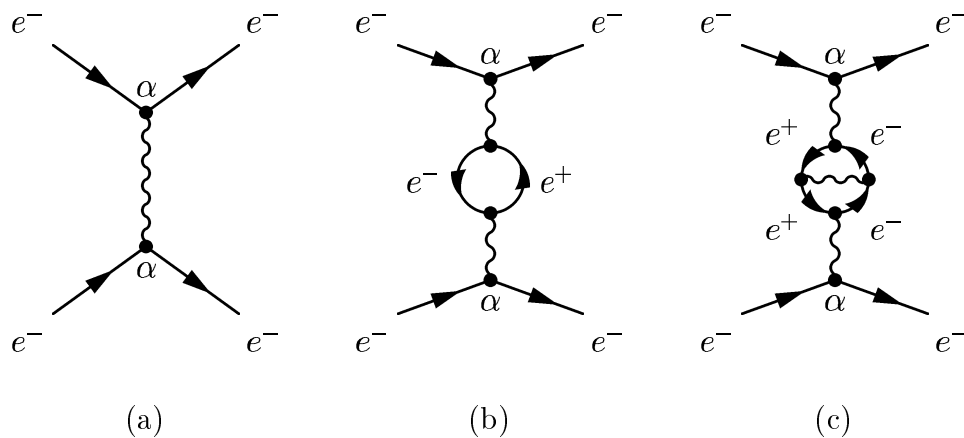


Figure 1.3

Feynman diagrams showing internal “corrective” processes for a scattering event.

These corrections effectively alter the measured coupling between the electrons (thus effecting the actual, measured charge, e) and surround the electron with a “cloud” of virtual particles (thus effecting its actual, measured mass). Without these corrections, the electron would act like an “ideal” particle with some “bare”

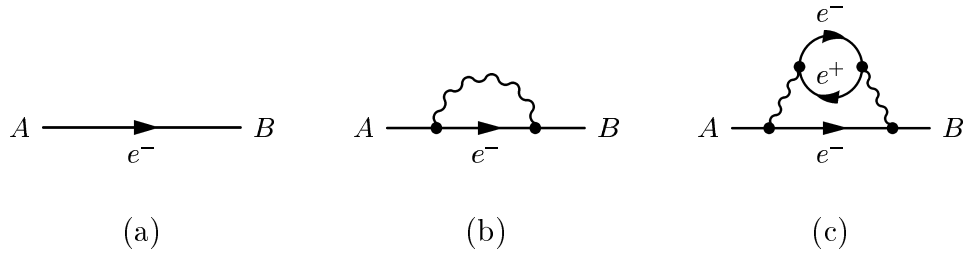


Figure 1.4

Feynman diagrams showing internal “corrective” processes via self-interaction.

mass m'_e and charge e' , which should then be used to properly compute these various corrective factors in all physical processes.

However, calculating such corrections must include possibilities where absorption and emission in the corrective effects are infinitesimally close; therefore, the calculation for any such correction will involve integrals over all possible momentum transfers up to infinity. The integrals (containing factors on the order of dk/k , which come from the momentum propagator term) are logarithmically divergent, and the calculated corrections become infinite for all amplitude computations [24, 25].

To overcome this problem in QED, a process known as *renormalization* was used in which all the divergences were absorbed into the bare mass and charge of the electron (arbitrary and unmeasurable quantities) so as to produce the actual, measured mass and charge of the electron. The process was developed in the 1940s by Richard P. Feynman, Julian Schwinger, and Sin-Itiro Tomonaga, who shared the 1965 Nobel Prize in physics for their contributions [23]. Renormalization allowed

the calculated correction factors in any event and at all orders in the coupling constant to be finite, and provided QED with computable predictive power.* A theory is thus said to be renormalizable if a *finite* number of parameters (which must be measured experimentally) are used to absorb *all* divergences at all orders in the coupling constant such that the amplitudes of physical processes become finite calculations.

One of the most elegant applications of QED's predictive power (made possible by renormalization) is in the calculation of radiative corrections to the magnetic moment of the electron (which affects its interactions with magnetic fields). For an ideal, point-like electron, its magnetic moment and its spin vector are related by a constant (the Landé g -factor) of $g = 2$. However, highly precise measurements of this factor have proved that it is not 2 by some small amount ($< 0.2\%$). The QED corrections provide a prediction of the actual g factor by including many corrective terms (each involving successively higher orders in α). A diagram of the basic process and three corrective terms is given in Figure 1.5. The correction involves a power series in α , and calculation of the coefficients for each term was made possible via renormalization. A comparison between highly precise measurement of the g factor for an electron (made in 1987) and a recent calculation using QED

*Feynman himself (a co-developer of renormalization) always considered it to be something of mathematical hocus-pocus, though the predictive power it provided has proven remarkable.

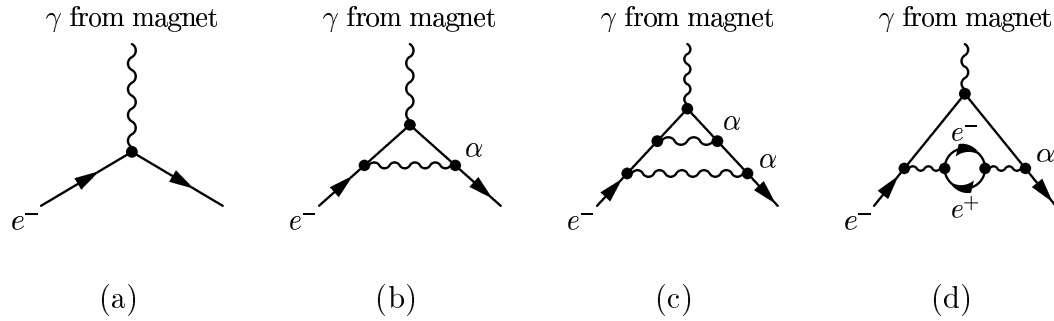


Figure 1.5

Feynman diagrams showing some radiative corrections to the electron's magnetic moment.

is given here [43, 44]:

$$g_e \text{ measured: } \quad (1159652188.4 \pm 4.3) \times 10^{-10} \% \text{ different from } 2,$$

$$g_e \text{ predicted: } \quad (1159652205.4 \pm 27.1) \times 10^{-10} \% \text{ different from } 2.$$

This is one of the the most precise experiments in physics, and it is said there is no better agreement between theory and experiment in all of science.

Renormalization generally arises in theories with a high degree of symmetry. However, when massive bosons are included (such as those in weak interactions), the terms in the calculations that diverge (originating in the boson propagator term) turn out to only be absorbed by introducing an indefinitely large number of arbitrary constants. Thus such theories are, in general, not renormalizable, and they tend to loose all predictive power. This seemed to spell trouble for a useful quantum field theory of weak interactions.

1.12 Gauge Invariance

Perhaps the most fundamental principle embodied in the field theories governing forces in the standard model is that of *gauge invariance*. Global gauge invariance implies that a system involving a given force is symmetric under some operation that is applied equally throughout space to the field governing the force. Such symmetry implies conservation laws (as noted above). For example, calculations in electrostatics depend only on the change in an electric potential field from one point in space to another, and no physical process can depend on the actual value of the field at just one point. This global gauge invariance dictates charge conservation. To demonstrate this, assume it were possible to create a charge, Q within a potential field, allow the force from the field to move the charge to another location, and then destroy it. Let the potential at the initial and final locations (on some chosen scale) be ϕ_i and ϕ_f . Further, let the work done in creating and destroying the charge be W_i and W_f . Given global gauge invariance, the work done at the two different locations in the potential field cannot depend on the actual values of ϕ_i and ϕ_f , therefore $W_i = W_f$; however, as the charge moved in the field, its potential energy is changed by $Q(\phi_f - \phi_i)$. The overall change in energy is then $\Delta E = W_f - W_i + Q(\phi_f - \phi_i) = Q(\phi_f - \phi_i)$. Thus, because of global gauge invariance, non-conservation of electric charge would imply non-conservation of energy—*global gauge invariance implies charge conservation*. (Mathematically, one could require global gauge invariance for the wave equation (or equation of motion) governing a charged particle in a potential field. The results would show

that the divergence of the four-dimensional current density is zero, which implies charge conservation.)

Gauge invariance can be investigated by considering a charged particle whose wave function is denoted $\psi(\mathbf{x})$ (where \mathbf{x} is in four dimensional space-time). The Lagrangian of such a particle will, in general, include terms similar to the following*:

$$\psi^\dagger(\mathbf{x})\partial_\mu\psi(\mathbf{x}), \quad (1.36)$$

where

$$\partial_\mu\psi(\mathbf{x}) = \frac{\partial\psi(\mathbf{x})}{\partial x^\mu} \quad (1.37)$$

is the gradient of $\psi(\mathbf{x})$ in four dimensions ($\mu \in (0, 1, 2, 3) = (ct, x, y, z)$, see Appendix B).

Global gauge invariance requires that a phase rotation in the wave function must leave the equation of motion unchanged. Such a rotation is given by

$$\psi(\mathbf{x}) \rightarrow e^{i\alpha}\psi(\mathbf{x}) \quad (\text{such that } \psi^\dagger(\mathbf{x}) \rightarrow e^{-i\alpha}\psi^\dagger(\mathbf{x})), \quad (1.38)$$

and terms in the Lagrangian involving the gradient thus become

$$\psi^\dagger(\mathbf{x})\partial_\mu\psi(\mathbf{x}) \rightarrow e^{-i\alpha}\psi^\dagger(\mathbf{x})\partial_\mu(e^{i\alpha}\psi(\mathbf{x})) = \psi^\dagger(\mathbf{x})\partial_\mu\psi(\mathbf{x}). \quad (1.39)$$

Such terms are thus left unchanged under a phase rotation specifically because α is a constant in \mathbf{x} ($\partial_\mu e^{i\alpha} = 0$), and thus *global* gauge invariance is obviously held.

*One could also consider the Klein-Gordon equation that is derived from such a Lagrangian, and which includes terms involving $(\partial/\partial x^i)^2\psi$, but looking at the gradient terms in the Lagrangian will suffice and allows for easier math.

However, a much more powerful requirement is that of *local* gauge invariance. That is, if the phase rotation is dependent on the particular position in space-time, then $\alpha \rightarrow \alpha(\mathbf{x})$ such that

$$\psi(\mathbf{x}) \rightarrow e^{i\alpha(\mathbf{x})}\psi(\mathbf{x}). \quad (1.40)$$

Terms involving the gradient then become

$$\begin{aligned} \psi^\dagger(\mathbf{x})\partial_\mu\psi(\mathbf{x}) &\rightarrow e^{-i\alpha(\mathbf{x})}\psi^\dagger(\mathbf{x})\partial_\mu(e^{i\alpha(\mathbf{x})}\psi(\mathbf{x})) \\ &= e^{-i\alpha(\mathbf{x})}\psi^\dagger(\mathbf{x})e^{i\alpha(\mathbf{x})}[\partial_\mu\psi(\mathbf{x}) + i\psi(\mathbf{x})\partial_\mu\alpha(\mathbf{x})] \\ &= \psi^\dagger(\mathbf{x})\partial_\mu\psi(\mathbf{x}) + i\psi^\dagger(\mathbf{x})\psi(\mathbf{x})\partial_\mu\alpha(\mathbf{x}) \\ &\neq \psi^\dagger(\mathbf{x})\partial_\mu\psi(\mathbf{x}). \end{aligned} \quad (1.41)$$

Thus, an equation of motion derived from a Lagrangian containing such a gradient term is not invariant under local gauge transformations; however, what if one forces local gauge invariance? To do so, one requires a different type of derivative (D_μ) such that $D_\mu(e^{i\alpha(\mathbf{x})}\psi(\mathbf{x})) = e^{i\alpha(\mathbf{x})}D_\mu\psi(\mathbf{x})$. To construct such a derivative requires the introduction of a new vector term, $A_\mu(\mathbf{x})$, in a way that will cancel out the unwanted terms in the previous equation. Thus one defines

$$D_\mu \equiv \partial_\mu - iA_\mu, \quad (1.42)$$

where A_μ transforms under a gauge transformation as follows:

$$A_\mu(\mathbf{x}) \rightarrow A_\mu(\mathbf{x}) + \partial_\mu\alpha(\mathbf{x}). \quad (1.43)$$

Then terms involving the new derivative transform as

$$\begin{aligned}
\psi^\dagger(\mathbf{x})D_\mu\psi(\mathbf{x}) &\rightarrow e^{-i\alpha(\mathbf{x})}\psi^\dagger(\mathbf{x})D_\mu(e^{i\alpha(\mathbf{x})}\psi(\mathbf{x})) \\
&= e^{-i\alpha(\mathbf{x})}\psi^\dagger(\mathbf{x})[\partial_\mu - iA_\mu - i\partial_\mu\alpha(\mathbf{x})](e^{i\alpha(\mathbf{x})}\psi(\mathbf{x})) \\
&= e^{-i\alpha(\mathbf{x})}\psi^\dagger(\mathbf{x})e^{i\alpha(\mathbf{x})} \\
&\quad \times [(i\partial_\mu\alpha(\mathbf{x}) + \partial_\mu) - iA_\mu - i\partial_\mu\alpha(x)]\psi(\mathbf{x}) \\
&= \psi^\dagger(\mathbf{x})[\partial_\mu - iA_\mu]\psi(\mathbf{x}) \\
&= \psi^\dagger(\mathbf{x})D_\mu\psi(\mathbf{x}),
\end{aligned} \tag{1.44}$$

and equations of motion derived from a Lagrangian that contains such derivative terms are invariant under local gauge transformations. However, such an equation is precisely the form of the electromagnetic field mediated by a massless boson (the photon) described by the vector field A_μ (associated with the classical electromagnetic vector potential). Thus, *requiring local gauge invariance under phase transformations demands the existence of the photon and all the laws governing quantum electrodynamics.*

Put forth in a more general way, demanding local gauge symmetry in a system requires a mediating field to be added (such as A_μ) whose response to any local operation on the field is to directly compensate for the variations in symmetry that would otherwise occur from point-to-point. The field thus propagates local symmetry throughout the system and provides an interaction mechanism. Such a field is called a *gauge field*, and the quanta that mediate it are called *gauge quanta*. Because the extent to which the variations can occur through space-time is unlimited, the effects of the gauge field must have infinite range, and thus such

gauge invariant systems require massless quanta. Further, gauge invariant theories impose constraints that cause them to contain a high degree of symmetry, and as a result they are always renormalizable.

A theory possessing local gauge-invariance thus *defines* a system of interaction (i.e., a force-carrying field). The gauge field provides the interaction medium, and the specific framework of the interaction (the format of the specific force) is determined by the type of symmetry being demanded. For example, the above set of infinite local phase transformations via the scalar α produces the complete description of the electromagnetic force. Those transformations form an Abelian, unitary symmetry group, U(1). In a similar way, color symmetry under the group SU(3) is a gauge invariance that implies the existence of the gluon and the laws governing quantum chromodynamics. It was hoped that such a gauge invariance application could also imply the weak field and its gauge bosons. However, since gauge invariance always implies massless bosons, the massive propagators of the weak field tend to defy gauge invariance (as well as the ability to renormalize).

In 1954, C. N. Yang and R. Mills suggested gauge invariance under the group SU(2) in isospin space [45]. Local invariance under isospin rotation can be imposed (similarly to how local gauge invariance was imposed in electrodynamics above) by adding a component to the derivative involving an isovector field with components in isospin space denoted $W_\mu^{(1)}$, $W_\mu^{(2)}$, and $W_\mu^{(3)}$. This implies a force mediated by both charged and neutral massless bosons; however, no charged, massless bosons are found to exist. Further, if one wishes to consider this as a description of the

weak force, a problem arises in that isospin conservation can be violated in weak interactions, implying that isospin symmetry cannot be strictly required.

Overcoming the problems of applying gauge invariance and renormalization to the weak force has been a major triumph for the standard model, and it is briefly explored in the next section.

1.13 Development of the Electroweak Theory

In the late 1960s [25, 46], Glashow, Salam, and Weinberg proposed a gauge theory based on an $SU(2)$ group in “weak isospin” (\mathcal{I}) and a $U(1)$ group in “weak hypercharge” (defined here as $Y = 2(Q - \mathcal{I}_3)$, where Q is the electric charge and \mathcal{I}_3 is the third component of weak isospin). The model possesses an underlying gauge symmetry and suggests massless boson fields consisting of a weak isospin triplet of vector particles ($W_\mu^{(1)}$, $W_\mu^{(2)}$, and $W_\mu^{(3)}$), an isospin singlet vector particle (B_μ), and an isospin doublet of scalar particles (ϕ^+ and ϕ^0 , known as Higgs scalars). Via self-interaction, the Higgs scalars generate mass in a process called *spontaneous symmetry breaking* (invoked by Glashow, Salam, and Weinberg).^{*} This breaking of the underlying local symmetry remarkably leaves the renormalizability of the theory intact and further allows the physical quanta to acquire mass. The Higgs scalars (complex fields) have a total of four real components: ϕ^+ , $\bar{\phi}^+ = \phi^-$, $(\phi^0 - \bar{\phi}^0)/\sqrt{2}$, and $(\phi^0 + \bar{\phi}^0)/\sqrt{2}$. The former three are “eaten” by the W fields, providing them with mass (and leaving one physical Higgs scalar in the basic model, for which

^{*}For a simple but instructive example of spontaneous symmetry breaking, see Appendix E.

physicist are currently searching). The physical bosons resulting from the model are then found to be combinations of the $W_\mu^{(i)}$ and B_μ fields: The W^+ and W^- massive, charged propagators of the weak force arise from combinations of $W_\mu^{(1)}$ and $W_\mu^{(2)}$, while mixing of the $W_\mu^{(3)}$ and B_μ fields give rise to a neutral, massive field (the Z^0 propagator of the weak force) and a neutral, massless field (the photon propagator of the electromagnetic force).

Thus, the Glashow, Salam, and Weinberg model invoked spontaneous symmetry breaking to make the γ , W^\pm , and Z^0 bosons originate from a group of four massless vector particles and two massless Higgs scalars. The theory, known as the *electroweak theory*, effectively combined the weak and electromagnetic interactions into one theoretical framework and suggested that the two forces would have the same coupling at high momentum transfers. As noted in Section 1.8.7, this helped to predict the masses of the W^\pm and Z^0 bosons..

The use of gauge invariance in numerous ways has thus lead to consistent field theories describing the electromagnetic force (QED), the strong nuclear force (QCD), and the weak force (electroweak theory). The success of the combination of electrodynamics and the weak force into one unified theory has started physicists down a path of trying to combine all the forces under one theoretical framework, the so-called “grand unified theory.” Obviously the power of gauge invariance is vital in the standard model.

1.14 Modern Study of High Energy Physics

The standard model provides a satisfactory description of many phenomena in high energy physics; however, not only does it leave much to be determined by experimentation (e.g., various particle masses, the coupling constants of the forces, mixing angles, etc.), but it also leaves a variety of questions unanswered and many possibilities exist for physics beyond the standard model. Modern study of high energy physics explores the questions and unknowns in the standard model, searches for experimental outcomes that the standard model does not account for, and develops theories within and beyond the framework of the standard model in an attempt to unify various parts of the model and predict a wide range of phenomena.

Some of the many research topics explored in modern high energy physics include the following: the investigation of non-zero neutrino masses, the search for lepton number non-conservation, the search for the Higgs and the prediction/measurement of its mass, precise measurement of the CKM matrix elements, the study of and search for $\tilde{C}\tilde{P}$ violation, the search for rare decays and their decay rates, the study of cosmology and cosmic-scale structures via high energy physics phenomena, etc. Some specific theoretical work in high energy physics includes formulation of a grand unified theory (attempts to unite the four forces under one framework), super symmetry (which attempts to relate fermions and bosons under one framework), and quantum gravity.

In these studies in general, and for this dissertation in specific, particle decay mechanisms are an important realm of investigation since they are controlled by the fundamental forces. The decay rate and manner in which a specific decay occurs is determined by how the fundamental force mediating the decay behaves. Models are often proposed to describe the specific resonance structure within a decay, but the relative importance of the resonances and tests of their modeling require experimental determination.

Experimentation provides the ultimate tests of the models in high energy physics and often furnishes the impetus for future theoretical development. In order to perform experiments in high energy physics, one requires the ability to detect and direct fundamental particles in a variety of ways, as discussed in the following section.

1.15 Particle Manipulation and Detection

The study of high energy physics requires the manipulation and detection of various fundamental particles. Charged particles can be manipulated by the use of electromagnetic fields, which are readily controlled with current technology. While one can find ways to generate neutral particles along some given path, controlled manipulation of such particles would require precise command over the gravitational, weak, and/or strong force (depending on the particle type), none of which is possible with current knowledge and technology. Detection of fundamental particles can be achieved for both charged and neutral particles given their interactions

with various materials. The following sections overview general principles and equipment used for charged particle manipulation and for various types of particle detection.

1.15.1 Accelerating and Directing Charged Particles

Charged particles can be accelerated by the proper use of electric fields*. One device used for such acceleration is illustrated in Figure 1.6. It displays a linear

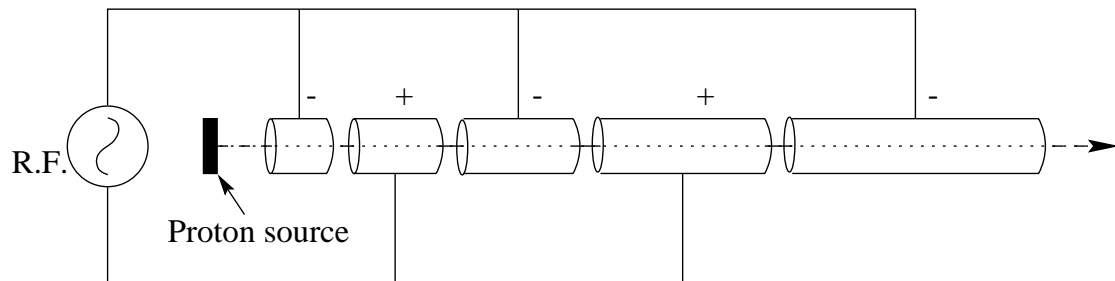


Figure 1.6

A diagram depicting a simple proton linear accelerator. Alternating potentials on the tube segments propel the proton, and successively longer segments are needed so the proton traverses each segment in the same length of time while it is also being accelerated.

accelerator consisting of tubular sections attached to a radio frequency (RF) alternating voltage source. In practice, the sections would all be within one evacuated tube. As the voltage changes, alternating sections of the accelerator are charged positively and negatively. Given the right alternating frequency and successively

*Information concerning general aspects of particle manipulation can be found in a variety of textbooks including [25].

longer tubes along the length, a proton[†] injected into the accelerator at the right time can be attracted into each successive section while being ejected from the previous such that somewhat continuous acceleration is provided through the length of the apparatus. The increasing lengths of each tube section should ensure that though the proton is accelerating, it spends the same amount of time in each section (thus allowing the accelerator to operate with a constant frequency voltage source).

Because of their small mass, the velocity of an electron with energy above a few MeV (in the laboratory frame of reference) is nominally close to the speed of light (in that frame). Force applied to such an electron can increase its energy but can only increase its velocity by an insignificant amount. Thus, in the above accelerator, successive tube lengths would become uniform. In practice, a series of radio frequency (RF) cavities is used to provide acceleration for high energy electrons.

An *RF cavity* is a specially designed chamber in which a microwave frequency electric field resonates back and forth. In the center of the cavity the field is strongest and an opening on either side allows particles to pass into and out of the cavity, thus experiencing a force from the electric field. A diagram of an RF cavity is shown in Figure 1.7. Whether a particle feels a force against its motion or with its motion as it enters an RF cavity depends on the direction of the field at that

[†]Protons can be collected by stripping an electron off of a hydrogen atom (i.e. they are hydrogen ions).

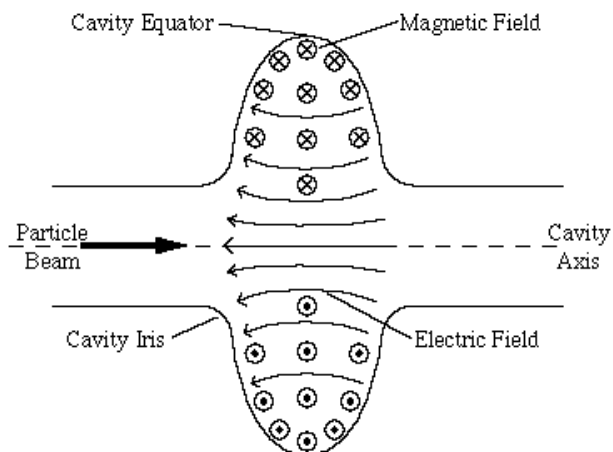


Figure 1.7

A generic RF cavity geometry showing electric and magnetic field lines. The peak of the oscillating electric field is strongest through the central axis of the cavity while the magnetic field is constrained towards the equatorial region of the cavity.

moment; thus the distance between cavities and the timing of the oscillating field in each must be properly synchronized so as push the electrons forward as they pass through each cavity. The electrons essentially ride on the wave crest of the electric field in each cavity as they are propelled down the beam pipe.

To keep charged particles along a desired path, magnetic fields can be used to manipulate their motion. Though magnetic fields do no work (they do not provide force in or against the direction of motion), they do provide a force perpendicular to the motion of a charged particle as it crosses the magnetic field lines. A *dipole magnet* is an electromagnet designed to have opposing poles pointing toward one another with a gap between them. The field lines pass straight from one pole to the next providing a somewhat uniform magnetic field between them. A particle

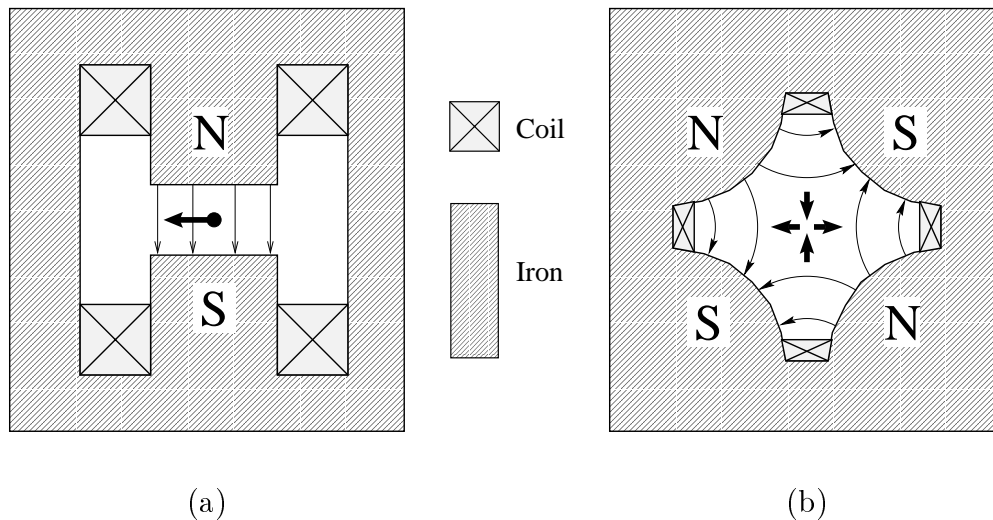


Figure 1.8

Cross-sectional diagrams of a dipole bending magnet (a) and a quadrupole focusing magnet (b). Thin arrows indicate the magnetic field lines while thick arrows show the force direction on a positive charge moving “into” the page.

moving between the poles and perpendicular to the field lines will be forced to veer “left” or “right” (perpendicular to the field lines) depending on its charge. Figure 1.8(a) displays a diagram of such a bending magnet showing the direction of force a positive particle would feel as it entered the field. The amount of bending will depend only on the strength of the magnet, the charge of the particle, and its momentum. Thus with proper positioning of bending magnets, one can direct moving charged particles as desired.

One generally wishes to keep particle bunches highly concentrated, which requires focusing of particle beams. Properly designed electromagnets with more than two inwardly facing poles (quadrupole, sextupole, etc.) produce field lines that provide a “focusing” force in the center of the magnet. An example of a

quadrupole magnet is shown in Figure 1.8(b) and shows that a positive charge entering the magnet would be experiencing a stable force pushing it inwards along one axis perpendicular to its motion while experiencing opposing forces outwardly along the other axis. By using a series of such magnets, each turned 90° from the previous one, a beam of charged particles passing through them would become focused in both directions.

Thus, by using electromagnetic fields in a variety of configurations, charged particles can be manipulated as needed to perform desired experiments.

1.15.2 Particle Detectors

As charged particles pass through a medium they will interact electromagnetically with the atoms in the medium, thus directly or indirectly transferring energy to the atoms. In general, the energy transfer will either excite the atoms, which will then de-excite and emit photons, or it will strip away electrons, turning the atoms into electrically charged ions. Various devices utilize and measure these effects to provide charged particle detection and tracking. Some devices also allow detection of certain neutral particles such as high energy photons. Brief descriptions for several detection devices are given here.*

Cloud Chambers: Under the right conditions, when a charged particle passing through a medium generates ions, the presence of the ions can produce visible effects in the surrounding medium. A cloud chamber (first conceived of and

*Greater details concerning such particle detectors can be found in various references including [25, 47].

used in the early part of the 20th century) generally contains gas saturated with water vapor. Charged particles passing through the chamber will leave a trail of ions, and under the right conditions the vapor will condense into a cloud of tiny water droplets along the ionization trail, thus producing a visible track where the particle had passed.

Bubble Chambers: Bubble chambers (invented in 1952 by Donald Glaser) are filled with superheated liquid in which an ion trail can form. When pressure on the liquid is released, boiling can occur, and tiny bubbles appear preferentially along any ionization trails in the chamber. As with cloud chambers, visible tracks form where charged particles have recently passed. The tracks can then be photographed and analyzed. Though bubble chambers have been an indispensable tool for high energy physics, they have major limitations: they are unable to quickly record a series of successive events, and analysis of the resulting films is very time consuming.

Spark Chambers: A spark chamber consists of a series of stacked plates (or a wire grid) separated by spaces where alternate plates are oppositely charged at high voltage. The surrounding chamber (including the gaps between the plates) is filled with gas in which ions form when a charged particle passes through. The electrons left along the trail are propelled by the high voltage, and the resulting spark passes through the chamber, indicating the path of the charged particle.

Proportional Counters: A single proportional counter consists of a gas filled hollow tube whose outer surface is maintained at a negative electric potential (thus acting as a *cathode*). Through the center of the tube is a fine wire kept at a positive potential (an *anode*). A charge particle passing through the tube leaves ions and liberated electrons in the gas. The electrons (with little mass) drift readily toward the positive “sense” wire, gaining energy and potentially liberating more electrons from the gas as they travel. Those secondary electrons will also drift and potentially liberate even more electrons, thus producing an “avalanche” effect. As electrons reach the anode wire they generate an electrical pulse that can be read out by electronics attached to the wire. Thus, a series of proportional counters can be used to track particles as they pass through each one, and the data can be quickly stored electronically for later analysis. The number of secondary electrons reaching the wire is generally directly proportional to the number of initial ions produced, thus the name “proportional counters.”

Multi-wire Proportional Counters: A useful extension of proportional counters is a multi-wire version introduced in the late 1960s by G. Charpak. It utilizes a series of anode wires strung in a plane between two cathode plates such that each wire acts as an independent detector. In practice the cathode plates are often made of strips running perpendicular to the anode wires.

The electromagnetic effects of the avalanche cause pulses on the the cathode strips as well, and further spatial information can be gained.

Drift Chambers: Drift chambers are designed to obtain the benefits of a multi-wire proportional counter over large tracking areas. They generally consist of many sense wires, each surrounded by an arrangement of field shaping wires to produce cells. The field wires are arranged and maintained at proper potentials so as to provide a uniform drift field for the liberated electrons. The electrons drift through this field until reaching a sense wire where an electric pulse is created and measured. By noting drift times and the series of wires that receive pluses, a reasonably high resolution measurement of a charged particle's path through the chamber can be obtained.

Scintillation Counters: When particles pass through certain media they can cause excitation of the atoms, which then emit light (luminescence) in a process called scintillation. This can occur in different ways for different scintillating media. The process is generally vary rapid, making scintillation counters useful for taking many consecutive measurements of extremely frequent events. The light produced in such a device can be recorded by various light-sensitive devices such as photomultiplier tubes and photodiodes. In a photomultiplier, light strikes a metal coated cathode, liberating electrons via the photoelectric effect. The electrons are attracted to and strike a positively charged "dinode" where they liberate more electrons that are in turn attracted to

more diodes, each with a successively larger potential. Through this amplification process a sizable electric pulse is produced. Photodiodes sense light using a solid-state effect by which light at a given frequency can create a current in the diode. Light produced in a scintillator can travel through it via internal reflection, and if needed it can be piped with a clear light guide to the detection device.

Čerenkov Counters: Though particles do not travel faster than the speed of light in a vacuum, in a translucent material light transmission is slowed as the light interacts with the medium. It is therefore possible for a highly energetic particle to traverse certain dielectric media faster than light is transmitted through the media. This creates a coherent wave-front of light (called Čerenkov radiation after its discoverer) in a fashion similar to the creation of a sonic boom when an object travels faster than sound through air. The angle the wave-front makes with respect to the direction of the particle is given by $\cos \theta = 1/(\beta n)$, where n is the index of refraction for the medium and the particle's velocity is given in terms of $\beta = v/c$. Thus, with a properly selected medium, high-speed particles can be detected by the Čerenkov radiation they produce; and even more useful, a measure of the wavefront angle provides a direct measurement of the particle's speed.

Shower Calorimeters: Calorimeters measure particles utilizing a total absorption method where nearly all of the particle's energy is absorbed in the detec-

tor (and they are thus composed of relatively dense, solid material). They provide for detection of charged particles as well as energetic photons and neutral hadrons. For example, an electron decelerated by electromagnetic interactions in a calorimeter releases photon radiation via bremsstrahlung (or an energetic photon can enter the calorimeter to start the process). In either case, the photon can interact with the material to produce an electron-antielectron pair, and they are caused to radiate more photons, quickly resulting in a shower of particles and radiation. Once the process produces photons without enough energy to generate more pairs, the cascade abruptly stops. The total energy of the photons that are finally emitted can be measured and will be proportional to the initial particle energy that was absorbed. Calorimeters can also be produced to detect hadrons through a similar process involving nuclear interactions. Calorimeters are thus useful for detecting and measuring the energy of particles that need not exit the device. They also have fast reaction times, making them useful when energy information needs to be used in make quick electronic decisions (e.g., for event selection).

Neutrino Detectors: While study of neutrinos is of relatively strong interest, the fact that they have little or no mass and only interact via the weak force makes them very hard to detect. They can very readily pass through vast amounts of material (such as the entire Earth) without being affected. Of particular interest is solar neutrinos because the rate at which they are de-

tected is lower than current theory can account for.* Neutrino study is generally undertaken by large, specialized experiments designed just for that purpose. For example, the largest underground neutrino detector to date (the Super-Kamiokande in Japan) is comprised of a vast tank filled with 50,000 tons of water buried thousands of meters underground (to shield it from unwanted interactions). Neutrinos can interact weakly with the electrons in the water and propel them to high speeds so as to produce Čerenkov radiation. The radiation can then be detected by the roughly 13,000 photomultiplier tubes that line the interior of the tank.

Large Hybrid Detectors: General purpose experiments in high energy physics require a variety of measurements on many different types of particles produced by the interactions they generate. Such facilities therefore utilize an assortment of detectors arranged into one hybrid detector array. Such an array was used to gather the data presented in this dissertation, as discussed below.

*Neutrinos are generated copiously by interactions within stars and pass through the stars and into space. The Earth is bombarded by on the order of one trillion neutrinos every second from the sun.

2. THE CESR AND CLEO II EXPERIMENTS

The data used for the analysis presented herein was taken at the Cornell Electron Storage Ring (CESR) using the CLEO II detector. These facilities are located at Cornell University in Ithaca, New York, and the data was taken between November 1990 and April 1995. Details concerning the data selection are presented in Chapter 4, while the experiments used to collect the data are described here.

2.1 The Cornell Electron Storage Ring

The Cornell Electron Storage Ring (CESR, pronounced “Caesar”) is a circular electron-positron collider with a circumference of 768 meters (roughly half a mile in circumference or 400 feet in diameter) [48]. It was constructed in the mid-1960s (though it began colliding beam experiments in 1979) and it is located about 12 meters under ground below an athletic field and a parking lot on Cornell University campus. Through a process described below, electrons and positrons (antielectrons) are accelerated and injected into the ring with electrons traveling counter-clockwise and positrons traveling clockwise. The beams are held in the storage ring, and with each pass around the ring they are brought into collision at a specific interaction region around which the CLEO II detector is centered. The by-products of the resulting electron-positron annihilations can then be analyzed.

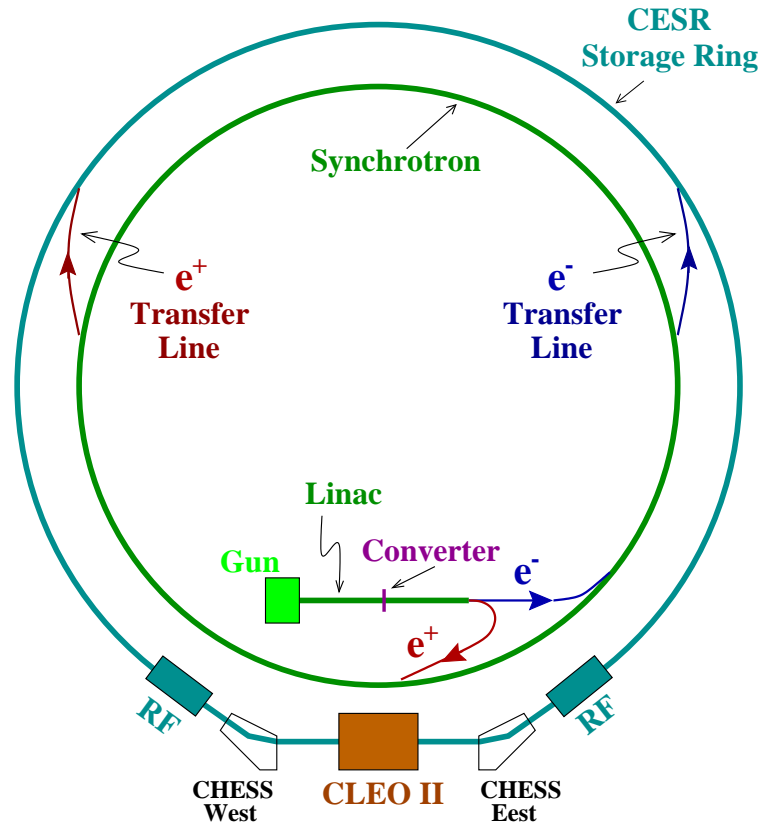


Figure 2.1

Diagram of the Cornell Electron Storage Ring (CESR)

CESR is suited for producing collisions with a center-of-mass energy range from 9.4 to 12.0 GeV, thus it operates in the range of the $\Upsilon(4S)$ resonance—an excited $b\bar{b}$ meson state with a peak mass of 10.58 GeV (just above the threshold to produce $B\bar{B}$ meson pairs). This makes CESR uniquely suited for production and study of the b and c heavy quarks as well as τ -pair events, providing a wide variety of research topics.

The electrons and positrons are created and manipulated using electromagnetic fields controlled in various components of CESR. The major components of CESR

are the linear accelerator, the synchrotron, and the storage ring (see Figure 2.1 for a schematic of CESR).

2.1.1 The Linear Accelerator

The *linear accelerator* (or *linac*) is used to generate and initially accelerate the electrons and positrons. Electrons are generated at the base of the linac by “boiling” them off of a heated filament (similarly to how electrons are generated in a television picture tube). After the beam of electrons is focused using electromagnetic fields (from a beam roughly 2 meters long into a bundle roughly 1 to 2 mm long containing over 20 billion electrons), the linac accelerates the electrons through a 30 meter long vacuum pipe using the actions of microwave electric fields generated in RF cavities.* The electrons reach an energy of about 300 MeV before being injected into the synchrotron, where most of the energy build up is performed. The positrons are generated at an intermediate point of the linac where electrons accelerated to 140 MeV strike a tungsten plate. This produces a spray of electrons, positrons, and X-rays, from which the positrons are selected, focused, and accelerated through the remaining length of the linac (to about 200 MeV) before they too are injected into the synchrotron’s beam pipe. This produces tight groups or bunches of electrons and positrons that take turns being accelerated (in opposite directions) in the synchrotron.

*See Section 1.15.1 for information on RF cavities.

2.1.2 The Synchrotron

The bulk of the particle acceleration is performed in a circular accelerator, the *synchrotron*, which sits just inside the storage ring. Acceleration is performed in 4 10-foot linear accelerators (again, using RF cavities) positioned around the synchrotron's beam pipe while the particles are bent around the ring via 192 10-foot sections of bending magnets. After roughly 4,000 cycles around the synchrotron over a period of about 10 ms, the electron or positron bunches reach their maximum desired energy of ~ 5.3 GeV and are injected into the storage ring.[†] The procedure is repeated, alternating between the electron and positron bunches, until the desired current for each is achieved in the storage ring (taking roughly 10 minutes at 60 alternations per second).

2.1.3 The Storage Ring

The *storage ring* is designed to maintain the energy level of the electrons and positrons while keeping them separate as they travel through the same beam pipe in opposite directions until they are purposefully brought together every cycle at the interaction point. The beams are kept in the circular ring by a series of dipole bending magnets while they are continually kept focused by quadrupole and sextupole focusing magnets. The electrons and positrons are kept separate in the horizontal plane using electrostatic separators.

[†]An electron or positron with roughly 5 GeV of energy is traveling at about 99.9999995% of the speed of light.

During each filling (done numerous times during a typical running day) the beams are held in the storage ring for times on the order of 90 minutes, crossing millions of times each second. This places rigorous demands on the precision of the magnets and requires that a high quality vacuum (many billions of times less dense than atmospheric pressure) be kept within the beam pipe. The vacuum is maintained by a series of vacuum pumps distributed around the ring that use a process called glow discharge to drive air molecules into metal electrodes. In addition, the vacuum chamber and its interconnections are made of metal, allowing them to be heated up to 150° C to drive out any trapped gas.

Though a circular path in the storage ring allows the beams to be maintained and collided many times, it comes at a cost. Like any charged particle that is accelerated, as you change the direction (and thus the velocity vector) of the electrons and positrons they emit radiation, in this case known as synchrotron radiation.* The power dissipated by the synchrotron radiation at CESR is about a megawatt. To restore the lost energy to the particles, another set of RF cavities are used operating at a frequency of about 500 MHz. The synchrotron radiation is emitted along the plane of the particle motion, colliding with the wall of the vacuum chamber along a narrow band and producing heat. The unwanted heat is removed using water circulating through a conduit in the vacuum chamber wall.

*At two points along the beam line (on either side of the collision region where there is a high degree of bending) the emitted synchrotron radiation is used to produce very useful analyses by a separate experiment known as the Cornell High Energy Synchrotron Source (CHESS).

2.1.4 CESR Performance

As indicated in Section 1.8.2, the instantaneous luminosity of the storage ring provides a measure of its performance since it is proportional to the rate for any given reaction produced in the storage ring. Further, the integrated luminosity can be used to find the total number of events generated over a given period of time. Two plots are provided to illustrate the luminosity performance of CESR:

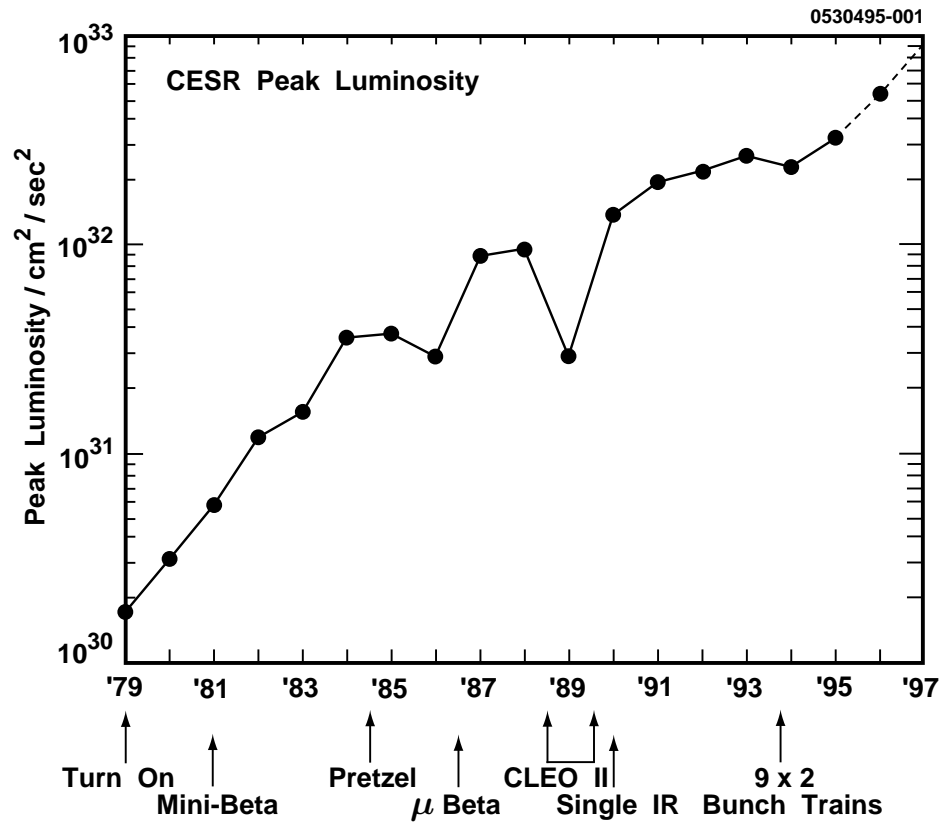


Figure 2.2

Peak (instantaneous) luminosities at CESR

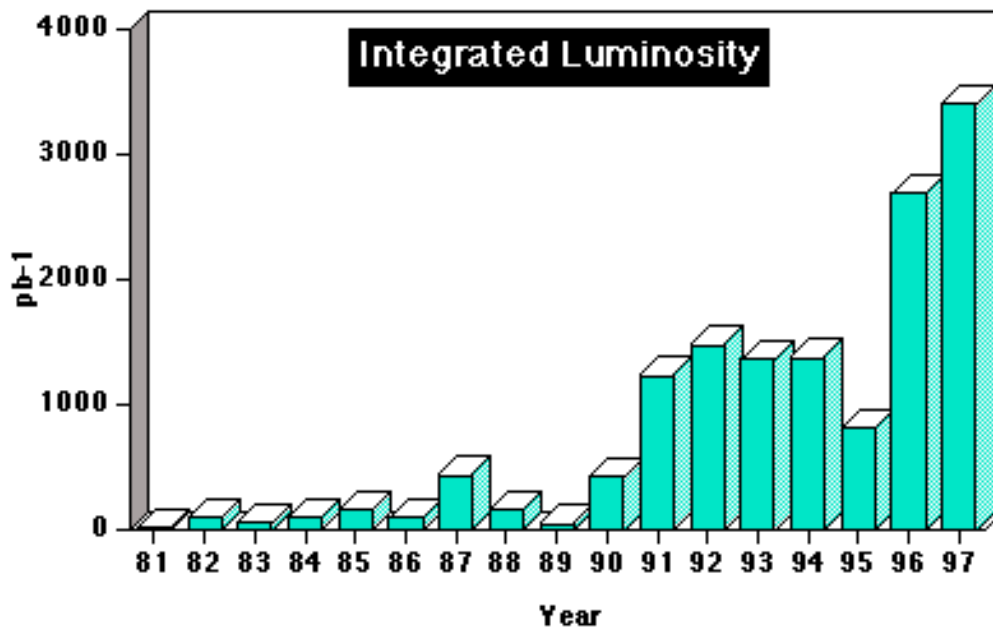


Figure 2.3

Integrated luminosity per year at CESR

Figure 2.2 shows CESR's peak instantaneous luminosity each year from 1979 to 1997 and Figure 2.3 showing its yearly integrated luminosity over roughly that period. CESR's peak luminosity during the running of CLEO II was consistently one of the world's highest for a colliding beam experiment at that time.

2.1.5 Summary of CESR Operating Parameters

Provided here is a table summarizing CESR's operating parameters [29, 48].

Table 2.1

A summary of operating parameters for CESR during the running of CLEO II.

Circumference:	768.43 m, Traverse Time = 2.56 μ s
Maximum Luminosity:	3×10^{32} cm ⁻² sec ⁻¹
Injector Energy:	120/300 MeV for linac 4-8 GeV for synchrotron
Operating Energy:	4.7 - 5.6 GeV per beam
Energy Spread (σ_E/E_0):	0.71×10^{-3} @ 5.3 GeV
Beam radius/Bunch Size:	[0.6(h) \times 0.01(w) \times 17(length)] mm
Particles per Bunch:	24×10^{10}
Bunches per Beam:	7
Beam Circulation Frequency:	396 kHz
Average Beam Current:	110 mA
Time Between Collisions:	0.36 μ s
Fill time:	10 minutes
Luminosity Lifetime:	3 hours
Magnets in Ring:	86 dipoles + 106 quadrupoles
Transverse Beam Emittance:	0.2-0.3 (h), 0.01 (v) rad-mm @ 5.3 GeV
β^* Amplitude Fcn. at I.P.:	1 m (h) , 15 mm (v)
Synchrotron Radiation Loss:	1.2 MeV/turn @ 5.3 GeV
RF Frequency:	499.765 MHz
RF Complement:	2 RF regions with 2 x 5-cell cavities each
Total RF voltage	5 MV operating, 6 MV available
Average RF power:	500 kW @ 5.3 GeV

2.2 The CLEO II Detector

The CLEO II detector [49] is a large, multipurpose, hybrid particle detector centered around the interaction region at CESR.* It provides a means of detecting many types of charged and neutral particles that are produced by the electron-positron annihilations so as to reconstruct a variety of events that researchers wish to study. It began taking data in October 1989 and finished its running in 1995 to shut down for further improvements.

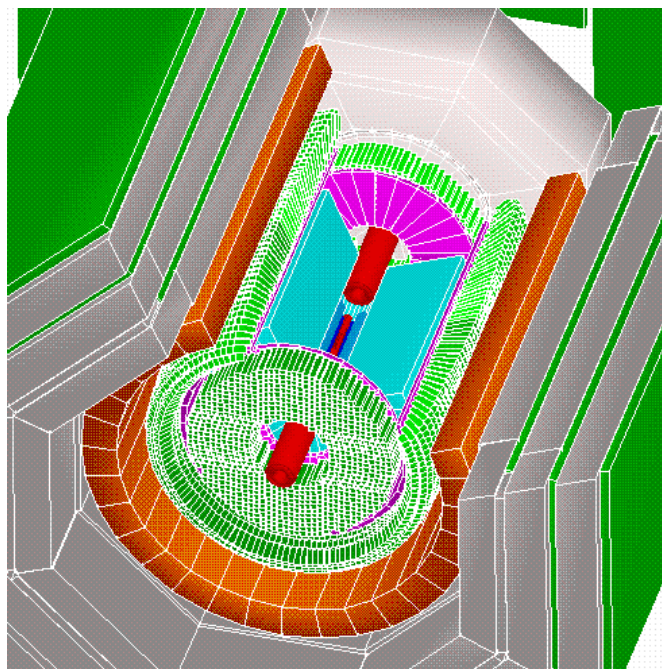


Figure 2.4

A three dimensional illustration of the CLEO II detector displaying its cylindrical design.

*CLEO is not an acronym but is short for Cleopatra—a fitting companion for CESR (Caesar).

CLEO II possesses a cylindrically symmetric design, surrounding a length of the beam pipe near the interaction point with a “barrel” of detectors and closing off the two ends (except where the beam pipe enters and exits) with two “end-cap” detector regions. This provides a large degree of solid-angle coverage around the interaction region. A three-dimensional illustration of the detector is provided in Figure 2.4.

Only particles that are stable or have lifetimes on the order of 10^{-9} s or more are directly detectable in CLEO II (other particles would decay before entering any of the detectors). Such particles directly detectable by CLEO II are photons (γ), electrons/positrons (e^\pm), muons (μ^\pm), pions (π^\pm), kaons (K^\pm), and protons (p^\pm). Other particles of interest must be reconstructed from their detected decay products.

In the barrel region, charged particles are first tracked in a series of three concentric drift chambers comprising the central tracking system (see Figure 2.5 for a side view and end view of CLEO II illustrating its main elements). Surrounding the outer drift chamber is a system of scintillation detectors used to measure the time-of-flight of the particles, and beyond that is a cylinder of crystal calorimeters, which provide energy detection for both charged particles and photons. These systems are placed within a 1.5 Tesla magnetic field provided by a super conducting solenoidal magnet that surrounds them.* The last detector system a particle could

*Within the magnetic field, a charged particle will follow a curved paths whose radius of curvature is proportional to the momentum of the particle.

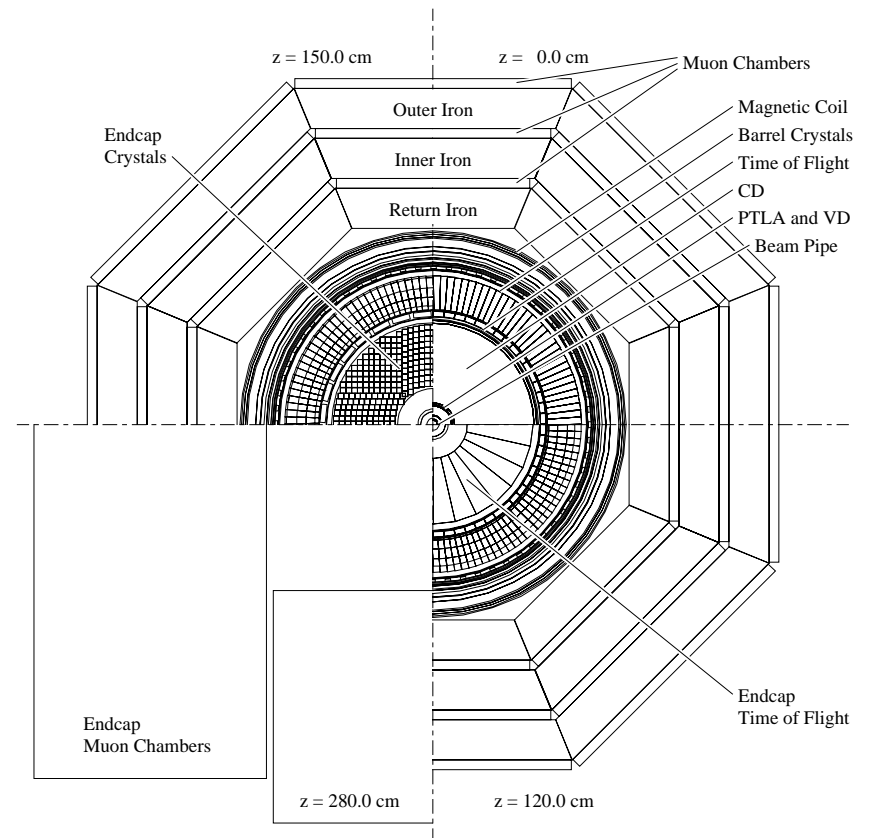
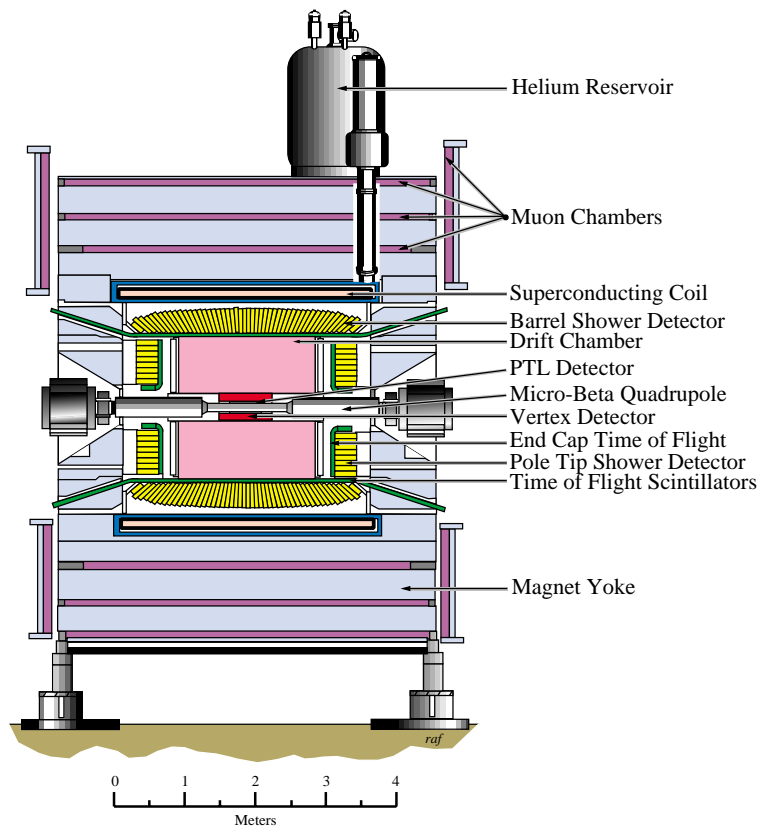


Figure 2.5

A side view and end view of the CLEO II detector. The end view provides a different cut-away segment in each quadrant.

encounter is the muon detection system, which consists of proportional counters interspersed with three layers of steel shielding (the steel return yokes of the aforementioned magnet). The end-caps consist of a time-of-flight counter as well as a set of crystal calorimeters and a layer of muon detectors to provide fuller coverage for those systems. Finally, the entire detector is encased by 2.5 cm thick steel sheets, forming the outer shell of CLEO II. The overall design of the experiment is meant to provide good resolution for spatial, momentum, and energy measurements as well as providing complete solid angle coverage.

For a general description of how each of these types of detectors work, see Section 1.15. In the following sections the specifics of these systems are discussed as they are implemented in CLEO II. Figure 2.6 provides a side view of one quarter of CLEO II, giving a closer view for reference.

2.2.1 The Beam Pipe

Particles exiting the interaction region first encounter the CLEO II beam pipe—a necessary but unwanted obstacle between the interaction point and the detector systems. It is a 33 cm long, thin walled beryllium (Be) pipe with a radius of 3.5 cm. The material and radial dimensions were chosen to minimize the wall thickness while providing an acceptable aperture and being capable of meeting vacuum requirements for CESR operation. To help protect the detector from synchrotron radiation, the beam pipe walls are coated with 25 μm of silver and

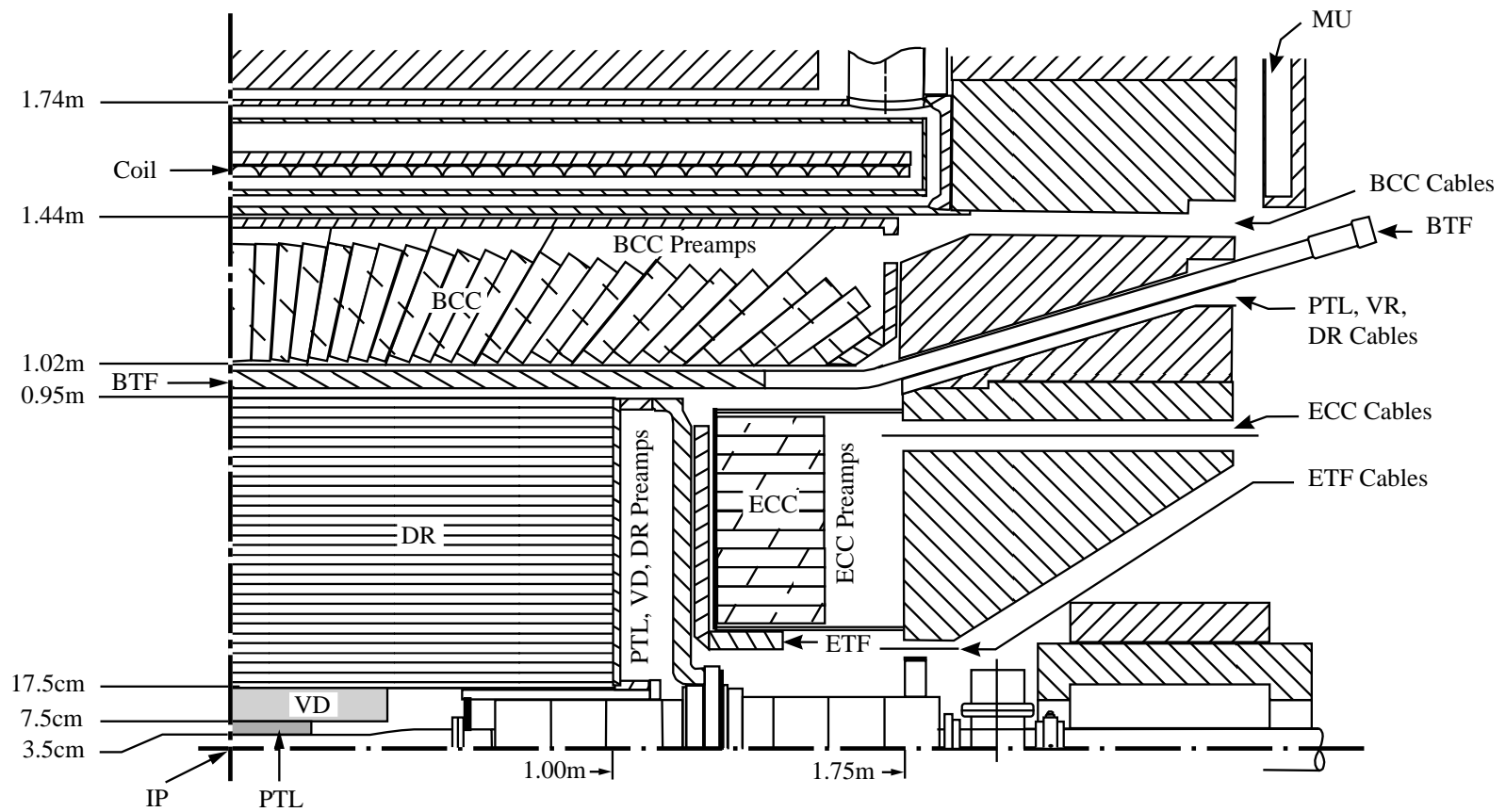


Figure 2.6

A close-up side view showing one quarter of the CLEO II detector.

$< 1 \mu\text{m}$ of nickel. The total thickness of the beam pipe wall is $500 \mu\text{m}$, contributing 0.44% of a radiation length in the radial direction.*

2.2.2 The CLEO II Magnet

The *CLEO II superconducting magnetic coil* permeates the inner detector systems (the central tracking, time-of-flight, and crystal calorimetry systems) with a uniform 1.5 Tesla magnetic field generated parallel to the beam line. It is wound from a length of cable made from 0.6 mm diameter copper/niobium-titanium (Cu/NbTi) superconducting strands surrounded by an aluminum stabilizer, giving the cable a total cross section of 5 mm by 16 mm. It operates at a current of 3,300 A and is cooled by a liquid helium refrigeration system.

The magnetic field (or flux) outside of the detector is confined within a steel return yoke running the length of the coil. The yoke is constructed of three layers, each 36 cm thick and made from eight slabs to produce three concentric octagonal cylinders surrounding the magnet. Each layer is separated by 9 cm from the next, providing space for muon chambers and allowing the yoke to act as shielding for the chambers. The flux return system is completed on either end by nested steel rings that form pole pieces for the system.

*A radiation length can be defined as the thickness through a material an electron beam must pass before its average energy is reduced by a factor of e^{-1} .

A charged particle passing through a magnetic field of B follows a curved path whose radius of curvature (ρ) is proportional to its momentum (p):

$$p = B\rho \times \left(\frac{0.2998}{\text{T m}} \right) \frac{\text{GeV}}{c}. \quad (2.1)$$

This allows precise measurement of a charged particle's momentum given precise measurement of its track (and thus its radius of curvature).

2.2.3 The Central Tracking System

The *central (drift) tracking system (CD)* is composed of three concentric drift chambers that provide charged particle tracking (see Section 1.15 for a general description of proportional counters and drift chambers). Each cylindrical chamber is composed of concentric layers aligned along the beam axis. A mixture of argon-ethane gas* is used to provide ionization and is maintained at different pressures depending on the needs of each chamber. As a whole, these tracking systems cover about 96% of the solid angle centered at the interaction region.

The innermost chamber is known as the *Precision Tracking Layer (PTL)* and immediately surrounds the beam pipe with an inner radius of 4.7 cm and an outer radius of 7.2 cm. It is composed of straw-tube proportional counters arranged in six concentric layers, each containing 64 cells and with each layer rotated by half a cell from the previous one. See Figure 2.7 for an illustration of the cell placement. Each cell is composed of a 15 μm diameter gold-plated tungsten anode wire held taut with 22 g of tension and surrounded by an aluminized Mylar tube, which

*In 1992, the gas in the PTL was replaced with dimethyl ether (DME)

forms the cell's field cage. The design of the chamber allows for tracking in the plane perpendicular to the beam axis (the $r - \phi$ or $x - y$ plane), but no information in z (along the beam axis) is provided.

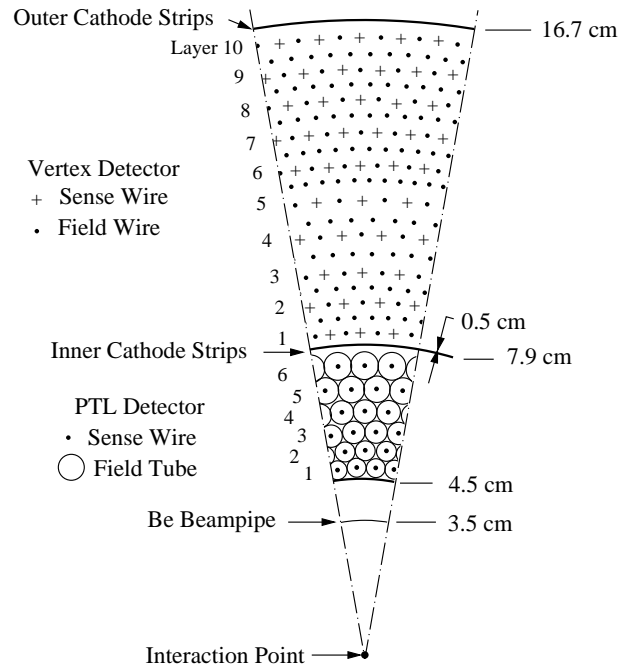


Figure 2.7

A section of the PTL and CD systems showing cell layouts.

The *vertex detector* (*VD*) is the second chamber in the CD and immediately surrounds the PTL with an inner radius of 8.1 cm and an outer radius of 16.4 cm. It is a drift chamber composed of 800 high voltage sense wires and 2,272 field-shaping wires arranged in 10 layers staggered by a half-cell spacing from one layer

to the next. The arrangement surrounds each sense wire with six field wires to form the field-shaping cell. Figure 2.7 shows a layout of the cells in the VD as well as in the PTL. The layers are divided into an inner group with 64 cells per layer and an outer group with 96 cells per layer. The sense wires are all axial (aligned parallel to the beam pipe and thus providing $r - \phi$ information). They are made of a nickel-chromium alloy with about three times the resistivity of gold-plated tungsten. This allows for charge division measurements where differences in pulses read at both ends of a wire (due to the different lengths the signal travels in each direction) are used to gain information about the z position of the track.

The inner and outer cylindrical shells of the VD are lined on the interior with a series of segmented rings, each composed of eight cathode strips etched in aluminum foil and bonded to Mylar sheets. See Figure 2.8 for an illustration of the placement of the cathode strips. These strips shape the field cage and allow position measurements along the z axis of the detector. They register an image of the charge deposited on adjacent anode wires with avalanches on a sense wire spread over three cathodes. In addition to providing tracking close to the interaction region for precise vertex finding, measurements from the PTL and VD are also important for low-momentum particles, which can form tight curls in the magnetic field and may not hit many wires in the outer drift chamber.

The *outer drift chamber (DR)* is the main tracking chamber and immediately surrounds the VD with an inner radius of 17.5 cm and an outer radius of 95 cm. It is composed of 12,240 high voltage sense wires and 36,240 field wires, arranged

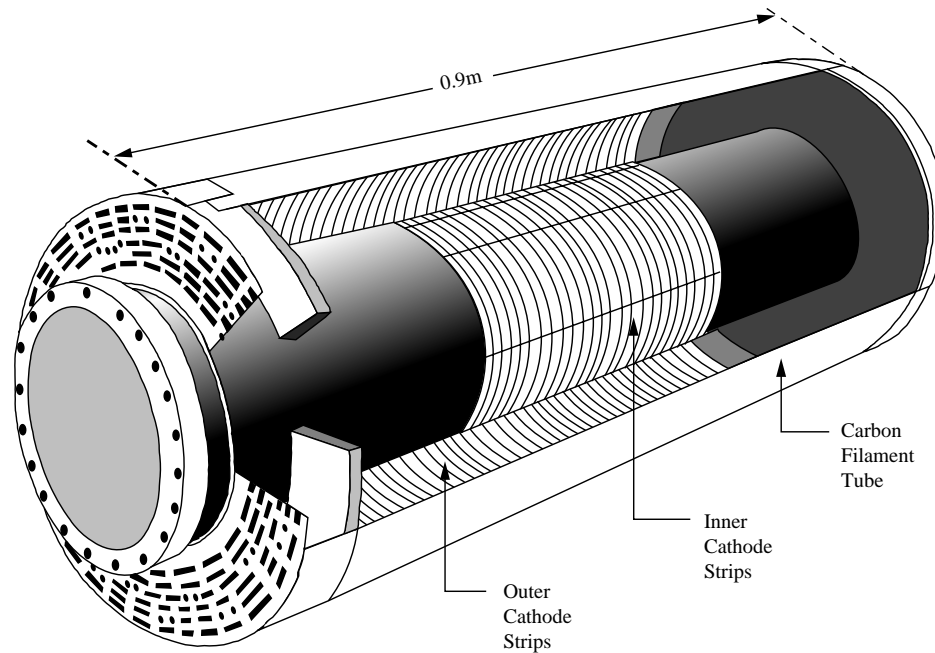


Figure 2.8

Cathode strip placement in the VD

in 51 layers of cells with 3 layers of field wires per cell (see Figure 2.9 for an illustration). Every other layer is offset by half a cell spacing. The sense wires are $20\ \mu\text{m}$ diameter gold-plated tungsten wires held taught with 50 g of tension. While 40 of the layers are aligned axially, staggered between those are 11 “stereo” layers that are strung with the ends offset from one another to produce an angle of 3.8° to 6.9° with respect to the beam axis. In conjunction with the other layers, the stereo layers allow for measurement of the z as well as r and ϕ positions of the tracks. The cathode strips used on the interior of the inner and outer shells of the

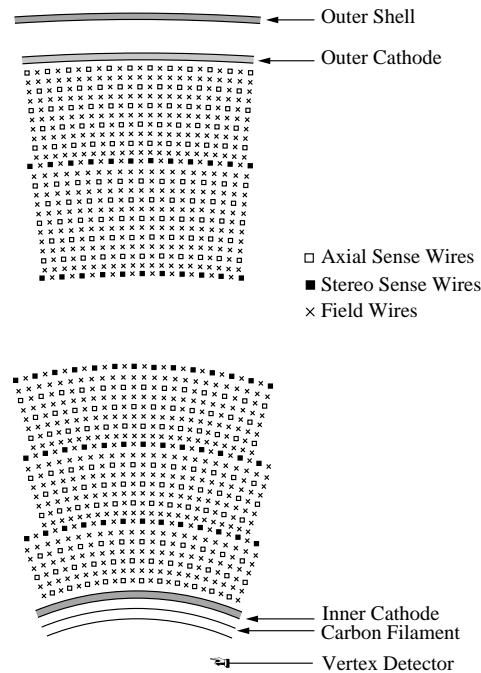


Figure 2.9

Cell structure of the outer drift chamber (DR).

DR provide further z information and are 1 cm wide in z and 7.35 cm in azimuth. Placement of these strips is illustrated in Figure 2.10. Avalanches from one wire are spread over six of these cathodes in the DR.

In addition to providing tracking and momentum measurements, the DR also allows for a degree of particle identification by measuring the energy lost by a particle (as it produced ions to form the track) per unit track length, which is known as specific ionization or dE/dx . Different particle types will have different dE/dx as a function of their momentum. Figure 2.11 shows a plot of this effect

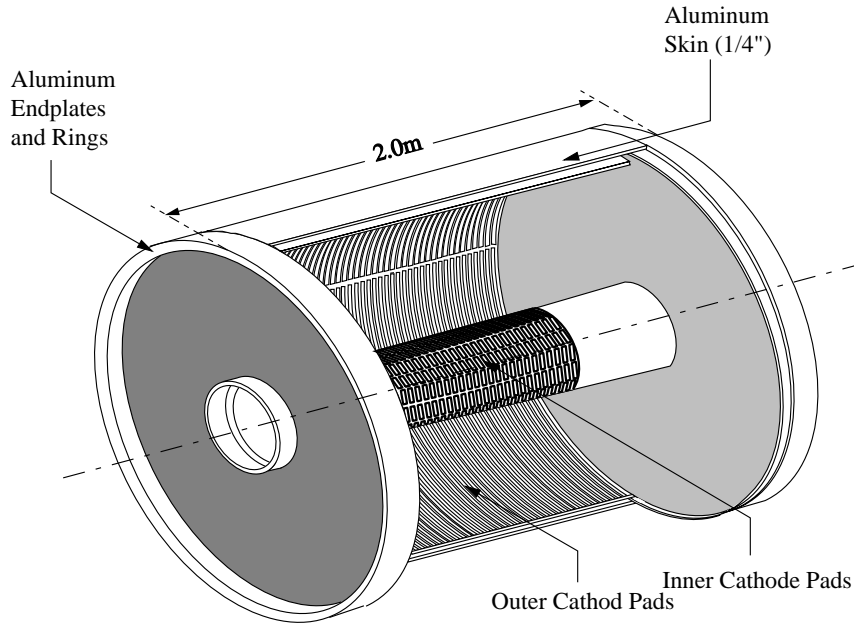


Figure 2.10

Cathode strip placement in the DR

for four particle types and shows that the best separation between them occurs at low momentum.

2.2.4 The Time-of-Flight System

The time between an e^+e^- crossing in the interaction region and when a resulting particle exits the central tracker is measured by the *time-of-flight* (*TOF*) system. Combined with the momentum and tracking measurements in the DR, the TOF information can aid in particle identification (see below). Its fast response

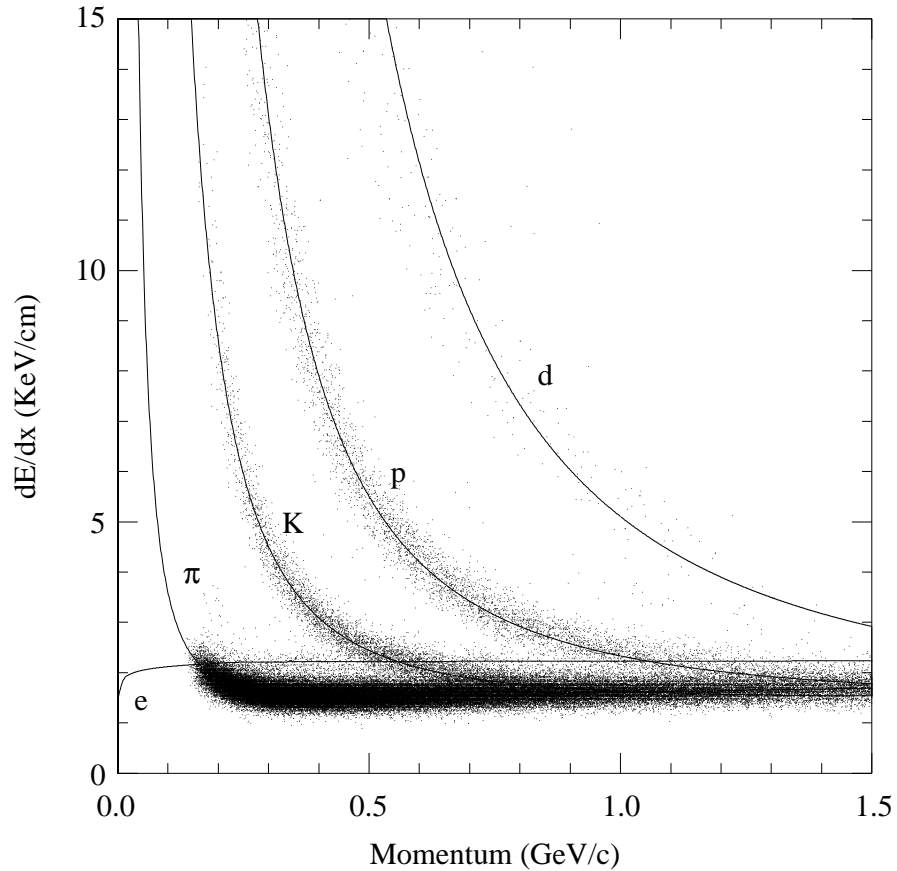


Figure 2.11

Plot of specific ionization (dE/dx) versus momentum for different particle types

time to charged particles also makes it a vital triggering component for the data acquisition system.

The barrel time-of-flight system directly surrounds the DR and consists of 64 Bicron BC-408 scintillation counters that are 5 cm to 10 cm thick and 279.4 cm in length (see Section 1.15 for general information on scintillation counters). Light produced in these scintillators is transmitted by connecting light pipes to a region

just outside of the magnetic flux return system where high quantum efficiency photomultiplier tubes read the output and can operate in a relatively low mag-

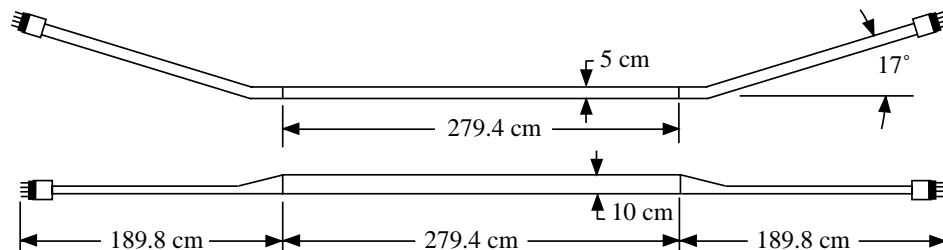


Figure 2.12

Side view of a single barrel TOF counter and connectors

netic field. Figure 2.12 displays a side view of a TOF counter and its connectors. Coverage on each end-cap is provided by 28 wedge-shaped scintillators that form a disk with an inside radius of 31.5 cm and an outside radius of 89.0 cm. Their photomultiplier tubes are attached directly to the scintillators and are designed to operate in a high magnetic field. The layout of the end-cap TOF counters is illustrated in Figure 2.13. The entire TOF system provides a solid angle coverage of about 97%.

A particle of mass m with a momentum p measured in the DR will have a velocity given as

$$\beta = \frac{1}{\sqrt{1 + \frac{m^2 c^2}{p^2}}}, \quad (2.2)$$

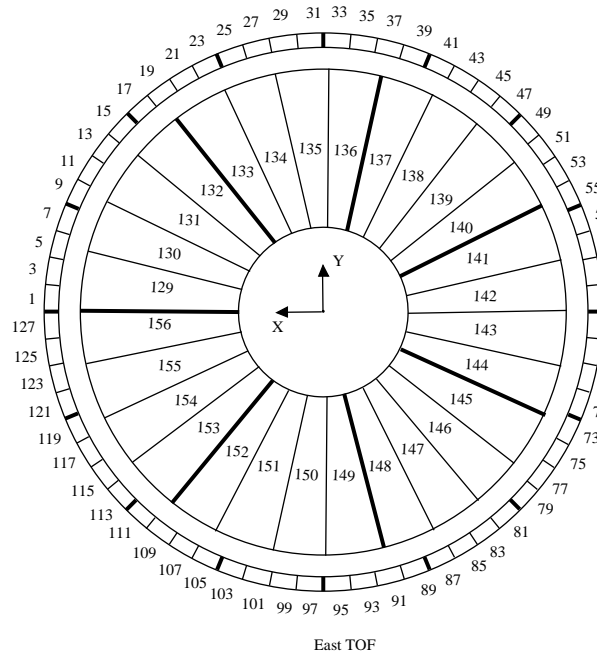


Figure 2.13

Configuration of End-cap TOF counters

where $\beta = v/c$. Thus if its flight path measured in the DR has a length of L , its time of flight would be

$$t = \frac{L}{\beta c} = \frac{L}{c} \sqrt{1 + \frac{m^2 c^2}{p^2}}. \quad (2.3)$$

Therefore, combined with the measured flight path and momentum in the DR, the time-of-flight information place constraints on the mass of the given particle and aids in identifying its type. Figure 2.14 displays a plot of measured $1/\beta$ versus particle momentum, indicating the different graphs for different particle types.

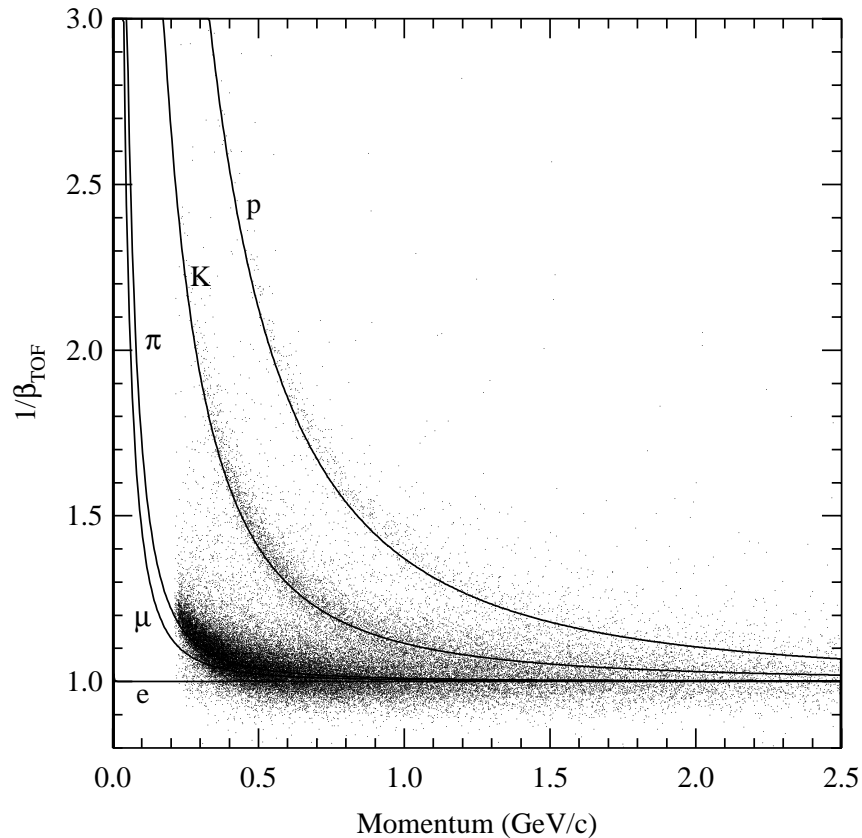


Figure 2.14

A graph of $1/\beta$ versus momentum (from measurements in the barrel TOF and drift chambers) for different particle types.

2.2.5 The Crystal Calorimeter

Energy from both charged particles and photons is deposited and measured in the *crystal calorimeter* (*CC*), a shower detector that surrounds the TOF system. The *CC* is composed of thallium-doped cesium iodide (CsI) crystals, each roughly 5 cm square by 30 cm long (the latter being 16.2 radiation lengths). The barrel portion of the *CC* contains 6,144 crystals arranged in a holder with a tube-like formation and with the inner face of each crystal pointing towards the interaction

region (see Figure 2.15). This provides coverage for 71% of the solid angle. Each end-caps is covered by 828 crystals in a formation illustrated in Figure 2.16. In all, the system covers 90% of the solid angle.

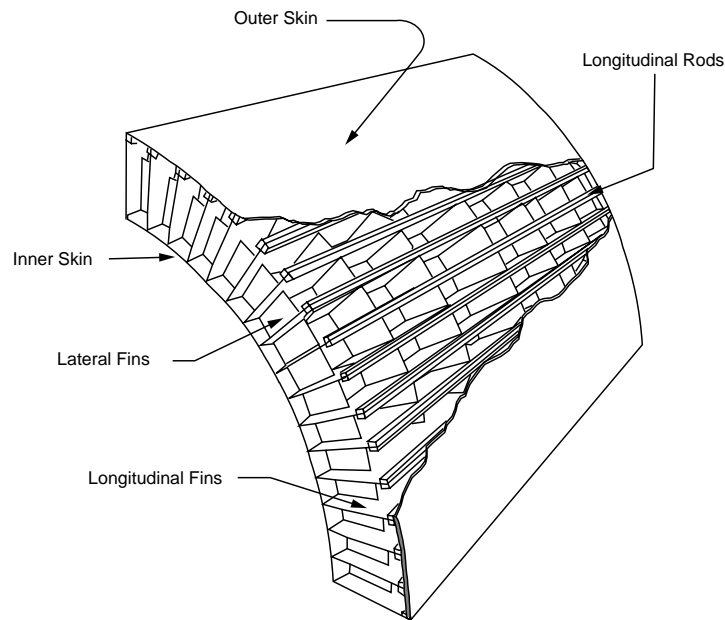


Figure 2.15

A section of the holder for crystals in the barrel CC

The light produced by showers in the crystals is detected by four silicon photodiodes mounted on a lucite window on the rear face of each crystal. They convert the light into electrical signals that are digitized for analyzing. The shower energy is proportional to the energy of the particle that produced it and is generally spread over many adjacent crystals. While hadrons will interact strongly in the crystals and spread energy over more crystals, photons and electrons interact only

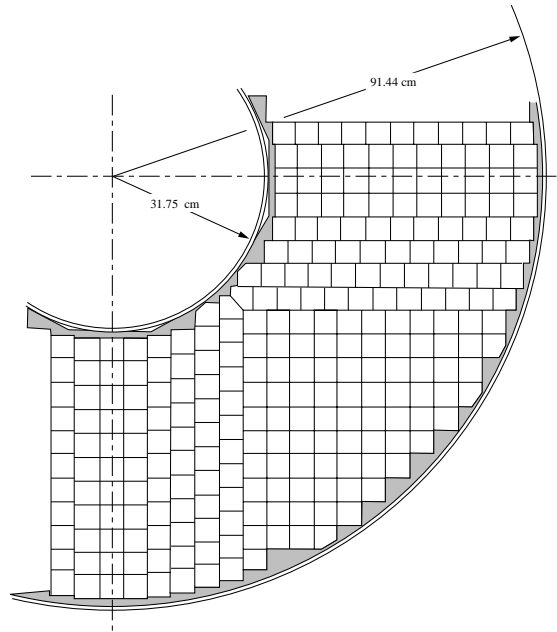


Figure 2.16

Layout of the end-cap crystals

electromagnetically, and their energy spread tends to be less. Special clustering algorithms help account for all the energy deposited by a given particle while analysis of the shower shape and spread can help distinguish hadrons from photons and electrons. Since photons, being neutral, leave no tracks in the CD, they can be further identified by showers that are not matched to CD tracks.

2.2.6 The Muon Detector

Due to their particular qualities, muons traveling through the detector can be identified via the *Muon Detector (MU)*. Because hadrons interact both electromagnetically and strongly they are generally stopped in the steel return yoke of

the CLEO magnet. Leptons do not interact strongly and the more massive they are, the further they can travel through matter before being stopped by electromagnetic interactions. A τ (the most massive lepton) generated at the interaction region does not live long enough to leave the beam pipe before it decays, while the stable electron (the least massive charged particle) is easily stopped in matter. However, the μ , having a mass over 200 times that of the electron and a lifetime long enough to pass through the detectors, is the most penetrating particle that is directly detected at CLEO. A μ with a momentum greater than $1.5 \text{ GeV}/c$ will not be stopped by the TOF or CC systems and will readily penetrate the steel return yoke. Thus, the gaps between the yoke layers and just outside the outer layer are filled with proportional counters, and a particle that pass through these detectors leaving a clear track can justly be considered a muon.

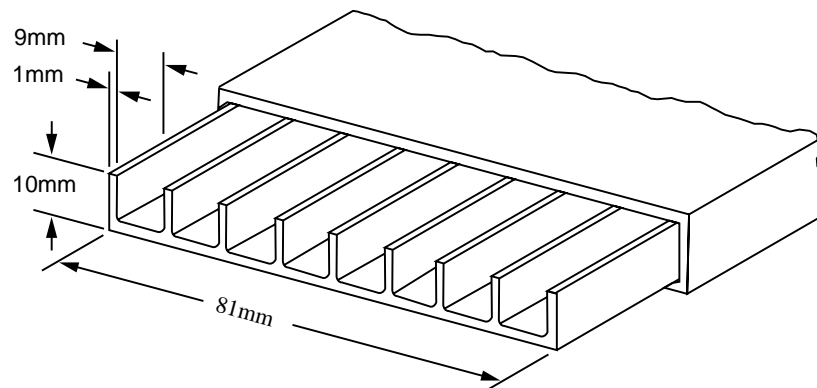


Figure 2.17

Schematic of muon chamber tubes

The muon detector around the barrel region consists of three “super-layers” in the shape of three concentric octagonal barrels (two between the yoke layers and one outside the outermost yoke layer). Each super-layer contains three layers of “plastic streamer counters,” which function similarly to drift chambers. Additional muon detectors cover each end-cap as well. Figure 2.17 shows one of the chambers that comprises the counters while Figure 2.18 displays the layout of the streamer tubes in a super-layer. Each tube contains a $50\ \mu\text{m}$ diameter gold-plated tungsten anode wire while copper graphite coating on three sides of each tube provides the cathode. Copper strips run perpendicular to the tubes along the uncoated side and provide an orthogonal coordinate along with the use of charge division.

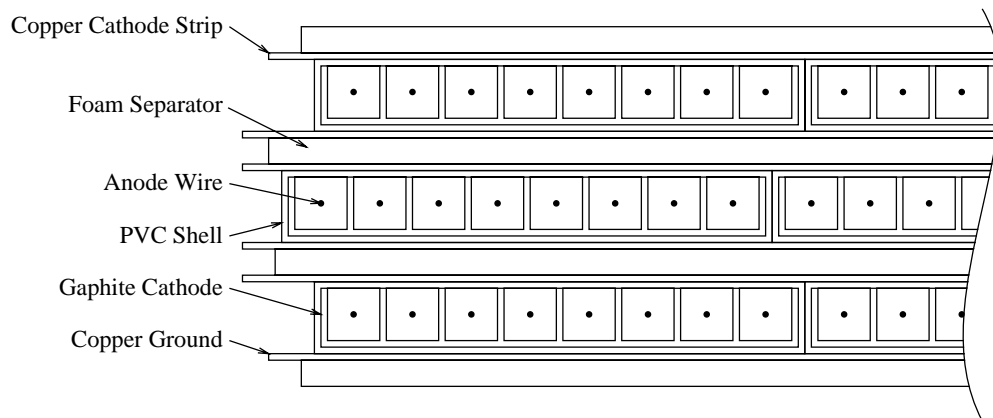


Figure 2.18

Layout of muon chambers in a super-layer

2.2.7 The Trigger System and Data Acquisition

During the running of CLEO II, the e^+ and e^- beams in CESR each contained seven bunches traveling the 768 m circumference of the ring at nearly the speed of light and thus producing over 2.7 million crossings per second. Only a fraction of those crossings produce events worth storing for analysis. The limitations of the tracking system electronics further reduces the rate at which events can be measured, but under this constraint alone, the data rate would still be unmanageable and an unacceptable number of unwanted “background” events would still be present. CLEO thus employs a *trigger system* that uses fast, hardware-based logic algorithms to select good candidate events while making the data acquisition rate more manageable.

There are three stages to the hardware-based trigger system known as *level 0* ($L0$), *level 1* ($L1$), and *level 2* ($L2$). The most basic trigger, $L0$, is designed to be fast and simple while still providing reasonable discrimination. The fastest system in CLEO II is the time-of-flight system with signals in the photomultiplier tubes being ready within 55 ns (a rate of ~ 18 MHz). It can thus be turned on and off fast enough to be active only during every beam crossing (a process known as gating). Along with the VD and the CC, the TOF thus composes the $L0$ trigger system, which reduces the rate of potentially useful events to about 20 kHz (once every 50 μ s).*

*As a side note, if not read out, data in the detector will decay away with a time constant of about 1.3 μ s.

while the L1 logic is initiated. The L1 trigger gathers information from the TF, CC, VD, and DR and requires about $1\mu\text{s}$ (thus causing about 2% dead time for the L0 trigger as it waits). If an event does not pass L1, the trigger logic is reset and detector gating is resumed, otherwise gating remains disabled. Events pass L1 at a rate of about 25 Hz, depending on CESR's luminosity, and are then passed to the highest level hardware trigger, L2. The L2 trigger has a readiness time of about $50\mu\text{s}$ (causing a negligible dead time given the ~ 25 Hz rate at which data passes L1) and includes tracking information from the VD and DR. The criteria for passing L2 further reduces the readout rate to about 10 Hz. Data that passes L2 is read out by the data acquisition system (DAQ), and after the L2 decision is made, the trigger logic is reset and detector gating is resumed.

Events read out by the DAQ are subjected to an additional "level 3" software filter that tests event quality and reduces the data rate by another 30-40%. Data passing L3 is stored for later analysis.

2.2.8 General Event Reconstruction and Display

The information stored while data is actually being taken (an "online" process) is ultimately run through an involved off-line reconstruction routine known as *PASS2*. That process performs complex tasks such as precise track fitting, vertex finding (determining where two tracks might have come from a single point, forming a vertex), matching CD tracks to hits in the CC, analyzing dE/dx data, etc. This information is then stored for further use by individual researchers who will run

their own routines to find and analyze events of interest to their specific research projects.

An *event display* is useful for visual inspection of individual events and to help ensure that the systems are producing proper results. Two examples of such displays are shown in Figures 2.19 and 2.20, the first showing a simple $e^+ + e^- \rightarrow \mu^+ + \mu^- + \gamma$ event, and the second showing a more complex $e^+ + e^- \rightarrow B^+ + B^-$ event (labels have been added for illustration). The center of these displays is an $r - \phi$ view of the hits in the CD (and can include the tracks fit through those hits). A small strip around the larger inner region shows the barrel TOF hits. Out from that, the CC chamber is displayed as if looking through a tube (thus indicating hits in z as well as ϕ while r is constant). Finally any hits in the muon chambers are shown in an $r - \phi$ projection of those chambers that sits out from the CC display. It is also possible for such displays to show hits on the end-cap detector elements as well.

2.2.9 Summary of CLEO II Parameters and Resolution

A series of tables is provided below to summarize the operating parameters and resolutions of various CLEO II components.

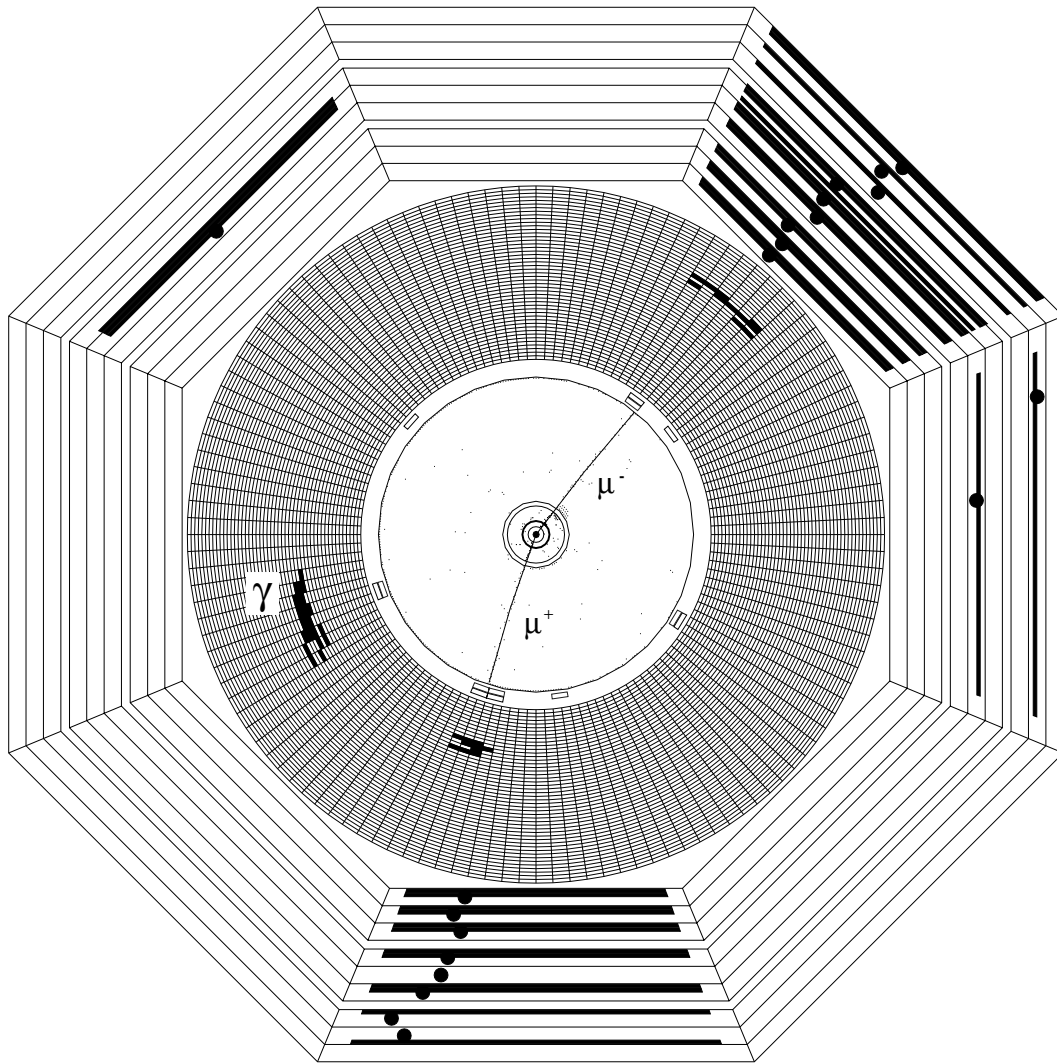


Figure 2.19

A CLEO II event display example showing a $e^+e^- \rightarrow \mu^+\mu^-\gamma$ Monte Carlo (computer simulated) event. The central region shows an $r - \phi$ projection of tracks in the CD (PTL, VD, and DR). A thin strip surrounding the DR shows hits in the barrel TOF. Out from there, hits in the barrel CC are displayed as if looking down the inside of a tube, providing information on hits in ϕ and z (with inner circles nearer the east end and outer circles nearer the west end of the detector). Finally, an $r - \phi$ projection of hits in the barrel muon chambers is given. In the event shown, the μ^\pm CD tracks leave hits in the calorimeter and clear tracks in the muon chambers. This is also a radiative event, and the photon (γ) was measured in the calorimeter. Random hits also appear from various sources of noise.

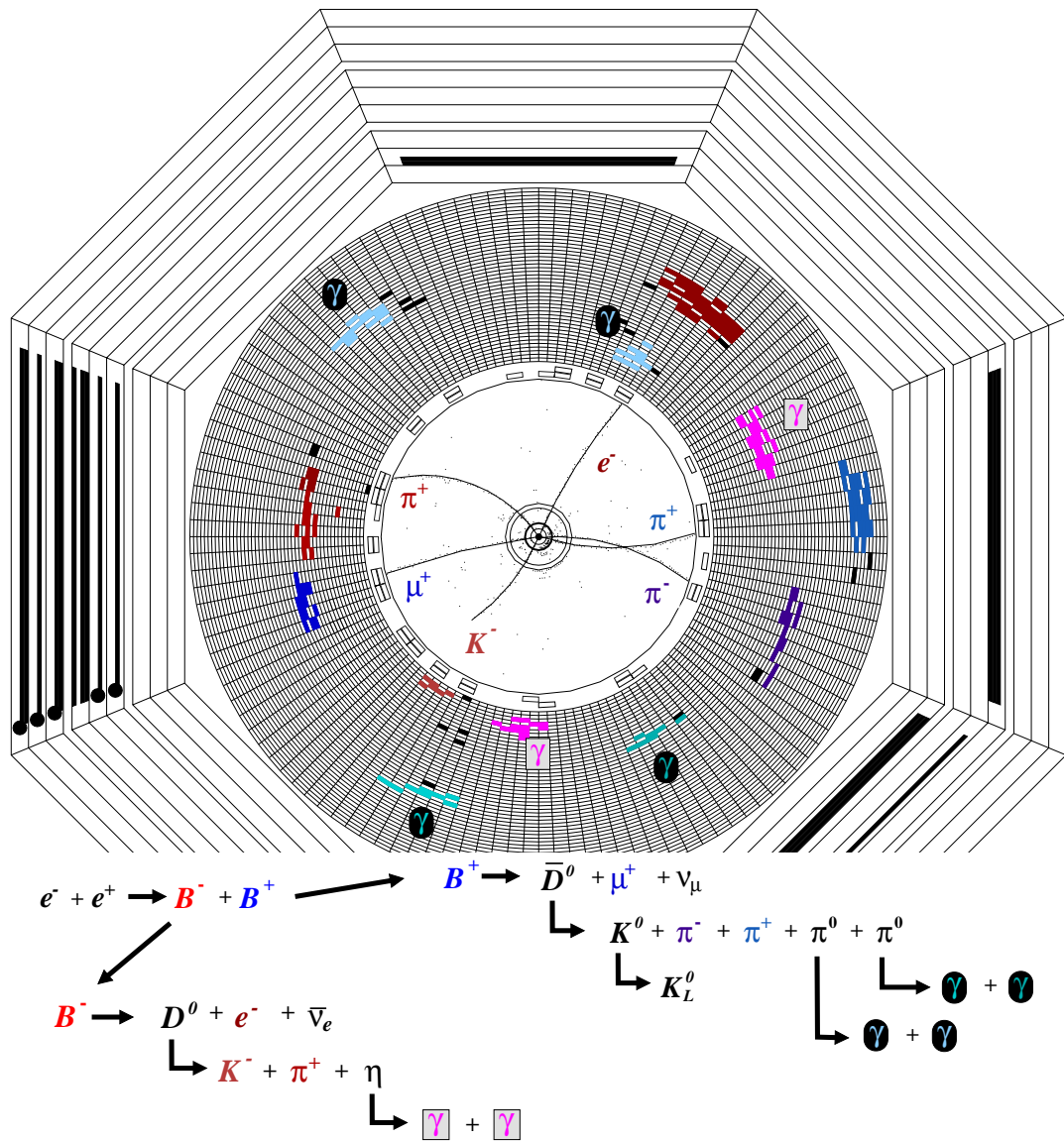


Figure 2.20

A CLEO II event display example showing an $e^-e^+ \rightarrow B^-B^+$ Monte Carlo event with each B further decaying in the detector. The decay chain for each is shown. The B , D , K^0 , η , ν , and π^0 particles do not appear in the detector and in practice are inferred from the data. Particle labels have been added for illustration.

Table 2.2

Parameters of the CLEO II superconducting coil.

The Superconducting Coil	
Magnetic field:	1.5 T, uniform to $\pm 0.2\%$ over 95% of the solid angle
Diameter:	2.9 m through bore, 3.1 m with coil
Length:	3.5 m coil, 3.8 m with cryostat
Weight:	700 kg coil, 20,000 kg cryostat, 800,000 kg return yoke
Coil Specific:	3,300 A, 4.6 H, 25 MJ
Cooling:	liquid helium via self-regulating thermosyphon

Table 2.3

Parameters of the CLEO II central tracking system.

The Central Tracking System	
Inner Radius (cm):	4.7 (PTL), 8.1(VD), 17.5(DR)
Outer Radius (cm):	7.2 (PTL), 16.4(VD), 95.0(DR)
Number of Axial Layers:	56 (PTL: 6, VD: 10, DR: 40)
Number of Stereo Layers:	11 (DR)
Number of Sense Wires:	64 (PTL), 800(VD), 12,240 (DR)
Number of Field Wires:	2,272 (VD), 36,240 (DR)
Cell Geometry:	straw tubes (PTL), hexagonal (VD), rectangular (DR)
Gas Used:	argon/ethane (50%/50% mix) (PTL gas replaced with DME in 1992)
Solid Angle Coverage:	96%
Transverse p Resolution:	$(\delta p_t/p_t)^2 \approx \left(0.0011 \frac{p_t}{\text{GeV}/c}\right)^2 + (0.0067)^2$
Angular Resolution:	$\delta\phi = 1 \text{ mrad}; \delta\theta = 4 \text{ mrad (at 5 GeV)}$

Table 2.4

Parameters of the CLEO II time-of-flight system.

The Time-of-Flight System	
Scintillator:	Bicron BC-408
Number of Counters:	64 Barrel, 28 per end-cap
Photomultiplier Tubes:	Modified Amperex XP2020 (barrel) Hamamatsu R2560 (end-cap)
Coverage in Polar Angle:	15° – 36° west end-cap 36° – 144° barrel 144° – 165° east end-cap
Time Resolution:	barrel: 139 ps (high- p electrons) 154 ps (low- p π) end-cap: 272 ps (high- p electrons)

Table 2.5

Parameters of the CLEO II crystal calorimeter.

The Crystal Calorimeter	
Crystal Material:	thallium doped cesium iodide [CsI(Tl)]
Number of Crystals:	6,144 barrel, 828 per end-cap
Solid Angle Coverage:	95%
Photon Energy Resolution:	Barrel: $\frac{\delta E}{E} = 0.019 + \frac{0.0035 \text{ GeV}}{E^{0.75}} - \frac{0.001E}{\text{GeV}}$ (1.5% at 5 GeV, 3.8% at 100 MeV) End-Cap: (2.6% at 5 GeV, 5.0% at 100 MeV)

Table 2.6

Parameters of the CLEO II muon detector.

The Muon Detection System	
Type of Chambers:	plastic streamer proportional counters
Number of Layers:	3 detector layers per super-layer 3 super-layers around barrel 1 super-layer on each end-cap
Shielding:	2.2 nuclear absorption lengths ($\lambda=16.8$ cm) for innermost layer
Depths of Steel Absorber:	36, 72, and 108 cm for layers in barrel
Identification Efficiency:	$98.6 \pm 1.6\%$ for penetration $\sim 5\lambda$
Solid Angle Coverage:	85%

Table 2.7

Parameters of the CLEO II trigger system.

The Trigger System		
<i>Trigger Type</i>	<i>Systems Used</i>	<i>Max. Acceptance Rate</i>
Level 0:	TOF, VD, and/or CC	20 KHz
Level 1:	TOF, VD, CC, and DR	50 Hz
Level 2:	VD and DR	25 Hz
Level 3:	Software Filter	10 Hz

3. INTRODUCTION TO THE ANALYSIS

The study of particle decays is a mainstay of high energy physics. Such study provides insight into the nature of both the fundamental particles involved and the forces that mediate the given decay. The τ , being the most massive lepton, produces a variety of interesting leptonic and semileptonic decay modes for study. This analysis pursues the study of $\tau^\pm \rightarrow \pi^\pm \pi^\pm \pi^\mp (\bar{\nu}_\tau/\nu_\tau)$ decays in an attempt to better understand its substructure.

There is much to learn about the complicated substructure of the $\tau^\pm \rightarrow \pi^\pm \pi^\pm \pi^\mp (\bar{\nu}_\tau/\nu_\tau)$ decay, which proceeds through a weak transition current with a dominant axial vector component and a meager but interesting pseudoscalar component. Although a model-independent description of the structure is desirable, for reasons given below this analysis pursues a model-dependent fitting technique that utilizes all available kinematic information from each selected decay. Motivation for this particular analysis is presented here while later chapters discuss the event selection, the model used, the fitting method, and the primary results of the analysis. Two variations to the model are also considered, and results produced by those variations are presented as well.

3.1 Motivation for Studying the $\tau^\pm \rightarrow \pi^\pm \pi^\pm \pi^\mp (\bar{\nu}_\tau/\nu_\tau)$ Decay

The $[3\pi^\pm]^-$ system in the $\tau^\pm \rightarrow \pi^\pm \pi^\pm \pi^\mp (\bar{\nu}_\tau/\nu_\tau)$ decay provides a means of studying the axial vector weak hadronic current. The transition is dominated by the $a_1(1260)$ primary resonance whose decay in turn is dominated by the (mainly s -wave) $\rho\pi$ intermediate state. While a variety of models have been proposed to describe the a_1 system [51–56], they provide a somewhat insufficient description of the data. In addition, even less is known of the pseudoscalar resonance contribution to the current, which, though small, should theoretically exist (presumably dominated by the π' primary resonance). Further experimental study is needed to better understand these systems.

The details of the $\tau^\pm \rightarrow \pi^\pm \pi^\pm \pi^\mp (\bar{\nu}_\tau/\nu_\tau)$ decay are contained in four form factors, F_1 , F_2 , F_3 and F_4 . Although this analysis provides a study of all the contributing form factors, it is particularly interested in extracting information about the pseudoscalar form factor, F_4 . If enough information is gained concerning this pseudoscalar contribution, it could be used to place a lower limit on the light quark running masses in the QCD Lagrangian [57].

The QCD Lagrangian involves seven parameters that must be experimentally determined: the gauge coupling constant (sometimes denoted g) and six “running masses” associated with the quarks. Of these parameters, m_u , m_d , and m_s are the least well measured. Obtaining experimental information concerning these light quark masses will increase knowledge of the standard model in general, and of the QCD Lagrangian parameters in particular. In addition, placing an experimentally

based limit on the light quark masses can theoretically provide checks for standard chiral perturbation theory and help in understanding of strong CP violation [57]. Specifically, results on pseudoscalar contributions in this analysis can be used to place a lower limit on the average of the up and down light quark running masses.

3.2 Using a Model

Although it would be desirable to experimentally characterize the structure of the $[3\pi^\pm]^-$ system while making no model-based assumptions, this analysis has focussed on a model-dependent approach for two main reasons. First, it is noted that a model-independent approach would assume a general format for the hadronic current that allows one to separate and analyze the complex magnitude of the axial vector and pseudoscalar components in bins of the invariant mass of the $[3\pi^\pm]^-$ system squared (Q^2) and in the two Dalitz plot variables (s_1 and s_2). That method would make no assumptions concerning resonances in the decay. However, in certain chiral limits, scalar effects can be induced in the current from both the broad a_1 resonance and non-resonance contributions in the current [58]. Although these effects are expected to be small compared to any real pseudoscalar effect, a model-dependent method can explicitly assume the resonance structure and thus resolve any possible fake, induced pseudoscalar effects. See Section 5.5 for further discussion.

Secondly, a model-independent method requires that one bin the data in three dimensions (Q^2 , s_1 , and s_2). To thoroughly explain the decay structure, rela-

tively small bins would be required, and the amount of data available for fitting in each bin would thus be greatly reduced from the entire set. This is especially problematic if one expects complicated resonance structures whose effects would only be noted by results in certain specific bins. If the binning is insufficient or the data in the important bins is inadequate for fitting, the resonance structure could be unnoticeable. By using a model-dependent fit, one can make reasonable assumptions about the resonance structure and study the likely existence of each resonance modeled while using the entire data set in the fitting and without the need for binning.

4. DATA SAMPLE AND EVENT SELECTION

The analysis uses 4.67 fb^{-1} of e^+e^- collisions with an average center-of-mass energy of around 10.6 GeV. This corresponds to the production of approximately 4.3×10^6 $e^+e^- \rightarrow \tau^+\tau^-$ events. The background analysis, testing procedures, and systematic error study require the use of τ Monte Carlo. The **KORALB/TAUOLA** [59] program was used to generate the events; however, the $\tau^\pm \rightarrow \pi^\pm\pi^\pm\pi^\mp(\bar{\nu}_\tau/\nu_\tau)$ decays were generated with CLEO-specific modifications based on results of the $\tau^\pm \rightarrow \pi^\pm\pi^0\pi^0(\bar{\nu}_\tau/\nu_\tau)$ analysis in [60] once they were isospin-rotated to the all charged mode. Events were then passed through the **GEANT**-based CLEO II detector simulation package [61]. Finally, the Monte Carlo events were processed using the full CLEO event reconstruction routines.

The τ 's in a pair produced in CESR with each receiving half of the center-of-mass energy will travel back-to-back from the interaction point, each with a velocity of $\sim 0.94 c$ in the lab. They would decay after traveling less than a quarter of a millimeter and their decay products tend to produce back-to-back "jets." The ν_τ and $\bar{\nu}_\tau$ produced are undetectable in CLEO, and events must be reconstructed with that in mind.

Given that general event anatomy, the criteria used by the event selection routine performed on both data and Monte Carlo can now be described (for a summary, see Table 4.1). The process only selects events that have a 1-charged-track versus 3-charged-track topology. The 1-track side is considered the “tag” side of the event, and it is used to help identify the event as a $e^+e^- \rightarrow \tau^+\tau^-$ process. It must either be classified as a τ^+ decaying to $e^+\nu_e\bar{\nu}_\tau$, $\mu^+\nu_\mu\bar{\nu}_\tau$, $\rho^+\bar{\nu}_\tau$ (in which $\rho^+ \rightarrow \pi^+\pi^0$), or $\pi^+\bar{\nu}_\tau$; or it can be classified as a τ^- decaying to the charge-conjugated counterparts of those modes.

Tracks from e^\pm are identified by first comparing the energy they deposit in the calorimeter to their track momentum. For electrons (which deposit much of their energy when they shower in the calorimeter) the ratio is expected to be $E/p > 0.85$. The specific ionization along the track (dE/dx) is also required to be within 2 standard deviations of the expected value for electrons. Tracks from μ^\pm (which are more penetrating due to their mass) are identified as tracks that leave a relatively small amount of energy in the calorimeter ($E < 0.6$ GeV) and have measured dE/dx within 2 standard deviations of the expected value for muons. Other tracks are assumed to be pions, which are plentiful in CLEO events. When a π track is identified on the “tag” side of the event (as determined below), the search for a corresponding ρ candidate begins by identifying well defined photon pairs in the calorimeter with a combined energy and momentum consistent with a π^0 coming from the “tag” side. Such a π^0 candidate is then combined with

the π track to produce a ρ candidate, which is then required to have a mass of $0.620 \text{ GeV} \leq m \leq 0.920 \text{ GeV}$ (where the nominal ρ mass is 0.770 GeV [29]).

For each event, tracks that could be “fakes” from secondary interactions with the beam pipe (or other detector components) or from poor track finding are first identified and removed. Four “true” tracks are then required to be present with a combined charge (deduced from the direction of curvature for each track in the magnetic field) of zero. To help ensure that these tracks did not come from a secondary decay process, their fit-projected tracks are required to have a close approach to the interaction point (0.01 m in $r - \phi$ and 0.10 m in the poorer measured z direction). To ensure they are reasonably well measured tracks, each is required to be found largely within the “barrel” region of CLEO II. Further, to reduce QED backgrounds such as two-photon interactions and radiative Bhabha scattering ($e^+e^- \rightarrow e^+e^-$ where a radiative effect produces other tracks), no more than one of the four tracks is allowed to be identified as an electron.

The 1-versus-3 topology is then required by finding the most isolated track and requiring that it be more than 90° away from all other tracks.* This divides the event into two hemispheres by defining the region of solid-angle within 90° of the most isolated track as the “tag-side” while defining the other hemisphere as the “signal-side” of the event. To help ensure a signal decay that is well measured, at least two of the three signal tracks are required to have momenta that can be best

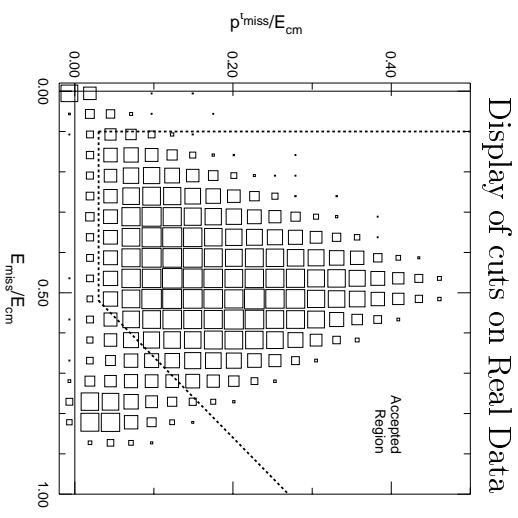
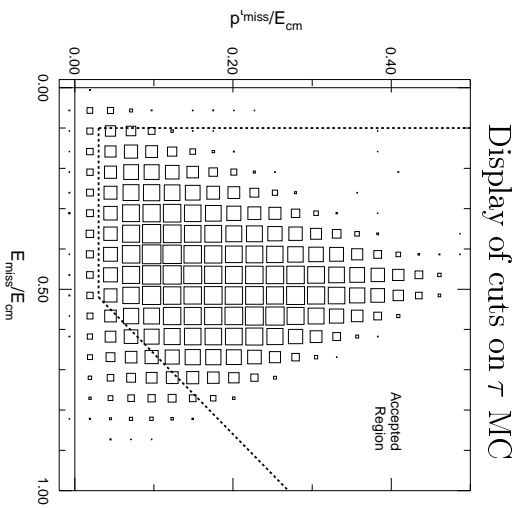
*Other topology selection methods were tested, but this one produced the best results in Monte Carlo tests.

measured in CLEO (between 0.3 MeV and 4.0 MeV), be within 0.005 m from the interaction point (to remove events that contain K_s^0 vertices, for example), have at least 39 hits in the central tracking system (CD), and have a reasonably good agreement between the fitted tracks and the actual CD hits (the total root-mean-square of the differences along a track is required to be less than 500.0×10^{-4}). Further, all three tracks are required to have at least two hits in the precision tracking layer (PTL) and eight hits in the main drift chamber (DR).

QED backgrounds are further reduced by making various cuts on the missing energy and missing momentum from charged tracks (since τ events must have a degree of missing energy and momentum from the unmeasured ν_τ 's). The missing energy (E_{miss}) is defined as the center-of-mass energy minus the combined energy of the charged tracks, while the total missing momentum vector (\vec{p}_{miss}) can be found from the vector sum of all the track momenta (which would be zero if all the momentum in the event were contained in the charged tracks). The cuts first reject events in which the missing momentum is directed down the beam pipe ($|\cos \theta_{\text{miss}}| \leq 0.9$, indicating that a decay product could have escaped without the chance of being measured). They further require that the missing energy and the transverse component of the missing momentum both be sufficiently large ($E_{\text{miss}} \geq 0.10 E_{\text{cm}}$ and $p_{\text{miss}}^t \geq 0.03 E_{\text{cm}}$). Comparisons between data and τ Monte Carlo additionally indicated that events with higher missing energy should be required to have higher missing transverse momentum. It is thus required that $p_{\text{miss}}^t/E_{\text{cm}} \geq 0.50 E_{\text{miss}}/E_{\text{cm}} - 0.25$. The last three cuts are displayed graphically in Figure 4.1,

Table 4.1
Summary of event selection criteria

“True” tracks:	Require 4 “non-fake” tracks with zero total charge
Quality of the 4 tracks:	Require close approach to interaction point (≤ 0.01 m in $r - \phi$, ≤ 0.10 m in z) Require each track have $\cos \theta \leq 0.85$ Require no more than one track ID’ed as e
1 vs 3 topology:	Find most isolated track Require it be $> 90^\circ$ from others Define “tag-side” by its direction
3-track quality:	Cuts are made to ensure that the signal tracks are reasonably well measured
Tags:	Use dE/dx and calorimetry to I.D. e and μ tags ρ : tag good candidates with $0.620 \text{ GeV} \leq m_\rho \leq 0.920 \text{ GeV}$ All others tagged as π
Missing E and p : (from charged tracks)	Require \vec{p}_{miss} not be down beam pipe Require $E_{\text{miss}} \geq 0.10E_{\text{cm}}$ Require $p_{\text{miss}}^t \geq 0.03E_{\text{cm}}$ (transverse missing momentum) Require 2-D cut: $p_{\text{miss}}^t/E_{\text{cm}} \geq 0.50E_{\text{miss}}/E_{\text{cm}} - 0.25$
Extra showers:	If photon-like or well isolated from tracks Cut event if $E_{\text{shower}} > 0.150 \text{ GeV}$ Otherwise Cut event if $E_{\text{shower}} > 0.300 \text{ GeV}$
K_s vertex cut:	Cut good vertex if $0.485 \text{ GeV} < m_{\text{vtx}} < 0.510 \text{ GeV}$



Comparisons of data and τ MC before (top) and after (bottom) cuts.

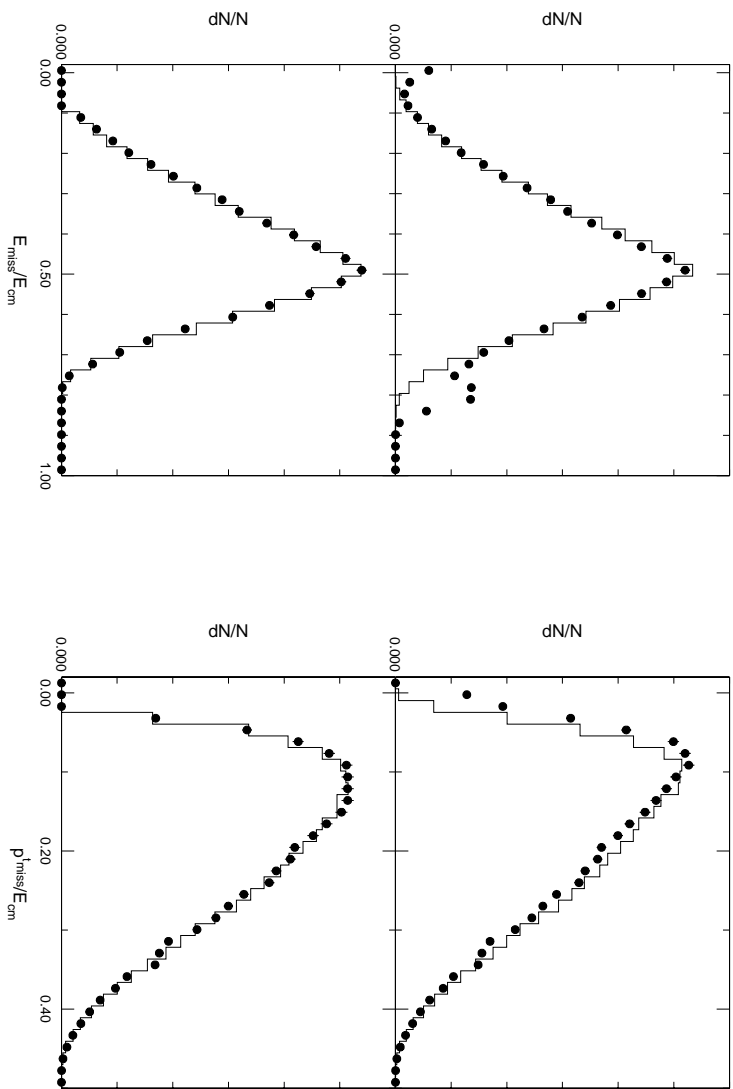


Figure 4.1

Display of p_{miss}^t vs. E_{miss} cuts and the effects on their 1-D projections. On comparison plots, the points mark data and the solid histogram marks the τ Monte Carlo

where the cuts are drawn on plots that show two dimensional distributions in $p_{\text{miss}}^t/E_{\text{cm}}$ and $E_{\text{miss}}/E_{\text{cm}}$ for both real and Monte Carlo data. Also shown are one dimensional data and τ Monte Carlo comparisons of $p_{\text{miss}}^t/E_{\text{cm}}$ and $E_{\text{miss}}/E_{\text{cm}}$ distributions before and after the cuts are applied.

Because extra photons in the event would indicate an undesired process (e.g., $\tau^- \rightarrow \pi^+\pi^-\pi^-\pi^0\nu_\tau$ or unwanted radiative events), cuts are performed based on extra showers found in the calorimeter for each event. First, the cuts ignore showers that are associated with charged tracks, shower fragments from larger showers, showers associated with a ρ on the tag side, showers within about 18° of a tagged electron (which can radiate), and showers with $\cos\theta > 0.95$ (which are not directly from the interaction region since such showers would have escape unmeasured through the ends of the detector). The remaining “extra” showers are then examined to determine if they are photon-like by comparing the energy deposited in the nine cells immediately surrounding the shower to the energy deposited in the 25 cells surrounding those nine (called an $E9/E25$ measurement). Photon showers are expected to form a tight cluster, and the $E9/E25$ measurement for a shower identified as photon-like is required to match the expected value for true photons with a 99% confidence level. Showers are also identified as being well isolated from all tracks if their distance from the closest track is greater than 25 cm. For extra showers that are either photon-like or well isolated, the event is cut if $E_{\text{shower}} > 0.150$ GeV. For other extra tracks, events are cut if $E_{\text{shower}} > 0.300$ GeV.

An additional background to reject are those containing decays through a K_s^0 . This background is largely reduced by the earlier requirement of a small distance of closest approach for each track on the signal side. However, an additional vertex cut is performed to further reduce this background. Vertices are considered in which neither track escapes through the end-caps of the detector and their distance from one another in z at the $r - \phi$ intersection point is no more than 5 times the error in the measurement of that distance. The vertex must also be at least 2 cm from the interaction point. For such vertices, the event is cut if the mass of the vertex is between 0.485 GeV and 0.510 GeV (the K_s^0 mass being 0.498 GeV [29]).

Figures 4.2 and 4.3 show CLEO event displays for a selected ρ -tag and a selected μ -tag event respectively (both Monte Carlo).

4.1 Backgrounds and Selection Results

Using the criteria given above, event samples (or *skims*) were chosen from data and Monte Carlo simulations to investigate background events in the final data selection. Studies on real data and non- τ Monte Carlo data indicate that the non- τ contamination in the event selection—consisting mainly of continuum ($e^+e^- \rightarrow q\bar{q}$ where q is either a u , d , c , or s), $B\bar{B}$, and two-photon events—is on the order of 1%. This insignificant source of background has thus been ignored in the analysis.

Backgrounds from τ events are studied using τ Monte Carlo simulation. All possible τ backgrounds are categorized using combinations of the Particle Data Group (PDG) basis modes (a selection intended to encompass all well established

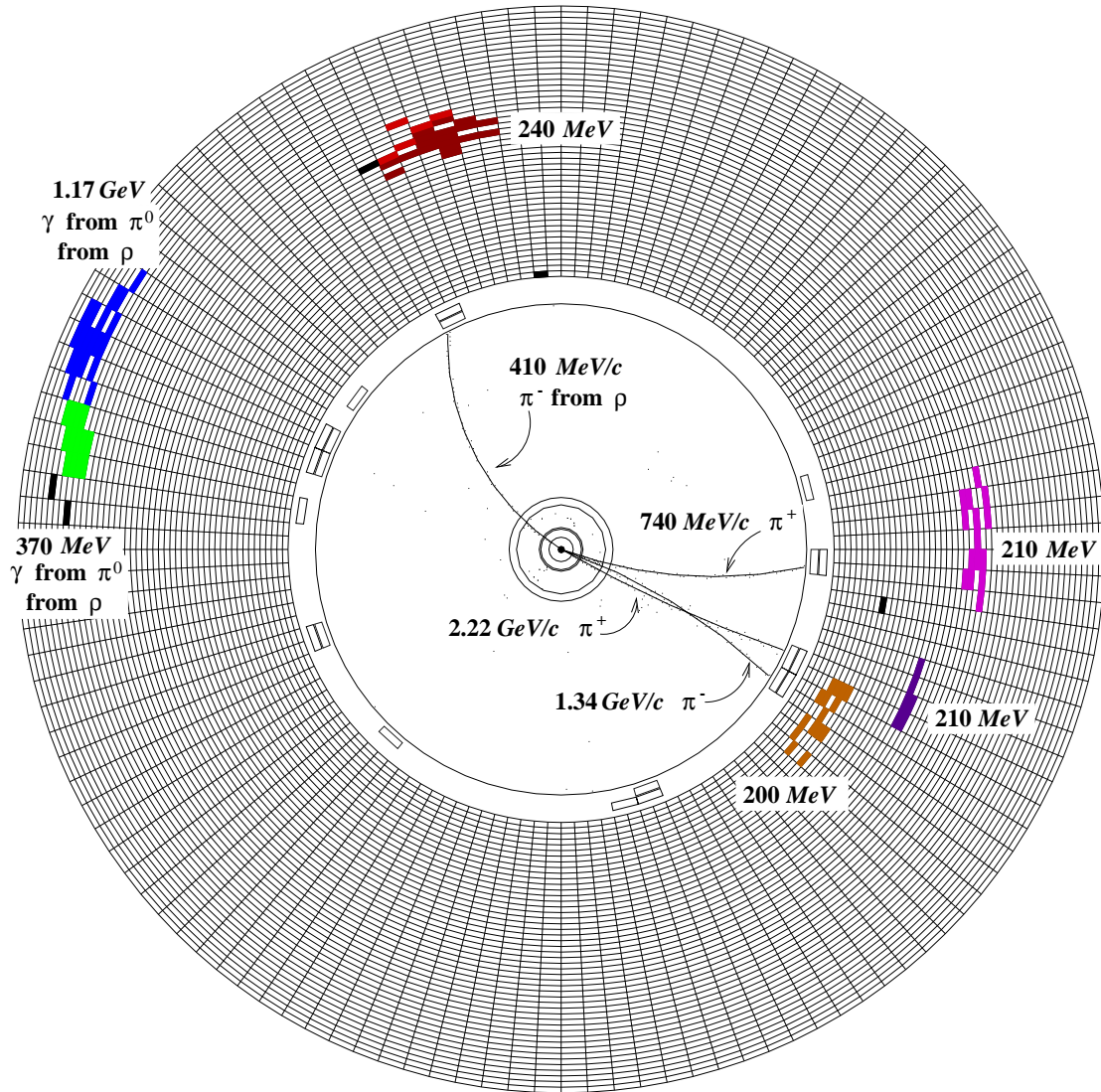


Figure 4.2

Event display of a Monte Carlo accepted event where the tag side is $\tau^- \rightarrow \rho^- \bar{\nu}_\tau \rightarrow \pi^- \pi^0 \bar{\nu}_\tau \rightarrow \pi^- \gamma \gamma \bar{\nu}_\tau$.

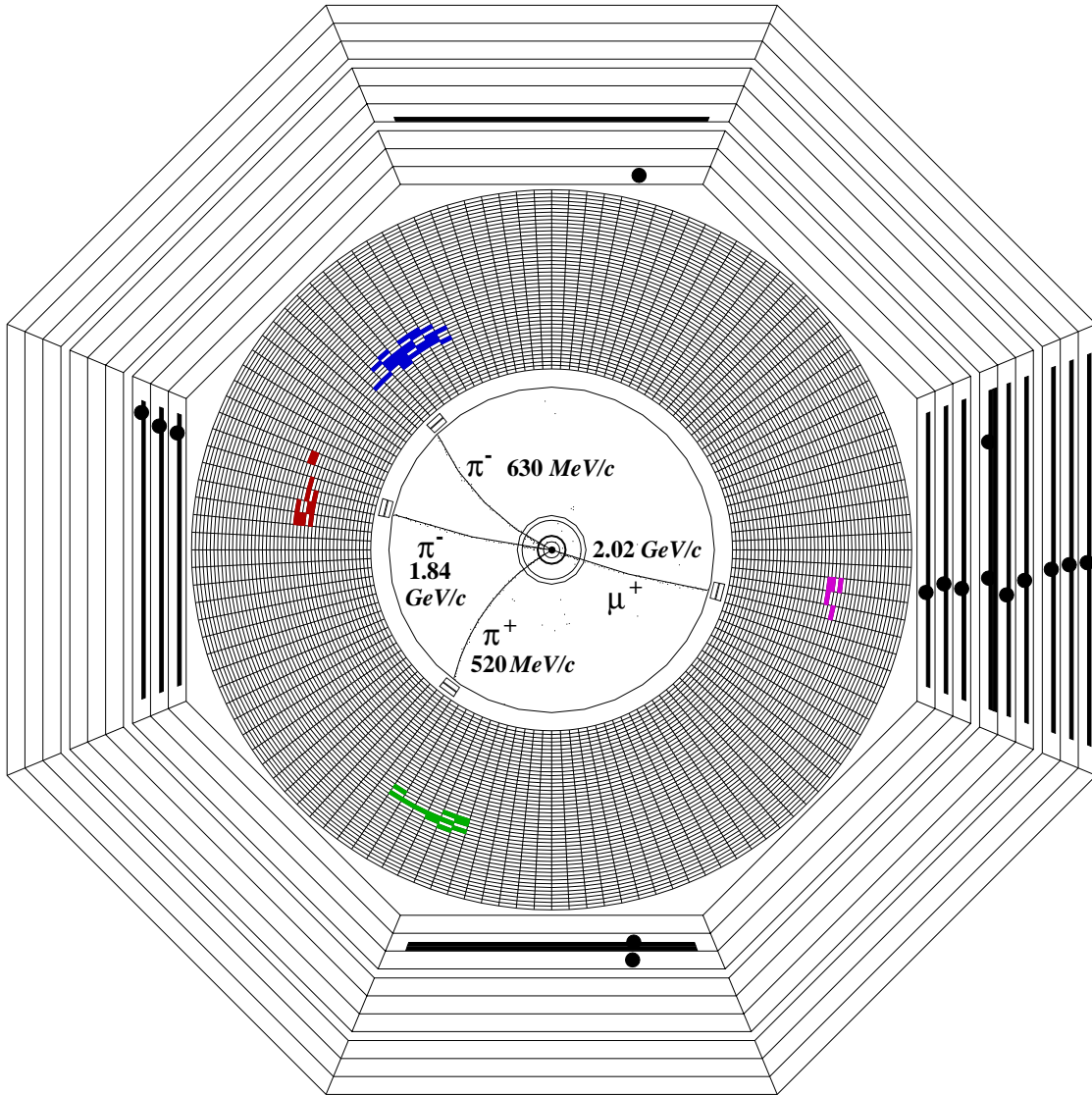


Figure 4.3

Event display of a Monte Carlo accepted event where the tag side is $\tau^+ \rightarrow \mu^+ \bar{\nu}_\tau$. The hits in the muon chamber on the tag side can be seen clearly.

τ decay modes and in which the branching fractions sum to 100%) [29]. The definitions of the signal and background modes used and the selection efficiencies for each (as found by applying the above selection criteria to Monte Carlo data) can be found in Table 4.2.

To help validate the results reported from the Monte Carlo skim, the following test was performed: using the reported efficiencies for the background modes, the PDG branching ratio of each mode, and the expected number of τ -pairs, one can estimate the total number of background events expected in the data skim. Subtracting that from the number of selected events and adjusting for the reported signal efficiency, one can estimate the total number of signal events expected in the original data sample. That result thus predicts a branching fraction for the signal mode, which should compare well with the PDG value if the reported efficiencies from Monte Carlo represent the actual efficiencies in the data skim. The test predicted a branching fraction of $0.0910 \pm 0.0003 \pm 0.0007$, whereas the PDG gives a value of 0.0913 ± 0.0011 . This indicates that the skim is valid and that efficiencies (and background fractions) are represented reasonably with the Monte Carlo.

The skim selects 148,000 data events. In addition to the given skim criteria, during the fitting procedure each event is required to meet reasonable kinematic requirements meant to ensure that the measured event could have been produced in a true $\tau^\pm \rightarrow \pi^\pm \pi^\pm \pi^\mp (\bar{\nu}_\tau / \nu_\tau)$ decay (see Section 6.2). This results in 145,000 events being used in the final fitting with an overall skim efficiency of approximately 0.176 and with 11.0% background from τ events as determined from Monte Carlo.

Table 4.2

Makeup of the τ background according to Monte Carlo studies. The “% of selected events” is the percentage of each mode in the final selection after accounting for difference between the PDG \mathcal{B} fractions and the percentage of input events found for each mode. The PDG basis modes sum to 99.995% due to round off, and the remaining 0.005% is arbitrarily assigned to all modes not found in the PDG basis.

Mode ID	# of input events	# of selected events	Skim eff.	\mathcal{B} Frac. from PDG (%)	% of input events	% of selected events
3π (signal)	2,973,307	521,915	0.17553	9.1300	8.9955	88.9650
1-prong, no π^0	12,478,521	486	0.00004	46.9890	47.1930	0.0810
1-prong, $> 0 \pi^0$	10,323,615	4,201	0.00041	36.2630	36.4810	0.7010
$3\pi\pi^0$ or $3h2\pi^0$	1,454,097	35,344	0.02431	2.5800	4.2944	3.5660
$3h > 2\pi^0$	3,506	1	0.00029	0.1300	0.0101	0.0020
$\pi 2K$ or $2\pi K$	158,907	29,380	0.18489	0.4310	0.4602	4.6210
$(\pi 2K$ or $2\pi K) \pi^0$	7,109	226	0.03179	0.1000	0.0205	0.1850
πK^0	294,096	3,101	0.01054	0.9000	0.8532	0.5490
KK^0	55,019	697	0.01267	0.1550	0.1591	0.1140
$hK^0\pi^0$	190,645	322	0.00169	0.5370	0.5524	0.0530
$\pi 2K^0$	34,922	189	0.00541	0.1190	0.1009	0.0370
$5h \geq 0\pi^0$	27,729	13	0.00047	0.1000	0.0802	0.0030
$h\eta \geq 0\pi^0$	65,173	138	0.00212	0.2010	0.1885	0.0250
$h\omega \geq 0\pi^0$	162,915	1,303	0.00800	2.3600	0.4718	1.0950
NOT IN BASIS	48,088	461	0.00959	0.0050	0.1390	0.0030

5. THEORY AND MODEL

In this section, the basic model used in the analysis will be presented, followed by modifications to that model. It begins with the proposed model-independent concepts used in describing the $\tau^\pm \rightarrow \pi^\pm \pi^\pm \pi^\mp (\bar{\nu}_\tau / \nu_\tau)$ decay and from which the standard (reduced) form factors arise. Also presented is a more model-dependent approach from which a set of “extended” form factors originate. The chapter goes on to explain how the form factors were modeled in this analysis, and two modifications to this model are presented. Finally, the differential decay rate is rewritten in light of the form factor formulas to make it more convenient in the fitting.

5.1 Description and Parameters of the Decay

A Feynman diagram of a $\tau^- \rightarrow \pi^- \pi^- \pi^+ \nu_\tau$ decay is shown in Figure 5.1, and an often used, full kinematic description of the decay is presented in Appendix G. In this section, specific notations used for describing the decay will be defined.

The 4-momenta of the three pions are denoted as \mathbf{q}_1 , \mathbf{q}_2 , and \mathbf{q}_3 such that $\mathbf{q}_3 = \mathbf{q}_{\pi^\mp}$ and $|\vec{q}_2| > |\vec{q}_1|$ in the three pion rest frame. As a convention, the components of the 4-momentum are denoted $\mathbf{q}_i = (E_i, \vec{q}_i)$.

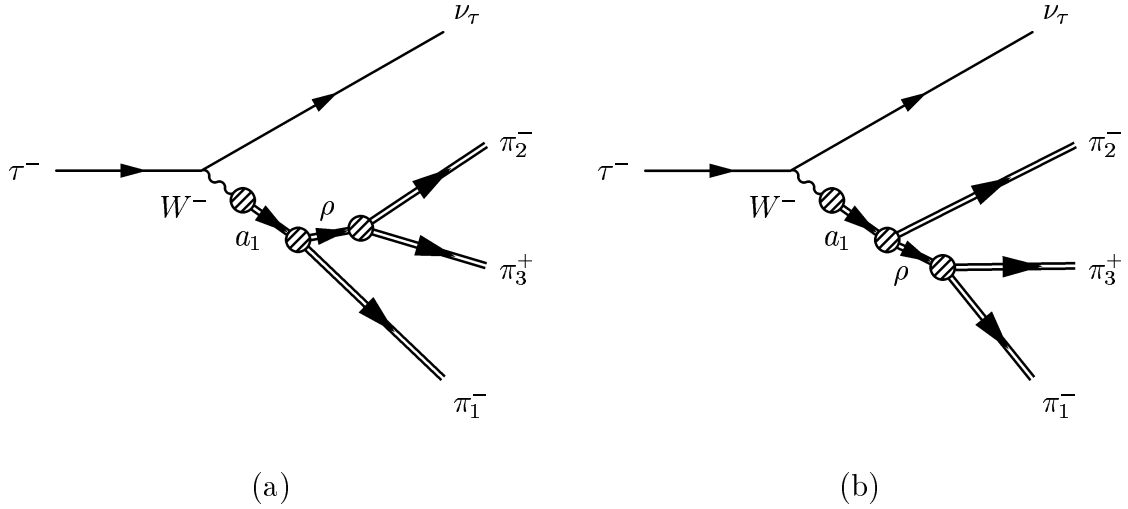


Figure 5.1

Feynman diagrams for a $\tau^- \rightarrow \pi^- \pi^- \pi^+ \nu_\tau$ process. The dominant resonance structure is shown through $a_1^- \rightarrow \pi^- \rho^0 \rightarrow \pi^- \pi^- \pi^+$. The two diagrams indicate an ambiguity from not knowing which π^- was produced from the ρ^0 .

The following kinematic factors are defined for convenience:

$$\begin{aligned}
 \mathbf{Q} &= \mathbf{q}_1 + \mathbf{q}_2 + \mathbf{q}_3, \\
 \mathbf{h}_i &= \mathbf{q}_j + \mathbf{q}_k, \\
 \mathbf{p}_i &= \mathbf{q}_j - \mathbf{q}_k, \\
 \mathbf{a}_i &= \mathbf{h}_i - \mathbf{q}_i,
 \end{aligned} \tag{5.1}$$

where i, j, k are cyclic $\in (1, 2, 3)$ and $i \neq j \neq k$.

The invariant mass-squared of the three pion system is thus denoted Q^2 , while the three 2-body invariant masses squared are defined by

$$s_i = h_i^2. \tag{5.2}$$

Note that the numbering scheme given above produces an ordered pair of Dalitz plot variables such that $s_1 > s_2$ in all cases. Also note that given Q^2 , s_1 , and s_2 , the value of s_3 is fully determined ($s_3 = Q^2 + 3m_\pi^2 - s_1 - s_2$).

5.2 The Differential Decay Rate and the Hadronic Current

The matrix element for this semileptonic τ decay can be written

$$\mathcal{M} = \cos \theta_c \frac{G_F}{\sqrt{2}} M_\mu J^\mu, \quad (5.3)$$

where θ_c is the Cabibbo angle ($\cos \theta_c = V_{ud}$), G_F is the Fermi coupling constant, M_μ describes the lepton current for the τ transition to the ν_τ , J^μ is the hadronic current describing the production of the three charged pions, and the Einstein summation convention is employed as usual (see Appendix B).

The lepton current is given via the standard $V - A$ theory of weak interactions:

$$M_\mu = \langle \bar{\psi}_{\nu_e} | \gamma_\mu (g_V - g_A \gamma_5) | \psi_\tau \rangle, \quad (5.4)$$

where the relative V and A couplings are equal ($g_V = g_A = 1$) in the standard model.

The differential decay rate for the decay is then obtained as usual from the square of the matrix element:

$$d\Gamma_{\tau^\pm \rightarrow [3\pi]^\pm (\bar{\nu}_\tau/\nu_\tau)} = \frac{1}{2m_\tau} \frac{G_F^2 V_{ud}^2}{2} \{L_{\mu\nu} H^{\mu\nu}\} dPS^{(4)}, \quad (5.5)$$

where $dPS^{(4)}$ is the proper four-body phase space element, $L_{\mu\nu} = M_\mu(M_\nu)^\dagger$ is the well understood lepton tensor,* and $H^{\mu\nu} = J^\mu(J^\nu)^\dagger$ is the hadronic tensor. This analysis intends to explore the structure of the hadronic current, J^μ .

Nominally, the hadronic current that describes the production of three hadrons is written in terms of axial vector and vector currents:

$$\begin{aligned} J^\mu(\mathbf{q}_1, \mathbf{q}_2, \mathbf{q}_3) &= J_A^\mu + J_V^\mu \\ &= \langle h_1(\mathbf{q}_1) h_2(\mathbf{q}_2) h_3(\mathbf{q}_3) | \bar{d}\gamma_\mu u + \bar{d}\gamma_5\gamma_\mu u | 0 \rangle. \end{aligned} \quad (5.6)$$

From here one can consider two ways to characterize the current. The first, more general characterization is conducive to a model-independent approach involving four form factors:

$$J^\mu(\mathbf{q}_1, \mathbf{q}_2, \mathbf{q}_3) = V_1^\mu F_1 + V_2^\mu F_2 + iV_3^\mu F_3 + V_4^\mu F_4, \quad (5.7)$$

where

$$\begin{aligned} V_1^\mu &= T^{\mu\nu} p_{1\nu}, \\ V_2^\mu &= T^{\mu\nu} p_{2\nu}, \\ V_3^\mu &= \epsilon^{\mu\alpha\beta\gamma} q_{1\alpha} q_{2\beta} q_{3\gamma}, \\ V_4^\mu &= Q^\mu, \end{aligned} \quad (5.8)$$

and $T^{\mu\nu} = g^{\mu\nu} - Q^\mu Q^\nu / Q^2$. Note that the form factors are functions of Q^2 , s_1 , and s_2 . Further, F_1 and F_2 moderate the axial vector components in the current, F_3 moderates the vector component, and F_4 moderates the pseudoscalar component. However, for the 3π final state, G-parity conservation would require that $J_V^\mu = 0$.

*A general formula for the lepton tensor is given in Appendix F.

Thus $F_3 = 0$ in the above equations, and here one need only be concerned with axial vector and pseudoscalar contributions to the transition current.

The current can also be characterized in a model-dependent approach as follows:

$$J^\mu(\mathbf{q}_1, \mathbf{q}_2, \mathbf{q}_3) = \sum_{k=1}^{N_{\text{res}}^{3\pi}} \left[B_k(Q^2) \sum_{i=1}^{N_{\text{sub}}^k} \beta_i^k j_i^{k\mu} \right], \quad (5.9)$$

where the first sum is over the primary resonances of the 3π system to be modeled, and the second sum extends over the modeled secondary resonances (or sub-resonances) of each primary resonance. Each $B_k(Q^2)$ factor provides the Breit-Wigner description of the k th primary resonance, while the \mathbf{j}_i^k factors each describe the modeling of the i th secondary resonance of the k th primary resonance. The relative strength of each secondary resonance is controlled by the corresponding β_i^k factor. The \mathbf{j}_i^k factors are termed “extended form factors” to distinguish them from the more general, “reduced” form factors given above.

These two descriptions of the current are basically interchangeable, though they represent different approaches. The following model construction will deal with the latter approach (modeling the extended form factors), while modeling of the reduced form factors will be addressed in Section 5.4.

5.3 Modeling the Extended Form Factors

The τ is expected to decay predominantly through resonance structures whose contributions to the hadronic current must thus be modeled in the form factor descriptions given above. The dominant resonances are the axial vector resonances ($J^P = 1^+$); however, pseudoscalar resonances ($J^P = 0^-$) are also possible, though

they are suppressed according to the partially conserved axial current hypothesis. Here is described the modeling of these resonances and their substructure.

For the axial vector contribution to the current, the dominant primary resonance is conventionally understood to be the lowest order axial vector meson, the $a_1(1260)$; however contributions from radial excitations (i.e., the a_1') could also be included in the model. This analysis does not include considerations for the a_1' . The possible pseudoscalar contributions are expected to be dominated by the $\pi'(1300)$. Using these primary resonances, one can rewrite the current in the form of Equation 5.9 as follows:

$$J^\mu(\mathbf{q}_1, \mathbf{q}_2, \mathbf{q}_3) = B_{a_1}(Q^2) \sum_{i=1}^{N_{\text{sub}}^{a_1}} \beta_i^{a_1} j_i^{a_1\mu} + B_{\pi'}(Q^2) \sum_{i=1}^{N_{\text{sub}}^{\pi'}} \beta_i^{\pi'} j_i^{\pi'\mu}. \quad (5.10)$$

Given this, the next challenges are as follows: (1) modeling must be specified for $B_{a_1}(Q^2)$ (the Breit-Wigner description for the a_1 resonance) as well as $j_i^{a_1\mu}$ (the full descriptions of its $N_{\text{sub}}^{a_1}$ secondary resonances), (2) modeling must be specified for $B_{\pi'}(Q^2)$ (the Breit-Wigner description for the π' resonance) as well as $j_i^{\pi'\mu}$ (the full descriptions of its $N_{\text{sub}}^{\pi'}$ secondary resonances), and (3) the unknown complex coupling constants, $\beta_i^{a_1}$ and $\beta_i^{\pi'}$, must be found via fitting.

5.3.1 Modeling the 1^+ Resonance

For this analysis, the a_1 line shape is taken from the results of a previously published CLEO analysis on $\tau^\pm \rightarrow \pi^\pm \pi^0 \pi^0 (\bar{\nu}_\tau / \nu_\tau)$ decays [60]. In that analysis, a reasonable fit for the a_1 line shape was found from the $[3\pi]^-$ mass spectrum,

though no correction was used for possible 0^- contributions. However, any effects from pseudoscalar contributions to the $[3\pi]^-$ mass spectrum are expected to be be miniscule, and the only hope for extracting information concerning pseudoscalar resonances is in detecting subtle effects in the substructure of the decay. Thus, it is reasonable for this analysis to assume the same a_1 line shape found in [60].

In summary, the previous analysis fit for parameters within the the a_1 Breit-Wigner:

$$B_{a_1}(Q^2) = \frac{m_{a_1}^2}{Q^2 - m_{a_1}^2 + im_{a_1}\Gamma_{tot}^{a_1}(Q^2)}, \quad (5.11)$$

where m_{a_1} is the nominal mass of the a_1 and $\Gamma_{tot}^{a_1}(Q^2)$ is the total mass-dependent width. Note that the previous analysis originally assumed a Q^2 -dependent mass; however, satisfactory fits were obtained using a constant mass.

The Q^2 -dependent behavior of the total a_1 width depends on all its possible channels, including $a_1 \rightarrow [3\pi]^-$ and $a_1 \rightarrow K\bar{K}\pi$. The previous analysis first conducted a study of the a_1 substructure using a technique that was largely independent of the full 3π mass spectrum. Using those results and attempting to make reasonable assumptions concerning contributions from other channels, it produced the following result for the total a_1 width:

$$\Gamma_{tot}^{a_1}(Q^2) = \frac{\Gamma_0^{a_1}}{\kappa_0^{a_1}} [C_{3\pi}^2 (W_{\pi^\pm\pi^\pm\pi^\mp}(Q^2) + W_{\pi^\pm\pi^0\pi^0}(Q^2)) + C_{K\bar{K}}^2 (W_{K^*K}(Q^2))], \quad (5.12)$$

where

$$\begin{aligned}
 \kappa_0^{a_1} &= 1.0704, \\
 C_{3\pi} &= 0.2384, \\
 C_{K\bar{K}} &= 4.7621C_{3\pi},
 \end{aligned} \tag{5.13}$$

and

$$W_{\pi^\pm\pi^\pm\pi^\mp}(Q^2) = \begin{cases} 0 & Q^2 < M_1^2 \\ X_0\Delta_1^3(1 + X_1\Delta_1 + X_2\Delta_1^2) & M_1^2 < Q^2 < M_{\rho\pi} \\ \sum_{i=0}^4 P_i Q^{2i} & \text{otherwise,} \end{cases}$$

$$\begin{aligned}
 \Delta_1 &= Q^2 - M_1^2, \\
 M_1 &= 3m_\pi, \\
 M_{\rho\pi} &= m_\rho + m_\pi, \\
 (X_0, X_1, X_2) &= (5.8090, -3.00980, 4.5792), \\
 (P_0, P_1, P_2, P_3, P_4) &= (-13.9140, 27.6790, -13.3930, 3.1924, -0.10487),
 \end{aligned} \tag{5.14}$$

and

$$\begin{aligned}
W_{\pi^\pm\pi^0\pi^0}(Q^2) &= \begin{cases} 0 & Q^2 < M_2^2 \\ Y_0\Delta_2^3(1 + Y_1\Delta_2 + Y_2\Delta_2^2) & M_2^2 < Q^2 < M_{\rho\pi^0} \\ \sum_{i=0}^4 R_i Q^{2i} & \text{otherwise,} \end{cases} \\
\Delta_2 &= Q^2 - M_2^2, \\
M_2 &= 2m_{\pi^0} + m_\pi, \\
M_{\rho\pi^0} &= m_\rho + m_{\pi^0}, \\
(Y_0, Y_1, Y_2) &= (6.2845, -2.9595, 4.3355), \\
(R_0, R_1, R_2, R_3, R_4) &= (-15.4110, 32.0880, -17.6660, 4.9355, -0.37498),
\end{aligned} \tag{5.15}$$

and

$$\begin{aligned}
W_{K^*K}(Q^2) &= \begin{cases} 0 & Q^2 < M_3^2 \\ \frac{\sqrt{\Delta_3\Delta_4}}{2Q^2} & \text{otherwise,} \end{cases} \\
\Delta_3 &= Q^2 - (m_{K^*} + m_K)^2, \\
\Delta_4 &= Q^2 - (m_{K^*} - m_K)^2.
\end{aligned} \tag{5.16}$$

Note that $\kappa_0^{a_1}$ is chosen to ensure that $\Gamma_{tot}^{a_1}(m_{a_1}) = \Gamma_0^{a_1}$.

5.3.2 Modeling the 1^+ Substructure

For this analysis, the decay of the a_1 is assumed to proceed through one of seven possible sub-resonances (thus $N_{\text{sub}}^{a_1} = 7$). The choices and the modeling reflect those used in [60] (though isospin rotated from the $\pi^\pm\pi^0\pi^0$ mode in that analysis to the all-charged mode considered here). The sub-resonances are denoted

as follows:

$$\begin{aligned}
\mathbf{j}_1^{a_1} &= s\text{-wave amplitude for } 1^+ \rightarrow \rho(770)\pi && (s\text{-wave } \rho\pi), \\
\mathbf{j}_2^{a_1} &= s\text{-wave amplitude for } 1^+ \rightarrow \rho(1450)\pi && (s\text{-wave } \rho'\pi), \\
\mathbf{j}_3^{a_1} &= d\text{-wave amplitude for } 1^+ \rightarrow \rho(770)\pi && (d\text{-wave } \rho\pi), \\
\mathbf{j}_4^{a_1} &= d\text{-wave amplitude for } 1^+ \rightarrow \rho(1450)\pi && (d\text{-wave } \rho'\pi), \\
\mathbf{j}_5^{a_1} &= p\text{-wave amplitude for } 1^+ \rightarrow f_2(1270)\pi && (p\text{-wave } f_2\pi), \\
\mathbf{j}_6^{a_1} &= p\text{-wave amplitude for } 1^+ \rightarrow f_0(400 - 1200)\pi && (p\text{-wave } \sigma\pi), \\
\mathbf{j}_7^{a_1} &= p\text{-wave amplitude for } 1^+ \rightarrow f_0(1370)\pi && (p\text{-wave } f_0\pi).
\end{aligned} \tag{5.17}$$

The amplitudes are then modeled as follows:

$$\begin{aligned}
j_1^{a_1\mu} &= C_1 T^{\mu\nu} \left\{ \begin{array}{l} p_{1\nu} B_\rho^1(s_1) - p_{2\nu} B_\rho^1(s_2) \end{array} \right\}, \\
j_2^{a_1\mu} &= C_1 T^{\mu\nu} \left\{ \begin{array}{l} p_{1\nu} B_{\rho'}^1(s_1) - p_{2\nu} B_{\rho'}^1(s_2) \end{array} \right\}, \\
j_3^{a_1\mu} &= C_1 T^{\mu\nu} \left\{ \begin{array}{l} a_{1\nu}(\mathbf{Q}\mathbf{p}_1) B_\rho^1(s_1) - a_{2\nu}(\mathbf{Q}\mathbf{p}_2) B_\rho^1(s_2) \end{array} \right\}, \\
j_4^{a_1\mu} &= C_1 T^{\mu\nu} \left\{ \begin{array}{l} a_{1\nu}(\mathbf{Q}\mathbf{p}_1) B_{\rho'}^1(s_1) - a_{2\nu}(\mathbf{Q}\mathbf{p}_2) B_{\rho'}^1(s_2) \end{array} \right\}, \\
j_5^{a_1\mu} &= -C_1 T^{\mu\nu} \left\{ \begin{array}{l} \left[p_{1\nu}(\mathbf{Q}\mathbf{p}_1) - \frac{1}{3} \left(Q_\nu - h_{1\mu} \frac{(\mathbf{h}_1\mathbf{Q})}{s_1} \right) (\mathbf{p}_1\mathbf{p}_1) \right] B_{f_2}^2(s_1) \\ + \left[p_{2\nu}(\mathbf{Q}\mathbf{p}_2) - \frac{1}{3} \left(Q_\nu - h_{2\mu} \frac{(\mathbf{h}_2\mathbf{Q})}{s_2} \right) (\mathbf{p}_2\mathbf{p}_2) \right] B_{f_2}^2(s_2) \end{array} \right\}, \\
j_6^{a_1\mu} &= -C_1 T^{\mu\nu} \left\{ \begin{array}{l} a_{1\nu} B_\sigma^0(s_1) + a_{2\nu} B_\sigma^0(s_2) \end{array} \right\}, \\
j_7^{a_1\mu} &= -C_1 T^{\mu\nu} \left\{ \begin{array}{l} a_{1\nu} B_{f_0}^0(s_1) + a_{2\nu} B_{f_0}^0(s_2) \end{array} \right\},
\end{aligned} \tag{5.18}$$

where $T^{\mu\nu} = g^{\mu\nu} - Q^\mu Q^\nu / Q^2$ as before in the nominal case (see Section 5.5 for variations), the dot product notation $(\mathbf{x}\mathbf{y}) \equiv x^\alpha y_\alpha$ is used, and the Breit-Wigner

functions in the above expressions are given by

$$\begin{aligned}
B_x^L(s) &= \frac{m_x^2}{m_x^2 - s - im_x \Gamma_{\pi\pi,L}^x(s)}, \\
\Gamma_{YZ,L}^x(s) &= \Gamma_0^x \left(\frac{p_{YZ}(s)}{p_{YZ}(m_x^2)} \right)^{2L+1} \frac{m_x}{\sqrt{s}}, \\
p_{YZ}(s) &= \frac{\sqrt{(s - (m_Y + m_Z)^2)(s - (m_Y - m_Z)^2)}}{2\sqrt{s}}.
\end{aligned} \tag{5.19}$$

The constant, C_1 , could be absorbed into the $\beta_i^{a_1}$ factors in Equation 5.10; however, to make these extended form factors consistent with typical, normalized equations for the reduced form factors F_1 and F_2 , this constant is taken to be

$$C_1 = \frac{2\sqrt{2}}{3f_\pi}, \tag{5.20}$$

where $f_\pi = 0.093$ GeV is the pion decay constant. For the masses and widths of the particles used in this analysis, see Table 5.1.

5.3.3 Modeling the 0^- Resonance

The structure of the π' is defined in terms of its Breit-Wigner:

$$B_{\pi'}(Q^2) = \frac{m_{\pi'}^2}{Q^2 - m_{\pi'}^2 + im_{\pi'} \Gamma_{tot}^{\pi'}(Q^2)}, \tag{5.21}$$

where $m_{\pi'}$ is the nominal mass of the π' (see Table 5.1) and $\Gamma_{tot}^{\pi'}(Q^2)$ is the total mass-dependent width.

The Q^2 -dependence of the π' total width, $\Gamma_{tot}^{\pi'}(Q^2)$, depends on all its possible channels, though little is known about those channels. This analysis considers contributions from the $\rho\pi$ and $\sigma\pi$ channels:

$$\Gamma_{tot}^{\pi'}(Q^2) = \frac{\Gamma_{\rho\pi,1}^{\pi'}(Q^2) + \alpha \Gamma_{\sigma\pi,1}^{\pi'}(Q^2)}{1 + \alpha}, \tag{5.22}$$

where $\Gamma_{YZ,L}^X$ was defined earlier and α is arbitrarily taken to be 0.25. Although this is a somewhat ad hoc construction, the uncertainty in the nominal width of the π' (200-600 MeV) overshadows this definition of the full width as a significant source of error.

5.3.4 Modeling the 0^- Substructure

The decay of the $\pi'(1300)$ is assumed to proceed through one of three sub-resonances (thus $N_{\text{sub}}^{\pi'} = 3$). They are denoted as follow:

$$\begin{aligned}
 \mathbf{j}_1^{\pi'} &= p\text{-wave amplitude for } 1^+ \rightarrow \rho(770)\pi && (p\text{-wave } \rho\pi), \\
 \mathbf{j}_2^{\pi'} &= p\text{-wave amplitude for } 1^+ \rightarrow \rho(1450)\pi && (p\text{-wave } \rho'\pi), \\
 \mathbf{j}_3^{\pi'} &= s\text{-wave amplitude for } 1^+ \rightarrow f_0(400 - 1200)\pi && (s\text{-wave } \sigma\pi).
 \end{aligned} \tag{5.23}$$

Table 5.1

Masses and widths of particles used in this analysis.

Particle (X)	Nominal Mass (m_X)	Nominal Width (Γ_0^X)	Reference
τ	1.777	—	[29]
a_1	1.230	0.400	[29]
π'	1.300	0.300	[29]
$\rho(770)$	0.774	0.149	[62]
$\rho(1450)$	1.370	0.386	[62]
$f_2(1270)$	1.275	0.185	[29]
σ	0.860	0.880	[63]
$f_0(1370)$	1.186	0.350	[63]

The amplitudes are then modeled as follows:

$$\begin{aligned}
j_1^{\pi'\mu} &= \frac{C_4 Q^\mu}{m_\rho^2} \left\{ (s_2 - s_3)B_\rho^1(s_1) + (s_1 - s_3)B_\rho^1(s_2) \right\}, \\
j_2^{\pi'\mu} &= \frac{C_4 Q^\mu}{m_{\rho'}^2} \left\{ (s_2 - s_3)B_{\rho'}^1(s_1) + (s_1 - s_3)B_{\rho'}^1(s_2) \right\}, \\
j_3^{\pi'\mu} &= \frac{C_4 Q^\mu}{m_\sigma^2} \left\{ B_\sigma^0(s_1) + B_\sigma^0(s_2) \right\},
\end{aligned} \tag{5.24}$$

where the Breit-Wigner functions were defined earlier. The constant, C_4 , could be absorbed into the $\beta_i^{\pi'}$ factors in Equation 5.10; however, to make these extended form factors consistent with typical, normalized equations for the reduced form factor F_4 , this constant is taken to be to be

$$C_4 = -\frac{i g_{\pi' \rho \pi} g_{\rho \pi \pi}}{m_{\pi'}^2}, \tag{5.25}$$

where $g_{\pi' \rho \pi} = 5.8$ and $g_{\rho \pi \pi} = 6.08$. For the masses of the particles used in this analysis, see Table 5.1.

5.4 Modeling the Reduced Form Factors

For completeness, the modeling of the reduced form factors is presented here. It can be formulated given the modeling of the extended form factors above. In accordance with the model-independent characterization of the hadronic current given in Equations 5.7 and 5.8, the axial vector resonance, a_1 , is nominally modeled in the F_1 and F_2 form factors; while the pseudoscalar π' resonance is modeled in

F_4 . A nominal treatment of these form factors can then be written as follows:

$$\begin{aligned}
F_1(Q^2, s_1, s_2) &= C_1 B_{a_1}(Q^2) \sum_{i=1}^{N_{\text{sub}}^{a_1}} \beta_i^{a_1} \mathcal{B}_i^{a_1}(Q^2, s_1, s_2), \\
F_2(Q^2, s_1, s_2) &= -F_1(Q^2, s_2, s_1), \\
F_4(Q^2, s_1, s_2) &= C_4 B_{\pi'}(Q^2) \sum_{i=1}^{N_{\text{sub}}^{\pi'}} \beta_i^{\pi'} \mathcal{B}_i^{\pi'}(Q^2, s_1, s_2),
\end{aligned} \tag{5.26}$$

where the sums extend over amplitudes from the a_1 and π' sub-resonances respectively, and the \mathcal{B}_i^X functions will be defined to model those sub-resonance contributions in each form factor. Note that C_1 and C_4 were defined earlier to be typical ‘‘normalization’’ factors for these form factor equations. Applying these to Equation 5.7, the hadronic current becomes

$$\begin{aligned}
J^\mu(\mathbf{q}_1, \mathbf{q}_2, \mathbf{q}_3) &= B_{a_1}(Q^2) \sum_{i=1}^{N_{\text{sub}}^{a_1}} \beta_i^{a_1} C_1 [V_1^\mu \mathcal{B}_i^{a_1}(Q^2, s_1, s_2) - V_2^\mu \mathcal{B}_i^{a_1}(Q^2, s_2, s_1)] \\
&\quad + B_{\pi'}(Q^2) \sum_{i=1}^{N_{\text{sub}}^{\pi'}} \beta_i^{\pi'} C_4 V_4^\mu \mathcal{B}_i^{\pi'}(Q^2, s_1, s_2),
\end{aligned} \tag{5.27}$$

or, substituting for the V_i functions:

$$\begin{aligned}
J^\mu(\mathbf{q}_1, \mathbf{q}_2, \mathbf{q}_3) &= B_{a_1}(Q^2) \sum_{i=1}^{N_{\text{sub}}^{a_1}} \beta_i^{a_1} C_1 T^{\mu\nu} [p_{1\nu} \mathcal{B}_i^{a_1}(Q^2, s_1, s_2) - p_{2\nu} \mathcal{B}_i^{a_1}(Q^2, s_2, s_1)] \\
&\quad + B_{\pi'}(Q^2) \sum_{i=1}^{N_{\text{sub}}^{\pi'}} \beta_i^{\pi'} C_4 Q^\mu \mathcal{B}_i^{\pi'}(Q^2, s_1, s_2).
\end{aligned} \tag{5.28}$$

When this equation is compared to the hadronic current given in Equation 5.10, one clearly finds that $\mathcal{B}_i^{a_1}(Q^2, s_1, s_2)$ and $\mathcal{B}_i^{\pi'}(Q^2, s_1, s_2)$ must be defined such that

the extended form factors can be rewritten as follows:

$$\begin{aligned}
 j_i^{a_1\mu} &= C_1 T^{\mu\nu} [p_{1\nu} \mathcal{B}_i^{a_1}(Q^2, s_1, s_2) - p_{2\nu} \mathcal{B}_i^{a_1}(Q^2, s_2, s_1)], \\
 j_i^{\pi'\mu} &= C_4 Q^\mu \mathcal{B}_i^{\pi'}(Q^2, s_1, s_2).
 \end{aligned}
 \tag{5.29}$$

Equating this format for each $j_i^{a_1\mu}$ to those modeled in Equation 5.18 is obviously non-trivial for $i > 2$. However, the difference between the two formats can be shown to always involve factors (denoted $\mathcal{B}'_i^{a_1}$) proportional to $T^{\mu\nu} Q_\nu$ (which is identically zero because of the form of $T^{\mu\nu}$). For a clearer picture of the equivalence between the two $j_i^{a_1\mu}$ formulations, one can include these (nominally irrelevant) factors in the above equation:

$$\begin{aligned}
 j_i^{a_1\mu} &= C_1 T^{\mu\nu} [p_{1\nu} \mathcal{B}_i^{a_1}(Q^2, s_1, s_2) - p_{2\nu} \mathcal{B}_i^{a_1}(Q^2, s_2, s_1) + Q_\nu \mathcal{B}'_i^{a_1}(Q^2, s_1, s_2)], \\
 j_i^{\pi'\mu} &= C_4 Q^\mu \mathcal{B}_i^{\pi'}(Q^2, s_1, s_2).
 \end{aligned}
 \tag{5.30}$$

In one of the model variations discussed in Section 5.5, those factors will no longer vanish, and they will therefore be defined here for convenience.

It thus remains to construct the $\mathcal{B}_i^{a_1}$, $\mathcal{B}'_i^{a_1}$, and $\mathcal{B}_i^{\pi'}$ factors used to model the reduced form factors such that Equation 5.30 is consistent with the models of the extended form factors produced earlier. They are given as follows (as functions of

(Q^2, s_1, s_2) :

$$\begin{aligned}
\mathcal{B}_1^{a_1} &= B_\rho^1(s_1), \\
\mathcal{B}_2^{a_1} &= B_{\rho'}^1(s_1), \\
\mathcal{B}_3^{a_1} &= -\frac{1}{3}(s_2 - s_3)B_\rho^1(s_1) - \frac{2}{3}(s_3 - s_1)B_\rho^1(s_2), \\
\mathcal{B}_4^{a_1} &= -\frac{1}{3}(s_2 - s_3)B_{\rho'}^1(s_1) - \frac{2}{3}(s_3 - s_1)B_{\rho'}^1(s_2), \\
\mathcal{B}_5^{a_1} &= \left\{ \frac{1}{2}(s_2 - s_3) - \frac{1}{18} \frac{(Q^2 - m_\pi^2 + s_1)(4m_\pi - s_1)}{s_1} \right\} B_{f_2}^2(s_1), \\
&\quad + \frac{1}{9} \frac{(Q^2 - m_\pi^2 + s_2)(4m_\pi - s_2)}{s_2} B_{f_2}^2(s_2), \\
\mathcal{B}_6^{a_1} &= -\frac{2}{3}B_\sigma^0(s_1) + \frac{4}{3}B_\sigma^0(s_2), \\
\mathcal{B}_7^{a_1} &= -\frac{2}{3}B_{f_0}^0(s_1) + \frac{4}{3}B_{f_0}^0(s_2),
\end{aligned} \tag{5.31}$$

and

$$\begin{aligned}
\mathcal{B}'_1^{a_1} &= \mathcal{B}'_2^{a_1} = 0, \\
\mathcal{B}'_3^{a_1} &= -\frac{1}{6} \left((s_2 - s_3)B_\rho^1(s_1) - (s_3 - s_1)B_\rho^1(s_2) \right), \\
\mathcal{B}'_4^{a_1} &= -\frac{1}{6} \left((s_2 - s_3)B_{\rho'}^1(s_1) - (s_3 - s_1)B_{\rho'}^1(s_2) \right), \\
\mathcal{B}'_5^{a_1} &= -\frac{1}{3} \left\{ \frac{(Q^2 - m_\pi^2 - 2s_1)(4m_\pi - s_1)}{3s_1} B_{f_2}^2(s_1) \right. \\
&\quad \left. + \frac{(Q^2 - m_\pi^2 - 2s_2)(4m_\pi - s_2)}{3s_2} B_{f_2}^2(s_2) \right\}, \\
\mathcal{B}'_6^{a_1} &= -\frac{1}{3} \left(B_\sigma^0(s_1) + B_\sigma^0(s_2) \right), \\
\mathcal{B}'_7^{a_1} &= -\frac{1}{3} \left(B_{f_0}^0(s_1) + B_{f_0}^0(s_2) \right),
\end{aligned} \tag{5.32}$$

and

$$\begin{aligned}
\mathcal{B}_1^{\pi'} &= \frac{1}{m_\rho^2} \left((s_2 - s_3) B_\rho^1(s_1) + (s_1 - s_3) B_\rho^1(s_2) \right), \\
\mathcal{B}_2^{\pi'} &= \frac{1}{m_{\rho'}^2} \left((s_2 - s_3) B_{\rho'}^1(s_1) + (s_1 - s_3) B_{\rho'}^1(s_2) \right), \\
\mathcal{B}_3^{\pi'} &= \frac{1}{m_\sigma^2} \left(B_\sigma^0(s_1) + B_\sigma^0(s_2) \right).
\end{aligned} \tag{5.33}$$

5.5 Model Variations

In addition to the base model given above, the analysis considers two variations in that model. Both of these variations focus on the pseudoscalar aspects of the modeled hadronic current, which is a prominent point of interest for this analysis.

The first variation considers a direct change to the modeling of both the overall width and the substructure of the 0^- resonance in accordance with certain theoretical treatments [64]. The overall π' width is changed by modifying the $\rho\pi$ and $\sigma\pi$ contribution as follows:

$$\Gamma_{tot}^{\pi'}(Q^2) = \frac{\Gamma_{\rho\pi,2}^{\pi'}(Q^2) + \alpha \Gamma_{\sigma\pi,2}^{\pi'}(Q^2)}{1 + \alpha}. \tag{5.34}$$

The changes to the sub-structure modeling are given here in terms of the $\mathcal{B}_i^{\pi'}(Q^2, s_1, s_2)$ factors (which can in turn be used to generate the $j_i^{\pi'\mu}$ extended form factors via Equation 5.30):

$$\begin{aligned}
\mathcal{B}_1^{\pi'} &= \frac{1}{m_\rho^4} \left(s_1(s_2 - s_3) B_\rho^1(s_1) + s_2(s_1 - s_3) B_\rho^1(s_2) \right), \\
\mathcal{B}_2^{\pi'} &= \frac{1}{m_{\rho'}^4} \left(s_1(s_2 - s_3) B_{\rho'}^1(s_1) + s_2(s_1 - s_3) B_{\rho'}^1(s_2) \right), \\
\mathcal{B}_3^{\pi'} &= \frac{1}{m_\sigma^4} \left(s_1 B_\sigma^0(s_1) + s_2 B_\sigma^0(s_2) \right).
\end{aligned} \tag{5.35}$$

For convenience, this modification will be termed *model variation 1*.

The second variation introduces scalar factors induced by off-mass shell contributions from the axial vector resonances modeled in F_1 and F_2 . These contributions arise when one considers, in the chiral limit, corrections due to the finite quark masses (i.e., considering the generalized rather than the strict chiral limit of vanishing quark masses) [58]. For the modeled hadronic current given earlier to reduce to the generalized chiral limit, two changes must be made to the extended form factor models: The format of $T^{\mu\nu}$ used in Equation 5.18 (or Equation 5.30) must be changed as follows:

$$T'^{\mu\nu} = g^{\mu\nu} - \frac{(m_{a_1}^2 - m_\pi^2) Q^\mu Q^\nu}{(Q^2 - m_\pi^2) m_{a_1}^2}. \quad (5.36)$$

An additional non-resonant contribution must also be added to the hadronic current, controlled by a new fit parameter, β^{non} . This makes the final form of the hadronic current as follows for this model:

$$J^\mu(\mathbf{q}_1, \mathbf{q}_2, \mathbf{q}_3) = B_{a_1}(Q^2) \sum_{i=1}^{N_{\text{sub}}^{a_1}} \beta_i^{a_1} j_i'^{a_1\mu} + B_{\pi'}(Q^2) \sum_{i=1}^{N_{\text{sub}}^{\pi'}} \beta_i^{\pi'} j_i^{\pi'\mu} + \beta^{\text{non}} \frac{C_1 m_\pi^2}{(Q^2 - m_\pi^2)} Q^\mu, \quad (5.37)$$

where the $j_i'^{a_1\mu}$ notations indicate the modification $T^{\mu\nu} \rightarrow T'^{\mu\nu}$ of their definitions in Equations 5.18 and 5.30. Note that in the strict chiral limit where $m_\pi \rightarrow 0$, this modification obviously reverts back to the original form.

Deriving the equivalent of these changes in the reduced form factor formalism reveals two sources of induced scalar contributions. To demonstrate this, the hadronic current above is first written in terms of the \mathcal{B}_i^X functions (using Equa-

tion 5.30):

$$\begin{aligned}
J^\mu(\mathbf{q}_1, \mathbf{q}_2, \mathbf{q}_3) = & \\
& C_1 B_{a_1}(Q^2) \sum_{i=1}^{N_{\text{sub}}^{a_1}} \beta_i^{a_1} T'^{\mu\nu} \left[p_{1\nu} \mathcal{B}_i^{a_1}(Q^2, s_1, s_2) - p_{2\nu} \mathcal{B}_i^{a_1}(Q^2, s_2, s_1) \right] \\
& + C_1 B_{a_1}(Q^2) \sum_{i=1}^{N_{\text{sub}}^{a_1}} \beta_i^{a_1} T'^{\mu\nu} Q_\nu \mathcal{B}'_i{}^{a_1}(Q^2, s_1, s_2) \\
& + C_4 B_{\pi'}(Q^2) \sum_{i=1}^{N_{\text{sub}}^{\pi'}} \beta_i^{\pi'} Q^\mu \mathcal{B}_i^{\pi'}(Q^2, s_1, s_2) + \beta^{\text{non}} \frac{C_1 m_\pi^2}{(Q^2 - m_\pi^2)} Q^\mu.
\end{aligned} \tag{5.38}$$

To equate this with the hadronic current derived from the reduced form factors (Equation 5.28) two induced scalar factors will be added to the latter:

$$\begin{aligned}
J^\mu(\mathbf{q}_1, \mathbf{q}_2, \mathbf{q}_3) = & \\
& C_1 B_{a_1}(Q^2) \sum_{i=1}^{N_{\text{sub}}^{a_1}} \beta_i^{a_1} T^{\mu\nu} \left[p_{1\nu} \mathcal{B}_i^{a_1}(Q^2, s_1, s_2) - p_{2\nu} \mathcal{B}_i^{a_1}(Q^2, s_2, s_1) \right] \\
& + C_4 B_{\pi'}(Q^2) \sum_{i=1}^{N_{\text{sub}}^{\pi'}} \beta_i^{\pi'} Q^\mu \mathcal{B}_i^{\pi'}(Q^2, s_1, s_2) + F'_S Q^\mu + F''_S Q^\mu.
\end{aligned} \tag{5.39}$$

The differences between Equations 5.38 and 5.39 are thus accounted for in F'_S and F''_S . The F'_S contribution is assigned to account for differences produced from the model format itself. With the modification of $T^{\mu\nu} \rightarrow T'^{\mu\nu}$, the previously irrelevant $\mathcal{B}'_i{}^{a_1}$ factors no longer vanish since

$$T'^{\mu\nu} Q_\nu = \left(1 - \frac{(m_{a_1}^2 - m_\pi^2) Q^2}{(Q^2 - m_\pi^2) m_{a_1}^2} \right) Q^\mu = \frac{m_\pi^2 (Q^2 - m_{a_1}^2)}{m_{a_1}^2 (Q^2 - m_\pi^2)} Q^\mu \neq 0. \tag{5.40}$$

Those factors must thus be explicitly included in the reduced form factor models; therefore, F'_S is defined accordingly:

$$F'_S = C_1 \left[\frac{m_\pi^2 (Q^2 - m_{a_1}^2)}{m_{a_1}^2 (Q^2 - m_\pi^2)} \right] B_{a_1}(Q^2) \sum_{i=1}^{N_{\text{sub}}^{a_1}} \beta_i^{a_1} \mathcal{B}'_i{}^{a_1}(Q^2, s_1, s_2). \tag{5.41}$$

The second scalar contribution comes explicitly from the $T^{\mu\nu} \rightarrow T'^{\mu\nu}$ modification and the addition of the non-resonance term. That is, the additional difference between Equations 5.38 and 5.39 (not accounted for by F'_S) is found to be such that:

$$\begin{aligned}
F''_S Q^\mu &= \\
&C_1 B_{a_1}(Q^2) \sum_{i=1}^{N_{\text{sub}}^{a_1}} \beta_i^{a_1} \left[p_{1\nu} \mathcal{B}_i^{a_1}(Q^2, s_1, s_2) - p_{2\nu} \mathcal{B}_i^{a_1}(Q^2, s_2, s_1) \right] (T'^{\mu\nu} - T^{\mu\nu}) \\
&+ \beta^{\text{non}} \frac{C_1 m_\pi^2}{(Q^2 - m_\pi^2)} Q^\mu.
\end{aligned} \tag{5.42}$$

It is then possible to show that F''_S simplifies to

$$\begin{aligned}
F''_S &= C_1 \frac{m_\pi^2}{Q^2 - m_\pi^2} \left\{ \frac{Q^2 - m_{a_1}^2}{m_{a_1}^2 Q^2} B_{a_1}(Q^2) \right. \\
&\quad \left. \times \sum_{i=1}^{N_{\text{sub}}^{a_1}} \beta_i^{a_1} \left[\frac{s_3 - s_2}{2} \mathcal{B}_i^{a_1}(Q^2, s_1, s_2) - \frac{s_3 - s_1}{2} \mathcal{B}_i^{a_1}(Q^2, s_2, s_1) \right] + \beta^{\text{non}} \right\}.
\end{aligned} \tag{5.43}$$

These two induced scalar contributions are added to the overall model of F_4 such that

$$F_4(Q^2, s_1, s_2) = C_4 B_{\pi'}(Q^2) \sum_{i=1}^{N_{\text{sub}}^{\pi'}} \beta_i^{\pi'} \mathcal{B}_i^{\pi'}(Q^2, s_1, s_2) + F'_S + F''_S. \tag{5.44}$$

If this variation provides a more accurate model, then the induced scalar components must be taken into account to gain a full understanding of the actual pseudoscalar contributions. For convenience, this modification of the model will be termed *model variation 2*.

5.6 Final Form of the Differential Decay Rate

It is convenient to combine factors in the hadronic current as follows:

$$\begin{aligned}
 J^\mu(\mathbf{q}_1, \mathbf{q}_2, \mathbf{q}_3) &= B_{a_1}(Q^2) \sum_{i=1}^{N_{\text{sub}}^{a_1}} \beta_i^{a_1} j_i^{a_1\mu} + B_{\pi'}(Q^2) \sum_{i=1}^{N_{\text{sub}}^{\pi'}} \beta_i^{\pi'} j_i^{\pi'\mu} \\
 &= \sum_{i=1}^{N_{\text{sub}}} \beta_i \mathcal{J}_i^\mu,
 \end{aligned} \tag{5.45}$$

where the sum is now over both the a_1 and π' amplitudes while the β_i factors incorporate all the $\beta_i^{a_1}$ and $\beta_i^{\pi'}$ factors and the \mathcal{J}_i^μ functions incorporate all the $B_{a_1}(Q^2)j_i^{a_1\mu}$ and $B_{\pi'}(Q^2)j_i^{\pi'\mu}$ functions. Note that in the case of model variation 2, the sum would also include the non-resonance contribution introduced by that model and its corresponding β^{non}

The differential decay rate can then be conveniently written as

$$\begin{aligned}
 d\Gamma_{\tau^\pm \rightarrow [3\pi]^\pm (\bar{\nu}_\tau/\nu_\tau)} &= \frac{G_F^2 V_{ud}^2}{4m_\tau} \{L_{\mu\nu} J^\mu (J^\nu)^\dagger\} dPS^{(4)} \\
 &= \frac{G_F^2 V_{ud}^2}{4m_\tau} \left\{ \sum_{jk} \beta_j \beta_k^* \times \mathcal{J}_j^\mu (\mathcal{J}_k^\nu)^\dagger L_{\mu\nu} \right\} dPS^{(4)} \\
 &= \sum_i a_i g_i(\vec{x}) \times dPS^{(4)},
 \end{aligned} \tag{5.46}$$

where one now has a sum of factors (a_i , which incorporate all combinations of $\beta_j \beta_k^*$) multiplied by functions ($g_i(\vec{x})$, which incorporate all the corresponding combinations of $\frac{G_F^2 V_{ud}^2}{4m_\tau} \mathcal{J}_j^\mu (\mathcal{J}_k^\nu)^\dagger L_{\mu\nu}$, and in which \vec{x} represents all kinematic variables needed to describe the decay). The g_i functions are derived from accepted theory and the models used in the form factors, while the a_i coefficients are derived from the ten β_j complex coupling constants.

6. FITTING METHOD

Everything needed to model the decay has been defined except for the ten unknown complex coupling constants, $\beta_i \in \{\beta_{1-7}^{a_1}, \beta_{1-3}^{\pi'}\}$. This section focuses on the unbinned maximum likelihood fit used to extract those parameters.

Note that a normalized distribution function can be defined from Equation 5.46 as follows:

$$\frac{d\Gamma}{d\vec{x}}(\vec{x}|\vec{a}) = \sum_i a_i g_i(\vec{x}) \frac{dPS^{(4)}}{d\vec{x}}, \quad (6.1)$$

such that

$$p(\vec{x}|\vec{a}) = \frac{\sum_i a_i g_i(\vec{x}) dPS^{(4)} / d\vec{x}}{\sum_i a_i \int g_i(\vec{x}) dPS^{(4)}}. \quad (6.2)$$

Using this probability distribution function (*pdf*) a maximum likelihood fitting method can be developed to extract the a_i parameters to within an overall constant (the basic method is developed in Section 6.3). One thus defines $a_1 = \beta_1 \beta_1^* \equiv 1$ (or $\beta_1 \equiv 1$), and the other parameters are defined with respect to a_1 (β_1). Further, Equation 6.2 depends on the true kinematic description of the decay (\vec{x}), and one must provide a distribution function that depends on the measured kinematic variables one has access to (\vec{x}'). Finally, the fit must be corrected for the presence of background in the sample.

6.1 Defining the True Kinematic Variables, \vec{x}

In the absence of radiative effects within the decay itself, one can give a complete kinematic description of a given $\tau^\pm \rightarrow \pi^\pm \pi^\pm \pi^\mp (\bar{\nu}_\tau/\nu_\tau)$ decay in the lab frame by specifying the 3-momentum of each pion (\vec{q}_i) and the 3-momentum of the τ (or the ν_τ) along with the particle masses: m_τ , m_π , and m_{ν_τ} (assumed to be zero). The τ momentum can be specified by its orientation with respect to the momentum of the 3π system ($\theta_\tau^{3\pi}$, $\phi_\tau^{3\pi}$) along with its magnitude. Its magnitude can be calculated from the energy of the τ , E_τ , which in turn can be derived from the beam energy (E_{beam}) minus the energy lost in initial state radiation, E_γ . Further, using energy and momentum conservation laws, the polar angle $\theta_\tau^{3\pi}$ can be calculated from the pion momenta and the energy of the τ . This leaves the following list of information (along with knowledge of the particle masses) needed to give a complete kinematic description of a given decay in the lab frame: $\vec{x} = (\vec{q}_1, \vec{q}_2, \vec{q}_3, E_{\text{beam}}, E_\gamma, \phi_\tau^{3\pi})$.

Measurements supply the 3-momenta of the pions to within measurement error and the beam energy gives the energy of the τ assuming no radiative energy loss. This leaves the following information that cannot be specified by the measurements, yet which are needed to completely describe a given decay:

1. The azimuthal orientation of the τ momentum with respect to the momentum vector of the 3π system, $\phi_\tau^{3\pi}$.
2. Effects on the true τ energy due to initial state radiation (ISR).

3. Corrections due to measurement uncertainties (e.g., acceptance, scattering, detector resolution, error in E_{beam} , and radiation effects other than ISR).

Again, in addition to correcting for the unmeasured information, the fit must also correct for the presence of background in the data sample.

6.2 Correcting for Unmeasured Information

In general, given a set of variables that truly describe a decay, \vec{x} , and the set of measured variables, $\vec{x}' = (\vec{q}'_1, \vec{q}'_2, \vec{q}'_3, E'_{\text{beam}})$, there is a probability distribution, $\rho(\vec{x}'|\vec{x})$, which provides the probability of measuring \vec{x}' given that the decay was generated at \vec{x} . Note that the form of ρ depends on physical properties and limitations of the detector and not on the form of the differential decay rate (i.e., it is independent of the fit parameters, β_i , and thus is independent of $\vec{a} = (\beta_1\beta_1^*, \beta_1\beta_2^*, \dots, \beta_2\beta_1^*, \beta_2\beta_2^*, \dots, \beta_{10}\beta_{10}^*)$). Therefore, using Bayesian statistics one can produce a differential decay rate in terms of the measured variables:

$$\frac{d\Gamma'}{d\vec{x}'}(\vec{x}'|\vec{a}) = \int \rho(\vec{x}'|\vec{x}) \frac{d\Gamma}{d\vec{x}}(\vec{x}|\vec{a}) d\vec{x}. \quad (6.3)$$

That equation effectively integrates over the information that is not measure, and ρ provides the distribution of the unmeasured information. In this analysis, ρ consists of four separate factors, each of which can be calculated from Monte Carlo studies and/or approximated measurement errors. First, the distribution of the unmeasured $\phi_\tau^{3\pi}$ (recall that this is the azimuthal orientation of the τ with respect to the 3π system) will not be uniform due to the τ -pair production dynamics. One thus includes a probability distribution, $\mathcal{P}_{\phi_\tau^{3\pi}}(\vec{x})$, to adjust for that effect. Note

that $\mathcal{P}_{\phi_{\tau}^{3\pi}}$ depends on the direction of the τ produced, which can be derived from the full kinematic description, \vec{x} . Second, one must include a factor to describe the probability distribution of the unmeasured E_{γ} (the energy of the possible ISR photon), $f(E_{\gamma})$. Third, one includes an acceptance factor for the given measured event, $\alpha(\vec{x}')$. Finally, one must include the probability of finding the measured momenta and beam energy given their generated values, $\sigma(\vec{x}'|\vec{x})$. Thus, one finds that

$$\rho(\vec{x}'|\vec{x}) = \alpha(\vec{x}') \times \mathcal{P}_{\phi_{\tau}^{3\pi}}(\vec{x}) \times f(E_{\gamma}) \times \sigma(\vec{x}'|\vec{x}), \quad (6.4)$$

such that

$$\frac{d\Gamma'}{d\vec{x}'}(\vec{x}'|\vec{a}) = \alpha(\vec{x}') \int \mathcal{P}_{\phi_{\tau}^{3\pi}}(\vec{x}) f(E_{\gamma}) \sigma(\vec{x}'|\vec{x}) \frac{d\Gamma}{d\vec{x}}(\vec{x}|\vec{a}) d\vec{x}. \quad (6.5)$$

It should be noted that because Equation 6.5 concerns events that have been detected and measured (at \vec{x}'), the acceptance is a function of the measured variables alone (and thus has been taken out of the integration). In a maximum likelihood fit, such a factor in the numerator of the probability distribution does not affect the fit. It is, however, important in the normalization, which integrates over $d\vec{x}'$. For this analysis, the normalization was calculated using skimmed Monte Carlo data, thus accounting for the acceptance.

It is useful to utilize the form of the differential decay rate from Equation 6.1 to rewrite Equation 6.3 as follows:

$$\begin{aligned} \frac{d\Gamma'}{d\vec{x}'}(\vec{x}'|\vec{a}) &= \sum_i a_i \left\{ \int \rho(\vec{x}'|\vec{x}) g_i(\vec{x}) \frac{dPS^{(4)}}{d\vec{x}} d\vec{x} \right\} \\ &= \sum_i a_i \mathcal{G}_i(\vec{x}'), \end{aligned} \quad (6.6)$$

where

$$\mathcal{G}_i(\vec{x}') = \int \rho(\vec{x}'|\vec{x})g_i(\vec{x})\frac{dPS^{(4)}}{d\vec{x}}d\vec{x}. \quad (6.7)$$

The proper distribution function can now be defined:

$$p'(\vec{x}'|\vec{a}) = \frac{d\Gamma'(\vec{x}'|\vec{a})/d\vec{x}'}{\int d\Gamma'(\vec{x}'|\vec{a})} \quad (6.8)$$

$$= \frac{\sum_i a_i \mathcal{G}_i(\vec{x}')}{\sum_i a_i \int \mathcal{G}_i(\vec{x}')d\vec{x}'}. \quad (6.9)$$

To calculate the integrals (one for each value of i) in Equation 6.7 a numeric integration is performed using an average value method: for a given event measured at \vec{x}' , a number of possible generated variables \vec{x} are randomly selected and used to calculate a series of values for $\rho(\vec{x}'|\vec{x})g_i(\vec{x})\frac{dPS^{(4)}}{d\vec{x}}$. The average of this series and the phase space volume over which they were selected are used to calculate the integral. In some cases, a randomly selected set of possible generated variables, \vec{x} , is not kinematically allowed to be a $\tau^\pm \rightarrow \pi^\pm \pi^\pm \pi^\mp (\bar{\nu}_\tau/\nu_\tau)$ event. The selection is ignored, and if this is the case for all the random selections for a given event, the event is thrown out as likely being background. That requirement removes just over 3,000 events from the fit sample (roughly 2% of the original), leaving 145,000 events in the fit.

This procedure provides a correction for the unmeasured information and leaves one with a distribution function for the measured data given \vec{a} ($p'(\vec{x}'|\vec{a})$).

6.3 Correcting for Background

Properly correcting for the presence of background events in the data sample posed a significant challenge for this analysis. The large number of kinematic dimensions significant to the fit tends to prohibit the use of a binned background subtraction method, and while the probability distribution function (*pdf*) for the signal distribution is well understood, the variety of background types (see Table 4.2) makes it difficult to include analytic functions in the fit that would model the background in the given kinematic space. The analysis utilizes Monte Carlo samples of the τ background to subtract the effects of the background in the unbinned maximum likelihood fit. The process is described here.

6.3.1 An Accepted Technique that Falls Short

If binning were acceptable, the distribution of the signal in the data could be approximated by subtracting the background contributions on a bin-by-bin basis. The number of signal events in the i th bin would then be approximated as follows:

$$Y_i^s \approx \mathcal{Y}_i^s = Y_i - \mathcal{Y}_i^b, \quad (6.10)$$

where Y_i is the actual number of data events in the bin and \mathcal{Y}_i^b is the approximated number of background events in the bin found from a properly scaled background sample. Given this approximated distribution of the signal in the data, one could calculate the likelihood that it is described by the signal *pdf* (for a given set of parameters, \vec{a}) by using a standard binned likelihood, which will now be developed.

The average number of signal events expected in the i th bin located at \vec{x}_i and with bin size $\Delta^n x$ can be written as

$$\mu_i^s = N_s p(\vec{x}_i|\vec{a}) \Delta^n x, \quad (6.11)$$

where N_s is the total number of signal events expected in the data and the *pdf* function, $p(\vec{x}|\vec{a})$, is normalized. From Poisson statistics, one finds the probability that Y_i^s events would be found in the i th bin:

$$\text{Prob}(Y_i^s|\mu_i^s) = \frac{(\mu_i^s)^{Y_i^s} e^{-\mu_i^s}}{Y_i^s!}. \quad (6.12)$$

The likelihood that the binned distribution of signal events in the data is described by the signal *pdf* is, then, proportional to the product of the above probability over all bins [65]:

$$\mathcal{L}_\Delta^s \propto \prod_{i=1}^{N_\Delta} \frac{(\mu_i^s)^{Y_i^s} e^{-\mu_i^s}}{Y_i^s!}, \quad (6.13)$$

where N_Δ is the number of bins. Taking the logarithm of this signal likelihood (and then expanding the expression for μ_i^s) one finds

$$\begin{aligned} \ln \mathcal{L}_\Delta^s &= \sum_{i=1}^{N_\Delta} \left\{ Y_i^s \ln(\mu_i^s) - \mu_i^s - \ln Y_i^s! \right\} \\ &= \sum_{i=1}^{N_\Delta} \left\{ Y_i^s \ln[p(\vec{x}_i|\vec{a})] + Y_i^s \ln[N_s] + Y_i^s \ln[\Delta^n x] \right. \\ &\quad \left. - N_s p(\vec{x}_i|\vec{a}) \Delta^n x - \ln[Y_i^s!] \right\} \\ &= \sum_{i=1}^{N_\Delta} \left\{ Y_i^s \ln[p(\vec{x}_i|\vec{a})] \right\} + N_s \ln[N_s] + N_s \ln[\Delta^n x] \\ &\quad - N_s \underbrace{\sum_{i=1}^{N_\Delta} p(\vec{x}_i|\vec{a}) \Delta^n x}_{\approx 1} - \sum_{i=1}^{N_\Delta} \ln[Y_i^s!]. \end{aligned} \quad (6.14)$$

Note that the fourth term given in the final equation involves a numerical integral of the (normalized) *pdf*. Its varying with respect to \vec{a} is expected to be insignificant. Therefore all terms but the first contribute constant values to the signal log-likelihood (independent of the parameters, \vec{a}) and thus are irrelevant in a maximum log-likelihood fit. Note too that bins without signal events (where $Y_i^s = 0$) do not contribute to the first term. Thus, the information contained in empty bins does not produce a useful contribution to the signal log-likelihood. One can write the simplified signal log-likelihood as

$$\ln \mathcal{L}'_{\Delta} = \sum_{i=1}^{N_{\Delta}} Y_i^s \ln[p(\vec{x}_i|\vec{a})]. \quad (6.15)$$

As mentioned above, the number of signal events in a given bin is estimated using the data and a background sample as in Equation 6.10. One thus approximates the signal log-likelihood as follows

$$\begin{aligned} \ln \mathcal{L}'_{\Delta} &\approx \sum_{i=1}^{N_{\Delta}} \mathcal{Y}_i^s \ln p(\vec{x}_i|\vec{a}) \\ &= \sum_{i=1}^{N_{\Delta}} \{Y_i \ln p(\vec{x}_i|\vec{a}) - \mathcal{Y}_i^b \ln p(\vec{x}_i|\vec{a})\}. \end{aligned} \quad (6.16)$$

Interpreting Equation 6.16, the log-likelihood that the signal in the data is described by the signal *pdf* involves a bin-by-bin contribution from the probability that the signal *pdf* describes the entire distribution of the data (signal and background: $Y_i \ln p(\vec{x}_i|\vec{a})$) minus the part of that contribution that was erroneously added due to the presence of background (as estimated from the background sample: $\mathcal{Y}_i^b \ln p(\vec{x}_i|\vec{a})$).

This is an accepted binned background subtraction method; however, since it requires binning, it doesn't quite fit the need of this analysis as noted earlier.

6.3.2 Expanding that Technique to the Unbinned Case

To expand the above binned method to an unbinned method, one lets the bin sizes in the technique become minute such that each bin contains no more than one event (either from data or from the background sample). This is analogous to the usual adaptation of a binned likelihood method to an unbinned method. In the infinitesimal bin limit where N_d is the number of data events and N_b is the number of events in the background sample, the signal log-likelihood in Equation 6.16 involves N_d bins in which $Y_i = 1$ and $\mathcal{Y}_i^b = 0$; N_b bins in which $Y_i = 0$ and $\mathcal{Y}_i^b = 1$; and some other number of bins in which $Y_i = \mathcal{Y}_i^b = 0$. As noted earlier, the empty bins do not produce useful contributions to the overall likelihood. Applying this to Equation 6.16 one finds that in the infinitesimal bin limit, the (now unbinned) signal log-likelihood can be written as follows:

$$\ln \mathcal{L}^s = \sum_{i=1}^{N_d} \ln p(\vec{x}_i | \vec{a}) - \sum_{i=1}^{N_b} \ln p(\vec{x}_i | \vec{a}), \quad (6.17)$$

where the summations are over all the events in the data set and all the events in the background sample set such that \vec{x}_i is the position of the i th event in each respective set.

Again there is a clear interpretation. The first summation calculates the log-likelihood that the signal distribution function describes the entire data distribution (including background). Obviously one does not want to maximize that log-

likelihood because it erroneously includes contributions from background events being described by the signal *pdf*. However, the second summation (subtracted from the first) uses the given background sample to calculate the total result of those erroneous contributions. Subtracting this from the first summation corrects for the presence of background in the data, producing the signal log-likelihood to be maximized.

6.3.3 Summary of Background Correction Method

A non-binning method is utilized for performing a maximum likelihood fit on data while using a sample of background to correct for the presence of background in the data. First one calculates the unbinned log-likelihood that the theoretical *pdf* for the signal alone describes the distribution of the data (which contains both signal and background). This log-likelihood is obviously erroneous because it has assumed that the background can be described using the signal *pdf*. However, using an acceptable distribution of background events, one can approximate the erroneous contribution to the unbinned log-likelihood and subtract it. This leaves the log of the likelihood that the signal alone in the data is described by the signal distribution function (Equation 6.17). Maximizing that likelihood thus produces a proper fit of the signal *pdf* to the signal information in the data. It is accomplished without binning, and the background correction comes not from knowing the analytical background distribution function, but rather by obtaining and utilizing an acceptable sample of background events from Monte Carlo.

6.4 Goodness of Fit

The goodness of fit calculations reported by the analysis were generated using a relatively standard technique: Consider a large group of data sets, each containing N events distributed via $p(\vec{x}|\vec{a})$, where \vec{a} was produced by a given fit. Let $\langle \ln p(\vec{x}|\vec{a}) \rangle$ be the average log of the *pdf* expected over the phase-space, and $\langle [\Delta \ln p(\vec{x}|\vec{a})]^2 \rangle$ be the expected variance of $\ln p(\vec{x}|\vec{a})$. The central limit theorem implies that as $N \rightarrow \infty$, the values of the log-likelihood calculated for each data set ($\ln \mathcal{L}_i$) will be distributed as a Gaussian with mean $\langle \ln \mathcal{L} \rangle = N \langle \ln p(\vec{x}|\vec{a}) \rangle$ and variance $[\Delta \ln \mathcal{L}]^2 = N \langle [\Delta \ln p(\vec{x}|\vec{a})]^2 \rangle$.

In practice, a relatively large, previously generated set of Monte Carlo events is used to find $\langle \ln p(\vec{x}|\vec{a}) \rangle$ and $\langle [\Delta \ln p(\vec{x}|\vec{a})]^2 \rangle$ by calculating weighted averages of $\ln p(\vec{x}_i|\vec{a})$ and $[\ln p(\vec{x}_i|\vec{a})]^2$ over the set. The weights are computed given the known distribution of the Monte Carlo set, $w_i = 1/p(\vec{x}_i|\vec{a}_0)$ (in effect, re-weighting the set to a “flat” distribution that can be used to calculate proper averages).

The maximum log-likelihood found for the given fit can then be compared to the expected value given the variance. The difference can be expressed in terms of the number of σ separating the two log-likelihood values. This goodness of fit method thus involves a comparison between the event-by-event log-likelihood distribution of the data being fitted and that of a Monte Carlo sample re-weighted to represent the fit results. To demonstrate this comparison, two plots are provided below. Figure 6.1(a) displays the results from an acceptable fit with a reported g.o.f. value of $\sim 0.6\sigma$ (using the method given above). Figure 6.1(b) shows the

results from a poor fit with a reported g.o.f. value of $\sim 9.0\sigma$. The good agreement between data and Monte Carlo shown in the first plot and the poor agreement in the second plot attest to the g.o.f. values reported.

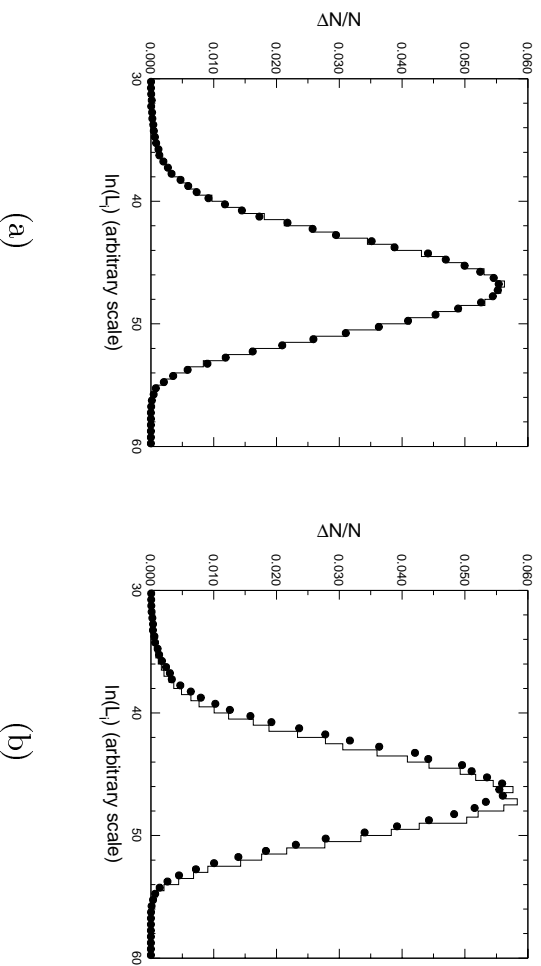


Figure 6.1

Demonstrations of the goodness of fit method by comparing log-likelihood distributions for data (represented by points) and Monte Carlo (represented by the solid histograms). Figure (a) displays such results for a fit with g.o.f. $\sim 0.6\sigma$, while (b) displays such results for a poor fit with g.o.f. $\sim 9.0\sigma$. The fits used for these plots were (a) the nominal fit to the data and (b) a fit without isoscalar resonances. Both fits are discussed below.

This method of deriving goodness of fit information is mainly limited by Monte Carlo statistics in conjunction with the accuracy with which the re-weighting of the Monte Carlo represents the actual distribution suggested by the given fit. The results are useful for ruling out fit results at, for examples, 90% (g.o.f. $> 1.65\sigma$) and 95% (g.o.f. $> 2.0\sigma$) confidence levels.

7. MONTE CARLO TESTS OF THE FIT

The fitting method was tested using full Monte Carlo data, including CLEO event reconstruction and background data processed by the skimming code. Two separate sets of Monte Carlo were used in the tests. The first was produced using the nominal model with β_i parameters motivated by the results of the $\tau^\pm \rightarrow \pi^\pm \pi^0 \pi^0 (\bar{\nu}_\tau / \nu_\tau)$ substructure fit presented in [60]. However, a small pseudoscalar contribution has also been included for this test fit. The results of this test are shown in Table 7.1. Parameters returned by the fit agree with the expected parameters within reasonable errors. The goodness of fit test for this fit indicated that the maximum log-likelihood was within 0.2σ of the expected value. Also shown are the significances of each sub-resonance found by evaluating the fit with that sub-resonance removed. Each sub-resonance seems to be reasonably significant to the fit, as expected.

The second test fit presented here was performed on Monte Carlo produced using the nominal model with β_i parameters motivated by the results of the real data fit presented below. Again, the fit produced results consistent with the generating parameters within the given statistical errors. The maximum log-likelihood found

by the fit was within 0.6σ of the expected, indicating a suitable goodness of fit; and again each sub-resonance seemed to be reasonably significant to the fit.

Table 7.1
Results of a first test fit to Monte Carlo data.

resonance		signif.		fit	expected	fit error
$a_1 \rightarrow \rho\pi$	s -wave	—	$\Re\beta_i :$	1	—	—
			$\Im\beta_i :$	0	—	—
$a_1 \rightarrow \rho'\pi$	s -wave	2.7σ	$\Re\beta_i :$	-0.118 ± 0.026	-0.120	0.08σ
			$\Im\beta_i :$	-0.027 ± 0.023	0.004	-1.35σ
$a_1 \rightarrow \rho\pi$	d -wave	5.7σ	$\Re\beta_i :$	0.352 ± 0.029	0.330	0.76σ
			$\Im\beta_i :$	-0.133 ± 0.045	-0.168	0.78σ
$a_1 \rightarrow \rho'\pi$	d -wave	3.6σ	$\Re\beta_i :$	-0.162 ± 0.141	-0.082	-0.57σ
			$\Im\beta_i :$	0.864 ± 0.103	0.866	-0.02σ
$a_1 \rightarrow f_2\pi$	p -wave	2.4σ	$\Re\beta_i :$	-0.057 ± 0.073	-0.133	1.04σ
			$\Im\beta_i :$	0.645 ± 0.062	0.697	-0.84σ
$a_1 \rightarrow \sigma\pi$	p -wave	7.8σ	$\Re\beta_i :$	1.551 ± 0.052	1.575	-0.46σ
			$\Im\beta_i :$	1.440 ± 0.055	1.389	0.93σ
$a_1 \rightarrow f_0\pi$	p -wave	2.4σ	$\Re\beta_i :$	-0.055 ± 0.044	-0.097	0.95σ
			$\Im\beta_i :$	-0.733 ± 0.038	-0.764	0.82σ
$\pi' \rightarrow \rho\pi$	p -wave	2.4σ	$\Re\beta_i :$	0.013 ± 0.002	0.012	0.50σ
			$\Im\beta_i :$	-0.002 ± 0.001	0.000	-2.00σ
$\pi' \rightarrow \rho'\pi$	p -wave	2.6σ	$\Re\beta_i :$	-0.010 ± 0.008	-0.002	-1.00σ
			$\Im\beta_i :$	-0.006 ± 0.010	0.000	-0.60σ
$\pi' \rightarrow \sigma\pi$	s -wave	2.5σ	$\Re\beta_i :$	0.008 ± 0.003	0.010	-0.67σ
			$\Im\beta_i :$	0.001 ± 0.002	0.000	0.50σ

Table 7.2
Results of second test fit to Monte Carlo data

resonance		signif.		fit	expected	fit error
$a_1 \rightarrow \rho\pi$	s -wave	—	$\Re\beta_i$:	1	—	—
			$\Im\beta_i$:	0	—	—
$a_1 \rightarrow \rho'\pi$	s -wave	1.9σ	$\Re\beta_i$:	0.041 ± 0.016	0.051	-0.62σ
			$\Im\beta_i$:	-0.221 ± 0.020	-0.248	1.35σ
$a_1 \rightarrow \rho\pi$	d -wave	2.5σ	$\Re\beta_i$:	0.624 ± 0.019	0.608	0.84σ
			$\Im\beta_i$:	0.310 ± 0.033	0.354	-1.33σ
$a_1 \rightarrow \rho'\pi$	d -wave	2.8σ	$\Re\beta_i$:	-1.674 ± 0.092	-1.598	-0.83σ
			$\Im\beta_i$:	-1.336 ± 0.099	-1.213	-1.24σ
$a_1 \rightarrow f_2\pi$	p -wave	2.6σ	$\Re\beta_i$:	-0.054 ± 0.074	-0.118	0.86σ
			$\Im\beta_i$:	1.057 ± 0.082	0.961	1.17σ
$a_1 \rightarrow \sigma\pi$	p -wave	6.7σ	$\Re\beta_i$:	2.077 ± 0.095	1.986	0.96σ
			$\Im\beta_i$:	2.802 ± 0.098	2.700	1.04σ
$a_1 \rightarrow f_0\pi$	p -wave	2.2σ	$\Re\beta_i$:	-0.096 ± 0.059	-0.041	-0.93σ
			$\Im\beta_i$:	-1.204 ± 0.057	-1.150	-0.95σ
$\pi' \rightarrow \rho\pi$	p -wave	1.9σ	$\Re\beta_i$:	0.003 ± 0.001	0.001	2.00σ
			$\Im\beta_i$:	-0.002 ± 0.001	-0.002	0.00σ
$\pi' \rightarrow \rho'\pi$	p -wave	2.1σ	$\Re\beta_i$:	-0.013 ± 0.007	-0.005	-1.14σ
			$\Im\beta_i$:	-0.012 ± 0.006	-0.014	0.33σ
$\pi' \rightarrow \sigma\pi$	s -wave	2.0σ	$\Re\beta_i$:	-0.003 ± 0.002	-0.005	1.00σ
			$\Im\beta_i$:	-0.010 ± 0.002	-0.008	-1.00σ

These Monte Carlo tests signify that the fitting method can return acceptable results, reasonably describing the fit data as expected.

8. FIT RESULTS AND ANALYSIS

The results of fits performed on the 145,000 data events are presented here along with a discussion of the systematic errors reported.

8.1 Presentation of Results

Table 8.1 summarizes the results of the fit to the nominal model described above. The maximum log-likelihood measured in the fit was 6,011,214, while Monte Carlo studies yield an expected value of $6,011,945 \pm 1,260$. The difference of 0.6σ indicates an acceptable goodness of fit. Also shown for each amplitude is its significance, found by repeating the fit with that amplitude excluded, and its background fraction, found from a numerical integration of the full $\tau^\pm \rightarrow \pi^\pm \pi^\pm \pi^\mp (\bar{\nu}_\tau / \nu_\tau)$ differential decay rate.

The results are graphically presented in four figures. Figure 8.1 compares the data to the fitted distributions of Q^2 , each of the Dalitz plot variables (s_1 and s_2), β , γ , $\cos\theta$, and $\cos\psi$ (see Appendix G for a description of the angular variables). Figure 8.2 compares the data to the fitted distributions of s_1 in bins of Q^2 , while Figure 8.3 displays the same plots for s_2 . Finally, Figure 8.4 shows the two dimensional distributions of the Dalitz plot variables within bins of Q^2 .

Table 8.1

Results of the fit to the nominal model. Statistical and systematic errors are shown respectively. The branching fractions are calculated from the squared amplitudes and are normalized to the total $\tau^\pm \rightarrow \pi^\pm \pi^\pm \pi^\mp (\bar{\nu}_\tau/\nu_\tau)$ rate. They do not sum to 100% due to interferences between the amplitudes.

Resonance	Signif.	$\Re\beta_i$	$\Im\beta_i$	\mathcal{B} Fraction (%)
$a_1 \rightarrow \rho\pi$	—	1	0	69.77
$a_1 \rightarrow \rho'\pi$	1.2 σ	0.05 \pm 0.02 \pm 0.02	-0.25 \pm 0.02 \pm 0.02	1.58 \pm 0.25 \pm 0.25
$a_1 \rightarrow \rho\pi$	4.1 σ	0.61 \pm 0.03 \pm 0.02	0.35 \pm 0.05 \pm 0.03	1.68 \pm 0.16 \pm 0.11
$a_1 \rightarrow \rho'\pi$	3.3 σ	-1.60 \pm 0.11 \pm 0.20	-1.21 \pm 0.10 \pm 0.08	2.77 \pm 0.29 \pm 0.45
$a_1 \rightarrow f_2\pi$	3.1 σ	-0.12 \pm 0.07 \pm 0.06	0.96 \pm 0.06 \pm 0.05	0.68 \pm 0.08 \pm 0.07
$a_1 \rightarrow \sigma\pi$	6.0 σ	1.99 \pm 0.06 \pm 0.10	2.70 \pm 0.06 \pm 0.10	48.40 \pm 1.61 \pm 2.91
$a_1 \rightarrow f_0\pi$	3.4 σ	-0.04 \pm 0.04 \pm 0.06	-1.15 \pm 0.04 \pm 0.03	11.51 \pm 0.72 \pm 0.66
$\pi' \rightarrow \rho\pi$	0.9 σ	0.001 \pm 0.002 \pm 0.002	-0.002 \pm 0.001 \pm 0.002	0.01 \pm 0.02 \pm 0.03
$\pi' \rightarrow \rho'\pi$	1.3 σ	-0.005 \pm 0.010 \pm 0.010	-0.013 \pm 0.009 \pm 0.004	0.02 \pm 0.03 \pm 0.01
$\pi' \rightarrow \sigma\pi$	1.2 σ	-0.005 \pm 0.003 \pm 0.002	-0.008 \pm 0.002 \pm 0.001	0.13 \pm 0.07 \pm 0.04

Table 8.2

Results of fit to model variation 1. Statistical and systematic errors are shown respectively. The branching fractions are calculated from the squared amplitudes and are normalized to the total $\tau^\pm \rightarrow \pi^\pm \pi^\pm \pi^\mp (\bar{\nu}_\tau / \nu_\tau)$ rate. They do not sum to 100% due to interferences between the amplitudes.

Resonance	Signif.	$\Re\beta_i$	$\Im\beta_i$	\mathcal{B} Fraction (%)
$a_1 \rightarrow \rho\pi$	—	1	0	69.46
$a_1 \rightarrow \rho'\pi$	1.4σ	$0.04 \pm 0.02 \pm 0.01$	$-0.27 \pm 0.02 \pm 0.02$	$1.78 \pm 0.25 \pm 0.27$
$a_1 \rightarrow \rho\pi$	4.0σ	$0.61 \pm 0.03 \pm 0.02$	$0.33 \pm 0.05 \pm 0.03$	$1.64 \pm 0.15 \pm 0.10$
$a_1 \rightarrow \rho'\pi$	3.5σ	$-1.59 \pm 0.08 \pm 0.16$	$-1.09 \pm 0.10 \pm 0.07$	$2.55 \pm 0.24 \pm 0.43$
$a_1 \rightarrow f_2\pi$	3.4σ	$-0.12 \pm 0.06 \pm 0.06$	$0.92 \pm 0.06 \pm 0.05$	$0.62 \pm 0.08 \pm 0.07$
$a_1 \rightarrow \sigma\pi$	6.3σ	$2.02 \pm 0.06 \pm 0.09$	$2.67 \pm 0.05 \pm 0.09$	$48.18 \pm 1.55 \pm 2.88$
$a_1 \rightarrow f_0\pi$	3.3σ	$-0.04 \pm 0.04 \pm 0.06$	$-1.14 \pm 0.03 \pm 0.03$	$11.22 \pm 0.59 \pm 0.65$
$\pi' \rightarrow \rho\pi$	1.0σ	$0.002 \pm 0.002 \pm 0.002$	$-0.002 \pm 0.001 \pm 0.002$	$0.02 \pm 0.03 \pm 0.03$
$\pi' \rightarrow \rho'\pi$	1.3σ	$-0.007 \pm 0.027 \pm 0.014$	$-0.022 \pm 0.024 \pm 0.009$	$0.01 \pm 0.01 \pm 0.00$
$\pi' \rightarrow \sigma\pi$	1.3σ	$-0.013 \pm 0.003 \pm 0.002$	$-0.011 \pm 0.003 \pm 0.002$	$0.24 \pm 0.09 \pm 0.04$

Table 8.3

Results of fit to model variation 2. Statistical and systematic errors are shown respectively. The branching fractions are calculated from the squared amplitudes and are normalized to the total $\tau^\pm \rightarrow \pi^\pm \pi^\pm \pi^\mp (\bar{\nu}_\tau / \nu_\tau)$ rate. They do not sum to 100% due to interferences between the amplitudes.

Resonance	Signif.	$\Re\beta_i$	$\Im\beta_i$	\mathcal{B} Fraction (%)
$a_1 \rightarrow \rho\pi$	—	1	0	74.73
$a_1 \rightarrow \rho'\pi$	1.4 σ	0.03 \pm 0.02 \pm 0.02	-0.21 \pm 0.01 \pm 0.02	1.14 \pm 0.14 \pm 0.25
$a_1 \rightarrow \rho\pi$	5.1 σ	0.56 \pm 0.02 \pm 0.01	0.42 \pm 0.04 \pm 0.04	1.80 \pm 0.16 \pm 0.14
$a_1 \rightarrow \rho'\pi$	3.0 σ	-1.04 \pm 0.09 \pm 0.20	-1.11 \pm 0.09 \pm 0.12	1.71 \pm 0.20 \pm 0.36
$a_1 \rightarrow f_2\pi$	2.3 σ	-0.30 \pm 0.05 \pm 0.08	0.93 \pm 0.05 \pm 0.07	0.76 \pm 0.08 \pm 0.12
$a_1 \rightarrow \sigma\pi$	9.2 σ	1.67 \pm 0.06 \pm 0.09	2.40 \pm 0.05 \pm 0.11	39.47 \pm 1.47 \pm 2.80
$a_1 \rightarrow f_0\pi$	2.2 σ	-0.16 \pm 0.02 \pm 0.04	-1.06 \pm 0.04 \pm 0.03	10.70 \pm 0.75 \pm 0.63
$\pi' \rightarrow \rho\pi$	1.3 σ	0.003 \pm 0.002 \pm 0.002	-0.006 \pm 0.001 \pm 0.001	0.18 \pm 0.07 \pm 0.08
$\pi' \rightarrow \rho'\pi$	1.7 σ	-0.036 \pm 0.009 \pm 0.015	0.008 \pm 0.008 \pm 0.005	0.15 \pm 0.07 \pm 0.12
$\pi' \rightarrow \sigma\pi$	1.4 σ	-0.021 \pm 0.003 \pm 0.002	-0.003 \pm 0.002 \pm 0.003	0.77 \pm 0.19 \pm 0.18
Non-Resonance	1.6 σ	-10.44 \pm 0.95 \pm 1.26	-5.17 \pm 0.92 \pm 0.98	0.87 \pm 0.14 \pm 0.18

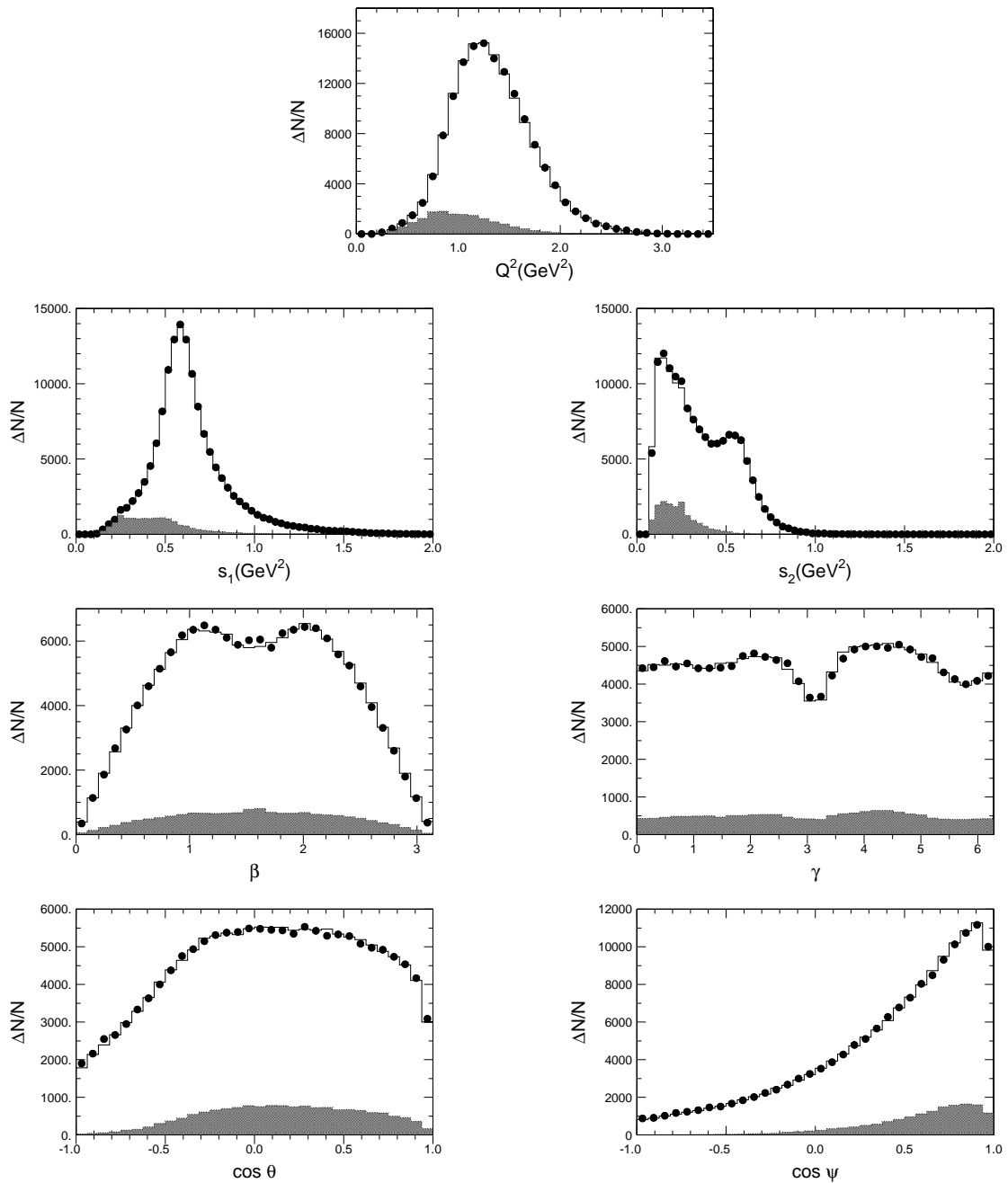


Figure 8.1

Display of nominal fit results in projections of Q^2 , s_1 , s_2 , β , γ , $\cos \theta$, and $\cos \psi$ (see Appendix G). The points represent the data, while the solid histograms show the fit results, and the shaded regions display the background distributions.

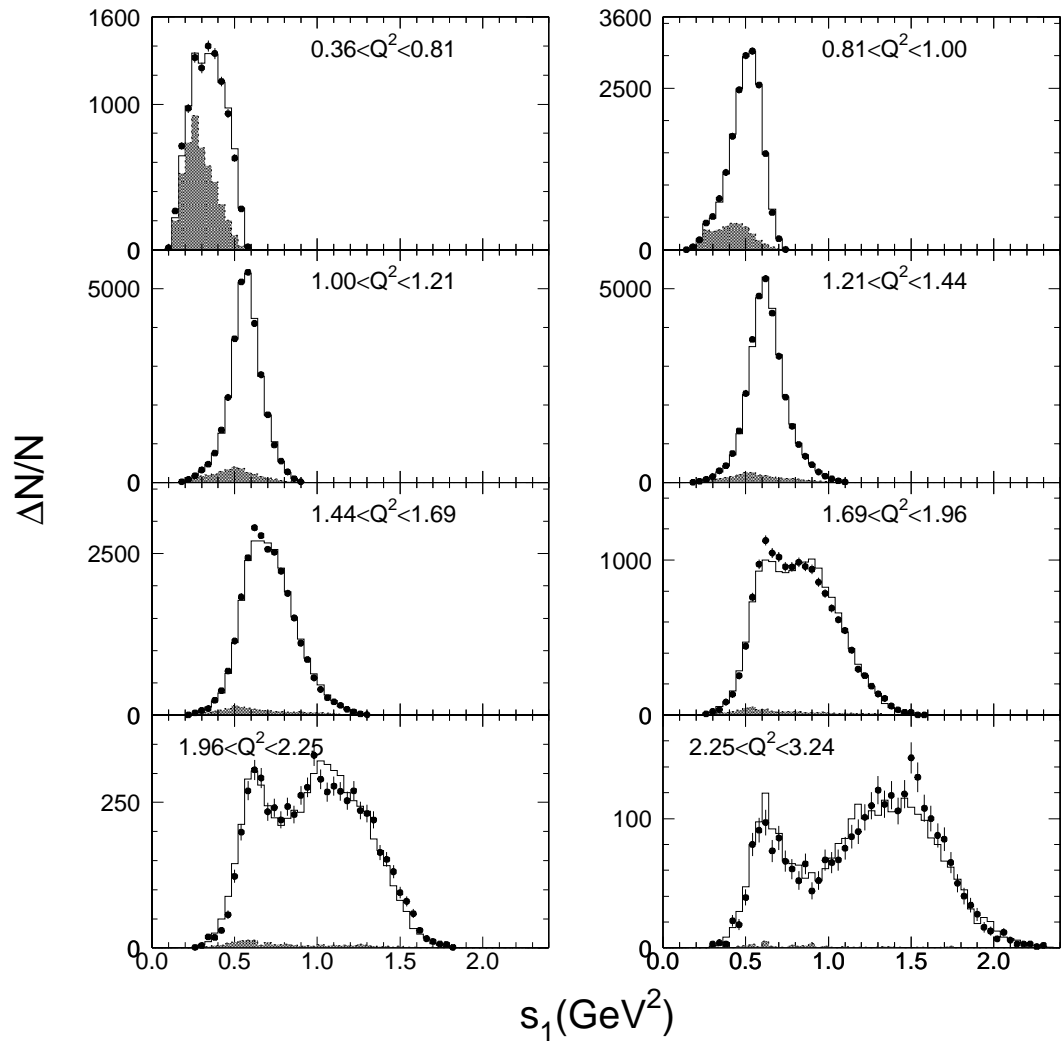


Figure 8.2

Display of nominal fit results in distributions of s_1 for various bins of Q^2 . The points represent the data, the solid histograms indicate the fit results, and the shaded regions display the background distributions.

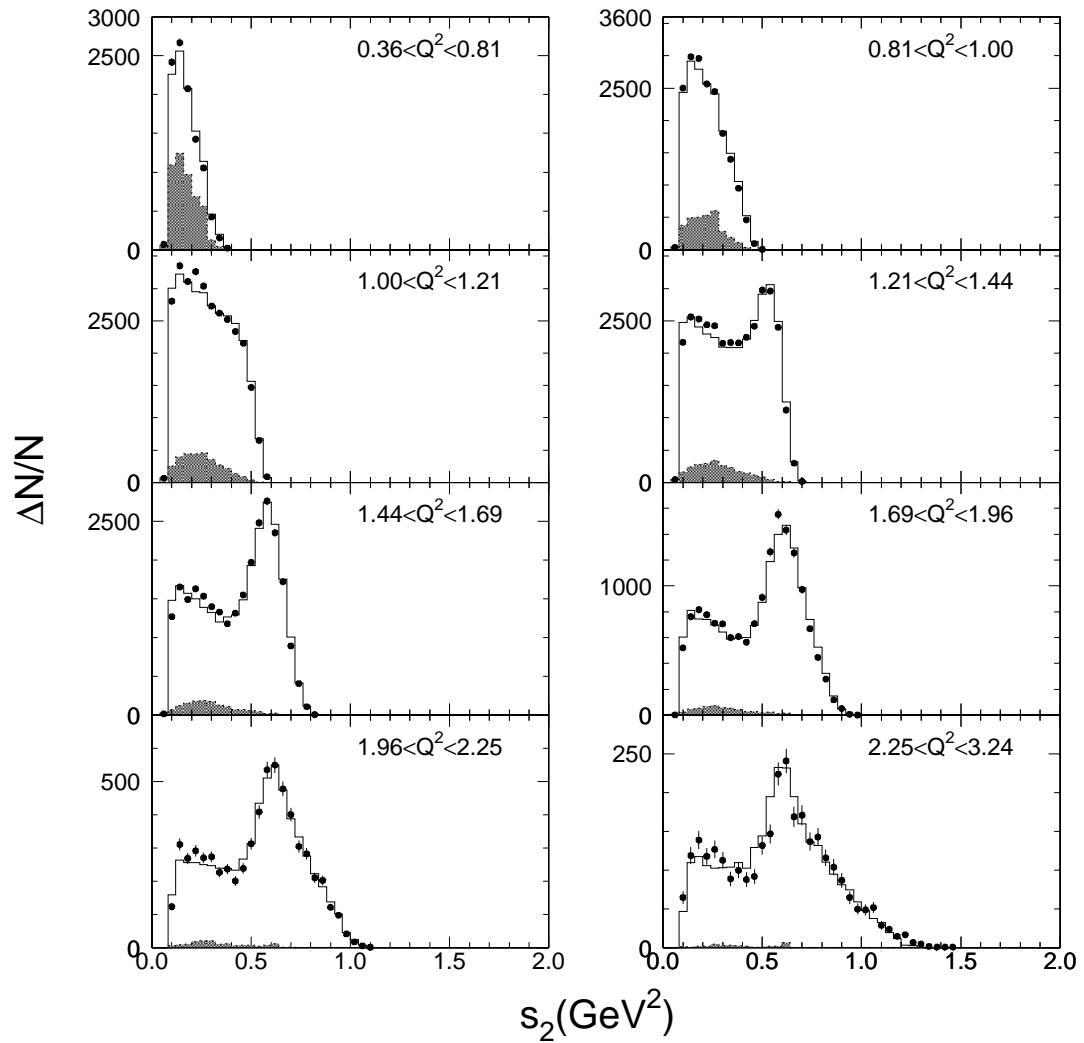


Figure 8.3

Display of nominal fit results in distributions of s_2 for various bins of Q^2 . The points represent the data, the solid histograms indicate the fit results, and the shaded regions display the background distributions.

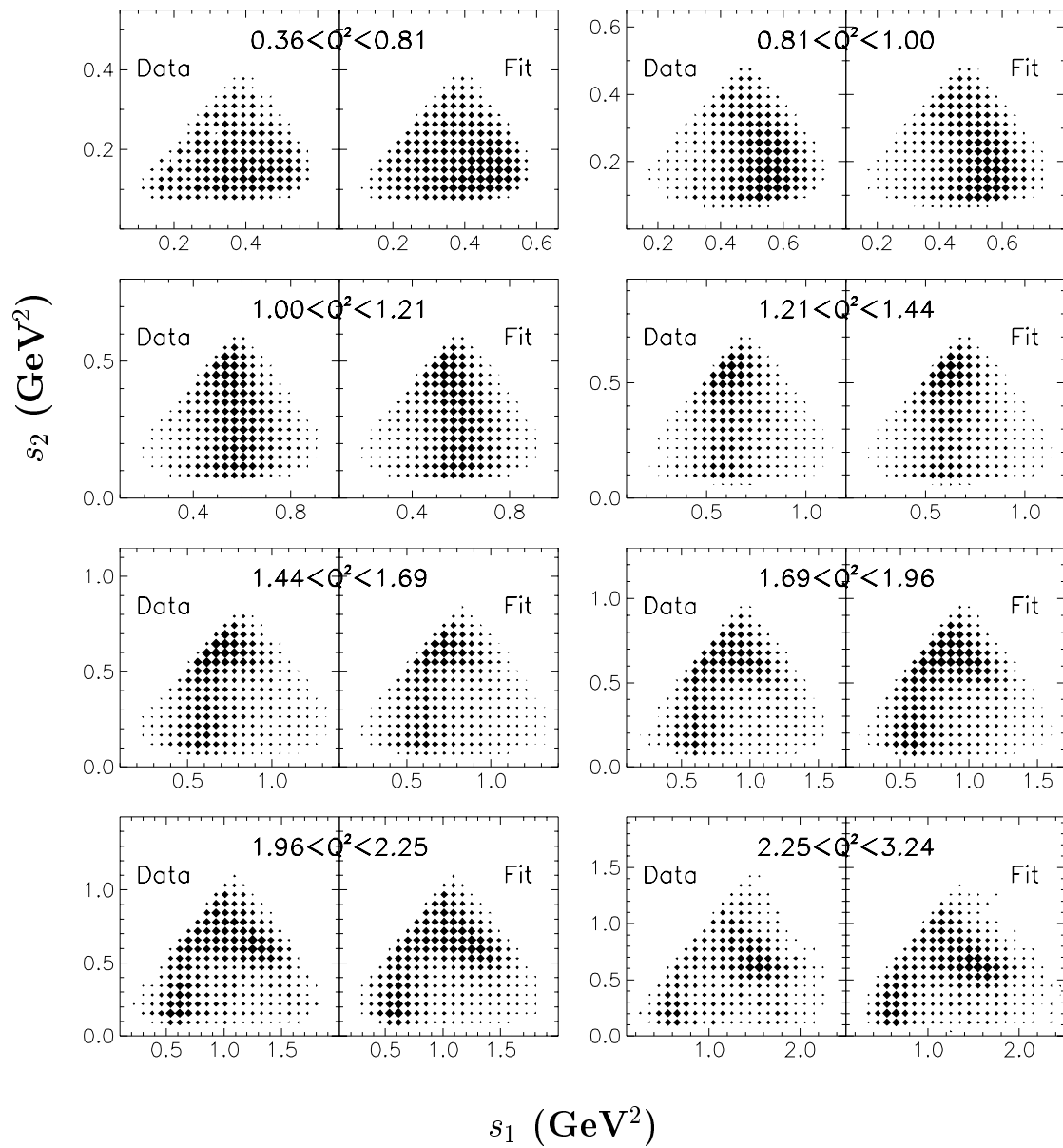


Figure 8.4

Display of nominal fit results on two dimensional distributions of s_1 and s_2 in different Q^2 bins. For each bin, data distributions are shown on the left while distributions generated from the fit are displayed on the right.

Table 8.2 presents the results of a fit using model variation 1. A reasonable goodness of fit was also found for this model, 0.7σ . Finally, results for a fit using model variation 2 are given in Table 8.3. The difference between the expected and measured log-likelihood for this fit was found to be 0.8σ , indicating an acceptable goodness of fit for this model as well.

8.2 Systematic Errors

The systematic errors presented in the analysis results arise from the following sources: There is uncertainty involved in estimating the distribution of the measured data from the theoretical distribution: $\frac{d\Gamma'}{d\vec{x}'}(\vec{x}'|\vec{a}) = \int \rho(\vec{x}'|\vec{x}) \frac{d\Gamma}{d\vec{x}}(\vec{x}|\vec{a}) d\vec{x}$. Errors from this source include both the Monte Carlo statistics used in performing the numerical integration as well as uncertainties in various detector resolutions (used to approximate $\rho(\vec{x}'|\vec{x})$). Uncertainty also exists in the background correction from both background Monte Carlo statistics and the background fraction estimations. Finally, the estimation of the normalization involves uncertainties from both Monte Carlo statistics and acceptance (recall from Section 6.2 that acceptance only affects the fit via the normalization estimation). The effects of acceptance are due to inaccuracies in how well the skimming of the Monte Carlo events used in the normalization represents the skimming of data events. Studies on the skim results indicate that such acceptance effects would be minor, and uncertainties due to Monte Carlo statistics are expected to strongly dominate the normalization error.

Statistical errors associated with the measurement of $\frac{d\Gamma'}{dx'}(\vec{x}'|\vec{a})$ are estimated from seven separate fits, each using a separate set of statistics to calculate the numerical integral and each assuming different detector resolutions (varied within reasonable limits). Errors due to background correction factors are derived from five separate fits using different background statistics and varying the background fraction within reasonable limits. Finally, errors caused by uncertainty in the normalization are estimated by dividing the normalization Monte Carlo into seven separate sets, performing a fit for each set and taking the variation in the results to calculate the associated statistical errors. Results from these systematic error studies are given in Tables 8.4 and 8.5.

In general, none of these sources considered tends to dominate the systematic error contributions in all cases. This is not unexpected given that Monte Carlo statistics should play a large role in these errors, and each of the given sources includes errors from some form of statistics used.

Note that the systematic errors on the fit parameters do not include considerations for possible, diverse variations in model assumptions. The parameters themselves are only meaningful in the context of the model to which they are associated. Different models can produce significantly different fit parameters, though this has no bearing on the accuracy of the parameters resulting from the fit in this analysis. The results of this analysis are inherently model dependent, and one must judge the use of various models depending on each's ability to describe the

Table 8.4

Systematic errors for the fit to the nominal model (continued on next table).

Resonance	Element	$\frac{d\Gamma'}{d\vec{x}}(\vec{x}' \vec{a})$	Back-	Normal-	Total	
		Calc.	ground	ization		
$a_1 \rightarrow \rho'\pi$	s -wave	$\Delta\Re\beta_i:$	± 0.012	± 0.008	± 0.006	± 0.02
		$\Delta\Im\beta_i:$	± 0.008	± 0.013	± 0.013	± 0.02
		$\Delta\mathcal{B}$ frac:	± 0.105	± 0.157	± 0.164	± 0.25
$a_1 \rightarrow \rho\pi$	d -wave	$\Delta\Re\beta_i:$	± 0.005	± 0.015	± 0.006	± 0.02
		$\Delta\Im\beta_i:$	± 0.018	± 0.026	± 0.009	± 0.03
		$\Delta\mathcal{B}$ frac:	± 0.047	± 0.089	± 0.034	± 0.11
$a_1 \rightarrow \rho'\pi$	d -wave	$\Delta\Re\beta_i:$	± 0.051	± 0.176	± 0.069	± 0.20
		$\Delta\Im\beta_i:$	± 0.041	± 0.049	± 0.045	± 0.08
		$\Delta\mathcal{B}$ frac:	± 0.130	± 0.395	± 0.169	± 0.45
$a_1 \rightarrow f_2\pi$	p -wave	$\Delta\Re\beta_i:$	± 0.023	± 0.041	± 0.034	± 0.06
		$\Delta\Im\beta_i:$	± 0.018	± 0.011	± 0.046	± 0.05
		$\Delta\mathcal{B}$ frac:	± 0.025	± 0.016	± 0.065	± 0.07
$a_1 \rightarrow \sigma\pi$	p -wave	$\Delta\Re\beta_i:$	± 0.015	± 0.095	± 0.019	± 0.10
		$\Delta\Im\beta_i:$	± 0.017	± 0.092	± 0.040	± 0.10
		$\Delta\mathcal{B}$ frac:	± 0.470	± 2.696	± 0.988	± 2.91
$a_1 \rightarrow f_0\pi$	p -wave	$\Delta\Re\beta_i:$	± 0.023	± 0.041	± 0.029	± 0.05
		$\Delta\Im\beta_i:$	± 0.013	± 0.029	± 0.007	± 0.03
		$\Delta\mathcal{B}$ frac:	± 0.250	± 0.591	± 0.140	± 0.66

data. Therefore systematic errors due to possible variations in the model used are not applicable to the results reported herein.

Table 8.5

Continuation of systematic errors for the fit to the nominal model.

Resonance	Element	$\frac{d\Gamma'}{d\vec{x}}(\vec{x}' \vec{a})$	Back-	Normal-	Total	
		Calc.	ground	ization		
$\pi' \rightarrow \rho\pi$	p -wave	$\Delta\Re\beta_i:$	± 0.0012	± 0.0001	± 0.0012	± 0.002
		$\Delta\Im\beta_i:$	± 0.0015	± 0.0001	± 0.0009	± 0.002
		$\Delta\mathcal{B}$ frac:	± 0.0213	± 0.0021	± 0.0136	± 0.025
$\pi' \rightarrow \rho'\pi$	p -wave	$\Delta\Re\beta_i:$	± 0.0070	± 0.0010	± 0.0073	± 0.010
		$\Delta\Im\beta_i:$	± 0.0039	± 0.0004	± 0.0010	± 0.004
		$\Delta\mathcal{B}$ frac:	± 0.0130	± 0.0016	± 0.0083	± 0.015
$\pi' \rightarrow \sigma\pi$	s -wave	$\Delta\Re\beta_i:$	± 0.0012	± 0.0002	± 0.0010	± 0.002
		$\Delta\Im\beta_i:$	± 0.0009	± 0.0001	± 0.0005	± 0.001
		$\Delta\mathcal{B}$ frac:	± 0.0278	± 0.0031	± 0.0202	± 0.035

9. DISCUSSION

Fit results produced by the analysis generally support the following points:

- The dominant amplitude in the decay is found to be the s -wave $a_1 \rightarrow \rho\pi$, with a branching fraction of around 70% to 75%, depending on the model used.
- Of the 1^+ sub-resonances, all but the $\rho'\pi$ s -wave are reasonably significant in the fits.
- Also prevalent in the 1^+ contributions to the $\tau^\pm \rightarrow \pi^\pm\pi^\pm\pi^\mp(\bar{\nu}_\tau/\nu_\tau)$ width is the σ isoscalar meson, with a branching fraction between 40% and 50% depending on the model used. Its presence in the nominal fit (with 6.0σ significance) cannot be ignored (see Section 9.2).
- The other two isoscalar mesons (f_2 and $f_0(1370)$) modeled in the a_1 decay are well warranted in the fits (given their significance measurements); however, only the $f_0(1730)$ contributes significantly to the $\tau^\pm \rightarrow \pi^\pm\pi^\pm\pi^\mp(\bar{\nu}_\tau/\nu_\tau)$ width, with a branching fraction of $\sim 11\%$. See Section 9.2 for further discussion of the isoscalar contributions.

- When taken as a whole (thus accounting for interferences between the amplitudes), the isoscalar resonances contribute around 15-17% to the overall $\tau^\pm \rightarrow \pi^\pm \pi^\pm \pi^\mp (\bar{\nu}_\tau/\nu_\tau)$ width, depending on the model used.
- The statistical significances of the 0^- sub-resonances are generally small in all cases and in all fits, usually ruling out their relevance to a given fit at the 90% confidence level (significance $< 1.65\sigma$). However, the overall effects of including these sub-resonances are generally consistent with expectations. See Section 9.4 for further discussion of the pseudoscalar contributions.

The following sections elaborate on various implications of the analysis.

9.1 Model Comparisons

As expected, results from fits to the nominal model and those from model variation 1 are largely in agreement with one another. These two models differ only in their treatment of the pseudoscalar π' and its decay, and because contributions from its sub-resonances are small, differences between the two fits were expected to be minimal. The fits produced only slightly different results for the pseudoscalar sub-resonances. Both find contributions from $\rho\pi$ and $\rho'\pi$ p -wave largely consistent with zero, while contributions from $\sigma\pi$ s -wave are found to be only slightly higher in the model variation 1 fit than found in the nominal fit (a somewhat insignificant difference, given the fit errors). See Section 9.4 for a discussion of these contributions.

Model variation 2 produces similar results for most of the 1^+ β_i factors, and though differences exist outside of the given error range in some cases, such differences themselves are not necessarily of physical importance given that each model explicitly treats the amplitudes differently. Comparisons of the calculated branching fractions, however, are more significant, indicating, to a degree, physically different predictions. In most cases, error bars on the predicted branching fractions would overlap with those produced by the other models, and the general trends are largely the same, as noted previously: The s -wave $a_1 \rightarrow \rho\pi$ dominates with significant contributions from $a_1 \rightarrow \sigma\pi$ and $f_0\pi$ p -wave. When isoscalar resonances are combined as one contribution, their combined branching fraction is found to be about 17% for the nominal case and about 15% for model variation 2. This model also predicts consistently larger effects from pseudoscalar contributions as discussed in Section 9.4. The non-resonance contribution in this model is also discussed in that section.

Comparisons between the model fits in a variety of projection plots were examined, and differences between the models were largely minimal. This is not an unexpected result, given that a reasonably acceptable fit was found with each model. Overall, there are no strong indications that any one model produces a definitively better fit than the others.

9.2 Significance of Isoscalar Resonances

The isoscalar meson sub-resonances of the a_1 included in this analysis (σ , f_2 , and $f_0(1370)$) play a large role in the fits for each model considered. A fit to the nominal model was performed without these amplitudes present to demonstrate their importance. The goodness of fit test for this fit yielded a result of $\sim 9\sigma$, attesting to its poor quality and thus the significance of the isoscalar resonances. Two figures have been included below to demonstrate where the need for these isoscalar amplitudes is most prevalent: Figures 9.1 and 9.2 display the results of this fit on distributions of s_1 and s_2 (respectively) in bins of Q^2 .

The isoscalar resonances seem to play an important role for data with $Q^2 \gtrsim 2.25$ GeV where there is broadening in the distribution of s_1 , and for data with $Q^2 \lesssim 1.44$ GeV as seen in the distribution of s_2 . The former region tends to attest to the significance of the f_2 and f_0 sub-resonances, while the latter attests to the significance of the σ sub-resonance.

9.3 Notes on Possible a'_1 Hypothesis

In the flux-tube-breaking model presented in references [66] and [67], one finds that the decay of a'_1 to $\rho'\pi$ prefers to precede through d -wave rather than s -wave, and that decay of the a'_1 to $\rho'\pi$ is preferred to $\rho\pi$. In all the preceding fits, the $a_1 \rightarrow \rho'\pi$ mode was more prominent in d -wave than in s -wave; and in the nominal model as well as model variation 1, the $\rho'\pi$ channel has a slightly higher branching fraction than the $\rho\pi$ in the the d -wave mode. Further, the need for enhancement

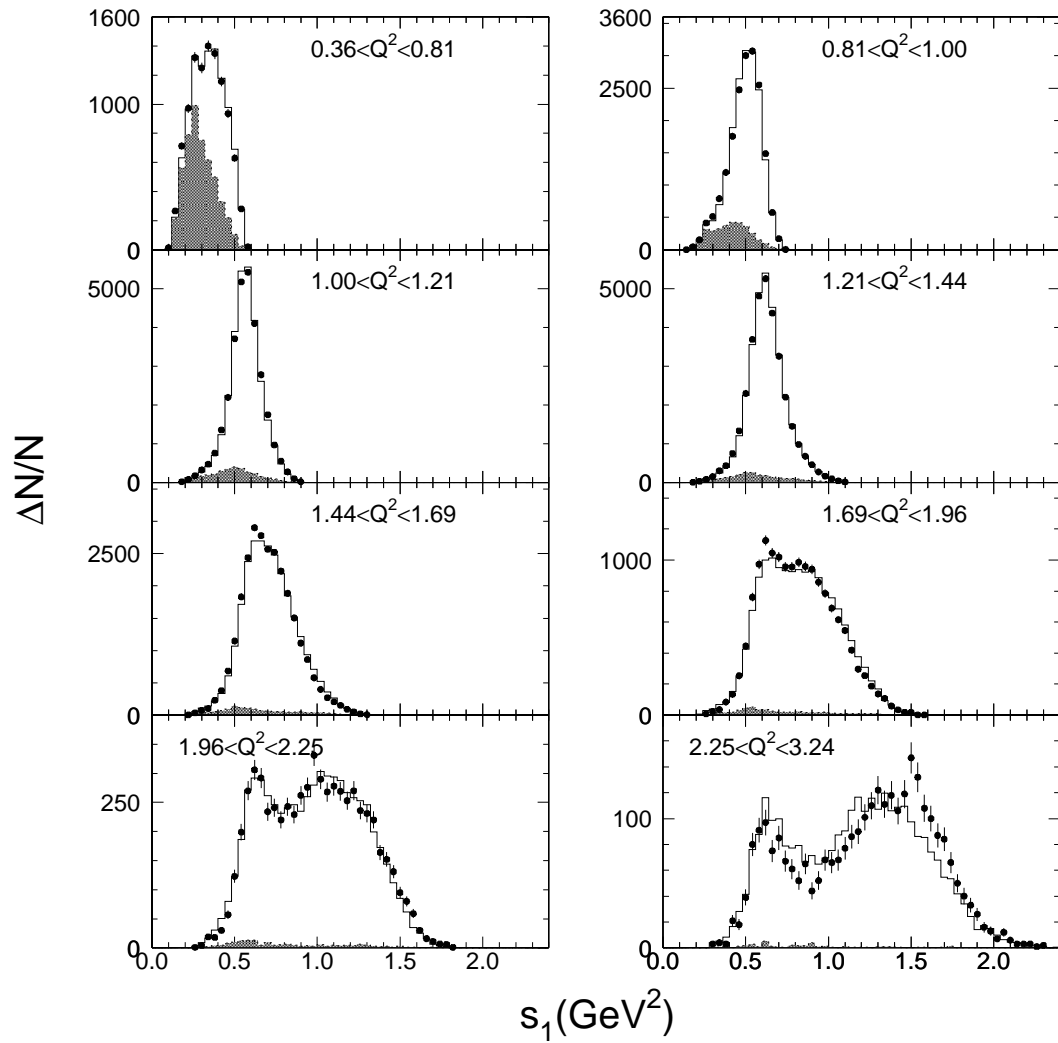


Figure 9.1

Display of s_1 distributions in various bins of Q^2 resulting from fitting without isoscalar resonances. The points represent the data, the solid histograms indicate the fit results, and the shaded regions display the background distributions.

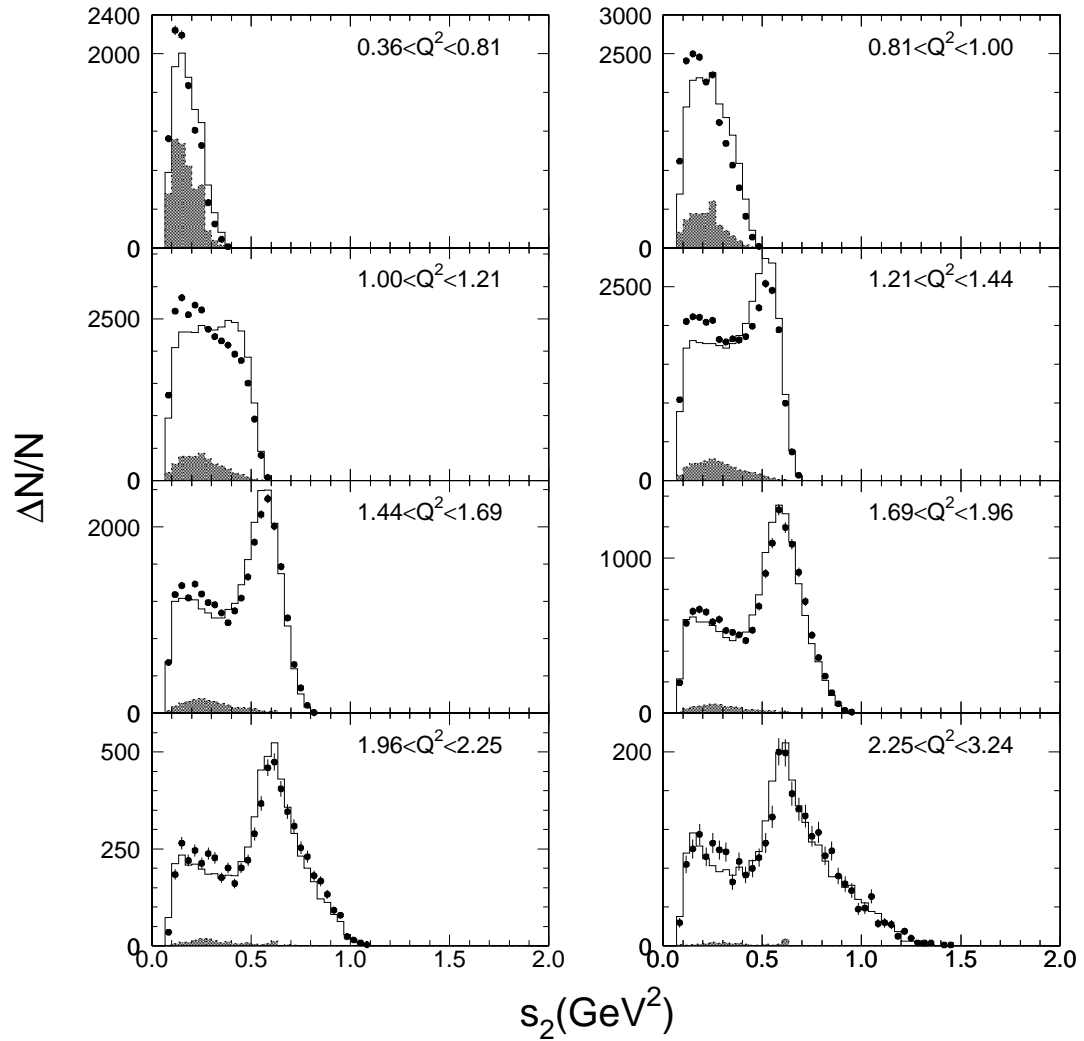


Figure 9.2

Display of s_2 distributions in various bins of Q^2 resulting from fitting without isoscalar resonances. The points represent the data, the solid histograms indicate the fit results, and the shaded regions display the background distributions.

from the $f_2\pi$ and $\sigma\pi$ in the upper Q^2 bins is also consistent with an a'_1 hypothesis. This possibility is left for future potential analysis.

9.4 Significance of Pseudoscalar Resonances

Of particular interest for this analysis was the inclusion of 0^- pseudoscalar resonances through the π' . In each model fit, the significance of these amplitudes can be ruled out if one requires a 90% confidence (significance $< 1.65\sigma$). A fit performed using the nominal model without any pseudoscalar contribution suggested an overall significance of, at most, $\sim 1.4\sigma$, indicating a moderately acceptable fit with no pseudoscalar contributions.

However, greater pseudoscalar significance is found in the fit to model variation two. Without the presence of pseudoscalar amplitudes, this fit returns a significance of $\sim 1.8\sigma$. Model variation 2 also indicates a slightly significant non-resonance contribution (which induces a scalar effect), with a branching fraction of around 0.9%.

Given the results of this fit, one can place the following 90% confidence level limits on the absolute branching fractions of the pseudoscalar modes:

$$\text{nominal model: } \left\{ \begin{array}{l} \mathcal{B}(\tau \rightarrow \pi' \nu_\tau \rightarrow \rho \pi \nu_\tau \rightarrow 3\pi \nu_\tau) < 4.3 \times 10^{-5}, \\ \mathcal{B}(\tau \rightarrow \pi' \nu_\tau \rightarrow \rho' \pi \nu_\tau \rightarrow 3\pi \nu_\tau) < 5.2 \times 10^{-5}, \\ \mathcal{B}(\tau \rightarrow \pi' \nu_\tau \rightarrow \sigma \pi \nu_\tau \rightarrow 3\pi \nu_\tau) < 2.1 \times 10^{-4}, \end{array} \right. \quad (9.1)$$

$$\text{model variation 1: } \left\{ \begin{array}{l} \mathcal{B}(\tau \rightarrow \pi' \nu_\tau \rightarrow \rho \pi \nu_\tau \rightarrow 3\pi \nu_\tau) < 6.3 \times 10^{-5}, \\ \mathcal{B}(\tau \rightarrow \pi' \nu_\tau \rightarrow \rho' \pi \nu_\tau \rightarrow 3\pi \nu_\tau) < 2.2 \times 10^{-5}, \\ \mathcal{B}(\tau \rightarrow \pi' \nu_\tau \rightarrow \sigma \pi \nu_\tau \rightarrow 3\pi \nu_\tau) < 3.3 \times 10^{-4}, \end{array} \right. \quad (9.2)$$

$$\text{model variation 2: } \left\{ \begin{array}{l} \mathcal{B}(\tau \rightarrow \pi' \nu_\tau \rightarrow \rho \pi \nu_\tau \rightarrow 3\pi \nu_\tau) < 2.8 \times 10^{-4}, \\ \mathcal{B}(\tau \rightarrow \pi' \nu_\tau \rightarrow \rho' \pi \nu_\tau \rightarrow 3\pi \nu_\tau) < 2.9 \times 10^{-4}, \\ \mathcal{B}(\tau \rightarrow \pi' \nu_\tau \rightarrow \sigma \pi \nu_\tau \rightarrow 3\pi \nu_\tau) < 1.0 \times 10^{-3}, \\ \mathcal{B}(\tau \rightarrow 3\pi \nu_\tau \text{ non-resonant}) < 1.1 \times 10^{-3}. \end{array} \right. \quad (9.3)$$

As shown, model variation 2 suggests significantly larger pseudoscalar contributions. The non-resonance contribution is also reasonably noticeable, and though it is not overly significant in the fit, the branching fraction of $(0.87 \pm 0.14 \pm 0.18)\%$ is not consistent with zero. It should also be noted that, though the fitted coupling constant for the non-resonance contribution is significantly higher than others (see Table 8.3), this could be due to a missing scale factor in the fit and does not affect the branching fraction calculation or errors.

It is instructional to investigate where the pseudoscalar amplitudes contribute what small significance they seem to have. Any small scalar contribution expected in the nominal fit would not produce noticeable effects on either the $3\pi^\pm$ mass spectrum, the s_1 , or the s_2 distributions. Any possible branching ratio from the square of the pseudoscalar amplitudes is also expected to be insignificant. However, as discussed in [57], more noticeable effects caused by interference terms involving

0^- amplitudes may be detectable from their effects on the distribution of γ (defined in Appendix G). The details of that distribution are discussed in Appendix H.

For the nominal fit, one finds that the effects of including the pseudoscalar amplitudes are statistically unnoticeable for the distributions of Q^2 , s_1 , s_2 , β , $\cos\theta$, and $\cos\psi$, improving the confidence level comparisons between the data and fit by a relative 1 to 4%. However, in the distribution of γ , the confidence level is improved by a relative 30% or so. Although statistically insignificant in the overall fit, the improvements caused by adding 0^- amplitudes are found where they are expected, indicating that while statistically small, the improvements are likely real.

9.5 Comparisons to Other Results

A variety of other collaborations have produced previous analyses of the $\tau^\pm \rightarrow \pi^\pm \pi^\pm \pi^\mp (\bar{\nu}_\tau/\nu_\tau)$ decay, including DELCO [68], Mark II [69], MAC [70], ARGUS [71–73], OPAL [74], and DELPHI [75]. Their reports generally involve various areas of study possible from $\tau^\pm \rightarrow \pi^\pm \pi^\pm \pi^\mp (\bar{\nu}_\tau/\nu_\tau)$ decays including the a_1 mass and width parameters (assuming model conditions), the neutrino helicity, and the Michel parameters, ξ and δ . However, since the analysis being reported on here (referred to in this section as the “current analysis”) has focused specifically on the carefully modeled substructure in the decay, previous results on these other areas of study are not reported on here. For a more complete comparison of previous results, see Reference [76].

These analyses generally focus on the model of Kühn and Santamaria presented in [52] (hereafter referred to as the KS model) and the model presented in [51] by Isgur, Morningstar, and Reader (hereafter referred to as the IMR model). The KS model includes resonances for $a_1 \rightarrow \rho\pi$ and a small admixture of $a_1 \rightarrow \rho'\pi$, both in what approximately coincides with s -wave amplitudes. The IMR model includes s -wave as well as d -wave $a_1 \rightarrow \rho\pi$, and unlike KS, it included the “turn on” effects of $K^*\bar{K}$ in the a_1 Breit-Wigner (see Section 5.3.1). IMR also includes a small amount of $\pi' \rightarrow \rho\pi$.

Using approximately 7,500 $\tau^\pm \rightarrow \pi^\pm \pi^\pm \pi^\mp (\bar{\nu}_\tau/\nu_\tau)$ decays, ARGUS [72], among other things, studied the Q^2 and Dalitz plot distributions to extract the ratio of D/S used in the IMR model. They obtained a value of $D/S = -0.11 \pm 0.02$, compared with the model prediction of $D/S = -0.15$ [51]. However, due to model differences, there is no simple comparison to the results presented in the current analysis. A later ARGUS analysis [73] focused mainly on the Michel parameters using approximately 3,300 $(\tau^\pm)(\tau^\mp) \rightarrow (l^\pm \nu \bar{\nu})([3\pi^\pm]^-)$ events (where l denotes a lepton). Both KS and IMR models proved inconsistent with the data in that analysis, though the goodness of fit was improved to an acceptable level by including the amplitudes listed in Table 9.1. To produce this result, the couplings used had to be made Q^2 dependent, and again, it is difficult to make direct comparisons between their results and results presented here. However, general conclusions can be drawn from these ARGUS analyses that match favorably with those of the current analysis:

- The structure in $\tau^\pm \rightarrow \pi^\pm \pi^\pm \pi^\mp (\bar{\nu}_\tau/\nu_\tau)$ decays is more complex than either the KS or IMR models can account for.
- It seems important to include some degree of isoscalars (f_2 and f_0) in the hadronic current.

Table 9.1

Amplitudes used by ARGUS [73]. Their fit significance and relative branching fraction are also given. Coupling constants for these amplitudes were made Q^2 dependent to get an acceptable fit.

	Resonance	Signif.	\mathcal{B} Fraction (%)
$a_1 \rightarrow \rho\pi$	<i>s</i> -wave	—	58.2%
$a_1 \rightarrow \rho\pi$	<i>d</i> -wave	6.4σ	7.2%
$a_1 \rightarrow \rho\pi$	Emulate Isgur	3.9σ	5.8%
$a_1 \rightarrow f_0(975)/f_0(1400)\pi$	<i>p</i> -wave	2.1σ	
$a_1 \rightarrow f_2(1270)\pi$	<i>p</i> -wave	4.2σ	3.6%
$\rho \rightarrow \omega\pi$	<i>p</i> -wave	2.4σ	0.6%
$\pi' \rightarrow f_0(1400)\pi$	<i>p</i> -wave	2.5σ	0.3%
$\pi' \rightarrow \rho\pi$	<i>s</i> -wave	2.8σ	0.7%

In reference [74], OPAL presented a study using approximately 6,300 $\tau^\pm \rightarrow \pi^\pm \pi^\pm \pi^\mp (\bar{\nu}_\tau/\nu_\tau)$ decays. They performed both a model-dependent analysis (using the KS and IMR models) and a model-independent analysis (using structure functions as presented in [64]). Their model-independent analysis placed a limit on the

non-axial vector contributions in $\tau^\pm \rightarrow \pi^\pm \pi^\pm \pi^\mp (\bar{\nu}_\tau/\nu_\tau)$:

$$\Gamma_{\text{non-AV}}/\Gamma_{\text{total}} < 26.1\% \quad \text{at 95\% C.L.} \quad (9.4)$$

Their model-dependent analysis assumed pseudoscalar contributions through $\pi' \rightarrow \rho\pi$ and place the following limit:

$$\Gamma(\tau \rightarrow \pi'\nu \rightarrow 3\pi)/\Gamma_{\text{total}} < 0.85\% \quad \text{at 95\% C.L.} \quad (9.5)$$

A display of their fit to the s_1 distribution is shown in Figure 9.3. The fit is shown to be poorer in the low s_1 region and there seems to be unmatched structure in the upper mass region as well. These results again seem indicative of the need for isoscalar resonances, though OPAL's analysis did not explore that possibility.

In each of these analyses, poor agreement between the data and both the KS and IMR models indicate that resonances beyond $\rho\pi$ are needed to describe the hadronic system in $\tau^\pm \rightarrow [3\pi]^\pm (\bar{\nu}_\tau/\nu_\tau)$ decays.

A separate report from the CLEO collaboration [60] studied the structure in $\tau^\pm \rightarrow \pi^\pm \pi^0 \pi^0 (\bar{\nu}_\tau/\nu_\tau)$ decays. In it, fits to the three pion mass spectrum were performed using approximately 30,800 events in which the ‘‘tag’’ side was identified as leptonic or hadronic. However, substructure fits were performed using only the somewhat more reliable lepton tagged events (approximately 14,600 decays). The a_1 sub-resonances used in the current analysis were motivated by those used in [60] (once they were isospin rotated to the all charged mode). The significances and branching fractions found in that analysis are given in Table 9.2. Though there are differences between those results and the all charged mode reported here, there are

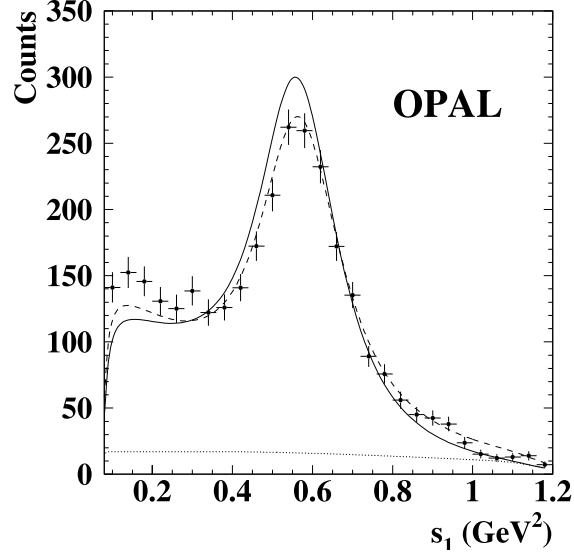


Figure 9.3

An OPAL result showing a Dalits plot projection of their background- and efficiency-corrected data (points with error bars), a fit result to the KS model (solid line), and a fit result to the IMR model (dashed line). The dotted line shows the polynomial background contribution for the IMR model.

some similar trends. The $a_1 \rightarrow \rho\pi$ s -wave accounts for about 70% of the branching fraction, consistent with the current results, and there is significant evidence for isoscalar resonances reported (when taken as a whole, they contributed $\sim 20\%$ compared to $\sim 17\%$ in the current analysis). The previous report also placed a limit on pseudoscalar components at a 90% confidence level:

$$\begin{aligned} \mathcal{B}(\tau \rightarrow \pi' \nu_\tau \rightarrow \rho \pi \nu_\tau \rightarrow 3\pi \nu_\tau) &< 1.0 \times 10^{-4}, \\ \mathcal{B}(\tau \rightarrow \pi' \nu_\tau \rightarrow \sigma \pi \nu_\tau \rightarrow 3\pi \nu_\tau) &< 1.9 \times 10^{-4}. \end{aligned} \tag{9.6}$$

It is instructional to compare the results reported in the current analysis with those from [60] (which will be called the “previous” results for convenience) by looking at Q^2 , s_1 , and s_2 projections compared to data. To that end, Figure 9.4

Table 9.2

Amplitudes used by an earlier CLEO study of $\tau^\pm \rightarrow \pi^\pm \pi^0 \pi^0 (\bar{\nu}_\tau/\nu_\tau)$ decays [60]. Their reported significance and relative branching fractions are also listed.

Resonance		Signif.	\mathcal{B} Fraction (%)
$a_1 \rightarrow \rho\pi$	<i>s</i> -wave	—	68.11
$a_1 \rightarrow \rho'\pi$	<i>s</i> -wave	1.4σ	$0.30 \pm 0.64 \pm 0.17$
$a_1 \rightarrow \rho\pi$	<i>d</i> -wave	5.0σ	$0.36 \pm 0.17 \pm 0.06$
$a_1 \rightarrow \rho'\pi$	<i>d</i> -wave	3.1σ	$0.43 \pm 0.28 \pm 0.06$
$a_1 \rightarrow f_2\pi$	<i>p</i> -wave	4.2σ	$0.14 \pm 0.06 \pm 0.02$
$a_1 \rightarrow \sigma\pi$	<i>p</i> -wave	8.2σ	$16.18 \pm 3.86 \pm 1.28$
$a_1 \rightarrow f_0\pi$	<i>p</i> -wave	5.4σ	$4.29 \pm 2.29 \pm 0.73$

displays four plots. The first two plots present comparisons in Q^2 and s_1 , where there is considerable agreement between the data, the current fit result, and the previous result. The third plot shows the distribution in s_2 , where the current fit result varies from the previous result and better matches the data. The final plot is a combination of both s_1 and s_2 (two entries for each event) and represents distributions of unordered Dalitz plot variables, which were used for plots in [60]. The differences between the current fit and the previous result are less pronounced in that plot than in the distribution of s_2 (the smaller of the two when the variables are ordered for each event).

The differences between the current results and the previous result clearly reside in the distribution of s_2 . A closer examination of that plot and the distribution of background in it indicates that a larger background fraction might bring the

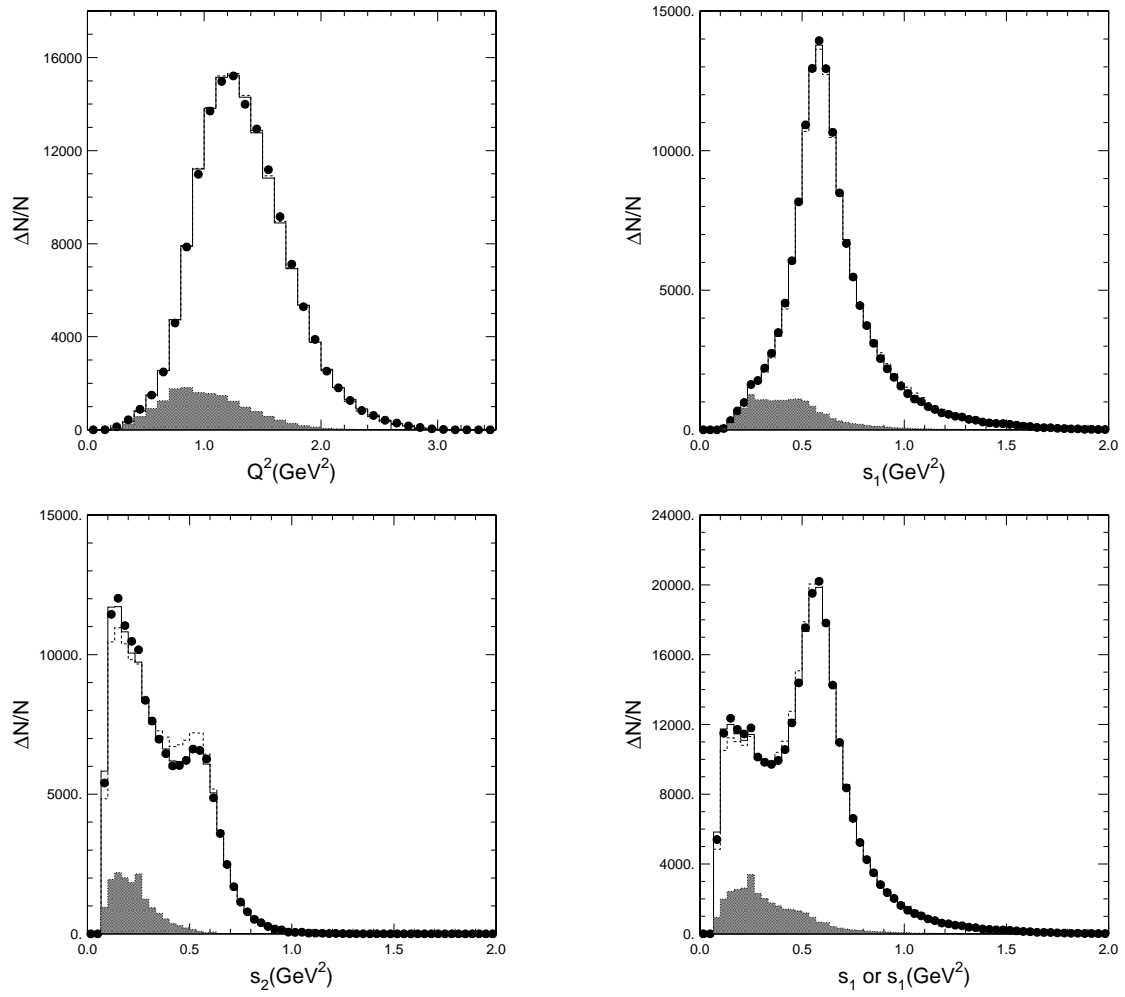


Figure 9.4

Plots comparing results from [60] adapted to the all charged mode (dashed histogram) to current results (solid histogram) and data (points). Shown are distributions in Q^2 , s_1 , s_2 , and a combination of s_1 and s_2 (two entries per event).

previous result into better agreement with the data without the need for the changes indicated by the current fit; however, such a change would disturb the agreement found in the distributions of Q^2 and s_1 . It is also possible that the background distribution (taken from Monte Carlo) is significantly erroneous in s_2 but well represented in the other two variables due to improper modeling of the background. This possibility is left for future analysis.

To summarize the comparisons made here to previous results, the current analysis continues to mount evidence for isoscalar in the $[3\pi^\pm]^-$ system of $\tau^\pm \rightarrow \pi^\pm \pi^\pm \pi^\mp (\bar{\nu}_\tau/\nu_\tau)$ decays. The current analysis also places smaller model-dependent limits on the pseudoscalar contributions. While there is some disagreement between the current results and those extracted from a similar fit to $\tau^\pm \rightarrow \pi^\pm \pi^0 \pi^0 (\bar{\nu}_\tau/\nu_\tau)$ decays, the extent to which these are from differences in the two modes, results of poor background modeling, or come from some other source is yet to be determined.

9.6 Implications on the Light Quark Masses

The connection between the scalar contribution in $\tau^\pm \rightarrow \pi^\pm \pi^\pm \pi^\mp (\bar{\nu}_\tau/\nu_\tau)$ decays and the average of the up and down quark running masses [$\hat{m} \equiv (m_u + m_d)/2$] is discussed in Appendix I. Here, the results of this analysis are applied to the given equations to determine a lower limit on \hat{m} ($\hat{m}(\mu^2) \geq \hat{m}'(\mu^2)$).

The method presented in Appendix I involves a squared cutoff mass, s_0 , taken to be within a typical range of $2 \text{ GeV}^2 \leq s_0 \leq m_\tau^2$, and the ranges of \hat{m} reported here

include the effects due to the variance in s_0 . Results from the scalar contributions in the three models suggest the following \hat{m}' values at $\mu = 1$ GeV (note that the third error indicates the systematic error due to the spread in s_0):

$$\begin{aligned}
 \text{nominal model: } \hat{m}'(1 \text{ GeV}^2) &= 13.3 \pm 2.6 \pm 3.5 \pm 0.4 \text{ MeV}, \\
 \text{model variation 1: } \hat{m}'(1 \text{ GeV}^2) &= 17.6 \pm 2.9 \pm 3.1 \pm 0.7 \text{ MeV}, \\
 \text{model variation 2: } \hat{m}'(1 \text{ GeV}^2) &= 25.4 \pm 4.9 \pm 5.8 \pm 0.9 \text{ MeV}.
 \end{aligned}
 \tag{9.7}$$

The results were also used to extract 90% confidence level lower limits on \hat{m} , given as follows:

$$\begin{aligned}
 \text{nominal model: } \hat{m}(1 \text{ GeV}^2) &\geq 8.3 \text{ MeV}, \\
 \text{model variation 1: } \hat{m}(1 \text{ GeV}^2) &\geq 12.5 \text{ MeV}, \\
 \text{model variation 2: } \hat{m}(1 \text{ GeV}^2) &\geq 14.2 \text{ MeV}.
 \end{aligned}
 \tag{9.8}$$

Without the information gathered from the $[3\pi]^-$ mode, the well-understood one-pion decay mode of the τ places a lower limit on $\hat{m}(1 \text{ GeV}^2)$ of around (4 – 5) MeV [57]. The additional $[3\pi]^-$ contribution indicated by the current analysis is thus on the same order as or higher than the one-pion contribution. While the resulting limits may be larger than expected (see Appendix I), they do lie close to nominal expectations [$4 \text{ MeV} \leq \hat{m}(1 \text{ GeV}^2) \leq 10 \text{ MeV}$]. Further, as noted earlier, the $\tau^\pm \rightarrow \pi^\pm \pi^\pm \pi^\mp (\bar{\nu}_\tau / \nu_\tau)$ substructure fit performs reasonably without the pseudoscalar modes, and thus it cannot statistically attest to the significance of the $[3\pi]^-$ additions to the \hat{m} limit. Overall, the results indicate that the level of pseudoscalar suggested by this analysis is not unreasonable.

10. CONCLUSIONS

This analysis has applied a model-dependent fit that reasonably describes the hadronic substructure in $\tau^\pm \rightarrow \pi^\pm \pi^\pm \pi^\mp (\bar{\nu}_\tau/\nu_\tau)$ decays. It utilized 145,000 events skimmed from the sample of 4.3×10^6 τ pairs present in the CLEO II data set. The nominal model contained both axial vector components (introduced through the $a_1(1260)$ primary resonance and its sub-resonances) as well as pseudoscalar contributions (via the $\pi'(1300)$ and its sub-resonances). Two model variations were also considered that concerned changes to the pseudoscalar contributions, a chief interest in this analysis. The first introduced changes to the modeling of the π' and its sub-resonances, while the second variation involved corrections due to the finite quark masses in the chiral limit—inducing pseudoscalar-like terms from the axial vector components and introducing a non-resonant term.

An unbinned maximum likelihood fit was used to extract the complex coupling constants that control the strength of each sub-resonance in the hadronic current. All models used tended to describe the data well, and none of the fits indicated a clearly preferable model.

As expected, the $a_1 \rightarrow \rho\pi$ s -wave channel dominated the decay with a contribution of around 70 – 75% to the overall $\tau^\pm \rightarrow \pi^\pm \pi^\pm \pi^\mp (\bar{\nu}_\tau/\nu_\tau)$ width, depending

on the model used. Though a non-zero but statistically small contribution was found for s -wave $a_1 \rightarrow \rho'\pi$, statistically significant contributions were found in the a_1 substructure for d -wave $\rho\pi$ and $\rho'\pi$ amplitudes as well as amplitudes involving isoscalars, $f_2(1270)\pi$, $\sigma\pi$, and $f_0(1270)\pi$. The isoscalar contributions were especially prominent, as were interferences involving those terms. The $\sigma\pi$ mode was particularly significant in all the fits, and though it contributed $\sim 40 - 50\%$ to the branching fraction independently, when combined with the isoscalars as a whole, they contributed around $15 - 17\%$ to the total $\tau^\pm \rightarrow \pi^\pm\pi^\pm\pi^\mp(\bar{\nu}_\tau/\nu_\tau)$ rate, again depending on the model. Certain aspects of the fit were also indicative of a possible a'_1 resonance, though this possibility is left for future potential analyses.

Contributions from the pseudoscalar π' sub-resonances were generally statistically insignificant, though their minimal improvements to the fitted distributions are shown to lie where one would expect. Upper limits are placed on each of the π' contributions at 90% confidence. The results found for the pseudoscalar contributions were used to place a lower limit on the average of the up and down quark running masses [$\hat{m} \equiv (m_u + m_d)/2$] that appear in the QCD Lagrangian [57]. This produced a 90% confidence limit of $\hat{m}(1 \text{ GeV}^2) > 8.3 - 14.2 \text{ MeV}$ depending on the model used, which, though higher than one might expect, is not unreasonable.

Principally, this analysis has endeavored to improve knowledge of the hadronic structure in $\tau^\pm \rightarrow \pi^\pm\pi^\pm\pi^\mp(\bar{\nu}_\tau/\nu_\tau)$ decays, and though the results are inherently tied to model assumptions, they have been able to capably describe the various characteristics in the data.

BIBLIOGRAPHY

BIBLIOGRAPHY

1. Ebbing, Darrel D. and Gammon, Steven D., *General Chemistry, 6th edition*, Houghton Mifflin Co., Boston, Massachusetts, 1999.
2. J. J. Thomson, *Phil. Mag.* **44**, 293 (1897); *Nature* **55** 453 (1897).
3. E. Rutherford, *Phil. Mag.* **21**, 669 (1911).
4. J. Chadwick, *Nature* **129**, 312 (1932).
J. Chadwick, *Proc. Roy. Soc.* **A136**, 692 (1932).
5. S. H. Neddermeyer and C. D. Anderson, *Phys. Rev.* **51**, 884 (1937).
6. D. H. Perkins, *Nature* **159**, 126 (1947).
C. F. Powell, G. P. Occhialini, D. L. Livesey, and L. V. Chilton, *J. Sci. Instrum.* **23**, 102 (1946).
C. M. Lattes, G. P. Occhialini, and C. F. Powell, *Nature* **160**, 453 (1947).
7. G. D. Rochester and C. C. Butler, *Nature* **160**, 855 (1947).
8. R. Armenteros, K. H. Barker, C. C. Butler, A. Cachon, A. H. Chapman, *Nature* **167**, 501 (1951).
9. A. Bonetti, R. Levi-Setti, M. Panetti, G. Tomasini, *Nuovo Cim.* **10** 345 (1953).
10. R. Armenteros, K. H. Barker, C. C. Butler, A. Cachon, C. M. York, *Phil. Mag.* **43** 507 (1952).
C. D. Anderson, E. W. Cowan, R. B. Leighton, V. A. J. Van Lint, *Phys. Rev.* **92** 1089(H3) (1953).
11. F. Reines and C. L. Cowan, *Phys. Rev.* **90**, 492 (1953).
C. L. Cowan, F. Reines et al., *Phys. Rev.* **90**, 493 (1953).
F. Reines and C. L. Cowan, *Phys. Rev.* **92**, 830 (1953).
C. L. Cowan, F. Reines, F. B. Harrison, H. W. Kruse, and A. D. McGuire, *Science* **124**, 103 (1956).

12. The neutrino was proposed by Pauli, W. in a letter to colleagues in Tübingen, Germany. Reprinted in *Lecture of W. Pauli Zur älteren und neueren Geschichte des Neutrinos* published in Vierteljahresschr. Naturforsch. Ges. Zürich **102** (1957) 387. (translation into English) *Physics Today* 31 (1978) 27.
13. G. Danby, J. M. Gaillard, K. Goulianos, L. M. Lederman, N. Mistry, M. Schwartz, and J. Steinberger, *Phys. Rev. Lett.* **9**, 36 (1962).
14. M. L. Perl *et al.*, *Phys. Rev. Lett.* **35**, 1489 (1975).
15. M. L. Perl *et al.*, *Phys. Rev. Lett.* **35**, 1489 (1975).
16. Newton, Sir Isaac, *Philosophiae naturalis principia mathematica*, Royal Society, London, 1687.
17. A. Einstein, *Annalen Phys.* **17S4**, 891 (1905).
18. A. Einstein, *Annalen Phys.* **49**, 769 (1916).
19. Griffiths, David J., *Introduction to Electrodynamics, 3rd edition*, Prentice Hall, 1999.
20. M. Planck, *Verhandl. Dtsch. phys. Ges.* **2**, 237 (1900).
(Translation into English) *The Old Quantum Theory*, ed. by D. ter Haar, Pergamon Press **82** (1967).
21. A. Einstein, *Annalen der Physik. Leipzig* **17**, 132 (1905).
22. N. Bohr, *Phil. Mag.* **26**, 1 (1913).
23. Brehm, John J. and Mullin, William J., *Introduction to the Structure of Matter: A Course in Modern Physics*, Wiley, New York, 1989.
24. Feynman, Richard P., *QED: The Strange Theory of Light and Matter*, Princeton University Press, Princeton, New Jersey, 1985.
25. Perkins, Donald H., *Introduction to High Energy Physics*, Addison-Wesley, Menlo Park, California, 1987.
26. G. Arnison *et al.* [UA1 Collaboration], *Phys. Lett. B* **122**, 103 (1983).
G. Arnison *et al.* [UA1 Collaboration], *Phys. Lett. B* **126**, 398 (1983).

27. Griffiths, David, *Introduction to Elementary Particles*, John Wiley and Sons, New York, 1987.
28. Halzen, Francis and Martin, Alan D., *Quarks & Leptons: An Introductory Course in Modern Particle Physics*. John Wiley and Sons, New York, 1984.
29. D. E. Groom *et al.* (Particle Data Group), E. Phys. J. **C15**, 1 (2000).
30. M. Gell-Mann, Phys. Lett. **8**, 214 (1964).
G. Zweig, CERN-8182-TH-401 (1964).
31. E. D. Bloom *et al.*, Phys. Rev. Lett. **23**, 930 (1969).
M. Breidenbach *et al.*, Phys. Rev. Lett. **23**, 935 (1969).
32. J. J. Aubert *et al.*, Phys. Rev. Lett. **33**, 1404 (1974).
J. E. Augustin *et al.*, Phys. Rev. Lett. **33**, 1406 (1974).
33. S. W. Herb *et al.*, Phys. Rev. Lett. **39**, 252 (1977).
34. F. Abe *et al.* [CDF Collaboration], Phys. Rev. D **50**, 2966 (1994).
35. Arfken, George, *Mathematical Methods for Physicists*, Academic Press, Inc., San Diego California, 1985.
36. Goldstein, Herbert, *Classical Mechanics*, Addison-Wesley, Menlo Park, 1980.
37. N. Cabibbo, Phys. Rev. Lett. **10**, 531 (1963).
38. S. L. Glashow, J. Iliopoulos, and L. Maiani, Phys. Rev. D **2**, 1285 (1970).
39. M. Kobayashi and T. Maskawa, Prog. Theor. Phys. **49**, 652 (1973).
40. T. D. Lee and C. N. Yang, Phys. Rev. **104**, 254 (1956).
41. C. S. Wu, E. Ambler, R. W. Hayward, D. D. Hoppes, and R. P. Hudson, Phys. Rev. **105**, 1413 (1957).
42. J. H. Christenson, J. W. Cronin, V. L. Fitch, and R. Turlay, Phys. Rev. Lett. **13**, 138 (1964).

43. R. S. Van Dyck, P. B. Schwinberg, and H. G. Dehmelt, *Phys. Rev. Lett.* **59**, 26 (1987).
44. T. Kinoshita, CLNS-96-1418 *Presented at Conference on Precision Electromagnetic Measurements, Braunschweig, Germany, 17-20 Jun 1996*.
45. C. N. Yang and R. L. Mills, *Phys. Rev.* **96**, 191 (1954).
46. S. L. Glashow, *Nucl. Phys.* **22**, 578 (1961).
47. Leo, W. R., *Techniques For Nuclear and Particle Physics Experiments*, Springer Verlag, Berlin, 1992.
48. General information concerning CESR can currently be found on the World Wide Web at <http://www.lns.cornell.edu/public/lab-info/cesr.html>.
49. Y. Kubota *et al.* [CLEO Collaboration], *Nucl. Instrum. Meth. A* **320**, 66 (1992).
50. C. Bebek *et al.*, *Nucl. Instrum. Meth. A* **302**, 261 (1991).
51. N. Isgur, C. Morningstar, and C. Reader, *Phys. Rev. D* **39**, 1357 (1989).
52. J. H. Kühn and A. Santamaria, *Z. Phys. C* **48**, 445 (1990).
53. M. Feindt, *Z. Phys. C* **48**, 681 (1990).
54. Y. P. Ivanov, A. A. Osipov, and M. K. Volkov, *Z. Phys. C* **49**, 563 (1991).
55. M. G. Bowler, *Phys. Lett. B* **209**, 99 (1988).
56. N. A. Törnqvist, *Z. Phys. C* **36**, 695 (1987) [Erratum-*ibid.* C **40**, 632 (1987)].
57. J. Stern, N. H. Fuchs, and M. Knecht, *Proc. Third Workshop on the τ -Charm Factory*, 197-221, (1993).
58. R. Decker, M. Finkemeier, and E. Mirkes, *Phys. Rev. D* **50**, 6863 (1994) [hep-ph/9310270].

59. **KORALB** (v.2.2)/**TAUOLA** (v.2.4) were used. References: S. Jadach and Z. Was, *Comput. Phys. Commun.* **36**, 191 (1985); **64**, 267 (1991); S. Jadach, J. Kühn, and Z. Was, *Comput. Phys. Commun.* **64**, 275 (1991); **70**, 69 (1992); **76**, 361 (1993).
60. D. M. Asner *et al.*, [CLEO Collaboration], *Phys. Rev. D* **61**, 012002 (2000) [hep-ex/9902022].
61. R. Brun *et al.*, **GEANT** 3.15, CERN DD/EE/84-1.
62. J. Urheim, *Nucl. Phys. B (Proc. Sppl.)* **55C**, 359 (1997), *Proc. Fourth Workshop on Tau Lepton Physics*, Estes Park Colorado, September 1996.
63. N. A. Törnqvist, *Z. Phys. C* **68**, 647 (1995) [hep-ph/9504372].
64. J. H. Kühn and E. Mirkes, *Z. Phys. C* **56**, 661 (1992) [Erratum-ibid. C **67**, 364 (1992)].
65. Roe, Byron P., *Probability and Statistics in Experimental Physics*, Springer-Verlag, New York, 1992.
Nelson, H., Nelson T. *A Guide to Unbinned Maximum Likelihood Fits*, CBX **98-61**, (1998).
66. R. Kokoski and N. Isgur, *Phys. Rev. D* **35**, 907 (1987).
67. S. Godfrey and N. Isgur, *Phys. Rev. D* **32**, 189 (1985).
68. W. Ruckstuhl *et al.* [DELCO Collaboration], *Phys. Rev. Lett.* **56**, 2132 (1986).
69. W. B. Schmidke *et al.* [Mark II Collaboration], *Phys. Rev. Lett.* **57**, 527 (1986).
70. H. Band *et al.* [MAC Collaboration], *Phys. Lett. B* **198**, 297 (1987).
71. H. Albrecht *et al.* [ARGUS Collaboration], *Z. Phys. C* **33**, 7 (1986).
72. H. Albrecht *et al.* [ARGUS Collaboration], *Z. Phys. C* **58**, 61 (1993).
73. H. Albrecht *et al.* [ARGUS Collaboration], *Phys. Lett. B* **349**, 576 (1995).
74. K. Ackerstaff *et al.* [OPAL Collaboration], *Z. Phys. C* **75**, 593 (1997).

75. P. Abreu *et al.* [DELPHI Collaboration], Phys. Lett. B **426**, 411 (1998).
76. M. Schmidtler, Nucl. Phys. Proc. Suppl. **76**, 271 (1999).
77. C. A. Dominguez and E. de Rafael, Annals Phys. **174**, 372 (1987).
78. Schutz, Bernard F., *A First Course in General Relativity*, Cambridge University Press, 1985.
79. Bjorken, J. D. and Drell, S. D., *Relativistic Quantum Mechanics*, McGraw-Hill, 1965.

APPENDICES

Appendix A: The Lagrangian and the Principle of Least Action

This appendix provides a brief overview of the useful Lagrangian of classical mechanics along with a basic description of the Principle of Least Action. See Reference [36] for more detail.

A particle's state in classical mechanics can be described by its position in some set of coordinates, noted q for brevity, and their time derivative, $\dot{q} \equiv dq/dt$, at some time t . The *Lagrangian* of the particle is defined as its kinetic energy (here denoted T) minus its potential energy, V :

$$L(q, \dot{q}, t) = T - V. \quad (\text{A.1})$$

In general, the coordinates need not be the spatial position of the particle, but can be any set that completely describes the state of the particle—they are called *generalized coordinates*. Further, a system can be composed of many particles, and its Lagrangian will be a sum over all the particles in the system. However, the above notation will suffice for this discussion.

Let the system be found at some position q_1 at time t_1 and at some position q_2 at a later time t_2 . One can consider any given path through space-time that would take the particle between those two states. The integral of the Lagrangian over time along some given path is defined as the *action* (S) of the system:

$$S = \int_{t_1}^{t_2} L(q(t), \dot{q}(t), t) dt. \quad (\text{A.2})$$

The action can be calculated for any path, $q(t)$, that satisfies the initial and final conditions.

One of the most general statements of the laws of motion in classical physics is that a system moving between two states will follow the path that minimizes the action.* This is known as the *principle of least action* (also known as *Hamilton's principle*). To derive equations of motion from that principle, one can begin by assuming that the path of least action has been found to be $q(t)$. Then one can consider any slight change to that path, $\delta q(t)$ such that

$$q'(t) = \dot{q}(t) + \delta \dot{q}(t) \quad \text{and} \quad \dot{q}'(t) = \dot{q}(t) + \delta \dot{q}(t), \quad (\text{A.3})$$

and the initial and final conditions obviously require

$$\delta q(t_1) = \delta q(t_2) = 0. \quad (\text{A.4})$$

The Lagrangian for this path can be expanded to first order to yield

$$L(q(t) + \delta q(t), \dot{q}(t) + \delta \dot{q}(t), t) \simeq L(q(t), \dot{q}(t), t) + \frac{\partial L}{\partial q} \delta q + \frac{\partial L}{\partial \dot{q}} \delta \dot{q}, \quad (\text{A.5})$$

and the difference between the action on the altered path and the least action (found using $L(q(t), \dot{q}(t), t)$) is obviously

$$\delta S = \int_{t_1}^{t_2} \left[\frac{\partial L}{\partial q} \delta q + \frac{\partial L}{\partial \dot{q}} \delta \dot{q} \right] dt. \quad (\text{A.6})$$

The principle of least action is thus satisfied when $\delta S = 0$. Applying this to the above and integrating the second term by parts ($\int u dv = uv - \int v du$, where $u = \frac{\partial L}{\partial \dot{q}}$ and $dv = \delta \dot{q} dt$) produces the following requirement:

$$\delta S = \left[\frac{\partial L}{\partial \dot{q}} \delta q \right]_{t_1}^{t_2} + \int_{t_1}^{t_2} \left[\frac{\partial L}{\partial q} + \frac{d}{dt} \left(\frac{\partial L}{\partial \dot{q}} \right) \right] \delta q dt = 0. \quad (\text{A.7})$$

*Strictly speaking, the path will produce an extremum in the action, but this does not affect the results of this discussion.

The first term vanishes due to the initial and final conditions (Equation A.4), and to meet the requirement for all possible path perturbations, δq , the second term requires

$$\frac{\partial L}{\partial q} + \frac{d}{dt} \left(\frac{\partial L}{\partial \dot{q}} \right) = 0. \quad (\text{A.8})$$

Given that q can be a series of coordinates, this provides a series of equations defining the motion of the system. These are the well known *Lagrange's equations* of motion as derived from the principle of least action.

In the description of quantum mechanics developed by Richard Feynman, a quantum system can follow any conceivable path between two states with each path given the same amplitude but a different phase. The phase of a given path is determined by the action equation, and the total probability amplitude for the transition of the system is given by adding all the amplitudes given their respective phases (some having phases that cancel one another and others having phases that contribute more to the final amplitude). The principle of least action comes into play in that the path of least action will contribute the most to the final amplitude. This can be conceptually argued as follows: Because of the format of the action, paths “near” the path of least action will have similar phases (the derivative of the action near the path of least action is small). However, for paths that deviate greatly from the path of least action, their phases can vary greatly and, as a result, tend to cancel out one another. Thus, the paths that contribute most to the final probability amplitude are those near the path of least action.

Therefore, in quantum mechanics, the probability that a system will undergo a given transformation receives contributions from every single path conceivable. Those contributions only differ in phase determined by the action along each path, and the path of least action provides the largest contribution. In general, the scale that determines what paths are “near to” or “far from” the path of least action is given by, in simple terms, the de Broglie wavelength of the system, $\lambda = h/p$ (which in non-relativistic cases is h/mv). For classical systems (where m is large and the λ scale is small), paths even slightly different from the path of least action (and thus the classical path of motion) tend to interfere in the final amplitude, which is thus very nearly determined solely by the path of least action. For quantum systems, one must consider a “cloud” of paths around the path of least action to reasonably calculate the final amplitude.

Thus the Lagrangian and the principle of least action have a variety of important implications in both classical and quantum physics.

Appendix B: Notes on Four-Vectors and the Metric Tensor

The use of four-component vectors is perhaps most associated with Einstein's relativity, which linked space and time together into a single, four-dimensional manifold*. The position in space where an event occurs and the time that it occurs in a given frame of reference are linked to form the four-dimensional space-time location of the event. By postulating that the laws of physics (including electrodynamics) were the same for all frames of reference, relativity claims that the speed of light should be the same for all frames, and that demands a specific relationship comparing space-time coordinates between observers in different frames of reference. Here, a few notes are given for the interested reader on the implications that arise from those relationships with regards to four-component vectors describing space-time properties.

The basic geometry of space-time (or any manifold) is defined by the form of its invariant interval in a given coordinate system on the manifold—the actual, physical, space-time length between two infinitesimally close events, which must be the same for all observers. In normal three-dimensional space, the distance between two points in Cartesian coordinates is given simply by the extension of the Pythagorean theorem to three dimensions:

$$ds_3^2 = dx^2 + dy^2 + dz^2. \tag{B.1}$$

*The formalities of four vectors can be found in a variety of texts, including [78].

Regardless of how one chooses to describe the space the two points are sitting in, that distance between them is a physical reality that doesn't change. For example, a rotation of the coordinate system can change dx , dy , and dz , but not the length given by the above combination.

For space-time in the absence of a gravitational field (“flat” space-time), the proper infinitesimal interval is given by*.

$$ds^2 = c^2 dt^2 - (dx^2 + dy^2 + dz^2), \quad (\text{B.2})$$

where c is the speed of light. Through relativity, the distances in the individual components of space and time between two infinitesimally close events are different for different observers, but this interval is always the same—it is the physical space-time distance between the two events. Its format defines all the consequences of special relativity (such as “time-dilation” and “length-contraction” effects as well as the connection between energy, momentum, and mass).

For convenience of notation, one often defines

$$x^0 = ct, \quad x^1 = x, \quad x^2 = y, \quad \text{and} \quad x^3 = z, \quad (\text{B.3})$$

and a generic invariant interval (for flat or curved space-time), can be written in terms of a 4×4 matrix, \mathbf{g} .

$$ds^2 = \sum_{\mu=0}^3 \sum_{\nu=0}^3 g_{\mu\nu} (dx^\mu dx^\nu) \equiv g_{\mu\nu} dx^\mu dx^\nu. \quad (\text{B.4})$$

*One could equivalently choose to use $ds^2 = -c^2 dt^2 + dx^2 + dy^2 + dz^2$ without changing the resulting mathematics.

The final equivalence defines a summation notation known as *Einstein's summation convention* in which repeated indices in the upper and lower positions imply summation.

The invariant interval (and the geometry of a manifold) is thus completely determined from the form of \mathbf{g} , which will transform as a tensor. It is known as the *metric tensor* (or simply *the metric*). Describing its significance another way, the format of the metric takes all the geometry of the manifold into account as it generates (among other things) the invariant interval. For flat space-time noted above, the metric is obviously given by

$$g_{\mu\nu} = \begin{pmatrix} +1 & 0 & 0 & 0 \\ 0 & -1 & 0 & 0 \\ 0 & 0 & -1 & 0 \\ 0 & 0 & 0 & -1 \end{pmatrix}. \quad (\text{B.5})$$

The metric is a powerful tool, defining various proper mathematical operations in the given space. Consider a vector \vec{V} being transformed from one set of coordinates (\mathbf{x}) to another (\mathbf{x}'). The vector's components transforms as

$$V^{\mu'} = V^\nu \frac{\partial x^{\mu'}}{\partial x^\nu}, \quad (\text{B.6})$$

using the summation convention. However, other forms of vectors exist that transform in a different way (e.g., a vector whose components are formed from the derivative of a scalar function with respect to each coordinate: $V^\mu = \partial f / \partial x^\mu$):

$$V^{\mu'} = V^\nu \frac{\partial x^\nu}{\partial x^{\mu'}}. \quad (\text{B.7})$$

Given that basis vectors transform like the latter case, the former (a “usual” vector) is often called *contravariant* (and their indices are placed in a superscript, as shown) while the latter is called *covariant* (distinguished by placing its indices in the subscript). However, for any contravariant (or covariant) vector there exists an associated covariant (or contravariant) vector, which can be found by “lowering” (or “raising”) the index using the metric tensor:

$$V_\nu = g_{\mu\nu} V^\mu, \quad (\text{B.8})$$

where one again uses Einstein’s summation convention*.

What one might call the “proper dot-product” (or scalar product) of two vectors in some space is then given by

$$\mathbf{v} \cdot \mathbf{v} \equiv v_\mu v^\mu = g_{\mu\nu} v^\nu v^\mu. \quad (\text{B.9})$$

As with any proper scalar, this always produces a result that is independent of the coordinate system used. Just as with the invariant interval (which can now be written $ds^2 = dx_\mu dx^\mu$), the form of the metric in different coordinates (or frames of reference) takes the effects of those differences into account to produce an invariant scalar. The metric is also used to find the proper gradient, divergence, etc. on a given manifold using some given set of coordinates in which the metric is defined. In the curved space-time of general relativity, the metric tensor describes the curvature and ultimately determines the equations of motion caused

*For the metric tensor, one finds $g^{\mu\nu}$ from the inverse of $g_{\mu\nu}$, which for a diagonal metric means $g^{\mu\mu} = 1/g_{\mu\mu}$ if $g_{\mu\mu} \neq 0$ and $g^{\mu\nu} = 0$ otherwise.

by Einstein's gravity. Because it is the mathematical description of a manifold's geometry, regardless of how complicated the manifold or the mathematics describing a geometrical problem on the manifold, at the heart of it is always the 4×4 metric tensor.

Returning to the discussion of four-vectors in flat space-time, the four-dimensional location of an event is but one combination that produces a proper four-vector. If a particle has energy E and three-momentum \vec{p} , then its four-momentum can be formed as a proper four-vector, written here as: $\mathbf{p}=(E, c\vec{p})$. Thus energy is simply the time component of the particle's momentum. The scalar product of a particle's four-momentum must define some invariant value, which turns out to be the particle's mass, in accordance with relativity:

$$\begin{aligned}
 p^\mu p_\mu &= (p^0 p_0 + p^1 p_1 + p^2 p_2 + p^3 p_3) \\
 &= p^0 (g_{0\mu} p^\mu) + p^1 (g_{1\mu} p^\mu) + p^2 (g_{2\mu} p^\mu) + p^3 (g_{3\mu} p^\mu) \\
 &= (p^0)^2 - (p^1)^2 - (p^2)^2 - (p^3)^2 \\
 &= E^2 - c^2 [(p^1)^2 + (p^2)^2 + (p^3)^2] \\
 &= m^2 c^4.
 \end{aligned} \tag{B.10}$$

In electrodynamics, the charge density (ρ) and the current density (\vec{J}) form a proper four-vector, $\mathbf{J} = (c\rho, \vec{J})$ as do the scalar (V) and vector potential (\vec{J}); and various vector manipulations form laws of electrodynamics.

Four-vectors are extremely useful tools in all realms of physics, and are used extensively in high energy physics as well as sections of this dissertation.

Appendix C: Common Wave Equations

Basic wave equations in quantum mechanics arise from the classic Hamiltonian.* The Hamiltonian is an equation for the total energy of a system, which can be derived in general from the equations of motion governing the system. For example, from a basic Lagrangian as discussed in Appendix A ($L(q, \dot{q})$), the Hamiltonian is given by

$$H = \dot{q} \frac{\partial L}{\partial \dot{q}} - L. \quad (\text{C.1})$$

For Newtonian physics, the Hamiltonian is the kinetic energy (T) plus the potential energy (V): $H = T + V$. By substituting quantum mechanical operators into the Hamiltonian, a wave equation is produced.

One can intuit the operators for momentum and energy by first considering a standard plane wave with wave number k and angular frequency ω (in one dimension for brevity):

$$\Psi(x, t) = A e^{i(kx - \omega t)}. \quad (\text{C.2})$$

The wave length (λ) and frequency (ν) of the wave are related to k and ω as

$$k = \frac{2\pi}{\lambda} \quad \text{and} \quad \omega = 2\pi\nu. \quad (\text{C.3})$$

If this describes an electromagnetic wave, then the quantization of electromagnetic energy requires

$$E = h\nu = \hbar\omega \quad \text{and} \quad p = \frac{h}{\lambda} = \hbar k. \quad (\text{C.4})$$

*The concepts presented here can be found in a number of quantum mechanics texts including [23, 79].

Noting the similarity between quantization of states and allowed frequencies for standing waves, and noting that the quantum picture of electromagnetic interactions requires particle-like and wave-like structures, Louis de Broglie argued that the quantum theory of matter should adopt a similar dual picture. The matter-wave hypothesis assigns a wavelength (the de Broglie wavelength) to any particle given its momentum, p , in accordance with the above description for the photon:[†]

$$\lambda = \frac{h}{p}. \quad (\text{C.5})$$

One can then apply the above energy and momentum notations to the Hamiltonian for, say, a non-relativistic particle of mass m (where $T = mv^2/2 = p^2/2m$):

$$E = \frac{p^2}{2m} + V \quad \Rightarrow \quad \hbar\omega = \frac{\hbar^2 k^2}{2m} + V. \quad (\text{C.6})$$

If V is an arbitrary constant in space and time, then the above relation does not cause it to affect derivatives of ω and k . In that case, given that the matter-wave is assumed to be described via Equation C.2, it can be noted that the above equation is obtained by interpreting E and p as operators acting on the wave function:

$$E \rightarrow \tilde{H} \equiv i\hbar \frac{\partial}{\partial t} \quad \text{and} \quad p \rightarrow \tilde{p} \equiv -i\hbar \frac{\partial}{\partial x}, \quad (\text{C.7})$$

such that the energy equation above becomes a wave equation:

$$\tilde{H}\Psi(x, t) = \frac{\tilde{p}^2}{2m}\Psi(x, t) + V\Psi(x, t), \quad (\text{C.8})$$

[†]The Bohr atom can be seen in this picture by requiring the electron to be a standing wave with integer de Broglie wavelengths ($\lambda = h/p$) around the circumference ($2\pi r$) of its orbit: $2\pi r = n\lambda$ so $r = n\hbar/p$ such that $L = pr = n\hbar$ is the obviously quantized angular momentum.

$$\begin{aligned}
i\hbar \frac{\partial}{\partial t} (A e^{i(kx-\omega t)}) &= -\frac{\hbar^2}{2m} \frac{\partial^2}{\partial x^2} (A e^{i(kx-\omega t)}) + V A e^{i(kx-\omega t)}, \\
\hbar\omega A e^{i(kx-\omega t)} &= \frac{\hbar^2 k^2}{2m} A e^{i(kx-\omega t)} + V A e^{i(kx-\omega t)}, \\
\hbar\omega &= \frac{\hbar^2 k^2}{2m} + V,
\end{aligned}$$

thus producing the same results as Equation C.6.* Though the assignment of operators for energy and momentum and the generated wave equation cannot be considered derived results, the hypothesis yields a variety of quantum mechanical predictions that match measurements on physical systems.

C.1 The Schrödinger Wave Equation

The *Schrödinger wave equation* is produced by writing Equation C.8 in three dimensions and allowing the potential to be an arbitrary function:

$$-\frac{\hbar^2}{2m} \nabla^2 \Psi(\vec{x}, t) + V(\vec{x}, t) \Psi(\vec{x}, t) = i\hbar \frac{\partial}{\partial t} \Psi(\vec{x}, t). \quad (\text{C.9})$$

It describes the quantum mechanical nature of a non-relativistic particle in a potential, V . The exact form of the wave function, Ψ , is determined by the form of the potential.

For a free particle ($V = 0$), the Schrödinger equation becomes

$$\frac{\partial}{\partial t} \Phi = \frac{i\hbar}{2m} \frac{\partial^2}{\partial x^2} \Phi, \quad (\text{C.10})$$

and the basic solution gives the wave function for a free, non-relativistic particle:

$$\Phi = e^{i[\vec{p}\cdot\vec{x} - (p^2/2m)t]}. \quad (\text{C.11})$$

*The fact that V can be any arbitrary constant, including zero, without changing the given results is an indication of a type of gauge invariance as discussed in Section 1.12.

C.2 The Klein-Gordon Equation

In the relativistic case, the energy equation for a free particle is given by the quadratic relation

$$E^2 = p^2c^2 + m^2c^4. \quad (\text{C.12})$$

The non-relativistic case is, of course, derived by expanding the energy in terms of p/mc ($E \simeq mc^2 + p^2/2m$) and, as with the case of an arbitrary constant potential, the mass energy can be ignored in the classic case (thus using $E = T + V$ rather than $E = T + V + mc^2$).

Applying the energy and momentum operators to the relativistic case produces the *Klein-Gordon equation*:

$$\hbar^2 \frac{\partial^2 \Psi}{\partial t^2} = \hbar^2 c^2 \nabla^2 \Psi - m^2 c^4 \Psi. \quad (\text{C.13})$$

Solutions to this equation describe free, relativistic, spinless particles. For a massless particle, the Klein-Gordon equation becomes

$$\nabla^2 \Psi = \frac{1}{c^2} \frac{\partial^2 \Psi}{\partial t^2}, \quad (\text{C.14})$$

which is precisely the equation for a classical oscillating wave traveling at velocity c . This equation can be used to describe either the electric or the magnetic portion of an electromagnetic wave, and for both cases it can be derived from Maxwell's equations where $c = \sqrt{\mu_0 \epsilon_0}$.* The solution to Equation C.14 thus describes a free

*In Maxwell's time, μ_0 and ϵ_0 were separate, experimentally determined constants governing electric and magnetic effects in free space. Their combination in the wave equation implied that light was an electromagnetic wave with speed

photon, but only if we argue that the equation describes two separate components of the photon's wave function—the E and B fields described in Maxwell's equations where they are coupled together in first order differential equations. This interpretation allows for the description of the spin-1 photon.

Finding useful solutions to the Klein-Gordon equation to describe a single, massive particle proved problematic due to its second order nature. In one sense, the proper relativistic energy equation to use is $E = \pm c\sqrt{p^2 + m^2c^4}$, though this doesn't lead to an obviously derivable wave equation. Dirac's approach provided a solution for this problem (as well as an interpretation for the indicated negative energy state).

C.3 The Dirac Equation

Dirac's formulation of the relativistic wave equation is analogous to the massless photon solution in which its wave must be described with two components, each of which satisfy the second-order wave equation, but which are also linked in first order differential equations. He assumed that only first order derivatives of both space and time should appear in the wave equation. The results describe spin- $\frac{1}{2}$ particles. The idea can first be applied to find solutions for massless, spin- $\frac{1}{2}$ particles (neutrinos) by forming the two *Weyl equations*, which differ in sign:

$$\frac{1}{c} \frac{\partial \Psi}{\partial t} = \pm \sum_{i=1}^3 \sigma^i \frac{\partial \Psi}{\partial x^i} = \pm \vec{\sigma} \cdot \frac{\partial \Psi}{\partial \vec{x}}, \quad (\text{C.15})$$

$c = \sqrt{\mu_0 \epsilon_0}$. As it turns out, if electrodynamic laws are frame-independent, then so are these constants and thus the speed of light is frame independent—the basis for special relativity.

where the σ 's are constants of a form to be determined. The equation is also required to satisfy the Klein-Gordon second order equation, and thus squaring the above and setting it equal to Equation C.14 yields

$$\begin{aligned} \frac{1}{c^2} \frac{\partial^2 \Psi}{\partial t^2} &= \sum_{i=1}^3 (\sigma^i)^2 \frac{\partial^2 \Psi}{\partial (x^i)^2} \\ &\quad + \{\sigma^1, \sigma^2\} \frac{\partial^2 \Psi}{\partial x^1 \partial x^2} + \{\sigma^1, \sigma^3\} \frac{\partial^2 \Psi}{\partial x^1 \partial x^3} + \{\sigma^2, \sigma^3\} \frac{\partial^2 \Psi}{\partial x^2 \partial x^3} \quad (\text{C.16}) \\ &= \nabla^2 \Psi = \sum_{i=1}^3 \frac{\partial^2 \Psi}{\partial (x^i)^2}, \end{aligned}$$

where $\{X, Y\} \equiv XY + YX$. The equality then requires

$$\sigma^i \sigma^j + \sigma^j \sigma^i = 2\delta_{ij} \quad \text{where} \quad \delta_{ij} = \begin{cases} 1 & \text{if } i = j \\ 0 & \text{if } i \neq j. \end{cases} \quad (\text{C.17})$$

Given these requirements, the σ 's cannot be numbers but must be matrices. In one (but not the only) solution, they are the 2×2 Pauli spin matrices:

$$\sigma^1 = \begin{bmatrix} 0 & 1 \\ 1 & 0 \end{bmatrix}, \quad \sigma^2 = \begin{bmatrix} 0 & -i \\ i & 0 \end{bmatrix}, \quad \sigma^3 = \begin{bmatrix} 1 & 0 \\ 0 & -1 \end{bmatrix}, \quad (\text{C.18})$$

where

$$\sigma^0 \equiv (\sigma^i)^2 = \begin{bmatrix} 1 & 0 \\ 0 & 1 \end{bmatrix}. \quad (\text{C.19})$$

Since the wave function is acted on by these matrices, it must now have two components (somewhat analogous to the requirements of both electric and magnetic components to describe a photon wave):

$$\Psi = \begin{bmatrix} \Psi_1 \\ \Psi_2 \end{bmatrix}. \quad (\text{C.20})$$

The addition of the mass term to the wave equation produces the *Dirac equation*, which can be written

$$\sum_{i=0}^3 \gamma^i \frac{\partial \Psi}{\partial x^i} + \frac{imc}{\hbar} \Psi = 0, \quad (\text{C.21})$$

where $x^0 = ct$. Requiring that the second order Klein-Gordon equation also be met produces a similar results as before:

$$\gamma^\mu \gamma^\nu + \gamma^\nu \gamma^\mu = 2g^{\mu\nu}, \quad (\text{C.22})$$

where $g^{\mu\nu}$ is defined in Appendix B. However, here four matrices are needed, and one property of the Pauli matrices is that there is no fourth 2×2 matrix that can meet the needed requirements and is independent of the already defined σ 's. The simplest set of four matrices that will meet the requirements are 4×4 , and one solution is often written

$$\gamma^0 = \begin{bmatrix} \mathbf{1} & \mathbf{0} \\ \mathbf{0} & -\mathbf{1} \end{bmatrix} \quad \text{and} \quad \gamma^k = \begin{bmatrix} \mathbf{0} & \sigma^k \\ -\sigma^k & \mathbf{0} \end{bmatrix} \quad \text{for } k = 1, 2, 3, \quad (\text{C.23})$$

where $\mathbf{0}$ represents the 2×2 zero matrix and $\mathbf{1}$ is the 2×2 identity matrix. Written out fully, the γ -matrices are thus

$$\begin{aligned}
 \gamma^0 &= \begin{bmatrix} 1 & 0 & 0 & 0 \\ 0 & 1 & 0 & 0 \\ 0 & 0 & -1 & 0 \\ 0 & 0 & 0 & -1 \end{bmatrix} & \gamma^1 &= \begin{bmatrix} 0 & 0 & 0 & 1 \\ 0 & 0 & 1 & 0 \\ 0 & -1 & 0 & 0 \\ -1 & 0 & 0 & 0 \end{bmatrix} \\
 \gamma^2 &= \begin{bmatrix} 0 & 0 & 0 & -i \\ 0 & 0 & i & 0 \\ 0 & i & 0 & 0 \\ -i & 0 & 0 & 0 \end{bmatrix} & \gamma^3 &= \begin{bmatrix} 0 & 0 & 1 & 0 \\ 0 & 0 & 0 & -1 \\ -1 & 0 & 0 & 0 \\ 0 & 1 & 0 & 0 \end{bmatrix}.
 \end{aligned} \tag{C.24}$$

The product of the γ 's is also a useful matrix and is often defined γ^5 (not γ^4 because it is used rather than γ^0 in some notations):

$$\gamma^5 = i\gamma^0\gamma^1\gamma^2\gamma^3 = \begin{bmatrix} 0 & 0 & -1 & 0 \\ 0 & 0 & 0 & -1 \\ -1 & 0 & 0 & 0 \\ 0 & -1 & 0 & 0 \end{bmatrix}. \tag{C.25}$$

Solutions to the Dirac equation (four simultaneous equations) are four component wave functions called *spinors*, which describe free spin- $\frac{1}{2}$ fermions. This is the origin of the general notation $|\Psi|^2 = \Psi^\dagger\Psi$ rather than the less general

$|\Psi|^2 = \Psi^* \Psi$. One can thus write

$$\Psi = \begin{bmatrix} \Psi_1 \\ \Psi_2 \\ \Psi_3 \\ \Psi_4 \end{bmatrix} \quad \text{and} \quad \Psi^\dagger = [\Psi_1^* \ \Psi_2^* \ \Psi_3^* \ \Psi_4^*]. \quad (\text{C.26})$$

Four “basis” solutions can be found for the Dirac equation,* and because of the form of the Dirac’s approach, it turns out that two of the solutions are associated with positive energy states, while the other two are associated with negative energy states. Dirac conjectured that the negative states comprised a sea that was completely filled. When a negative energy electron received enough energy to put it into a positive state, the “hole” left in the sea could be interpreted as having properties of an antielectron (this then is a description of pair production). Thus Dirac correctly predicted antimatter.

The γ -matrices act on the wave functions to produce a variety of useful operations. For example, γ^0 is the parity operation for the spinors. It is also useful to define the notation

$$\bar{\Psi} = \Psi^\dagger \gamma^0, \quad (\text{C.27})$$

such that $\bar{\Psi} \gamma^0 = \Psi^\dagger$, and $\bar{\Psi}$ is also a solution to the Dirac equation.

*Specific solutions are given in [25].

Five independent combinations of the operators can be identified by their Lorentz behavior (see Section 1.7.7):

$$\begin{aligned}
 \text{scalar (S): } & \bar{\Psi}\Psi = \Psi^\dagger\gamma_0\Psi, \\
 \text{pseudoscalar (P): } & \bar{\Psi}\gamma^5\Psi. \\
 \text{vector (V): } & \bar{\Psi}\gamma^\mu\Psi, \\
 \text{axial vector (A): } & \bar{\Psi}\gamma^5\gamma^\mu\Psi, \\
 \text{tensor (T): } & i\bar{\Psi}\gamma^\mu\gamma^\nu\Psi,
 \end{aligned}
 \tag{C.28}$$

The γ -matrices thus provide various operations for forming matrix elements that describe fermion interactions given the transformation properties governing the interaction.

Appendix D: A Simple Example of a Symmetry Group

To present a basic example of symmetry for the interested reader, the symmetry operations on an equilateral triangle will be briefly discussed here. Such a triangle is presented in Figure D.1. One example of a symmetry operation on the triangle is that of rotating it clockwise by 120° (noted R_{120}), which leaves it looking the same as it did before. Similarly, one could rotate it by 240° (R_{240}). However, continuing the trend to turn it 360° returns it back to its original orientation, and there is no difference between such an action and the identity operation (1, which is effectively defined as doing nothing to it). Similarly, rotating counter-clockwise only reproduces either one of the two rotations already defined or the identity operation.

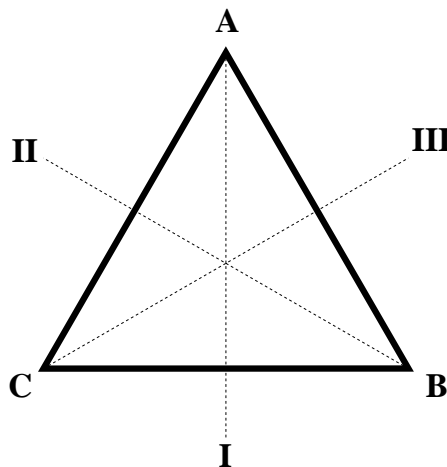


Figure D.1

An equilateral triangle with vertices and symmetry axes marked.

Three axes are also shown on the diagram denoted I , II , and III . By reflecting the triangle through any of these axes, one produces a symmetry operation unlike any of the rotations. These reflections are denoted R_I , R_{II} , and R_{III} . Thus the complete set of operators under which the equilateral triangle is symmetric consists of the operators 1, R_{120} , R_{240} , R_I , R_{II} , and R_{III} .

By performing one operator after another, one can create various combinations. For example rotating by 240° places the vertex labeled B in the upper position, followed clockwise by C in the lower right, and A in the lower left. If one then reflects the triangle through the I axis (which doesn't move with the operations), then A and C trade places, leaving the sequence (starting from the top and going clockwise) as B , A , then C . However, this is the same as a single reflection through the III axis, and one can thus write:

$$R_I \times R_{240} = R_{III}, \quad (\text{D.1})$$

where the \times symbol is defined as first performing the operator to its right, then the one to its left*.

Further, following an R_{240} by an R_{120} produces the same results as the identity matrix. One thus sees here the possibility of these operations forming a group by satisfying the conditions given in Section 1.10. Table D.1 gives the results of performing an operation across the top followed by an operation down the left side (note that the ordering does matter). The result of the two operations is

*This direction of notation is chosen to reflect the action of having two operators act on a wave-function, $\tilde{B}\tilde{A}\Psi$, in which the one to the right acts first.

Table D.1

Combinations of symmetry operators on an equilateral triangle.

		Operator A					
		1	R_{120}	R_{240}	R_I	R_{II}	R_{III}
Operator B	1	1	R_{120}	R_{240}	R_I	R_{II}	R_{III}
	R_{120}	R_{120}	R_{240}	1	R_{III}	R_I	R_{II}
	R_{240}	R_{240}	1	R_{120}	R_{II}	R_{III}	R_I
	R_I	R_I	R_{II}	R_{III}	1	R_{120}	R_{240}
	R_{II}	R_{II}	R_{III}	R_I	R_{240}	1	R_{120}
	R_{III}	R_{III}	R_I	R_{II}	R_{120}	R_{240}	1

given by the matching entry in the table. The reader can then easily verify that the set meets all the group requirements listed earlier. Specifically, this is the full symmetry group of an equilateral triangle and an example of a finite group.

Appendix E: A Simple Example of Spontaneous Symmetry Breaking

A simple example of spontaneous symmetry breaking can be demonstrated [23] by considering a particle with wave function ψ that obeys the Klein-Gordon equation (see Appendix C). However, one allows the mass term in the equation to include contributions proportional to the probability density ($\psi^\dagger\psi$):

$$m^2 = \mu^2 + \lambda\psi^\dagger\psi. \quad (\text{E.1})$$

Since $\psi^\dagger\psi$ is invariant under a phase transformation on ψ , the equation of motion will still possess that gauge invariance.

Because one generally wishes to solve equations of motion perturbatively by expanding around the lowest energy state, the value(s) of the parameter λ of interest are those that minimize m for the given μ . If μ^2 is allowed to be negative (though keeping m real), the solution for the lowest m state becomes $m_{\min} = 0$ when

$$\psi^\dagger\psi = -\frac{\mu^2}{\lambda} \equiv a^2, \quad (\text{E.2})$$

or, letting the real and imaginary parts of ψ be denoted $\psi_R = \Re\psi$ and $\psi_I = \Im\psi$ respectively:

$$\psi_R^2 + \psi_I^2 = a^2. \quad (\text{E.3})$$

That solution is simply the equation for a circle of radius a in the complex plane. Note that only the overall complex radius (or *modulus*) of ψ matters, and not its phase (i.e., a symmetry concerning the phase still appears to hold).

However, to expand around the lowest energy state, a specific solution to the above equation (and therefore a specific phase for ψ) must be chosen (e.g., $\psi_R = a$, $\psi_I = 0$). This choosing immediately “hides” or *breaks* the symmetry by demanding a specific phase. As one tries to impose local gauge invariance by, as before, including some field, A_μ , the spontaneous breakdown of gauge invariance manifests itself by making the field’s range finite, and thus its gauge bosons are no longer massless.

The Higgs mechanism that provides mass to the W^\pm and Z^0 is more complicated than this due to its more complex gauge invariance under $SU(2)\times U(1)$; however, the example given here provides insight into the general notion of symmetry breaking.

Appendix F: The Lepton Tensor in $\tau^\pm \rightarrow \pi^\pm \pi^\pm \pi^\mp (\bar{\nu}_\tau/\nu_\tau)$ decays

In the $\tau^\pm \rightarrow \pi^\pm \pi^\pm \pi^\mp (\bar{\nu}_\tau/\nu_\tau)$ differential decay rate, the lepton tensor appears from the square of the lepton current in the matrix element as noted in Section 5.2. The general, well understood form of the lepton tensor is given in [64] and is repeated here for completeness.

The lepton tensor can be written as four components:

$$L_{\mu\nu} = \frac{1}{2}(g_V^2 + g_A^2) [L_{\mu\nu}^1 + L_{\mu\nu}^2 - \gamma_{VA} (L_{\mu\nu}^3 + L_{\mu\nu}^4)]. \quad (\text{F.1})$$

where

$$\gamma_{VA} = \frac{2g_V g_A}{g_V^2 + g_A^2}. \quad (\text{F.2})$$

In the standard model, the relative V and A couplings are equal such that $g_V = g_A = \gamma_{VA} = 1$.

Noting the 4-momentum of the initial τ as \mathbf{q} , the 4-momentum of the final state neutrino as \mathbf{q}' , and the polarization 4-vector of the τ as \mathbf{s} , the four components of the lepton tensor are given as

$$\begin{aligned} L_{\mu\nu}^1 &= 4 \{q, q'\}_{\mu\nu}, \\ L_{\mu\nu}^2 &= -4 i m_\tau \epsilon_{\alpha\beta\mu\nu} q'^\alpha s^\beta, \\ L_{\mu\nu}^3 &= -4 i \epsilon_{\alpha\beta\mu\nu} q'^\alpha q^\beta, \\ L_{\mu\nu}^4 &= 4 m_\tau \{s, q'\}_{\mu\nu}, \end{aligned} \quad (\text{F.3})$$

where the following notation has been used:

$$\{a, b\}_{\mu\nu} \equiv a_\mu b_\nu + b_\mu a_\nu - a^\alpha b_\alpha g_{\mu\nu}, \quad (\text{F.4})$$

and $\epsilon_{\alpha\beta\mu\nu}$ is the four-dimensional Levi-Civita symbol.* The metric tensor used here is the same as defined in Appendix B.

Note that the polarization 4-vector satisfies the following:

$$q_\mu s^\mu = 0 \quad \text{and} \quad s_\mu s^\mu = -P^2, \quad (\text{F.5})$$

where P is the polarization of the τ in the lab frame. At CESR, τ pairs are produced unpolarized, and thus $P = 0$ for the analysis reported herein.

*If $(\alpha\beta\mu\nu)$ can be formed by performing an even number of permutations (switching two adjacent indices) on (0123) then $\epsilon_{\alpha\beta\mu\nu} = 1$ (e.g., $\epsilon_{0123} = \epsilon_{1032} = \epsilon_{1320} = 1$). If they can be formed by an odd number of permutations on (0123) then $\epsilon_{\alpha\beta\mu\nu} = -1$ (e.g., $\epsilon_{0132} = \epsilon_{1023} = \epsilon_{1230} = -1$). Finally, if any of the four indices are equal, then $\epsilon_{\alpha\beta\mu\nu} = 0$ (e.g., $\epsilon_{0023} = \epsilon_{0101} = \epsilon_{3132} = 0$).

Appendix G: Another Description of the Decay

A useful description of the $\tau^\pm \rightarrow [3\pi]^\pm(\bar{\nu}_\tau/\nu_\tau)$ decay can be found in [64] and will be presented here.

G.1 The S and S' Systems

Two frames of reference are defined—one useful for describing the lepton distribution and one useful for describing the pion distribution. The two are then related through an Euler rotation, thus completely describing the decay.

Both systems are defined in the 3π rest frame. The S' system allows for a simple description of the τ direction. The z' axis is defined in the direction of the laboratory (\hat{n}_L) as viewed from the 3π rest frame (thus the direction of the 3π rest frame in the laboratory system can be denoted $\hat{n}_Q = -\hat{n}_L$). The x' axis is then defined such that the direction of the τ as seen in the 3π rest frame (\hat{n}_τ) is in the (x',z') -plane. The angle between \hat{n}_τ and the z' axis is defined to be ψ (which can be found without measuring the overall τ direction—see below). Note that in the 3π rest frame, the direction of the ν_τ is $\hat{n}_{\nu_\tau} = \hat{n}_\tau$. The y' axis is then defined to produce a right handed system ($\hat{y}' \equiv (\hat{n}_L \times \hat{n}_\tau)/|\hat{n}_L \times \hat{n}_\tau|$). See Figure G.2 for a graphical description of S' .

The S system allows for a simple description of the hadronic tensor. The (x,y) -plane is aligned with the three pion momenta, which lie in a plane in the 3π rest frame. The x axis is defined in the direction of \hat{q}_3 (recall that the “third” pion was defined in Section 5.1 as the one whose charge differs from the other

two). The z axis is then defined in the direction of the normal to the 3π plane ($\hat{z} \equiv \hat{n}_\perp \equiv (\vec{q}_1 \times \vec{q}_2)/|\vec{q}_1 \times \vec{q}_2|$), and the y axis is defined as needed to produce a right handed system. See Figure G.1 for a graphical description of S .

The two systems, S and S' , are related through an Euler rotation (R):

$$\vec{v} = R(\alpha, \beta, \gamma)\vec{v}', \quad (\text{G.1})$$

where

$$\begin{aligned} R(\alpha, \beta, \gamma) &= \begin{pmatrix} c_\gamma & s_\gamma & 0 \\ -s_\gamma & c_\gamma & 0 \\ 0 & 0 & 1 \end{pmatrix} \begin{pmatrix} c_\beta & 0 & -s_\beta \\ 0 & 1 & 0 \\ s_\beta & 0 & c_\beta \end{pmatrix} \begin{pmatrix} c_\alpha & s_\alpha & 0 \\ -s_\alpha & c_\alpha & 0 \\ 0 & 0 & 1 \end{pmatrix} \\ &= \begin{pmatrix} c_\alpha c_\beta c_\gamma - s_\alpha s_\gamma & s_\alpha c_\beta c_\gamma + c_\alpha s_\gamma & -s_\beta c_\gamma \\ -c_\alpha c_\beta s_\gamma - s_\alpha c_\gamma & -s_\alpha c_\beta s_\gamma + c_\alpha c_\gamma & s_\beta s_\gamma \\ s_\beta c_\alpha & s_\beta s_\alpha & c_\gamma \end{pmatrix}, \end{aligned} \quad (\text{G.2})$$

and in which one defines the notations $c_x = \cos x$ and $s_x = \sin x$.

Given this rotation, the Euler angles are defined as follows: The azimuthal angle α is defined as the angle between the $(\hat{n}_L, \hat{n}_\tau)$ -plane and the $(\hat{n}_L, \hat{n}_\perp)$ -plane.

Calculating this angle requires knowledge of the τ direction:

$$\cos \alpha = \frac{(\hat{n}_L \times \hat{n}_\tau) \cdot (\hat{n}_L \times \hat{n}_\perp)}{|\hat{n}_L \times \hat{n}_\tau| |\hat{n}_L \times \hat{n}_\perp|}, \quad (\text{G.3})$$

$$\sin \alpha = \frac{\hat{n}_\tau \cdot (\hat{n}_L \times \hat{n}_\perp)}{|\hat{n}_L \times \hat{n}_\tau| |\hat{n}_L \times \hat{n}_\perp|}. \quad (\text{G.4})$$

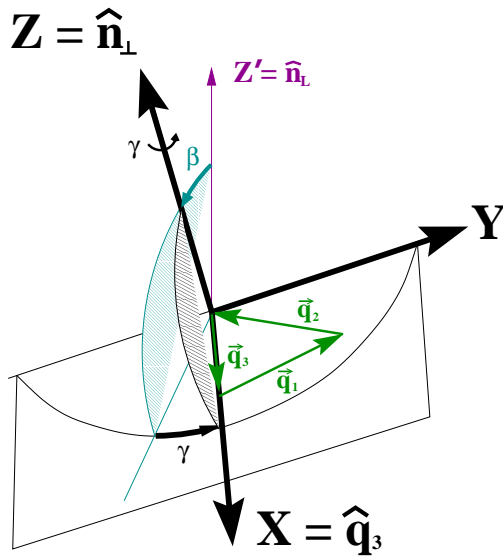


Figure G.1

A representation of the S system defined in the 3π rest frame such that z is perpendicular to the 3π plane and $x = \hat{q}_3$. Also shown are two of the Euler angles, β and γ (see Figure G.3).

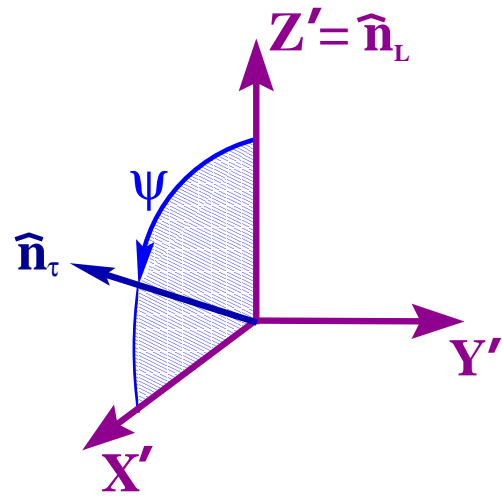


Figure G.2

A representation of the S' system defined in the 3π rest frame. The x' and z' axes are defined such that \vec{q}_τ lies in their plane (ψ being the angle between z' and the τ direction in this frame).

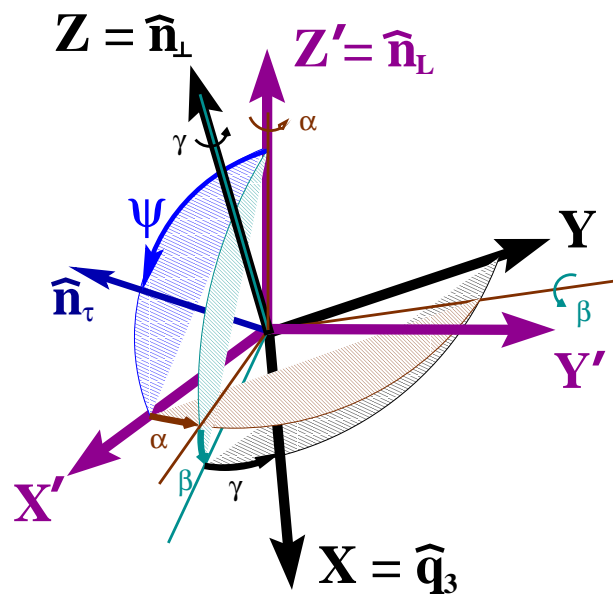


Figure G.3

A display of the Euler angles, α , β , and γ , which relate the S frame to the S' frame.

The polar angle β denotes the angle between \hat{n}_\perp and \hat{n}_L . It can be defined without knowledge of the τ direction:

$$\cos \beta = \hat{n}_L \cdot \hat{n}_\perp \quad (0 \leq \beta < \pi). \quad (\text{G.5})$$

Finally, the angle γ is a rotation about \hat{n}_\perp and determines the orientation of the pions with their production plane (i.e., γ denotes the angle between the $(z', z) \equiv (\hat{n}_L, \hat{n}_\perp)$ -plane and the $(z, x) \equiv (\hat{n}_\perp, \vec{q}_3)$ -plane). As with β , γ can be defined without knowledge of the τ direction:

$$\cos \gamma = -\frac{\hat{n}_L \cdot \hat{q}_3}{|\hat{n}_L \times \hat{n}_\perp|}, \quad (\text{G.6})$$

$$\sin \gamma = \frac{(\hat{n}_L \times \hat{n}_\perp) \cdot \hat{q}_3}{|\hat{n}_L \times \hat{n}_\perp|}. \quad (\text{G.7})$$

The Euler angles are displayed in Figure G.3, while β and γ are reiterated in Figure G.1.

G.2 Describing the Decay

Using these two frames, and assuming knowledge of the three Euler angles, one can describe the decay fully in the laboratory frame as follows: Given Q^2 , s_1 , and s_2 , one can construct the S system by defining the pion momenta as measured in the 3π rest frame:

$$\begin{aligned}
q_i^0 &= E_i = \frac{Q^2 - s_i + m_\pi^2}{2Q}, \\
q_3^1 &= \sqrt{E_3^2 - m_\pi^2}, \\
q_3^2 &= 0, \\
q_3^3 &= 0, \\
q_2^1 &= (2E_2E_3 - s_1 + 2m_\pi^2)/(2q_3^1), \\
q_2^2 &= -\sqrt{E_2^2 - (q_2^1)^2 - m_\pi^2}, \\
q_2^3 &= 0, \\
q_1^1 &= (2E_1E_3 - s_2 + 2m_\pi^2)/(2q_3^1), \\
q_1^2 &= \sqrt{E_1^2 - (q_1^1)^2 - m_\pi^2} = -q_2^2, \\
q_1^3 &= 0.
\end{aligned} \tag{G.8}$$

The three Euler angles are then used to rotate the S system to the S' system ($\vec{v}' = R^{-1}(\alpha, \beta, \gamma)\vec{v} = R(-\gamma, -\beta, -\alpha)\vec{v}$). In this system, the direction of the τ is defined given ψ , which can in turn be calculated given Q^2 , the energy of the 3π system in the lab ($E_{3\pi}$), and the energy of the τ in the lab (E_τ):

$$\cos \psi = \frac{E_{3\pi}(m_\tau^2 + Q^2) - 2E_\tau Q^2}{(m_\tau^2 - Q^2)\sqrt{E_{3\pi}^2 - Q^2}} \quad (0 \leq \psi < \pi/2). \tag{G.9}$$

The z' axis establishes the direction back to the lab frame, and given $E_{3\pi}$ it is possible to boost the pion momenta and the τ direction from the S' frame back to the lab frame. (Alternatively, it is possible to transform E_τ to S' , thus completely describing the decay in that system.) To complete the description of the event in the lab system, one must rotate the boosted S' system to the lab system. However,

if one is not interested in the orientation of the decay in the lab, a full description of the decay can be found given Q^2 , s_1 , s_2 , α , β , γ , $E_{3\pi}$, and E_τ (the last of which can, as noted in Section 6.1, be found from E_{beam} and E_γ). Of those, α is the only variables that depends on full knowledge of the τ direction.

As an alternative, $E_{3\pi}$ and E_τ can be replaced by $\cos \psi$ and $\cos \theta$. The angle θ is defined as the angle between the direction of the τ in the laboratory rest frame and the direction of the hadrons as seen in the τ rest frame. As with $\cos \psi$, it is possible to calculate $\cos \theta$ from Q^2 , $E_{3\pi}$, and E_τ :

$$\cos \theta = -\frac{E_\tau(m_\tau^2 + Q^2) - 2E_{3\pi}m_\tau^2}{(m_\tau^2 - Q^2)\sqrt{E_\tau^2 - m_\tau^2}}. \quad (\text{G.10})$$

A complete description of the decay in the S' system can thus be defined given Q^2 , s_1 , s_2 , α , β , γ , $\cos \theta$, and $\cos \psi$.

Appendix H: The γ Distribution

The distribution in γ will be described here in a similar fashion to its description in [57]. Integrating the basic differential decay rate given in [64] over α and β (defined above), one finds the following at a given E_τ (or, ideally, at a given beam energy):

$$d\Gamma(Q^2, s_1, s_2, \gamma, \cos \theta) = \frac{G_F^2 V_{ud}^2}{128 m_\tau (2\pi)^5} \left(\frac{m_\tau^2 - Q^2}{Q^2} \right)^2 \frac{m_\tau^2 + 2Q^2}{3m_\tau^2} \quad (\text{H.1})$$

$$\times W(Q^2, s_1, s_2) \omega(\gamma, Q^2, s_1, s_2, \cos \theta) dQ^2 ds_1 ds_2 \frac{d\gamma}{2\pi} \frac{d\cos \theta}{2},$$

where W gives the differential decay rate integrated over all angles, and is defined in terms of the hadronic structure functions in [64] as follows:

$$W(Q^2, s_1, s_2) = W_A + \frac{3m_\tau^2}{m_\tau^2 + 2Q^2} W_{SA}. \quad (\text{H.2})$$

Note that the W_A term is composed of second order terms in the F_1 and F_2 form factors; however, the W_{SA} term is dependent on the square of the minute scalar form factor ($W_{SA} = Q^2 |F_4|^2$) making it insignificant in the makeup of W .

The ω factor can be thought of as the normalized distribution in the azimuthal angle γ for a given Q^2 , s_1 , s_2 , and $\cos \theta$. It can be written as follows:

$$\omega(\gamma, Q^2, s_1, s_2, \cos \theta) = 1 + \lambda_2 (A_C \cos 2\gamma + A_D \sin 2\gamma) + \lambda_1 (A_{SB} \cos \gamma + A_{SD} \sin \gamma). \quad (\text{H.3})$$

The A_C and A_D coefficients involve terms chiefly dependent on the F_1 and F_2 form factors. They are “large” in that they are $O(1)$ in the chiral limit. In terms of the

structure functions, they are defined as follows:

$$A_C = \frac{m_\tau^2 - Q^2}{m_\tau^2 + Q^2} \frac{W_C}{W}, \quad A_D = \frac{m_\tau^2 - Q^2}{m_\tau^2 + Q^2} \frac{W_D}{W}. \quad (\text{H.4})$$

The A_{SB} and A_{SD} coefficients are chiral symmetry breaking quantities dependent on combinations of $F_1 F_4^*$ and $F_2 F_4^*$ interference terms. In terms of the structure functions, they are defined as follows:

$$A_{SB} = \frac{\pi}{4} \frac{3m_\tau^2}{m_\tau^2 + 2Q^2} \frac{W_{SB}}{W}, \quad A_{SD} = -\frac{\pi}{4} \frac{3m_\tau^2}{m_\tau^2 + 2Q^2} \frac{W_{SD}}{W}. \quad (\text{H.5})$$

Finally, the λ_1 and λ_2 coefficients in Equation H.3 describe distributions in $\cos \psi$, which is a non-trivial function of Q^2 , $\cos \theta$, and E_τ (as can be inferred from Equations G.9 and G.10, the equations for $\cos \psi$ and $\cos \theta$ respectively, in Appendix G).

The λ_n functions are defined in terms of the Legendre polynomials, P_n :

$$\lambda_n(Q^2, \cos \theta, E_\tau) = P_n(\cos \psi). \quad (\text{H.6})$$

Therefore, though the reliance of λ_n on Q^2 , $\cos \theta$, and E_τ is generally non-trivial, for any event one can calculate λ_n by way of calculating $\cos \psi$.

In Equation H.3, the presence of non-zero scalar effects would be indicated by asymmetries in the γ distribution (specifically, in the existence of A_{SB} and A_{SD} terms). For the greatest sensitivity to these terms, one could hypothetically use a large data set and examine the γ distribution in bins of Q^2 , s_1 , and s_2 . However, even integrating over all other factors, the presence of any non-zero scalar effects would be expected to show up in the distribution of γ .

Appendix I: Placing a Lower Bound on the Light Quark Masses

As developed in [57] and noted in Section 3.1, experimentally extracting information regarding the scalar effects in $\tau^\pm \rightarrow \pi^\pm \pi^\pm \pi^\mp (\bar{\nu}_\tau/\nu_\tau)$ decays allows one to place a lower limit on the light quark running masses in the QCD Lagrangian. The QCD Lagrangian involves seven parameters that must be experimentally determined: the gauge coupling constant (denoted g) and six quark masses. After renormalization, these parameters become scale dependent, thus the term “running masses.” Hadronic τ decays provide a unique source of information concerning the light quark running masses, m_u , m_d , and m_s because they determine the absolute strength of chiral symmetry breaking in such decays. This follows from the fact that the divergences of observable axial and vector weak-transition currents are given by the following:

$$\begin{aligned}
 \partial^\mu(\bar{d}\gamma_\mu\gamma_5 u) &= (m_d + m_u)\bar{d}i\gamma_5 u, \\
 \partial^\mu(\bar{s}\gamma_\mu\gamma_5 u) &= (m_s + m_u)\bar{s}i\gamma_5 u, \\
 \partial^\mu(\bar{d}\gamma_\mu u) &= (m_d - m_u)i\bar{d}u, \\
 \partial^\mu(\bar{s}\gamma_\mu u) &= (m_s - m_u)i\bar{s}u.
 \end{aligned}
 \tag{I.1}$$

In particular, the $\tau^\pm \rightarrow [3\pi]^\pm (\bar{\nu}_\tau/\nu_\tau)$ decay contributes to $m_u + m_d$, and the average of the two will be termed $\hat{m} \equiv (m_u + m_d)/2$. The other combinations ($m_s + m_u$, $m_s - m_u$, and $m_d - m_u$) could, in principle, be studied using τ decays to $K\pi\pi\nu_\tau$, $K\pi\nu_\tau$, and $\eta\pi\nu_\tau$ respectively [57].

Extracting information on \hat{m} involves the spectral function $\rho(Q^2)$, which measures the amount of explicit chiral symmetry breaking at squared momentum trans-

fer Q^2 . It is given by the expression

$$\rho(Q^2) = \frac{1}{2\pi} \sum_n (2\pi)^4 \delta^{(4)}(\mathbf{Q} - \mathbf{P}_n) |\langle n | \partial^\mu (\bar{d} \gamma_\mu \gamma_5 u | 0 \rangle|^2, \quad (\text{I.2})$$

where the sum extends over all states with quantum numbers of the pion and with squared invariant mass $P_n^2 = Q^2$:

$$n = \pi^\pm, \pi^\pm \pi^\pm \pi^\mp, \pi^\pm \pi^0 \pi^0, \pi^\pm \pi^\pm \pi^\mp \pi^0 \pi^0, \dots \quad (\text{I.3})$$

For large Q^2 , QCD perturbation theory gives the following expression for the spectral function [77]:

$$\rho(Q^2) \rightarrow \frac{3}{2\pi^2} [\hat{m}(Q^2)]^2 Q^2 \left\{ 1 + \frac{17}{3} \frac{\alpha_s(Q^2)}{\pi} + \dots \right\}. \quad (\text{I.4})$$

Therefore, measurement of $\rho(Q^2)$ at sufficiently large Q^2 provides a measurement of $\hat{m}(Q^2)$. The spectral function can be separated into several individual components:

$$\rho(Q^2) = \rho_\pi(Q^2) + \rho_{3\pi}(Q^2) + \rho_{K\bar{K}\pi}(Q^2) + \rho_{5\pi} + \dots, \quad (\text{I.5})$$

where only the one pion contribution is well known given the pion mass and the pion decay constant, f_π :

$$\rho_\pi(Q^2) = 2f_\pi^2 m_\pi^4 \delta(Q^2 - m_\pi^2). \quad (\text{I.6})$$

The remaining components must be experimentally determined.

The $\rho_{3\pi}(Q^2)$ component contains two contributions, $\rho_{\pi^\pm \pi^\pm \pi^\mp}$ and $\rho_{\pi^\pm \pi^0 \pi^0}$, though isospin symmetry implies that

$$\rho_{3\pi} \geq \frac{5}{4} \rho_{\pi^\pm \pi^\pm \pi^\mp}. \quad (\text{I.7})$$

Therefore, by experimentally determining the value of $\rho_{\pi^\pm\pi^\pm\pi^\mp}$, one can place better a lower limit on $\rho(Q^2)$. It is useful to define

$$\rho'(Q^2) \equiv \rho_\pi(Q^2) + \frac{5}{4}\rho_{\pi^\pm\pi^\pm\pi^\mp}(Q^2), \quad (\text{I.8})$$

such that

$$\rho(Q^2) \geq \rho'(Q^2). \quad (\text{I.9})$$

Experimental determination of $\rho_{\pi^\pm\pi^\pm\pi^\mp}$ and its contribution to the light quark running mass is problematic for two reasons: First, $\rho_{\pi^\pm\pi^\pm\pi^\mp}$ is given by the square of the $J = 0$ contribution to the decay rate, which, as previously discussed, is meager and difficult to measure. As noted in Appendix H, interferences between the $J = 0$ and $J = 1$ components provide the most reasonable potential for detecting the scalar contributions and deriving the square of its amplitude. Given such a determination of the amplitude of the scalar form factor, $|F_4(Q^2, s_1, s_2)|$, one could then find:

$$\rho_{\pi^\pm\pi^\pm\pi^\mp}(Q^2) = \frac{Q^2}{512\pi^4} \int |F_4(Q^2, s_1, s_2)|^2 ds_1 ds_2. \quad (\text{I.10})$$

Secondly, Equation I.4 implies that Q^2 is known over a large, asymptotic region, though Q^2 in $\tau^\pm \rightarrow \pi^\pm\pi^\pm\pi^\mp(\bar{\nu}_\tau/\nu_\tau)$ decays is obviously limited by m_τ^2 and strongly suppressed as $Q^2 \rightarrow m_\tau^2$. This issue is resolved by the use of QCD sum rules as noted in [57]. A final equation is presented for a lower bound to \hat{m} , which can be written

$$\hat{m}'^2_{s_0}(\mu^2) \equiv \left(\frac{\ln(s_0/\Lambda^2)}{\ln(\mu^2/\Lambda^2)} \right)^{\frac{24}{29}} \frac{4\pi^2}{3s_0^2} [1 + R_2(s_0) + 2C_4\langle O_4 \rangle/s_0^2]^{-1} \int_0^{s_0} \rho'(Q^2) dQ^2, \quad (\text{I.11})$$

where μ is the running variable, while the two-loop expression for $R_2(s_0)$ and the value of the dimension-4 condensate $C_4\langle O_4 \rangle$ are discussed in [77]. The variable s_0 represents a squared cutoff mass and introduces a source of systematic error arising from imperfections in the method. It is taken to be within a typical range

$$2 \text{ GeV}^2 \leq s_0 \leq m_\tau^2, \quad (\text{I.12})$$

and $\hat{m}'_{s_0}(\mu^2)$ is not expected to depend strongly on its value within that range.

Therefore, by experimentally determining the amplitude of the scalar contributions in $\tau^\pm \rightarrow \pi^\pm \pi^\pm \pi^\mp (\bar{\nu}_\tau/\nu_\tau)$ decays, one could add to the knowledge of the spectral function, $\rho(Q^2)$, and place an improved lower limit on the running mass of the light quarks:*

$$\hat{m}(\mu^2) \geq \hat{m}'_{s_0}(\mu^2). \quad (\text{I.13})$$

An acceptable theoretical estimation constrains \hat{m} at $\mu = 1 \text{ GeV}$ to the range

$$4 \text{ MeV} \leq \hat{m}(1 \text{ GeV}^2) \leq 50 \text{ MeV}, \quad (\text{I.14})$$

though it would be difficult for standard chiral perturbation theory to support a value of \hat{m} significantly higher than $\sim 10 \text{ MeV}$ [57]. One should also note that the light quark masses reported in the PDG [29] are for $\mu = 2 \text{ GeV}$, which must be multiplied by 1.35 to compare to the case were $\mu = 1 \text{ GeV}$. The range for \hat{m} they report, when properly scaled, suggests $3.4 \text{ MeV} \leq \hat{m}(1 \text{ GeV}^2) \leq 8.1 \text{ MeV}$.

Thus, placing a lower limit on \hat{m} provides a test for chiral perturbation and helps to quantify the statement that the u and d quark masses are not zero.

*The one-pion contribution alone suggests $\hat{m}(1 \text{ GeV}^2) \geq (4 - 5) \text{ MeV}$.

VITA

VITA

Jason W. Hinson was born on June 11, 1969 in Griffin, Georgia. After living in Mississippi, Louisiana, and Tennessee, his family settled in Mobile, Alabama in 1979. He attended John S. Shaw High School, where he met the love of his life, Tabitha L. Shellman, and graduated in the honors society in 1987. After a year of class work at the University of South Alabama, he moved from home and began attending the University of Alabama in Huntsville (UAH). While there, he worked for UAH as a laboratory assistant in N.A.S.A.'s Magnetospheric Branch. He received his Bachelor of Science degree from UAH, graduating Summa Cum Laude in May of 1991 with a double major in physics and math. On August 10, 1991 Jason and Tabitha were married, and a week later they moved to West Lafayette, Indiana, where he began graduate work at Purdue University. In May of 1993, he received his Master of Science degree from Purdue. That year, Prof. Edward Shibata graciously agreed to be Jason's doctoral thesis advisor, and Jason began working as a graduate research assistant. In June of 1994 Jason and Tabitha moved to Ithaca, NY, where he began his thesis research at the Cornell Electron Storage Ring (CESR) as a member of the CLEO collaboration. On September 29, 2000, Jason and Tabitha became the proud parents of Hannah Louise Hinson.